Hallvard Berner Hammer

Physical experiments on CPTU thin-layer effects of thin clay layers embedded in sand

With analysis and possible correction of cone resistance in layered profiles

Master's thesis in Civil and Environmental Engineering

August 2020

Master's thesis

NTNU
Norwegian University of Science and Technology
Faculty of Engineering
Department of Civil and Environmental Engineering

NTNU
Norwegian University of
Science and Technology

Hallvard Berner Hammer

Physical experiments on CPTU thin-layer effects of thin clay layers embedded in sand

With analysis and possible correction of cone resistance in layered profiles

Master's thesis in Civil and Environmental Engineering

Supervisor: Professor Steinar Nordal

Co-supervisor: Dr. Jean-Sébastien L'Heureux, NGI

August 2020

Department of Civil and Environmental Engineering

Faculty of Engineering

Norwegian University of Science and Technology (NTNU)

NTNU

Norwegian University of
Science and Technology

PREFACE

This document contains the study through literature review, large scale physical experiments and the development of analysis methods on the detection and interpretation of CPTU measurements of thin clay layers in sand. The study is performed as a Master's thesis in geotechnics in the course TBA4900 as part of the Master of Science in Civil and Environmental Engineering at the Norwegian University of Technology and Science (NTNU). The supervisor of the study was Steinar Nordal, professor in geotechnics at NTNU, together with co-supervisor Dr. Jean-Sébastien L'Heureux of the *Norwegian Geotechnical Institute* (NGI).

Most of the work in this study was related to the physical experiments performed. A new chamber model was designed, and procedures of sample creation were developed. The work on the design included selection and acquisition of a chamber, soil materials and other equipment needed to perform CPTU tests in large sand samples with thin clay layers. Planning and preparation of the physical experiments started at the end of 2019 and continued through the first months of 2020. By mid-March the work on sample creation was ready to begin. However, work in the laboratory was abruptly halted soon after due to the extraordinary events of the spring of 2020 caused by the COVID-19 pandemic. The ensuing lockdown of NTNU including the laboratory area of the experiment, for more than one and a half months severely affected the time schedule of the physical experiments and the thesis.

There were uncertainties at the time of the lockdown regarding whether laboratory work could be continued. As a result, much time was spent on alternative objectives outside the original scope of the thesis. This primarily consisted of a numerical method for evaluation of layering effects based on the inverse filtering procedure developed by Boulanger & DeJong which was presented at the CPT'18 conference in Delft. Much of the available time during the lockdown was spent on development of a new procedure inspired by this.

Fortunately, through the effort of Steinar Nordal and other members of the geotechnical staff, the laboratory work of this study was prioritized during the gradual re-opening of NTNU. This allowed for the work to commence in the start of May. However, due to limited availability of technical staff, some operations caused bottlenecks which further extended the needed time in the laboratory. Each sample created in the chamber required careful preparation. The first sample was finished and tested in the end of May. This test was primarily intended to control the procedures and equipment, and did not contain the thin clay layers, which was planned for the second test. Since it was of great significance to create the sample of thin layers, such a sample was made. Laboratory work were completed by the end of June.

Many people were involved in the different stages of the laboratory work, whom are rightfully acknowledged in the following chapter. However, the total time spent by the author of planning, preparation and execution of the physical experiments far exceeded a normal workload. In the end,

the total time spent directly related to the physical experiments exceeded two thirds of the total expected workload on the 30 ECTS Master's thesis. Much of this was spent in May and June, giving little time to report the work in this thesis.

The uncertainties of the prospect for the laboratory work in March and April resulted in much time spent on alternative objectives. The developed numerical procedure was at the time of the lockdown intended as a substitute in case the laboratory work could not continue during the spring of 2020. However, even after the laboratory work commenced the work was included due to the promising results.

As a result of the ambitions scope of large scale physical experiments and analysis with a developed procedure, most of the work on writing the thesis was left for the summer months of 2020 and by the sacrifice of any summer vacation. Still, the work of this study has been very rewarding. I was given a unique opportunity to design the experiments with magnificent support of a large group of helpful and enthusiastic staff which was a great experience.

Trondheim, 15/08/2020

Hallvard Berner Hammer

ACKNOWLEDGMENTS

SUMMARY

The cone penetrometer is an excellent tool to characterize stratigraphy and have good abilities for parameter interpretation in homogenous soils. However, in soils with small layer thickness, in terms of cone diameters, this thickness combined with the soil properties of the thin layer compared to the surround layers will greatly impact the measured values. Measured cone resistance is a result of complex flow mechanisms that is dependent on the soils property ahead of and behind the advancing cone. The effect of layer thicknesses of sand with varied density has received significant attention and some studies have also been performed on layered clays. There is however little available research on accurate detection of thin clay layers in sand with the CPTU.

Cone resistance measurements in sand normally yields significantly larger values than in clay. Thin clay layers in sand is greatly affected by the surrounding soil and the measurements in these thin layers does therefore not only reflect the clay. Interpretation of properties in clay such as undrained shear strength without taking this effect into consideration will cause overprediction. The magnitude of the overprediction depends primarily on layer thickness and the contrast in strength and stiffness between the clay layer and sand layers above and below.

A large scale chamber model was established to allow for CPTU testing of thin clay layers in saturated sand. The chamber had a diameter of $1.2m$ and a height of $2.5m$. Procedures to create uniform loose to medium dense sand samples were developed. The samples consisted of homogenous, uniformly graded sand and non-sensitive clay with an undrained shear strength of $27.5kPa$. Two samples were made and tested, one of which had clay layers of thicknesses 4, 8 and $12cm$. The other had a single thick clay layer to determine the cone resistance unaffected by layering effects, called the characteristic cone resistance. CPTUs were performed using a standard $10cm^2$ cone. A vertical stress of $11.4kPa$ was added on top of the sample and vertical stress was recorded in the sample during construction. The stress development in the sample resulted in good approximation of the stress level, which showed significant silo effects by frictions along the chamber walls.

The characteristic cone resistance in the clay was between 10% and 20% of that of the sand. In the $4cm$ clay layers the minimum measured cone resistance was 3.5 times higher than the characteristic value. While the difference decreased with increasing thickness, the effect of thin layers was significant for the 8 and $12cm$ thick clay layers as well. The cone resistance in sand was influenced by thin clay layers three cone diameters prior to the layer interface. When the cone entered the thin clay layers the cone resistance appeared to be significantly more affected by the sand layer above the clay layer than the one below. This dependence on the layer above is an important factor for the thin layer effects in clays.

Detection of clay layers is typically done through interpretation of the pore pressure measurements in practice. However, the results from the experiments showed how excess pore pressure

measurements did not reflect the clay layer thickness. In fact, no significant response was seen in the $4cm$ clay layer. This was due to deformations of the clay layer during penetration.

A procedure for simplified numerical cone resistance analysis in layered profiles was developed. It consisted of spatial weighting filters for advanced averaging of the characteristic cone resistance profiles in order to approximate measured profiles. This procedure was applied to the determined characteristic profiles of the physical experiments of this study and the results compared well. Possible methods of correction of cone resistance measurements in thin clay layers in sand was estimated from the procedure together with the results of the physical experiments. Examples of correction is presented.

The experimental work performed in this MSc study has provided high quality CPTU data together with detailed information on material properties and soil stresses. The data can be used in further interpretations aiming to accurately interpret measurements of thin clay layers in sand. The experimental work has been comprehensive, but further testing is recommended. Repeating the tests with other combinations of sand density, thin layer thickness and clay strengths would be of interest.

SAMMENDRAG

CPTU er et utmerket verktøy for å karakterisere stratigrafi og målinger kan brukes til parametertolkning i homogene jordarter. Målinger i lagdelt jord med tynne lag, relativt til diameteren på sonden, vil påvirkes betydelig av en kombinasjon av lagtykkelsen og jordegenskapene til det tynne laget sammenlignet med jorden den er omgitt av. Den målte spissmotstanden er et resultat av en kompleks bruddmekanisme som er avhengig av jordegenskapene både foran og bak spissen. Flere studier har blitt utført vedrørende effekten av tynne lag av sand med variert densitet, men få studier er tilgjengelig angående presis detektering av tynne leirelag i sand med CPTU.

Målinger av spissmotstand i sand er normalt langt høyere enn i leire. Tynne leirelag i sand er svært påvirket av sanden den er omgitt av som medfører at målingene reflekterer leiren dårlig. Parametertolkning i slike lag uten korreksjon for effekt av tynne lag vil medføre overvurdering av for eksempel den udrenerte skjærstyrken. Graden av overvurdering er avhengig av tykkelsen på det tynne leirelaget og kontrasten i spissmotstandene, upåvirket av nærliggende lag, for leira og sanden den er omgitt av.

Et storskala labforsøk i en sylindermodell var etablert for å teste CPTUer i sand med tynne leirelag. Sylinderen hadde diameter på $1.2m$ og høyde på $2.5m$. Prosedyrer for å lage homogene prøver av ensgradert sand og ikke-sensitiv leire med udrenert skjærstyrke på $27.5kPa$ ble utviklet. To prøver ble laget og testet, hvorav en inneholdt tynne lag med tykkelse 4, 8 og $12cm$. Den andre inneholdt et enkelt tykt leirelag for å bestemme den spissmotstanden upåvirket av lagtykkelse, kalt karakteristisk spissmotstand. Standard CPTUer med tverrsnittsareal på $10cm^2$ ble brukt. En spenning på $11.4kPa$ ble påført på toppen av prøven og vertikalspenninger ble loggført under prøvebyggingen. Detaljert informasjon om spenningsnivået i prøven ble tolket fra dette, som viste at betydelige friksjonskrefter virket langs sylinderveggene.

Den karakteristiske spissmotstanden i leira var mellom 10% og 20% av sandens. I det $4cm$ tykke leirelaget var den minste målte spissmotstanden 3.5 ganger høyere enn den karakteristiske verdien. Mens forskjellen minket med økende tykkelse, var effekten av lagtykkelsene tydelige for de 8 og $12cm$ tykke lagene også. Spissmotstanden i sand var påvirket av et leirelag tre ganger sonde-diameteren over det kommende leirelaget. Etter at spissen entret leirelaget framstod målingen av spissmotstanden som langt mer avhengig av sanden over leirelaget enn under. Denne avhengigheten til det passerte laget er ansett som en viktig faktor for tynne lag-effekten i leire.

I praksis brukes som regel poretrykksmålingene fra CPTU til å påvise leirelag. Resultatene fra de labforsøkene viste hvordan det målte poreovertrykket ikke gjenspeilet lagtykkelser. I $4cm$ tykke leirelag viste målingene ingen betydelig respons. Dette skyltes deformasjon av leirelaget fra penetrasjonen.

En prosedyre ble utviklet for å analysere spissmotstandsprofil på en forenklet måte. Det bestod av et dynamisk vektingsvindu som gjennom avansert midling av karakteristiske spissmotstandsverdier

approksimerte målte profil. Prosedyren ble anvendt på det karakteristiske profilet som representerte prøvene i labforsøkene og resultatene samsvarte godt. Mulige metoder for å korrigere spissmotstand i tynne leirelag i sand ble estimert fra denne prosedyren sammen med resultatene fra de fysiske forsøkene. Eksempler på korreksjon er presentert.

Det eksperimentelle arbeidet som ble utført i denne masteroppgaven har gitt CPTU data av høy kvalitet og detaljert informasjon om materialegenskaper og spenninger i prøvene. Dataene kan brukes til videre tolkning med mål om å kunne tolke målinger i tynne leirelag i sand på nøyaktig vis. Labarbeidet har vært omfattende, men videre forsøk anbefales. Det er av interesse å gjenta forsøk med andre kombinasjoner av sanddensitet, lagtykkelser og udrenert skjærstyrke i leire.

TABLE OF CONTENTS

LIST OF FIGURES

LIST OF TABLES

SYMBOLS

a Attraction [kPa]

a Cone area factor for water pressure effect [ ]

B_q Normalized pore pressure parameter [ ]

D_r Relative density [%]

δ Soil-structure interface friction angle [°]

d_c Cone penetrometer diameter [cm]

D_c Chamber diameter [cm]

e Void ratio (volume of pores divided by volume of solids) [ ]

E Young's modulus [MPa]

E_{50} Secant stiffness [MPa]

E_{oed} Oedometer stiffness [MPa]

$\eta,\ \eta_{min}$ Cone resistance ratio [ ]

f_s Side friction [kPa]

F_r Friction ratio [%]

ρ Unit mass density [g/cm^3]

g Gravity acceleration ($g \approx 9.82 m/s^2$ in Norway) [m/s^2]

G Shear stiffness [MPa]

γ Unit weight [kN/m^3]

γ' Effective unit weight [kN/m^3]

γ_w Unit weight of water [kN/m^3]

H Thin layer thickness [cm]

h Sample build height [cm]

I_r Rigidity index [ ]

I_P Plasticity index [ ]

K_H Thin layer correction factor [ ]

K_0 Earth pressure coefficient [ ]

n Soil porosity (volume of pores divided by total volume) [%]

OCR Overconsolidation ratio, $OCR = \sigma'_c / \sigma'_{v0}$ $[kPa]$

p_a Reference/Atmospheric pressure ($\approx 100 \; kPa$) $[kPa]$

ϕ Soil internal friction angle [°]

Q Normalized cone resistance parameter [ ]

Q_{tn} Normalized cone resistance parameter [ ]

q_c Cone resistance $[MPa]$

q_t Cone resistance, corrected for water pressure $[MPa]$

q_{net} Net cone resistance $[MPa]$

q_t^{char} Characteristic cone resistance $[MPa]$

σ_{v0} Initial vertical total stress $[kPa]$

σ'_{v0} Initial vertical effective stress $[kPa]$

$\sigma'_{m0}, \, p'$ Initial mean effective stress $[kPa]$

$s_u, \, s_{u,c}$ Undrained compression shear strength $[kPa]$

σ'_c Preconsolidation stress $[kPa]$

u_2 Pore pressure behind cone $[kPa]$

u_0 In situ pore pressure [kPa]

Δu_2 Excess pore pressure $[kPa]$

w Water content

z Sample/cone penetration depth $[m]$

z_L Local depth of sample $[m]$

1 INTRODUCTION

Detection and accurate characterization of weak layers is critical in most types of geotechnical investigations since failures occur along the path of least resistance in the soil. This is especially important in assessments of geohazards such as landslides. The thickness of these weak layers may not impact the likelihood of failure; however it greatly affects the challenge in detection and interpretation of properties of the layers.

Thin, weak layers may be a result of layering from sedimentation or from distinct events (Locat et al., 2014). An event can for instance be a quick-clay slide where clay deposits are distributed over a large area, forming event beds of thin, clay rich layers (Hansen et al., 2011). The strength of these event beds can differ vastly from the surrounding layers and act as slip planes for slides. The Finneidfjord slide of 1996 is an example of such a slide with catastrophic consequences (L'Heureux et al., 2012). **Figure 1**.**1** presents site investigations performed at the site of the slide. The slip plane was in *regional event bed I* (see **Figure 1**.**1**), an event bed caused by prehistoric quick-clay slide activity. This event bed had a significantly lower shear strength than the surrounding deposits. A sample from the event bed is shown in the figure, illustrating the thin layers of clay.
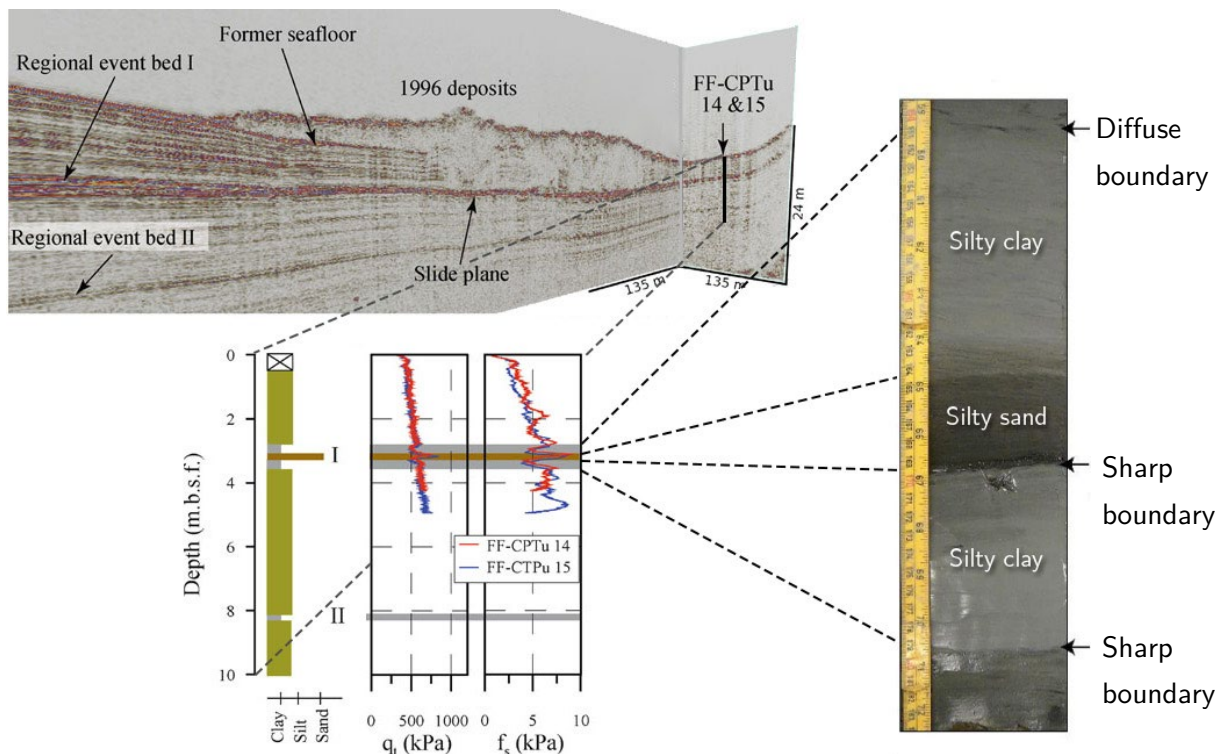
Figure 1.*1. Site investigation from Finneidfjord with seismic measurements (top), CPTU measurement (bottom) and an image of a sample (right). Thin clay layers of thickness less than 10cm were discovered from the samples. Note that the sample is not from the exact same position as the CPTU. Edited after L'Heureux et al. (2012).*

Detection of thin clay layers in sand and silt deposits is a challenging task in standard soil investigations. Investigations consists of a combination of field testing and laboratory testing. Through extensive sampling and laboratory testing, advanced tests can be performed, and various parameters can be interpreted. However, such tests are costly, time consuming and includes uncertainties regarding sample disturbance. Furthermore, sampling in some conditions may not even be possible such as of loose sands.

Field testing includes the Cone Penetration Test (CPT) which consists of pressing a series of rods through the soil with a probe at the end that measures tip resistance and the friction along the sides. This tool encounters the soils in situ and is thus very favorable in for instance sands. An enhanced version of the CPT that is used the most in Norway today is called CPTU, which also includes a measurement of the pore pressure. This tool is known to be a cost effective method of in situ testing and is appraised due to the ability to discover stratigraphic details and is today a vital part in geotechnical field investigations.

This equipment gives continuous and repeatable measurements with depth. From the response of the measurements in the soil it penetrates, the soil can be characterized, and interpretation of geotechnical parameters can be done. However, the measurements of tip resistance and side friction is known to be dependent of the soil properties around the probe of some distance. This typically results in inaccurate interpretation close to the layer boundaries. Furthermore, if the layers are thin compared to the diameter of the CPTU cone, the measurements may not properly reflect the properties of the soil in the thin layers.

An example of CPTU measurements in thin layers is presented in **Figure 1**.**1**. The measurements in the thin clay layers appear to be affected by the presence of a silty sand layer. Direct interpretation of undrained shear strength of these clay layers from the CPTU presented in **Figure 1**.**1** would result in a significant overprediction in the thin weak layer.

Thin layer effects have been studied in various combinations of soil materials. Many of which consider thin dense sand layers in loose sands or clay in relation to liquefaction evaluation. This has resulted in some proposed correction factors for measurements in thin dense sands. Very few physical or numerical studies are however conducted on the influence of the thickness of weak layers of clay in stronger sediments such as sand. There is a lack of suitable methods to correct cone resistance measurements in thin clay layers in sand, such as for the example above.

1.1   Objectives

The purpose of this study is to examine thin layer effects on CPTU measurements for thin clay layers in sand. A new chamber model is designed and procedures to create samples of sand and clay are established. CPTU results from the experiments are then analyzed through a procedure developed in this study which aims to assess the effect of layering on the cone resistance measurement.

The following three main objectives are determined for this research:

- Learn about the effects of thin layers on CPTU measurements and the existing methods to correct for these from relevant available research.
- Quantify the effect of the clay layers thickness in saturated sand on the CPTU measurements through large scale physical experiments.
- Develop a simplified numerical procedure that relates a cone resistance profile without layering effects to a measured cone resistance with layering effects.

The second main objective shall be reached through the following, secondary objectives:

- Design a large scale chamber model.
- Acquire suitable sand and clay materials and characterize these.
- Develop a repeatable method to reconstitute loose sand samples with thin clay layers.
- Perform multiple CPTUs in the samples according to the standard test procedures.

Thin layers are in this context based on the ability of the CPTU to discover layering. While the proper definition is presented in the next chapter, a rough description of thin layers can be layers thinner than $20cm$. A large chamber is here meant as both diameter and height larger than one meter for a cylindrical chamber.

1.2   Limitations

The physical experiment aims to create samples of sand and thin clay layers of varying thickness. Limitations concerning the physical experiments of this study includes:

- A single type of uniformly graded sand and non-sensitive clay are used in the experiments. The CPTU measurements in the specific sand and clay materials are however assumed to reflect the general behavior of other types of uniform sand and non-sensitive clays.
- Only saturated sand and clay at a specific stress state achieved in the samples is considered.
- The stress level is influenced by the chamber size due to silo effects with friction along the walls and the measurements are influenced by this.
- Only standard CPTU equipment are used, according to the Norwegian standard.

Regarding the analysis of results the following limitations are determined:

- Only effects of layering between sand and clay are considered. Inhomogeneities in sand or clay are commented but not analyzed and
- CPTUs were closely spaced and tests influence each other. Measurements are similarly influenced by proximity to walls and by the chamber boundary conditions. These measurements are still used for analysis.
- A procedure to analyze the cone resistance profile numerically is presented, however, this was done without analysis of the mechanics behind the cone penetration. Theoretical and empirical correlations are used to relate geotechnical parameters to the cone resistance.
- Measurements are considered as deterministic. Measurement accuracy is included in the literature review but is not regarded in analysis.
- Results from a limited number of CPTUs from physical experiments is used to determine trends.

1.3   Structure of the report

The literature review of this study is presented in two parts. First, the cone penetration test is presented in chapter **2** with emphasis on layering effects. The second consists of relevant literature on chamber testing and preparation of specimen, which is presented in section **3.1**, the first part of chapter **3**.

A summary of the methods and equipment for the physical experiments performed in this study is presented in section **3.2**, the second part of chapter **3**. This section gives the outlines of the procedures performed in the experiments. Appendix **A** provides full details on the experiments. The structure of section **3.2** and appendix **A** section **A.1** through **A.7** are the same. Thus, these chapters of the appendix may be read instead of section **3.2**.

Chapter **4** presents a procedure of analysis of cone resistance in a layered profile which is developed in this study. Some aspects of the procedure are presented together with examples. The full description of the method with the background of the procedure is presented in appendix **B**.

Result of the physical experiments are presented and analyzed in chapter **5**. CPTU measurements are first presented without interpretation followed by a description of the characteristics of the tests. Appendix sections **A.8** and **A.9** presents additional results and images of the experiments. Analysis of the measurements are done using the method presented in the previous chapter. Finally, possible methods of correction based on the results and analysis is presented.

Discussion of the results are presented in chapter **6**, followed by conclusions, recommendations and comments on further work.

2 LITERATURE ON CPTU LAYERING EFFECTS

Cone penetrations tests (CPT/CPTU) allow for reliable and cost-effective investigations of soils, especially for homogenous of sands or fine grained soils. The application of CPT/CPTU has received tremendous attention the last decades which has resulted in improved accuracy of the equipment and methods of interpretation. This chapter first presents the measurements and information that can be obtained from a standard CPTU test. Some assessments on the accuracy and repeatability of the measurement are included to substantiate the suitability of using CPTU measurements for characterization and determination of geotechnical parameters.

Lunne et al. (1997) summarizes the three primary applications of CPTs as:

1. to determine sub-surface stratigraphy and identify materials present,
2. to estimate geotechnical parameters, and,
3. to provide result for direct geotechnical design

Some methods on the first two of these applications will then be assessed for sand and clay. Correlations between the geotechnical parameters and cone resistance for these materials will be presented followed by a brief presentation on some of the methods of determining material types from CPTU measurements. Layering effects on CPTU measurements are presented with the relevant literature in the final section.

2.1 CPTU measurements

The three different parameters of the soil recorded from a standard CPTU are the cone resistance, side friction and pore pressure, see **Figure 2.1** for terminology. Various positions of the pore pressure filters can be used and are shown in the figure. These are at the cone face (u_1), behind the cone/cone shoulder (u_2) or behind the friction sleeve (u_3).
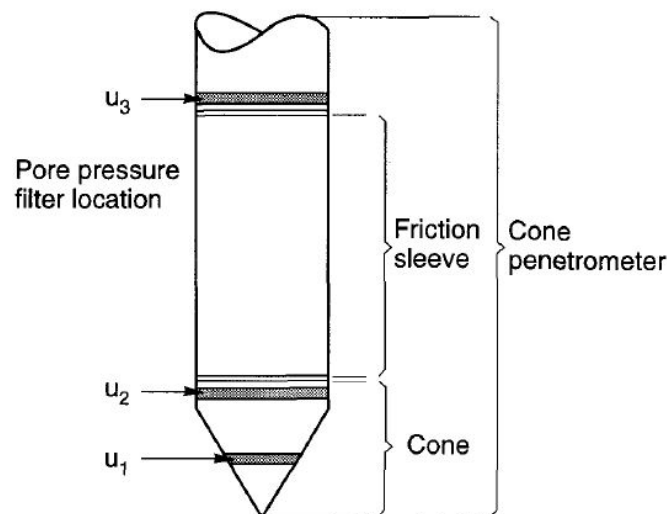
Figure 2.1. CPTU terminology (Lunne et al., 1997).

The tip resistance is in principle measured as the force applied to the cone, which divided by the cross section area yields the cone resistance stress, q_c. This measurement should be corrected for effects from unequal areas of pore water pressure on each side of the cone, given by:

$$q_t = q_c + u_2 \cdot (1 - a) \tag{2.1}$$

where a is unequal area factor. The uncorrected cone resistance, q_c, is often used in literature when the difference to q_t is neglectable, such as in sands. The corrected cone resistance q_t is consistently used for formulas in this study and is hereafter referred to as simply the cone resistance. Due to the large disturbance of the soil around the cone tip, as illustrated in **Figure 2.2**, the measured cone resistance during penetration is the result of a combination of the strength and stiffness of the soil over some distance around the cone. The distance depends on the soil material.

(1) Disturbed soil subject to shearing
(2) Direct disturbance zone when cone passes point A
(3) Previously disturbed soil
(4) Pre-compressed zone
(5) Undisturbed zone
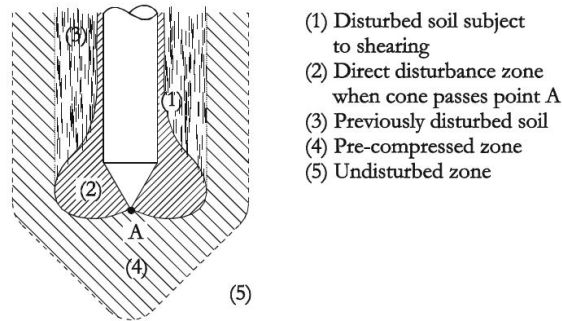
Figure 2.2. Soil disturbance during cone penetration (Silva & Bolton, 2004)

Soil behind the cone is significantly disturbed, and the measurement of the sleeve friction is the result of the average friction along the length of the sleeve. Measurements of sleeve friction is normally evaluated based on the value relative to the net cone resistance. The net cone resistance is defined as:

$$q_{net} = q_t - \sigma_{v0} \tag{2.2}$$

where σ_{v0} is the in situ vertical total stress. The friction ratio is then defined as:

$$F_r = \frac{f_s}{q_{net}} \tag{2.3}$$

The measured pore pressure in saturated soil depends on the filter location. The largest values are measured in front of the cone tip as a result of compression forces, while measurements behind the cone are rather influenced by the shear stresses along the cone shaft (Lunne et al., 1997). The recommended placement of the pore pressure filter in the European Standard (ISO 22476-1:2012) is behind the cone, where u_2 is measured. The excess pore pressure measurement is defined as:

$$\Delta u_2 = u_2 - u_0 \tag{2.4}$$

where u_0 is the initial pore pressure. When penetration is done according to the standard continuous rate of $2cm/s$, sands behaves fully drained while clays behave undrained. Thus, the excess pore pressure in permeable materials are typically zero, though for dense sands the value often becomes negative due to suction caused by dilation. For clays, the excess pore pressure is expected to be large. This is caused by the shearing of soil as well as the increase in total stress due to the insertion of the cone (Schneider et al., 2008).

The standard cone penetrometer, according to the European Standard (ISO 22476-1:2012), has a cone with $60°$ apex and cross section area of $10cm^2$. This gives a cone diameter, d_c, of $3.57cm$. The friction sleeve has an area of $150cm^2$, with diameter equal to d_c and length of $13.38cm$. Tolerances of these dimensions are given in the standard. Cone penetrometer of different sizes may also be used, for example in physical research studies where smaller cone often are used.

Special equipment can also be added, such as seismic and resistivity sensors, that measures other properties in addition to the three mentioned parameters. Some examples of cone penetrometers with properties other than the standard for use in layered soils is presented later in this chapter.

Measurements are recorded near continuous, normally at intervals of $1 - 2cm$ for the standard penetration speed of $2cm/s$. While CPTU measurements in general are reliable, the accuracy of the measurements depend on multiple factors, including the execution of the tests (Sandven, 2010). Disregarding these effects, the accuracy of the three parameters depends on the equipment used and that necessary corrections are performed. These corrections include correction of depth due to inclination and corrections of the cone resistance and sleeve friction measurements due to temperature changes. While the water pressure correction of the cone resistance is mentioned, a similar correction should be done on the friction sleeve if the u_3 pore pressure is measured. Even with these corrections the friction sleeve is known to be less reliable than the other three parameters. One explanation to this is that the tolerances of friction sleeve diameter allow for a diameter slightly larger than the cone which causes an applied force at the bottom of the oversized friction sleeve (Cabal & Robertson, 2014). This has a significant effect on measurements, particularly in fine grained soils.

Studies on the accuracy of the parameters and effects of cone penetrometer in soft clay (Lunne et al., 2018) and quick clay (Lindgard et al., 2018) show that the pore pressure measurements are the most accurate parameter in homogenous clay. In the soil evaluated in these studies the cone resistance was found to vary somewhat more with different cone penetrometers, while the sleeve frictions had significantly more variation. The European standard (ISO 22476-1:2012) defines allowable minimum accuracy of CPTU measurements. The accuracy is measured as the difference to the correct value and is given as the largest of an absolute value and a percentage of the correct measurement. For CPTUs with the highest requirements, these accuracy requirements in percentages are 5%, 10% and 2% for the cone resistance, sleeve friction and pore pressure measurement, respectively. This reflects the expected precision of the equipment.

The two previously mentioned studies on the accuracy of CPTU measurements were performed in two of the five national test sites in Norway (L'Heureux et al., 2017). Another of these test sites is of a deltaic silty sand site at Øysand (Quinteros et al., 2019). A study of the accuracy and effect of cone penetrometers were studied of the data from this site (Hammer, 2019). **Figure 2.3** presents the results of 12 CPTUs performed at the site. As described in the study, depths of these CPTUs were adjusted to match a reference measurement due steep layer inclination as a result of the sedimentation process in the delta. Layering effects, which is later described and is the focus of this study, is an important reason of some of the differences occurring in the cone resistance measurements. However, these results are an excellent example of the repeatability of the cone resistance measurement in layered soils.
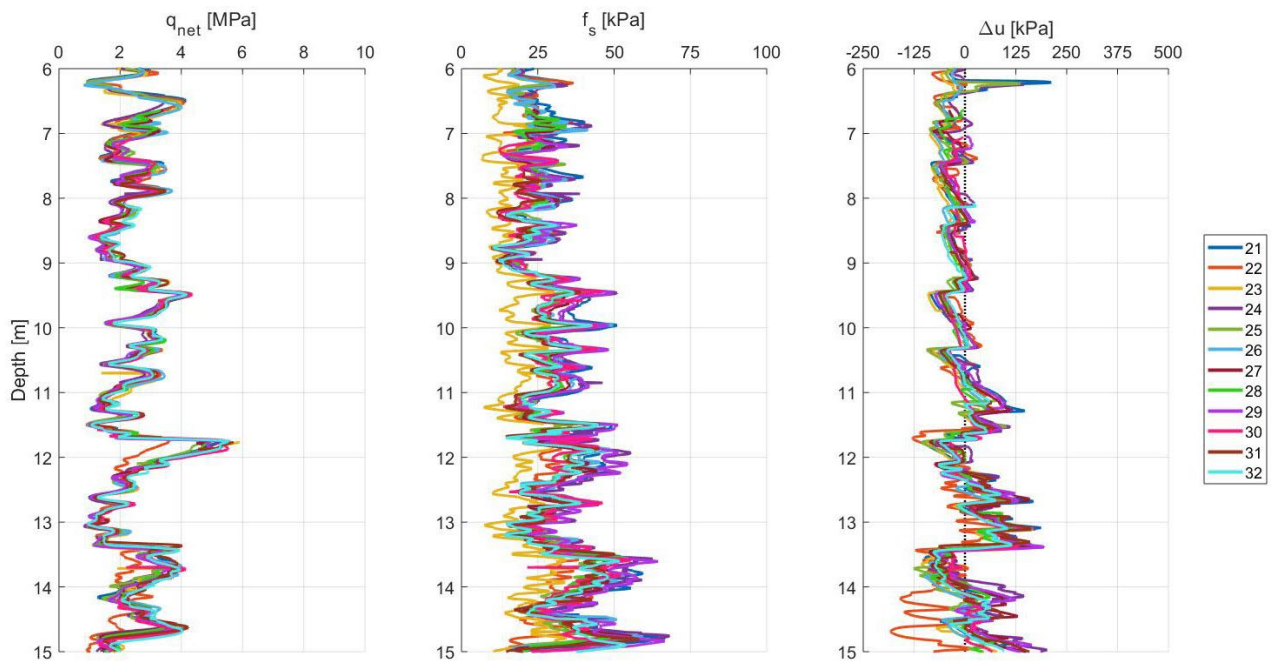
Figure 2.3. An example of the repeatability of CPTU measurements. 12 CPTUs performed in layered deltaic sediments at Øysand, Norway (Hammer, 2019)

2.2   Interpretation of measurements

Various theoretical idealizations and empirical correlations are proposed to relate geotechnical parameters to the measured cone resistance. While no set of formulas may define exact correlations between these parameters and the measurements due to the complex nature of the mechanical process during penetration, many have proven to be useful for interpretation. The cone resistance measurement is often used together with the sleeve friction and pore pressure measurement for classification of the soil materials.

2.2.1   Cone resistance in sand

A summary of recommended methods of interpretation of cone resistance measurements in sand was presented by Lunne & Christoffersen (1983) and Lunne et al. (1997). An example of a

theoretical approximation of the cone penetration is the method of Janbu & Senneset (1974) describing the resistance through bearing capacity formulation:

$$q_c = N_q \cdot (\sigma'_v + a) - a \tag{2.5}$$

where N_q is the bearing capacity factor, a function of the friction angle as well as the angle of plastification, and a is the attraction. The proposed relationship of the bearing capacity factors as well as an illustration of the idealized flow mechanism is presented in **Figure** 2.**4**.
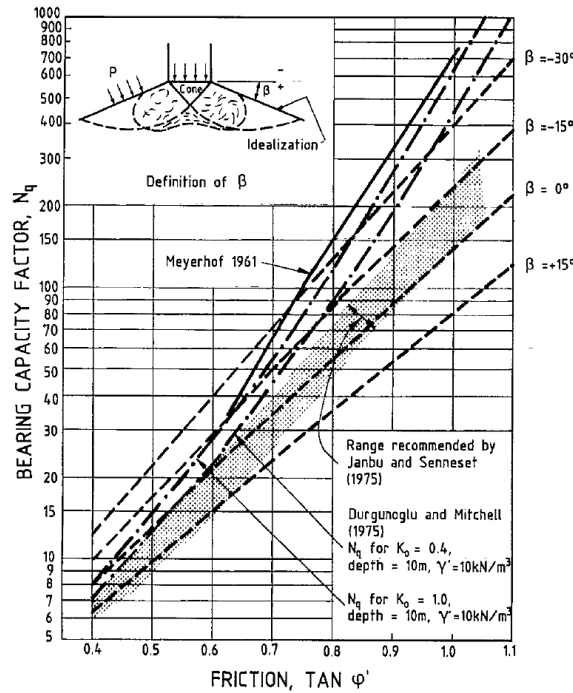
Figure 2.*4. Theoretical bearing capacity factor and the idealized flow mechanism*
(Lunne & Christoffersen, 1983)

A limitation of this method is the assumption that the soil is incompressible, which normally is far from the reality. The compressibility of sands is dependent on its density. Schmertmann (1976) proposed an indirect method to interpret geotechnical parameters of sands through an empirical relation as a function of the relative density and the stress state. The relative density, D_r, is given as:

$$D_r = \frac{e_{max} - e}{e_{max} - e_{min}} \tag{2.6}$$

where e is the void ratio and e_{max} and e_{min} are the estimated loosest and densest states of the sand found through laboratory procedures. Labels on sand in terms of *loose* and *dense* are normally used depending on the value of relative density for low and high values, respectively. Loose may for instance be $D_r < 30\%$ while dense can be $D_r > 80\%$. The empirical formula may be written in many forms, for example on the form presented by Jamiolkowski et al. (2003):

$$q_c = C_0 \cdot p_a \cdot \left(\frac{\sigma'}{p_a}\right)^{C_1} \cdot \exp\left(C_2 \cdot D_r\right) \tag{2.7}$$

where p_a is a reference pressure set to atmospheric pressure (here set to $100kPa$) given in the units used for the σ' and q_c. In this study the cone resistance is given in MPa and the soil stress in kPa. The effective stress σ' may be the vertical effective stress, σ'_{v0}, mean stress σ'_{m0}, or the horizontal stress σ'_{h0}. The three constants C_0, C_1 and C_2 have been calibrated for specific sand, which is normally performed through calibration chamber tests. Different sets of constants have been determined through large amounts of calibration chamber tests, including for instance that of Lunne & Christoffersen (1983) where the constants were found to be. $C_0 = 16.0$, $C_1 = 0.71$ and $C_2 = 2.93$ from correlation to the vertical effective stress:

$$q_c = 61 \cdot \sigma'^{0.71}_{v0} \cdot \exp(2.93 \cdot D_r) = 1.6MPa \cdot \left(\frac{\sigma'_{v0}}{100kPa}\right)^{0.71} \cdot \exp\left(2.93 \cdot D_r\right) \tag{2.8}$$

Other constants were calibrated in the study by Jamiolkowski et al. (2003) which gave $C_0 = 17.7$, $C_1 = 0.55$ and $C_2 = 2.90$, also using the vertical effective stress. It has been pointed out how the cone resistance is best compared to the horizontal effective stress (Houlsby & Hitchman, 1988). However, most of the developed correlations either use the vertical effective stress or the mean effective stress. Furthermore, the estimated horizontal stress is normally more uncertain than the vertical stress.

Equation (**2.7**) may be expressed for the relative density as a function of the cone resistance. Geotechnical properties in sand such as friction angle may then be estimated indirectly from the approximations of the relative density.

These empirical correlations have considerable scatter even for measurement on the sand it is calibrated on, and even greater uncertainty should be expected if for other sand types. Most correlations are presented for σ'_{v0} greater than about $50kPa$ as the correlations are less accurate in low stress states. Another reason lies in the difference in *shallow* and *deep* penetration of sand. Penetration in sands in vicinity to a free surface will influence the measurements to some depth, called the critical depth. An illustration of this is presented in **Figure 2.5**, where the critical depth is z_C. Empirical formulas have been developed to as a factor multiplied to Equation (**2.7**) to include this effect, for instance Senders (2010).
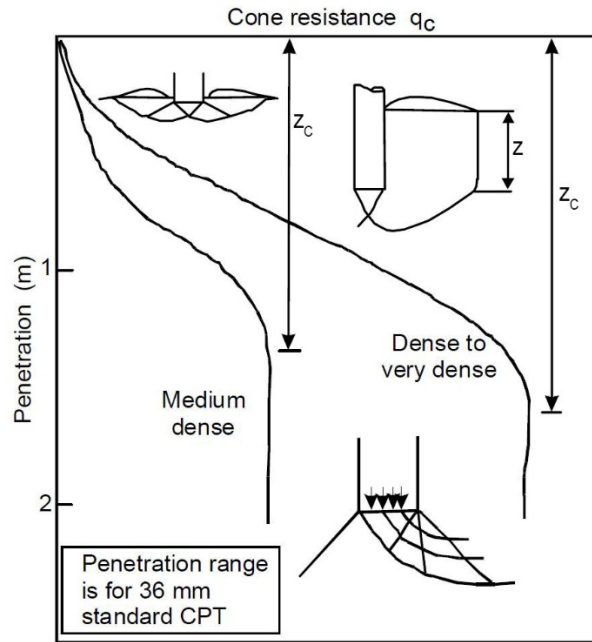
Figure 2.5. *Influence of a free surface on cone resistance (Puech & Foray, 2002)*

An example of a different method on parameter interpretation from cone resistance measurements is through the *state parameter*, defined by Been & Jefferies (1985). The state parameter is a measure on the difference in void ratio to the constant volume void ratio which may be found through triaxial tests of the sand. Use of this has been presented by Been et al. (1987).

2.2.2 Cone resistance in clay

The primary parameter of interest from CPTUs in clays is the undrained shear strength, s_u. Different values are measured in laboratory, of either compression, direct shear or extension undrained shear strength. This study only regards the compression shear strength and denotes it by s_u. C.C Ladd & Foott (1974) established a relationship between the vertical effective stress (σ'_{v0}), overconsolidation ratio (OCR) and the undrained shear strength as

$$\frac{s_u}{\sigma'_{v0}} = \alpha \cdot OCR^m \tag{2.9}$$

where m is a material coefficient and α is the value of s_u/σ'_{v0} for normal consolidated clay. The relationship between cone resistance and s_u is given as:

$$q_t = N_{kt} \cdot s_u + \sigma_{v0} \tag{2.10}$$

where N_{kt} is the cone factor and is defined through various relationships of properties of the clay and in some cases also the cone penetrometer. Multiple studies have analyzed penetration of clay numerically, where relationships were given between the cone factor and parameters such as the rigidity index $I_r = G/s_u$, friction coefficient between clay and cone as well as the horizontal stress, e.g. Teh & Houlsby (1991). Correlations based on field data have been developed, for instance by

Karlsrud et al. (2005) where the cone factor of clays with sensitivity of less than 15 was determined through:

$$N_{kt} = 7.8 + 2.5 \cdot \log(OCR) + 0.082 \cdot I_P \tag{2.11}$$

where I_P is the plasticity index. The correlation includes significant scatter, and values of N_{kt} was found to lie mostly between 6 and 12. Other cone factors are also proposed between the undrained shear strength and effective cone resistance ($q_e = q_t - u_2$) and Δu_2. These are however not regarded here. A recent study by Paniagua et al. (2019) presented an updated review of the CPTU correlations in clays.

2.2.3 Classification and soil behavior types

As previously mentioned, a primary goal of performing a CPTU is to determine sub-surface stratigraphy and identify materials present (Lunne et al., 1997). While the three recorded parameters are not enough to perfectly characterize the soil, interpretation methods that fairly accurately characterize the soil it encounters has been developed. This has been done through good understanding of the physical properties of the soil which the parameters reflect and extensive calibration tests. Typical classification of soils from CPTU measurements are done through charts. Here, the measurements are interpreted in pairs, either q_t and f_s or q_t and u_2. Normalized parameters are used for interpretation, where the cone resistance is normalized by

$$Q_{tn} = \left(\frac{q_{net}}{p_a}\right)\left(\frac{p_a}{\sigma'_{v0}}\right)^n \tag{2.12}$$

where p_a is the reference pressure ($p_a = 100kPa = 0.1MPa$) and n is the effective stress exponent. The exponent n is often set to 1, giving

$$Q = \frac{q_{net}}{\sigma'_{v0}} \tag{2.13}$$

The normalized cone resistance Q and the friction ration F_r is used together in charts such as Robertson (1990), presented to the left in **Figure 2.6**. The soil behavior type index, I_c, was defined by Robertson & Wride (1998) as:

$$I_c = ((3.47 - \log(Q))^2 + (\log(F_r) + 1.22)^2)^{0.5} \tag{2.14}$$

Low values of I_c indicates dense, coarse grains while fine weak soils are correlated to large values. A stress exponent was defined by Robertson (2009) as:

$$n = 0.381 \cdot I_c + 0.05\left(\frac{\sigma'_{v0}}{p_a}\right) - 0.15 \tag{2.15}$$

An updated interpretation chart using the normalized cone resistance with the exponent presented above (Q_{tn}) was presented by Robertson (2016), also shown in **Figure 2.6**. These charts build on the same principles to classify soil by their behavior during penetration. As the figures present, materials that behave sand-like are expected to give low friction ratio, and the higher the normalized cone resistance the denser the material is expected to be. Non sensitive clays on the other hand yield large friction ratios and low cone resistance.
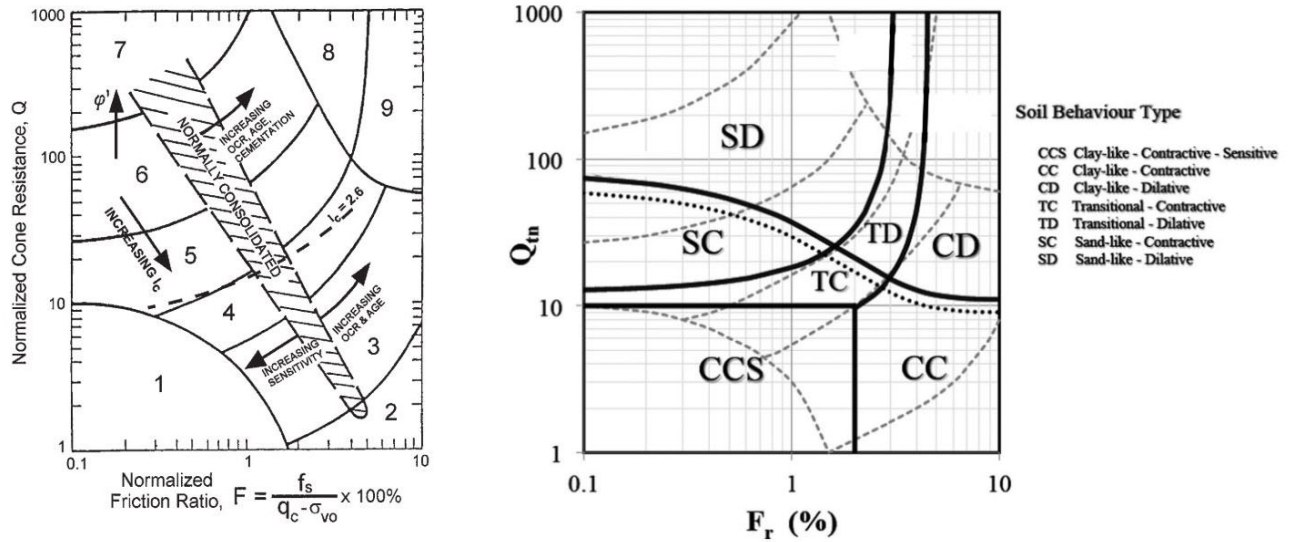
Figure 2.6. *Left: F_r vs. Q (Robertson & Wride, 1998). Right: F_r vs. Q_{tn} (Robertson, 2016). The numbers in the chart to the left each represents a soil behavior type. For instance, number 3 is clay and number 6 is clean to silty sands. Note the different parameters of the vertical axis.*

Silts and clays are normally characterized using Q and normalized pore pressure measurements. The normalized pore pressure ration B_q is often used:

$$B_q = \frac{u_2 - u_0}{q_{net}} = \frac{\Delta u_2}{q_{net}} \tag{2.16}$$

Other studies favor the use of the excess pore pressure divided by the effective stress as the normalized pore pressure:, i.e. $\Delta u_2 / \sigma'_{v0}$, such as Schneider et al. (2008), (2012). Charts for these two normalized pore pressure parameters against the normalized cone resistance is presented in **Figure 2.7**.

The classification of clays by Schneider et al. (2008) is divided between sensitive clays, clays and clay with low rigidity index, I_r. The article states that typical values of I_r are in the range of $150 - 500$.
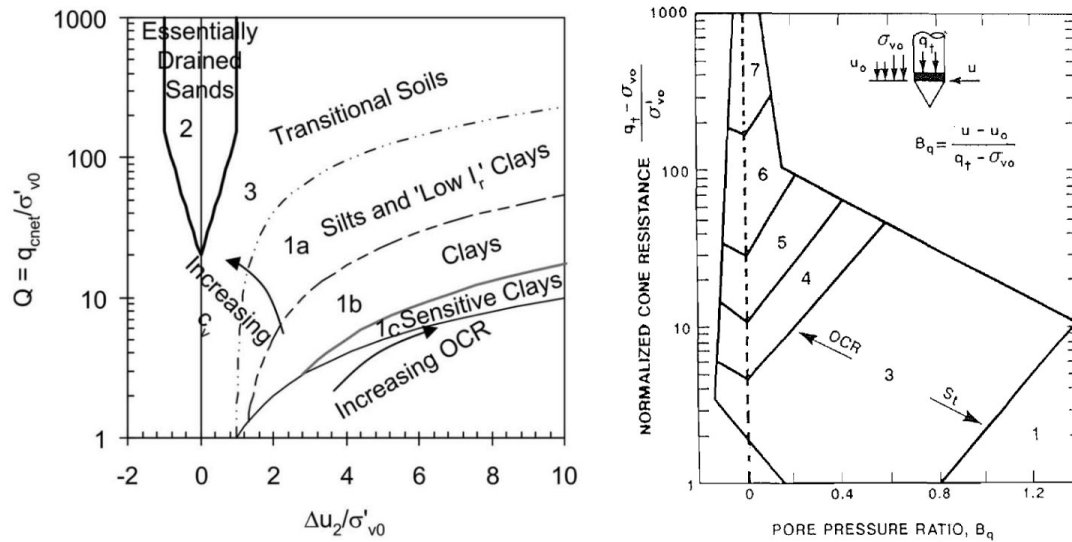
Figure 2.7. Left: $\Delta u_2/\sigma'_{v0}$ vs. Q (Schneider et al., 2008). Right: B_q vs. Q (Robertson, 1990). The vertical axis in these charts are the same, while the horizontal is not. Note that the numbering in zones in these charts does not correspond to each other.

While classifications charts as those mentioned here should not be expected to always reflect the soil exactly, they are proven to be accurate in homogenous materials. In layered soils of varied materials the change in cone resistance from one layer to the next does not occur instantaneously, but rather over some distance. Similar behavior is the case for the sleeve friction measurement, while pore measurements is expected to react almost instantly to the change from a drained to undrained material. All these charts depend on the cone resistance measurements and poor interpretation may be caused by the lack of sharp transitions of q_t between layers.

2.3   Layering effects on the cone resistance

A CPTU performed in completely uniform, homogenous soil material below the critical depth (see **Figure 2.5**) is expected to yield an almost constant cone resistance measurement. In this situation, only the increasing stress state will cause an increase in the cone resistance. This cone resistance value is as previously described a result of the strength and stiffness properties of the specific soil. When all material influencing the measured cone resistance has the same strength and stiffness as the material at the depth of the cone, the resulting value is here called *the characteristic cone resistance*. Other terms that may be used to describe this include ultimate and steady state cone resistance. Steady state cone resistance is however also used to describe the cone resistance after the critical depth is reached in contrast to that of shallow depths (**Figure 2.5**).

Now consider that a soil with constant characteristic cone resistance lies above another uniform and homogenous soil material with different properties. It is assumed that there is a sharp physical interface between the two materials. The bottom material is assumed to have a different characteristic cone resistance than the one on top. When the cone tip is approaching the second layer it will at some distance prior to the layer interface be influenced by the underlying layer.

Instead of an instant change at the depth of this interface from the characteristic cone resistance of the first layer to that of the second layer, the value will over a distance change between these two. This distance, as well as how the transition is depends on properties of the material and the size of the probe.

Due to the complexity of the penetration process, a simplification is made by using the characteristic cone resistance of layers to define the layer effects. A characteristic profile is a profile that reflects the characteristic cone resistance of the soil at each depth, while the measured profile is the result of the actual cone penetration. The measured profile has a shape of the transition which is assumed to be dependent of the contrast between the characteristic cone resistance in these two layers. That is, an important measurement on the change of the cone resistance is the relative characteristic cone resistance of the bottom layer to the top layer. If the characteristic cone resistance of the upper layer is called $q_{t,a}^{char}$ and that of the lower layer is called $q_{t,b}^{char}$, the relationship $q_{t,b}^{char}/q_{t,a}^{char}$ is expected to be a good measurement on the layering effect. If this relationship is greater than one, the underlying layer is *stronger* than the top layer. Alternatively, if the relation it is lower than one than one it is *weaker*.

Layers are labeled strong and weak in a relative sense compared to neighboring layers. As previously described, a dense sand layer typically causes large cone resistances while on the other hand lower values are expected in loose sands. In a layered sand with a dense sand layer over a loose sand layer, the top layer is strong, and the bottom layer is weak. Clays with high cone resistances is labeled stiff, while the opposite is labeled soft. These values are then expected to be labeled strong and weak, respectively. However, in a layered soil with sand and clays, the label strong and weak may not be defined solely on the density of sand or the stiffness of clay, but rather the characteristic cone resistance in each material. In most cases the sand is the strong material and clays are weak.

The most significant factor of layering effects measured by a cone penetrometer is believed to be the cone diameter, d_c. That is, if the effects of grain size to cone diameter is ignored, an infinitely small cone diameter would be assumed to yield no layering effects. Thus, measurements of layering are often given in terms of cone diameters. The depth of penetration divided by the cone diameter is called the normalized depth.

A physical explanation of the layering effect lies in the flow mechanism that occurs around the advancing cone tip, and how it is influenced by soil properties of some distance. Examples of flow mechanism in two layered profiles of sand and of clays are therefore presented in the following subsection to illustrate the effects and present the labels used. Following is a presentation of the resulting thin layer effects. Relevant literature on layering effects for two-, three- and multilayered profiles on the CPT/CPTU is presented from numerical and physical experiments.

2.3.1 Examples of layering effect and flow mechanism

The flow mechanism during cone penetration in layered soil is first illustrated through physical experiments performed in a study by Tehrani et al. (2017). This article considers the effect of sand layering with varied density and the flow mechanism around the cone tip of a two layered profile. A $180°$ chamber with a window on one side was used with cameras to measure displacements. Here, the test with loose and dense sand is considered, with relative density of about 40% and 85% respectively. Homogenous samples of each density were tested as well as combinations of two layered profiles. A load of $50kPa$ additional vertical stress was added on the top of the sample. The cone diameter, d_c, was $31.8mm$.

The results of the two cases of loose over dense (LOD) and dense over loose (DOL) sand are summarized in **Figure 2.8** and **Figure 2.9**. These figures are edited for a concise representation of the results. The figures present the cone resistance profile to the left together with the layering of the sample in terms of the normalized depth. Deformation patterns are presented to the right, which are later described. The layer interface was at depth $12.3d_c$ for both cases. Measured cone resistances in homogenous samples (loose, L and dense, D) are also included for comparison. The characteristic profile for the LOD sample would be the measured cone resistance of the loose sample (T5-L) to a depth of $12.3d_c$, then an instant change to the cone resistance of the dense sample (T7-D) from that depth.

Both tests clearly show how q_c at some distance above the interface begins to change. This distance is called *sensing distance* and is defined as the largest distance above the layer interface influenced by the underlying layer. Then, when the cone has passed the layer interface the value of q_c gradually approaches the characteristic cone resistance of the layer over a length called *developing distance*. That is defined as the largest distance below an interface that an overlying layer influences the cone resistance.

In the case of this experiment, the two-layered sample with loose over dense sand gives a sensing distance, here called H_s, of $2.8d_c$ and a developing distance, H_d, of $3.8d_c$. For the sample with dense over loose sand the developing distance was significantly larger, $5.1d_c$, while the developing distance was only $2.2d_c$. This reflects how both the sensing and developing distance in sand increase with the density.

Note that the measured profile of both sample deviates slightly from the characteristic profiles defined by measurements of loose and dense homogenous samples. This is due to difficulties of creating sand sample of exact densities and is an example of how the characteristic profile merely is an estimation of the cone resistance uninfluenced by layering effects. Furthermore, the sensing and developing distances are only approximated from visual assessment.
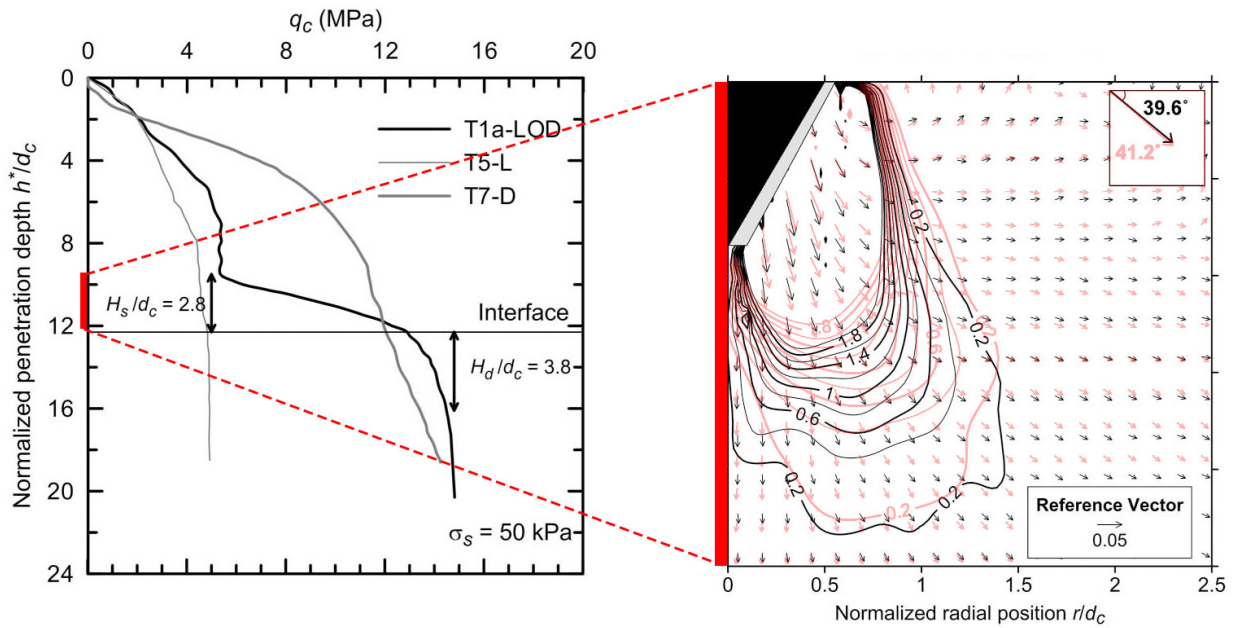
Figure 2.8. *Loose over dense sand. Left: tip resistance measurement. Right: displacement field and contours of the incremental shear strain at depth 9.5d_c with shadows of the same values in a homogenous loose profile. Edited after Tehrani et al (2017).*
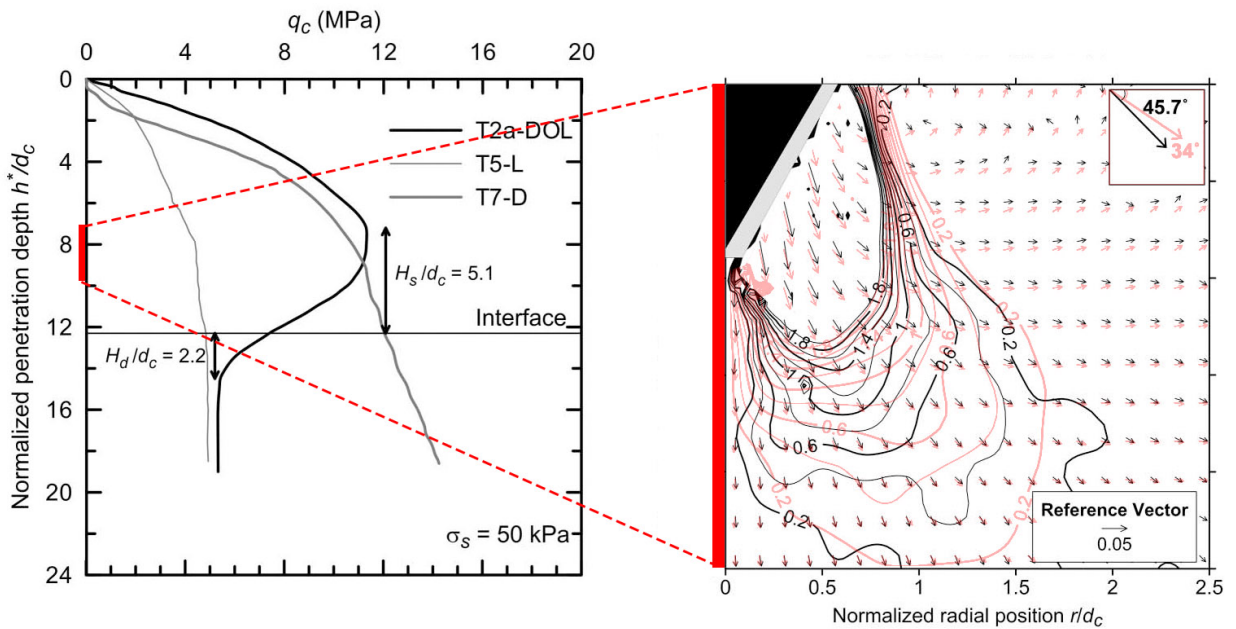
Figure 2.9. *Dense over loose sand. Left: tip resistance measurement. Right: displacement field and contours of the incremental shear strain at depth 7.2d_c with values in light red from a homogenous dense profile. Edited after Tehrani et al (2017).*

To the right is the incremental displacement vector field together with the contours of the incremental shear strain, collectively referred to as the flow mechanism plot. This plot presents values from a single depth of the cone. This depth is the depth of layering interface minus the sensing distance. Vertical red lines are used to represent the scale. The flow mechanism plot is presented over a window of $2.5d_c$ both vertically and radially. Incremental shear strain is in this experiment the shear strain due to a vertical displacement of the cone of $0.13d_c$. The flow mechanism of the layered profile (LOD or DOL) is presented in black, while the corresponding flow mechanism for the homogenous sample (L or D) is presented in light red. Thus, the difference between the values in black and red represent the difference in the flow mechanism due to the sensing of an underlying layer of different properties. From this difference the effect of an underlying layer can be seen. As stated by authors of the study, the zone with greater than 2% incremental shear strain increased in weak soil when approaching a strong layer compared to that of a uniform weak sample. This means the zone of influence on the cone resistance increases in weak sand when approaching strong sand. Similarly, the zone of influence decreases when strong sand approaches weaker sand.

A measure that is called *the average displacement vector* is presented in the top right corner of the flow mechanism plots. This is the weighted average of the displacement vectors in the flow mechanism plot and is a measure of the representative direction of the flow. These shows how for loose sand entering dense sand, the direction of the failure mechanism become more horizontal, while it become more vertical for dense sand approaching loose sand. These trends are possible to see in **Figure 2.8** and **Figure 2.9**, but note that these flow mechanisms plot show the effect a sensing distance away, i.e. the effects are expected to be more evident closer to the interface.

A similar experiment was performed by Mo et al. (2017) and a schematic of the displacements in layered sand with different densities is presented in **Figure 2.10**.
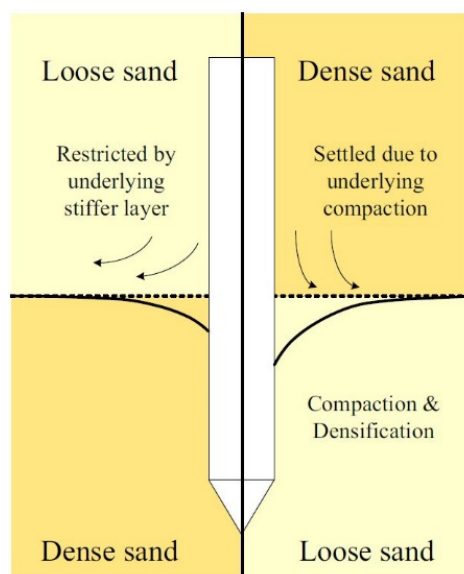
Figure 2.10*. Schematic of the effects of layered sands (Mo et al., 2017).*

Another study on the flow mechanism of the CPT from layered physical experiments was performed on layered clay by Wang (2019). Samples were created with a centrifuge and tested using a cone of $10mm$ diameter. Clay layers were made from kaolin clay powder and consolidated to give undrained shear strength of either $7.5kPa$ or $29.1kPa$, labeled soft and stiff respectively. The cone resistance results of the two layered systems with soft over stiff and stiff over soft is presented in **Figure 2**.**11**. From the results shown in the two-layered systems in the figure it is evident that the behavior in loose and dense sand is not transferable to soft and stiff clay. The results show cone resistance profiles with sensing distances in both soft and stiff clay of almost zero. Developing distances, however, were large and the greatest in soft clay.
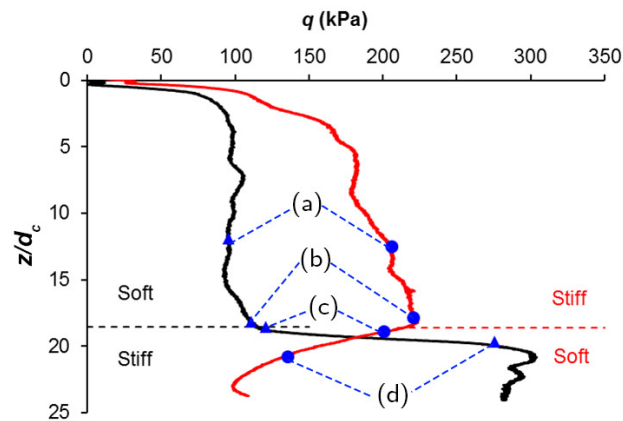
Figure 2.**11**. *Cone resistance profile of the two samples and the positions of flow mechanism plots (Wang, 2019). The black profile is a sample with a soft over stiff layer, while the red is stiff over soft.*

Displacement fields at the four points marked in **Figure 2**.**11** of these two samples are presented in **Figure 2**.**12** and **Figure 2**.**13**. These figures reflect that the change in flow mechanism between strong and weak clays are more subtle than the changes seen in strong and weak sands. The layer interface is significantly deformed when the underlaying layer is soft, however, little deformation is apparent when the underlying layer is stiff. The failure mechanism from stiff to soft clay was characterized as *punch-through* failure, with large vertical deformation at the interface.
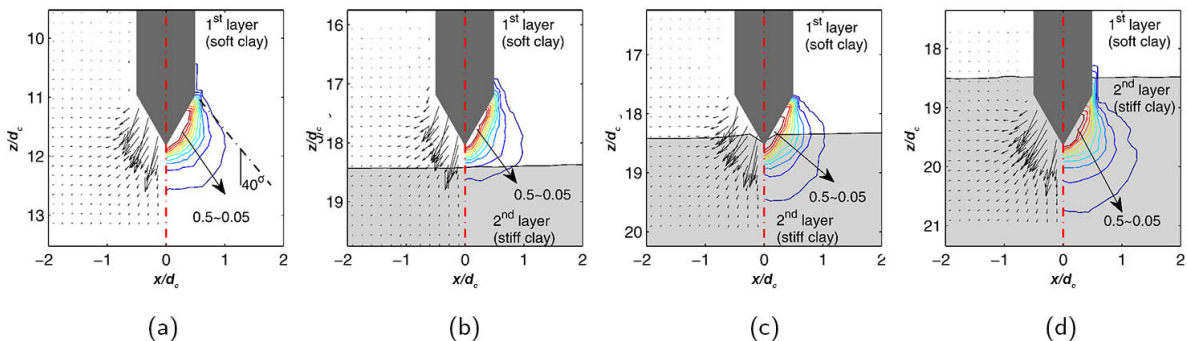
Figure 2.**12**. *Flow mechanism around the advancing cone in soft over stiff clay layers (Wang, 2019).*
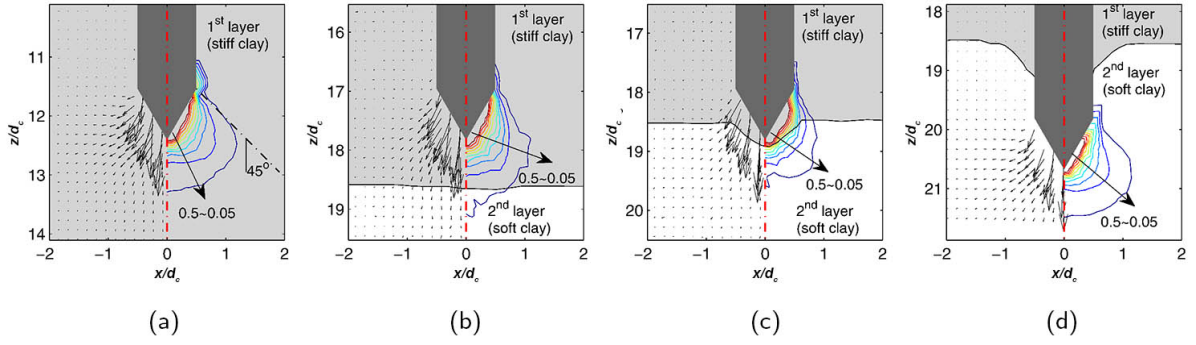
***Figure 2**.13. Flow mechanism around the advancing cone in stiff over soft clay layers (Wang, 2019).*

2.3.2   Thin layer effect

While the consequence of layering effect in a two layered profile is the lack of a sharp transition to reflect the material change, the effect on thin layers is more significant. In a profile of three layers, a thin layer of thickness H and characteristic cone resistance $q_{t,a}^{char}$ is placed between thick layers of characteristic cone resistance $q_{t,b}^{char}$. If H is greater than the sum of the developing distance to the first layer and the sensing distance to the third layer, the characteristic cone resistance is reached in the second layer. The sum of the sensing and developing distance is in this study labeled the *influence length*. If H is smaller than this, the measured cone resistance in the second layer, $q_{t,a}$, will not be equal to $q_{t,a}^{char}$. The measured value will be smaller or larger than $q_{t,a}^{char}$ depending on the relationship between $q_{t,a}^{char}$ and $q_{t,b}^{char}$. The cone resistance ratio of a thin layer compared to the thick layer is described with η_{thin}:

$$\eta_{thin} = \frac{char.\,cone\,resistance\,in\,thin\,layer}{char.\,cone\,reistance\,in\,surrounding\,soil\,deposit} = \frac{q_{t,a}^{char}}{q_{t,b}^{char}} \qquad (2.17)$$

The assumption is that the thin layer lies between two thick layers of equal properties. If η_{thin} is larger than one, the second layer is strong while the first and third layer is weak. In this case the measured cone resistance in the thin layer will be lower than $q_{t,a}^{char}$. The opposite is the case when η_{thin} is less than one. As presented in the previous subchapter, in dense sand both the sensing and developing distance is larger than in loose sands. This indicates that the effect of layer thickness is more significant in strong soils interbedded in weak deposits. An illustration of the thin layer effect for η_{thin} greater than one is presented in **Figure 2**.14. The characteristic cone resistance in the thin layer with symbol $q_{t,a}^{char}$ in equation (**2.17**) is in this figure called given as q_c^*, while $q_{t,b}^{char}$ is called q_{cB}. The peak measurement, named q_{cA} in the figure is called $q_{t,a,peak}$ or $q_{t,thin,peak}$ in this study.
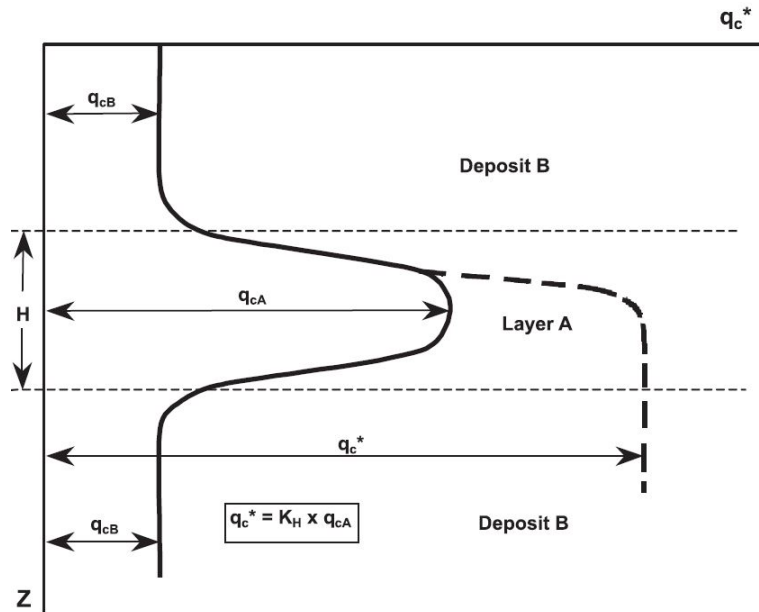
Figure 2.14. *Illustration of thin layer effect of a strong layer (layer A) with thickness H embedded in weak deposits (Ahmadi & Robertson, 2005). The value of η_{thin} in this situation is greater than one.*

As a measure to correct for thin layer effects, Robertson & Fear (1995) defined the thin layer correction factor which is called K_H and defined by:

$$K_H = \frac{char.\ cone\ resistance\ in\ thin\ layer}{peak\ measured\ cone\ resistance\ in\ thin\ layer} = \frac{q_{t,a}^{char}}{q_{t,a,peak}} \qquad (2.18)$$

Note that the term peak refers to the minimum measurement for thin weak layers and the maximum measurement for thin strong layers. The value of K_H depends on multiple factors but is simplified by assuming dependence on the cone resistance ratio η_{thin} and the layer thickness H. Literature on layering effects and further description of correction procedures are presented in the following subsections.

2.3.3   Thin layer correction for liquefaction evaluation

Many studies on thin layer effects are motivated by the desire to correct for these effects in thin strong sand layers in weak deposits for liquefaction evaluation. During earthquakes loose sands under low in situ stress is prone to liquefy under the earthquake load. CPTUs performed in a thin dense sand layer between weak layers of for instance clay will yield low cone resistance in the sand layer due to thin layer effects. The consequence is erroneous interpretation of the dense sand as loose sand, which is liquefiable. One may avoid false positive indications of liquefaction potential by correcting the measurements for such effects. Measurements can be corrected through the peak thin layer values, as previously presented with the factor K_H (Robertson & Fear, 1995). Factors of K_H based on field data were reported by Youd & Idriss (2001). Thin strong layers in weak deposits were analyzed in a numerical study by Ahmadi & Robertson (2005). Thickness, density and stress state of the thin layer was varied. From this, recommendations on correction factors,

K_H were presented. The values of K_H are given as a function of the layer thickness in **Figure 2.15**. The symbols in this figure corresponds with **Figure 2.14**. The correction factors presented in this study indicate significant thin layer effects even for layers thicker than $40d_c$.
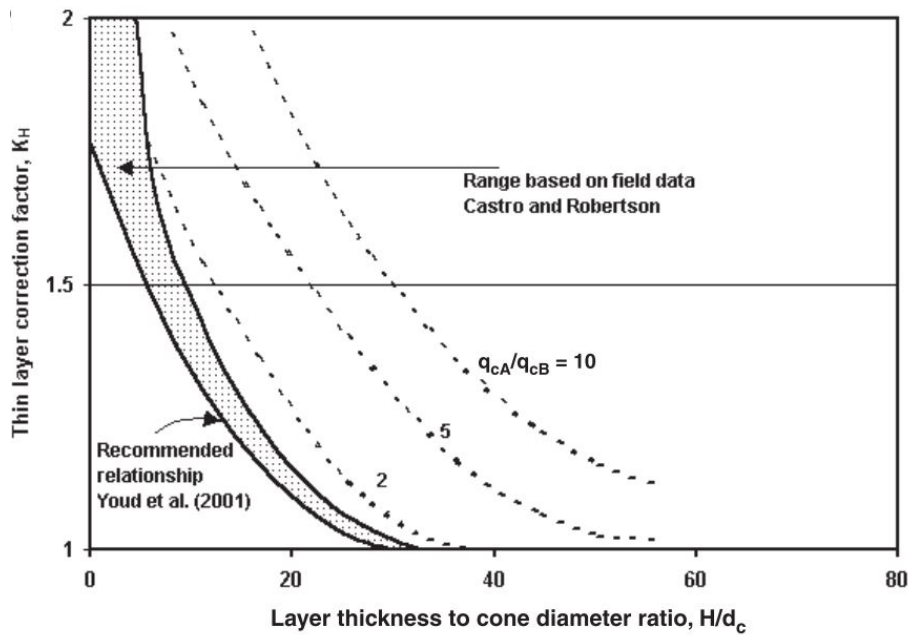
Figure 2.15. Thin layer correction factors, K_H, for thin strong layers in weak deposits from numerical simulations and field data (Ahmadi & Robertson, 2005).

A procedure intended to correct for thin layer effects of cone resistance profiles, primarily intended for liquefaction evaluation, was developed by Boulanger & DeJong (2018). The method is called *inverse filtering procedure*, where the term *inverse* refers to the attempt to convert a measured cone resistance profile to a characteristic profile (called true in the article). This procedure consists of a method to determine a measured cone penetration profile through an advanced form of averaging of the characteristic profile. The cone penetration is considered a *low pass spatial filter*, meaning that weak materials influence the measured cone resistance more than the strong materials. This is reflected in the procedure, where the spatial filter called the cone penetration filter, with symbol w_c, is determined for each depth. A measured cone resistance value, q^m, is determined from the integral of the characteristic profile q^t and the spatial filter w_c. This is illustrated in **Figure 2.16**.

Thin layer correction factors of thin strong layers in weak deposits from this method is presented in **Figure 2.17**, which is the same diagram as in **Figure 2.15**. There are however considerable differences, where small correction factors are given for thin layer thicknesses larger than $20d_c$. This fits better with the field data by Youd & Idriss (2001) shown in **Figure 2.15**. Note that the factors presented in **Figure 2.15** is a function of $q_{t,a}/q_{t,b}^{char}$ while **Figure 2.17** uses $q_{t,a}^{char}/q_{t,b}^{char}$.
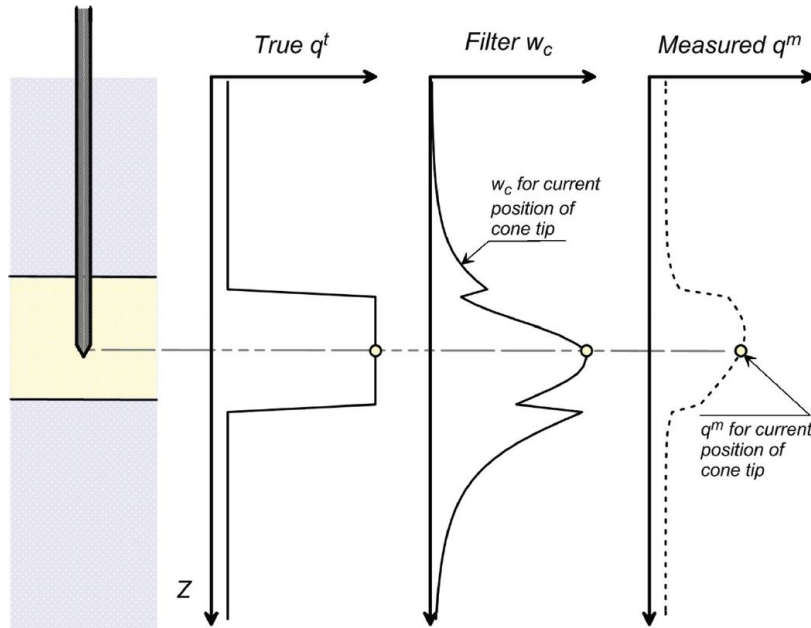
Figure 2.*16. Illustration of the spatial filter from the inverse filtering process (Boulanger & DeJong, 2018). Note that the spatial filter w_c is different for each depth.*

The inverse filtering procedure of a measured profile to a characteristic profile is performed using the spatial filter in an iteration process. Layering effects on cone resistance is analyzed in the current study through a method based on the framework of the spatial filter presented above. The procedure developed in the current study is presented in chapter **4**. Details on both the procedure of the current study and the inverse filtering procedure is described in further detail in appendix **B**.
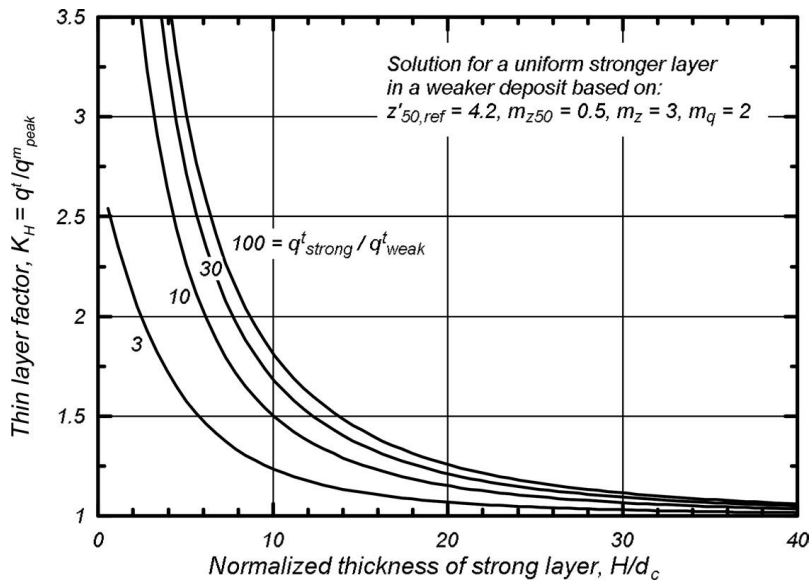
Figure 2.*17. Thin layer correction factors, K_H, for thin strong layers in weak deposits from the inverse filtering procedure (Boulanger & DeJong, 2018). The symbol q^t is used for the characteristic/true cone resistance, while q^m is used for the measured cone resistance. The four control parameters are given in the text in the top right corner.*

2.3.4 Numerical and physical studies of layering effects

The general effects of layering on the cone resistance measurements has been studied extensively through numerical and physical experiments. Though even more studies on other penetration methods are available, such as piles, T-bar, balls, spundcans, only literature on the CPT/CPTU is considered here.

A physical model study of the effect of layering of sand with varied density on CPT measurements was performed by Treadwell (1977). Loose layers of sand, with D_r of about 10% were made in samples of dense sand, with relative density of about 80% and height of about $80cm$. One of the experiments was of a loose sand layer of thickness $8d_c$ between dense sand layers. The cone diameter d_c was about $2cm$. The results indicated a sensing distance of about $2d_c$ both from the dense to loose layer and the loose to dense layer.

Another physical experiment of three-layered profiles of sand were presented in a study by Joer et. al. (1996). A $175mm$ tall sample was tested by a cone of $10mm$ diameter. Samples were made out of silty sand, and strong layers were prepared by cementing. Weak uncemented soil was sandwiched between strong cemented soil, and the top and middle layer thickness was varied. Sensing distance appeared to vary from $0.5d_c$ to $2.5d_c$, depending on the thickness of the upper and middle layer.

Numerical studies includes linear elastic analyses performed by Vreugdenhil et al. (1994) and Yue & Yin (1999) on multilayered soils. The cone penetration test yields far from elastic responses of the soil and the penetration process may not be approximated with a linear elastic model. However, the elastic model was used only to describe the effect of the stiffness of nearby soil on the tip resistance measurements. From this, the cone resistance was approximated through the stiffness and layering.

Multiple non-linear large-strain numerical analysis has been carried out to determine the layering effect. Van den Berg et al. (1996) performed tests on two layered profiles with Eulerean large-strain finite elements with clay over sand and sand over clay. Tests were run with varying stiffnesses. One of which gave a characteristic cone resistance in sand which was about six times that of the clay. For this case, it was found that for sands coming into soft clay the sensing distance was $3d_c$ and the development distance in sand below soft clay was $4d_c$. Sensing and developing distances in clay for both cases were small.

Xu & Lehane (2008) studied the layering effect of mostly two layered systems through spherical cavity expansion in order to assess the pile end bearing resistance. Results from centrifuge testing of two-layered profiles were also included. The study defined the cone resistance ratio as:

$$\eta = \frac{q_t}{q_{t,strong}^{char}} \tag{2.19}$$

where q_t is the measured cone resistance and $q_{t,strong}^{char}$ is the characteristic cone resistance in the strong layer. The lower bound of the value is η_{min}, which represents the characteristic cone resistance ratio in the weak layer:

$$\eta_{min} = \frac{q_{t,weak}^{char}}{q_{t,strong}^{char}} \tag{2.20}$$

The symbol η_{thin} was previously used to describe the relationship between the characteristic cone resistance in the thin layer compared to the surrounding layers. For thin, weak layers in stronger deposits, the symbol η_{min} is hereafter used. The study by Xu & Lehane (2008) compared the results of cavity expansion to physical tests in a centrifuge. Sensing distances were found to be about twice the developing distances in the layered sands. In the layered system of sand over clay, the sensing distance was were large in the sand. Two different cone sizes, 6 and $16mm$, were used which indicated that while the sensing distance is larger with increasing diameter, it is not increasing exactly with the diameter.

Mo et al. (2014) (2016) used cavity expansion to estimate the cone resistance in both two- and three-layered systems with thin layers. Thin layers of dense sand were considered in loose sand and soft clay layers, as well as thin loose sand layers in dense sand. The estimation of thin layers was done through superpositions of estimated transition functions of two-layered transition and the influence of soil behind and ahead of the cone was assumed to be the same.

Walker & Yu (2010) analyzed numerically the effect of layered clay in three layer systems with varying thickness of the middle layer. Results indicated that the thickness of the middle layer did not impact the sensing distance in the first layer. Their results showed that a thin layer thickness of $2d_c$ was enough to reach the characteristic value for a thin clay layer with s_u of one fifth of the surrounding clay layers.

A large amount of numerical large deformation finite element analyzes were performed by Ma et al. (2015), (2017) in layered clays. Correction factors of thin layer effects were proposed for the net cone resistance, q_{net}, given the symbol k:

$$k = \frac{q_{net,thin}^{char}}{q_{net,thin,peak}} \tag{2.21}$$

The proposed correction factor k was curve fitted as a function undrained shear strength (s_u), rigidity index (I_r), layer thickness of the thin layer as well as the surrounding layers. The correction was given for soft clay in stiff clay and the opposite.

Silva & Bolton (2004) performed physical experiments on $25cm$ tall centrifuge samples which were tested with a $12mm$ piezocone. This study focused on the effect of layering using soils with varying grain sizes. Fine sand with relative density of about 75% was placed between layers of coarse sand with relative density of about 90%. Only subtle effects of layering were seen, with very gradual

variation in tip resistance through the layers. This reflects how layering effects between layers of similar characteristic cone resistance is difficult to detect using CPTU.

An example of equipment that are suited to discover such layering of varied grain size was studied by Hryciw et al. (2009). In this study, a camera was attached behind the probe. Grain size of the penetrated soil could then be interpreted from images, thus discovering variation in the soil stratigraphy. This attachment adds to the long list of available sensors to attach to the CPT probe; however, such attachments are rarely used in practice and discovery of layering should therefore preferably not rely on such equipment as of now.

Hird et al. (2003) performed physical experiments of thinly layered soils. Samples consisted of thin layers of $1-8mm$ of sand or silts between clay layers of thickness of about $60mm$. Cones of cross section areas of $1cm^2$ and $5cm^2$ were used with a variety of pore pressure filters at the tip (u_t), cone face (u_1) and shoulder (u_2). Results showed how smaller cone diameters give much better representation of the layering with the cone resistance. Furthermore, the excess pore pressure measurements show how filters at the cone tip and cone face yields a clear indication of where the permeable layers are. While these properties of the penetrometer are favorable for thin layer detection, the thin layer detection of this study relies on the use of standard cone penetrometers.

2.3.5 Physical experiments with thin clay layers in sand deposits

Although the studies mentioned above confirms that much research have been focused on the issue of layering effects on the CPTU, there is a lack of studies on the effect of a single thin weak clay layer in thick strong sand deposits. In fact, only one article where physical experiments were performed on this matter was found. This was the study of Młynarek et al. (2012), where samples of sand and clay layers of varying thickness was made. The sand in these samples had a relative density of about 80% and the clay layers were normal consolidated with a low undrained shear strength of about $5kPa$. Three samples, with layer thicknesses of 10, 20 and $40cm$ were made and a vertical stress of $50kPa$ was applied to the samples. The results of the three chamber tests are presented in **Figure 2**.18. Only the cone resistance is presented here, and the pore pressure was not measured. The layering of each sample is presented to the left of the tip resistance measurements. Here, grey symbolize sand layers and white symbolize clay layers.

Due to the high relative density in sand and the low strength of the clay, the differences in cone resistance are very large. The profiles show clearly how the measurement in sand is greatly influenced by the weak clay layer before the layer interface. The maximum cone resistance reached in the top layer of sand increases with the thickness of the upper sand layer. The peak cone resistance measurements in the clay layer for the $40cm$ clay layer was $0.13MPa$, while the peak value for the $20cm$ and $10cm$ clay layer is $0.22MPa$ and $0.27MPa$ respectively.
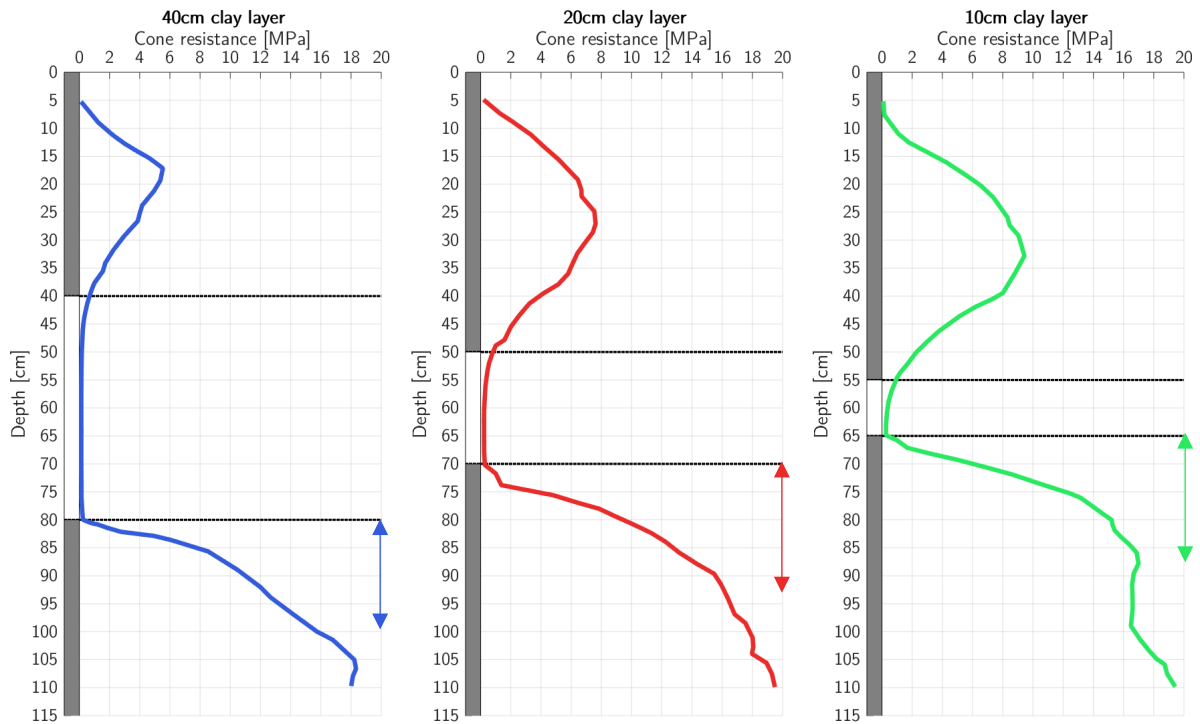
Figure 2.18*. Cone resistance measurements of the three samples with clay layers in sand, edited after the study of Młynarek et al. (2012). Arrows mark the approximate developing distances in the second sand layer determined in the study.*

The article recognizes the developing distance in the bottom sand layer to be $20 - 25cm$, as shown in **Figure 2.18**. The sensing distance in the top sand layer appear to be the same for the three tests, of approximately $22cm$. The sensing distance in the clay layers, i.e. sensing of the bottom sand layer, are very small, while the developing distance in clay from the upper sand layer is more significant.

A correction factor for the cone resistance in clay was proposed from regression. However, this correction was not made for the minimum measured cone resistance, such as presented for the thin layer correction factor K_H (**2.20**). An average cone resistance in the weak clay layer was rather selected which partly neglects the effect of thin layers. This correction factor is therefore not presented here. In order to determine correction factors the characteristic cone resistance above and below the weak layer should ideally be equal, as emphasized in subsection **2.3.2**.

Although the focus of this study is to assess the influence of single thin layers it is of interest to include studies of multiple thin layers as well. Physical experiments on multilayered samples with sand and clay were studied by Van der Linden (2016). Multiple layers of sand and clay of equal thickness were tested with a cone penetrometer with diameter of $2.52cm$. The results of the cone resistance in samples with sand and clay layer thicknesses of 30, 8 and $2cm$ are presented in **Figure 2.19**. The relative density of the sand around the $30cm$ clay layer was 91%, while it was about 55% for the other samples. The clay had an undrained shear strength of about $15kPa$.
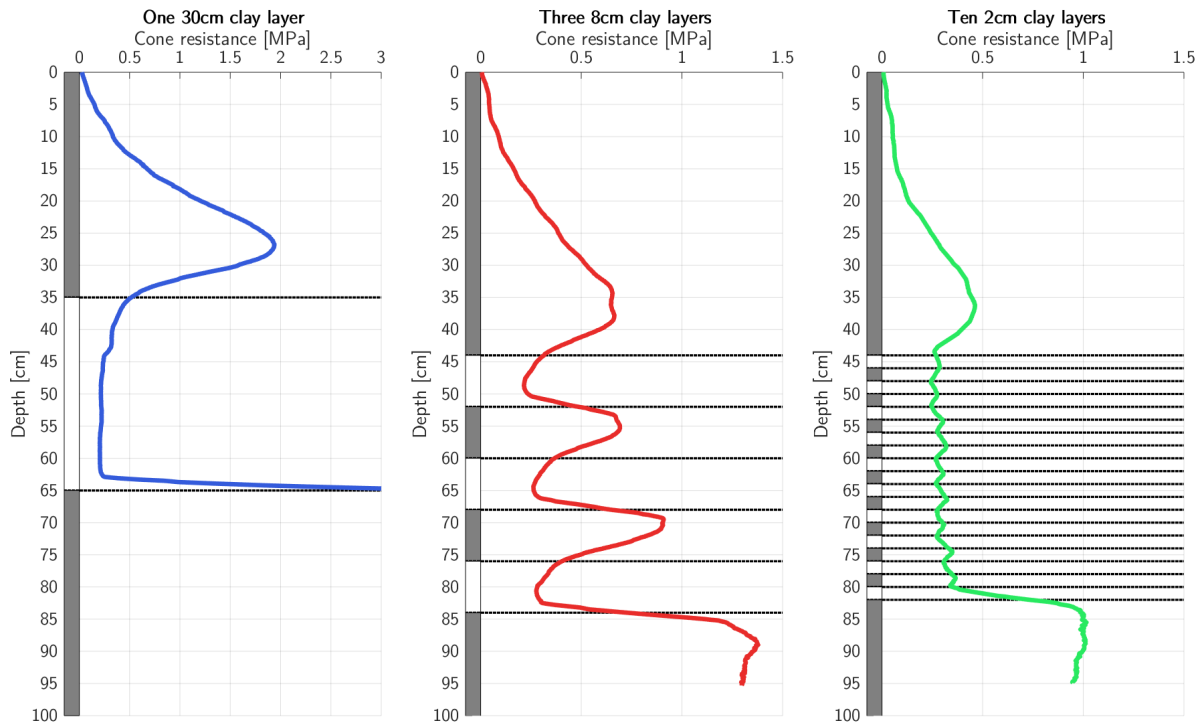
***Figure 2**.19. Cone resistance measurements in multiple clay layers of varying thickness, edited after the study of Van der Linden (2016)*

The result of the sample with a $30cm$ layer resembles those previously presented by Młynarek et al. (2012). The effect of decreasing layer thickness highlights the averaging effects during the cone penetration. For the sample with ten clay layers of thickness $2cm$, with sand layers of equal thickness in between, the cone resistance is almost the same in sand and clay.

Sleeve friction and pore pressure was presented in the article, though it is not included here. Measurements of excess pore pressure showed an increase only after the cone was penetrated some distance past the original depth of the clay layers. This was concluded to be due to sand being pushed in front of the cone and was seen in images of the sample during dismantling.

Further testing using the same equipment was done by de Lange et al. (2018). Experiments were performed with the addition of increased overburden stress, $\Delta\sigma'_v$. No overburden stress was applied in the study by Van der Linden (2016). Horizontal stress equal to 0.5 times the vertical stress was added. Two samples were presented in the article, these were a sample with four $4cm$ clay layers, and six $2cm$ clay layers, presented in **Figure 2**.**20**. The same sand and clay materials as in the previous study was used, and the sand had a relative density of about 30% for these tests. Tests were run in the same sample with overburden stress, $\Delta\sigma'_v$, of both $25kPa$ and $50kPa$.

Similar results to those of Van der Linden (2016) were found, however, the influence of the free surface was reduced significantly due to the added stress.
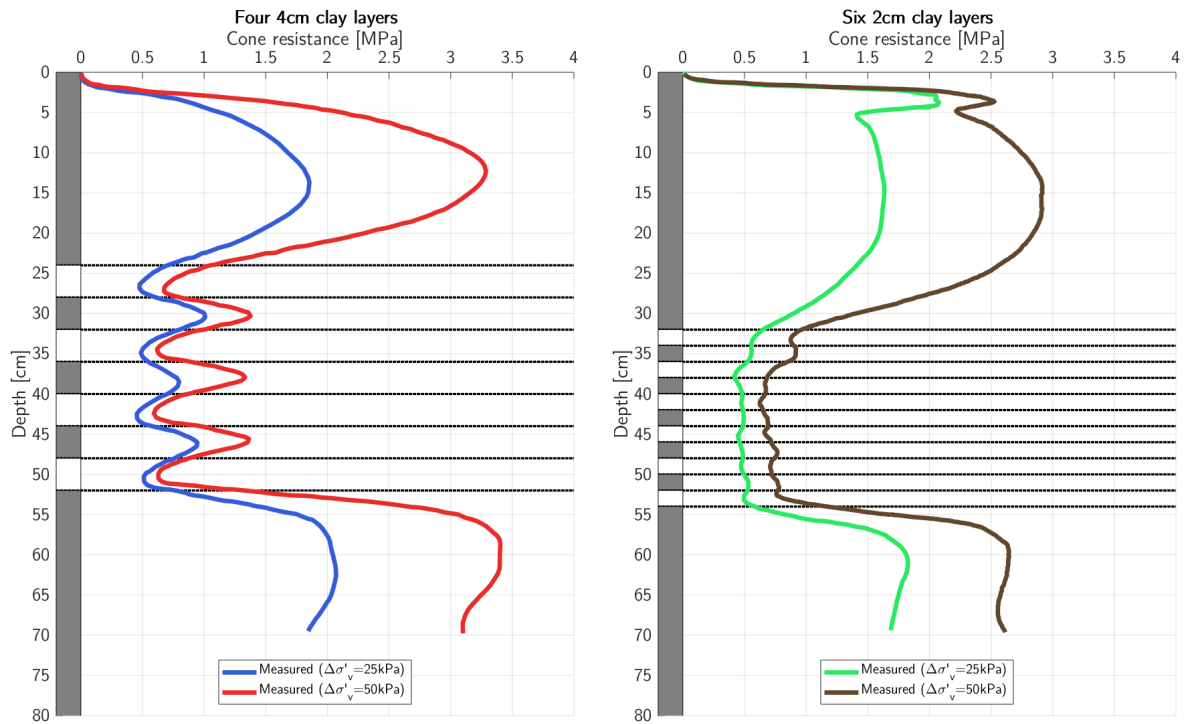
Figure 2.20. *CPTU tip resistance in interlayered clays in sands at different stress states (de Lange et al., 2018)*

These studies show how significant research has been done to understand and characterize layering effects on the CPTU. However, there is a lack of studies on the effect of a single clay layer with thickness of less than $10cm$ using a standard sized CPTU between thick sand layers of constant characteristic cone resistance.

A method of analysis of cone resistance in layered profiles were developed in the current study. The results from the three studies of Młynarek et al., Van der Linden and de Lange et al. were used for calibration of parameters of this method.

3 PHYSICAL EXPERIMENTS

Physical experiments were performed in order to gain a better understanding of the thin layer effect of clays in sand. While CPTUs could have been performed and analyzed from in situ tests at a site with known thin clay layers in sand, it was rather desired to manually control all aspects through creating soil sampled with desired properties. The experiments were conducted in a chamber that was established for this study. The first section of this chapter presents literature on chamber testing with some considerations for the chamber testing of this study. In the following section the materials and procedures of the chamber testing of the current study is presented.

3.1 Literature on chamber testing

Multiple conducted chamber tests were presented in the previous chapter. Preparation of such tests require careful considerations regarding the properties of the chamber model as well as the method used to prepare the soil within for a test. In this study the term chamber is used for a container, usually a cylinder, that contains reconstituted soil that is to be tested. The soil within the chamber is referred to as the sample. Chambers with the ability to apply a desired horizontal and vertical stress is referred to as calibration chambers.

Details on the design and use of calibration chambers have been extensively studied, including studies by Sweeney & Clough (1990) and Lunne et al. (1997). Important effects and considerations to a chamber model as well as the preparation of sand samples is presented in this section.

3.1.1 Chamber size and boundary effects on cone resistance

An ideal chamber should have a diameter such that boundary effects does not influence the cone resistance measurements. This measurement, unaffected by boundaries is called the *free field* value. While clay is to a little extent effected by the boundaries, the sand is. The symbol $q_{c,\infty}$ is used for the free field measurement. The diameter of chambers have limitations for practical reasons, and measurements are rather performed with an approximated relationship with measured values and free field values. The influence of this relationship is also dependent on the boundary conditions of the chamber. Four different sets of boundary conditions were named by Ghionna & Jamiolkowski (1991). These are combinations of horizontal and vertical boundary conditions of either constant stress or zero strain. The measured value in the chamber varies depending on the combination. There is also a dependence on the relative density, D_r, of the sand. Higher relative density is found to give larger difference between the measured value and the free field value in small chambers. An example of a correction of measurements was defined by Mayne & Kulhawy (1991) through the relation:

$$q_{c,\infty} = q_c \cdot \left(\frac{D_c/d_c - 1}{70} \right)^{-D_r[\%]/200}$$

(3.1)

where D_c is the chamber diameter, q_c is the measured cone resistance of sand in the calibration chamber and d_c is the diameter of the cone penetrometer. This indicates that a chamber to cone diameter ratio of 71, which for a $3.6cm$ cone is $256cm$, is necessary to avoid boundary effects. The influence of the boundaries is however small for much lower chamber diameters. Equation (**3.1**) is based on tests with a vertical effective stress of $142kPa$. Numerical studies by Salgado et al. (1998) and Ahmadi & Robertson (2008), where the effect of varied stress level is considered, indicates that larger differences are expected for lower stress states. The latter study considers the effect of different boundary conditions, and results show that zero horizontal strain boundary conditions yields the lowest difference to the free field cone resistance measurements. The chamber used in this study had boundary conditions of zero horizontal strain along the chamber walls.

Measured values in chambers at low stress states is not expected to accurately reflect free field measurements, which is important to consider when evaluating empirical relationships such as those presented for sand in subsection **2.2.1**.

The boundary effect of chamber tests is as presented above measured in terms of the ratio between the chamber diameter and the cone diameter. However, that is with the assumption of penetration through the center of the sample. It was determined in the current study that multiple CPTUs were to be performed in the samples in order to extract more results. The influence on tests were therefore a combination of distance to the wall and nearby tests. The influence of this is addressed in the results, however, methods to relate the chamber cone resistance to the free field cone resistance such as in equation (**3.1**) will not be used.

3.1.2 Stress state

As presented in subsection **2.2.1**, cone penetration in sands can be separated between shallow and deep penetration. For shallow penetration the free surface influence the measurements. These measurements are often of less interest than those of deep penetration. Deep penetration is achieved at smaller depths if stress is applied on top of the sample. The resulting increase in the effective stress is also favourable.

It is well-known that the stress levels of granular material such as sand in chambers with stiff walls is influenced by the width of the container, due to *silo effects*. Shear stress along the walls, as a result of friction between the material and chamber walls, cause the stress increase from added soil on top of the sample to decrease with depth. The friction is dependent on the lateral earth pressure coefficient and the interface friction between the granular material and chamber wall. Stress levels further depend on the height of the material in the chamber and the chamber diameter. Resulting vertical stress of dry granular material in a silo or chamber due to these effects were presented by Janssen (1895):

$$\sigma_v = \gamma \cdot l \cdot (1 - \exp{(-\frac{z}{l})}) \tag{3.2}$$

where z is the distance below the top of the granular material, γ is the unit weight of the dry granular material and l is the decay length. Thus, the maximum vertical stress achieved in a silo from this equation is $\gamma \cdot l$. The decay length in a 3D cylinder was defined as Duran (2000) as:

$$l = \frac{D_c}{4 \cdot K \cdot \tan{(\delta)}} \tag{3.3}$$

where D_c is the diameter of the chamber and K is the earth pressure coefficient between the horizontal and vertical stress of the soil in the chamber. The friction between the soil and chamber walls are defined by $\tan{(\delta)}$, where δ is the friction angle of the interface. These formulas are used to represent dry materials in a silo. For fully saturated soils, only the effective stress is influenced by the silo effect, while the water pressure remains hydrostatic. The vertical effective stress is assumed to be given by the same formulas (**3.2**) using the effective unit weight γ' rather than the total unit weight γ.

$$\gamma' = \gamma - \gamma_w. \tag{3.4}$$

Assuming the water level at the same height as the top of the soil, the resulting total vertical stress becomes:

$$\sigma_v = \gamma' \cdot l \cdot \left(1 - \exp\left(-\frac{z}{l}\right)\right) + \gamma_w \cdot z \tag{3.5}$$

This estimation of silo effect assumes an increase of shear stress along the walls from zero at the top to a maximum shear stress of $\gamma' \cdot D_c/4$ if the sample is tall enough. While it is unlikely that the maximum shear stress occurs at the bottom of the chamber, this approximation of the stress level is nonetheless used in this study. The additional stress from an applied vertical effective stress, here called $\Delta\sigma'_{v1}$, at depth $z = 0$ results in the following increased vertical effective stress ($\Delta\sigma'_v$) at depth z:

$$\Delta\sigma'_v(z) = \Delta\sigma'_{v1} \cdot \exp{(-\frac{z}{l})} \tag{3.6}$$

3.1.3   Preparation of a sand sample

Partly due to the difficulties in sampling of undisturbed sand, a great amount of literature is available on the preparation of reconstituted sand samples. Testing of sand in a small scale like a triaxial test or in a large scale such as a calibration chamber tests for CPTs requires the sand to be prepared in an effective and repeatable manner, and different techniques are used. The methods used to create sand samples is aimed to simulate the natural processes that forms sand deposits in order to create specimens that resembles that in the field. The goal is normally to achieve a uniform density and different methods are suitable depending on the desired density. Smaller samples are normally made through tampering, while larger samples are rather made from pluviation or

vibration. It is challenging to create large samples of uniform density, and loose samples are often more difficult to make.

A typical pluviation systems is presented in **Figure 3.1**, which shows an example from Sweeney & Clough (1990). The setup consists of dry sand poured from a certain fall height on to a sand diffuser causing it to then raining down evenly distributed. The effect of fall height, shutter opening and diffuser type on the sand density has been studied by Rad & Tumay (1987). An efficient method of compaction of sand samples are through vibration (Raihane et al., 2011). Undercompaction should be considered in order to create uniform density of sand samples when the sand sample is made in layers (R. Ladd, 1978).
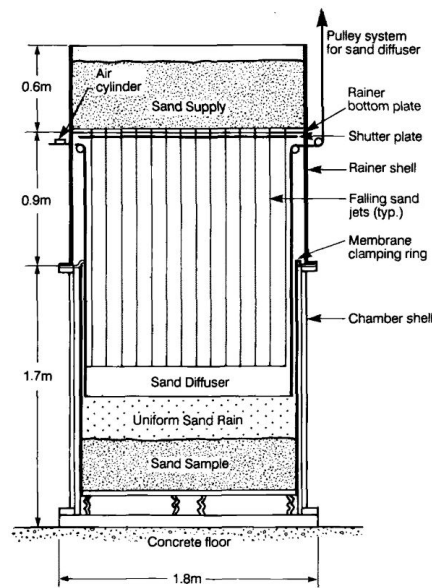
Figure 3.1. An example of a rainer system (Sweeney & Clough, 1990).

3.2 Physical experiments in this study of thin clay layers in sand

The experiments were desired to to consist of loose to medium dense homogenous sand with clay layers of thickness in the order of one to four cone diameters. In order to represent a typical CPTU test, a standard cone penetrometer of cross section area $10cm^2$ was used. A new chamber model of diameter $1.2m$ was established with the previously mentioned effects of chamber size effect in mind. Suitable soil materials were acquired and procedures to create loose sand samples were developed. Dead weight was added to increase the stress state of the samples. The complete composition of a sample is here referred to as a *test case* or simply *case*. CPTUs performed in each test case are called tests.

The development of the chamber and procedures, and the work on preparation and testing of samples required much consideration and documentation. Only a brief presentation on the methods of the physical experiments is given in this section, while the full details are presented in appendix **A**. These methods are presented in the same order both places, i.e. details on subsection **3.2.1** is given in **A.1**, **3.2.2** in **A.2** and so on.

3.2.1 Sand material

The sand used in this experiment was determined to be homogenous and characterized as uniformly graded sand through sieve testing, with the properties presented in **Table 3**.**1**. The determined grain density, minimum and maximum void ratios are presented in **Table 3**.**2**.

Table 3.*1. Grain size characteristics of the sand*

d_{10}	d_{50}	d_{60}	C_u
$0.175mm$	$0.492mm$	$0.742mm$	4.24

Table 3.*2. Characteristic density measurements of the sand*

ρ_s	e_{min}	e_{max}
$2.73g/cm^3$	0.50	0.87

Strength and stiffness properties of the sand was interpreted from two triaxial compression tests, the results are presented in **Table 3**.**3**. One of these was a very loose sample $(D_r \approx 0)$ while the other was medium dense $(D_r \approx 60\%)$. The friction angles were interpreted assuming an attraction, a, of $1kPa$ for both tests.

Table 3.*3. Sand strength and stiffness parameters*

e	ϕ	E_{50}
0.86	$24°$	$4MPa$
0.65	$43°$	$18MPa$

3.2.2 Clay material

A clay material normally used for pottery and ceramics was used to create clay layers. The clay was packaged in blocks units each weighing $10kg$ with length of $32cm$ and square sides of $12.5cm$. Water content was tested for all blocks was measured with an average of 23.8% and a standard deviation of 0.55%. Atterberg limits are presented in **Table 3**.**4**. Triaxial and oedometer tests were performed on clay blocks. Determined parameters are presented in **Table 3**.**5**. A similar type of clay was used in the previously presented studies of de Lange et al. (2018) and Van der Linden (2016).

Table 3.*4. Water content and Atterberg limits of the clay*

w	w_L	w_p	I_P
23.8%	30.5%	18.5%	12%

Table 3.**5**. *Strength and stiffness of the clay*

E_{oed}	σ'_c	s_u	$I_R = \dfrac{G}{s_u}$
$4MPa$	$100kPa$	$27.5kPa$	37

3.2.3 Chamber model and equipment

The setup of the chamber model is presented in **Figure 3**.**2**. The chamber elements were concrete cylinders of $120cm$ diameter. The bottom chamber element had wall heights of $95cm$. Additional cylinder extensions were used, each of height $51cm$. Water was filled into the chamber from the bottom and a $10cm$ thick layer of gravel layer formed the bottom to ensure even pressure during saturation of the sand. The water flowing into the chamber had a constant head equal to the final sample build height. Heights in the chamber were measured as elevation over the chamber floor with symbol h. Scaffolding was used during sample construction and as a platform to run tests on. An image of the complete setup in the laboratory, of the chamber, scaffolding and testing equipment is presented on .
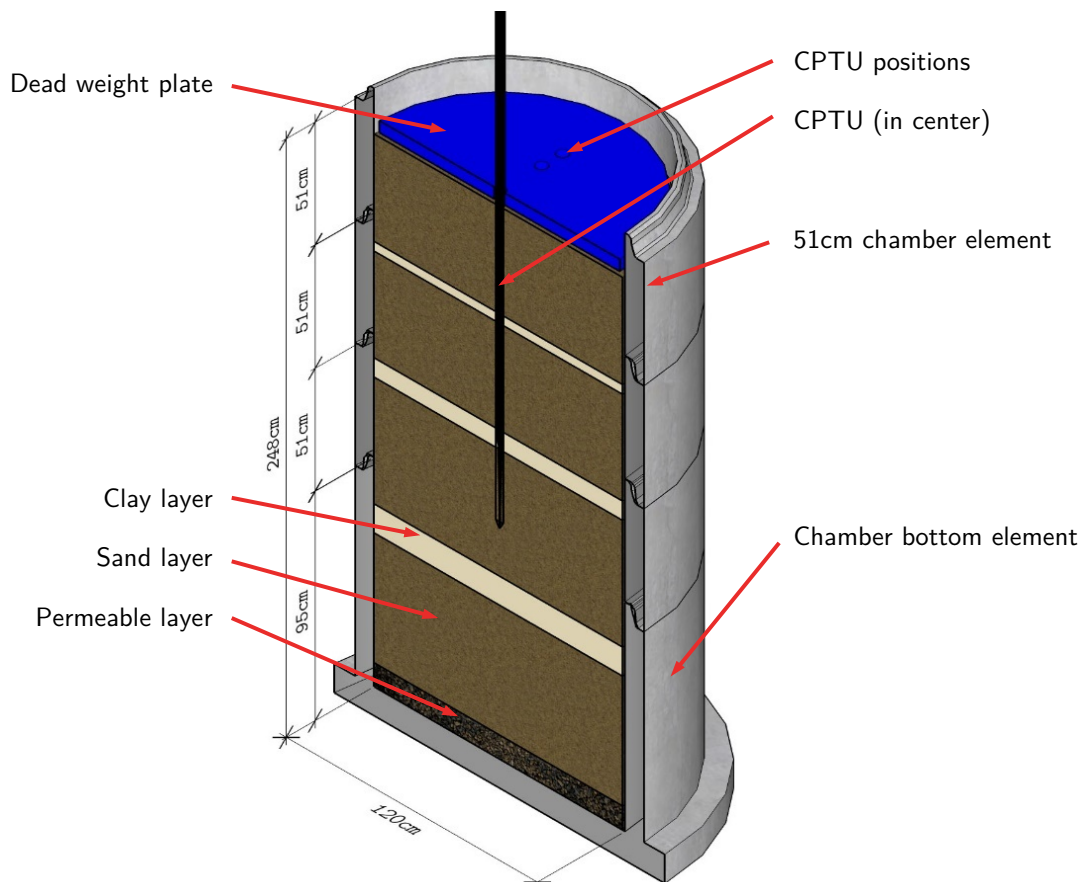
Figure 3.**2**. *Illustration of the chamber model.*

A steel plate with added dead weight was used in order to increase the stress level in the sample. The steel plate was $2.5cm$ thick with diameter of $115cm$. The total mass of the plate with dead weights was $1380kg$ with center of gravity at the center of the plate. The resulting stress was $11.4kPa$ distributed over the sample area with $120cm$ diameter. Test locations were positioned in the plate, as illustrated in **Figure 3**.**3**. Seven holes for testing were made, one in the center (*1*) and six along three lines from center with a $120°$ angle in between. These directions were called a, b and c, each with two holes with distance $20cm$ from center called *2x* (*2a, 2b, 2c*) and $30cm$ from center called *3x* (*3a, 3b, 3c*).
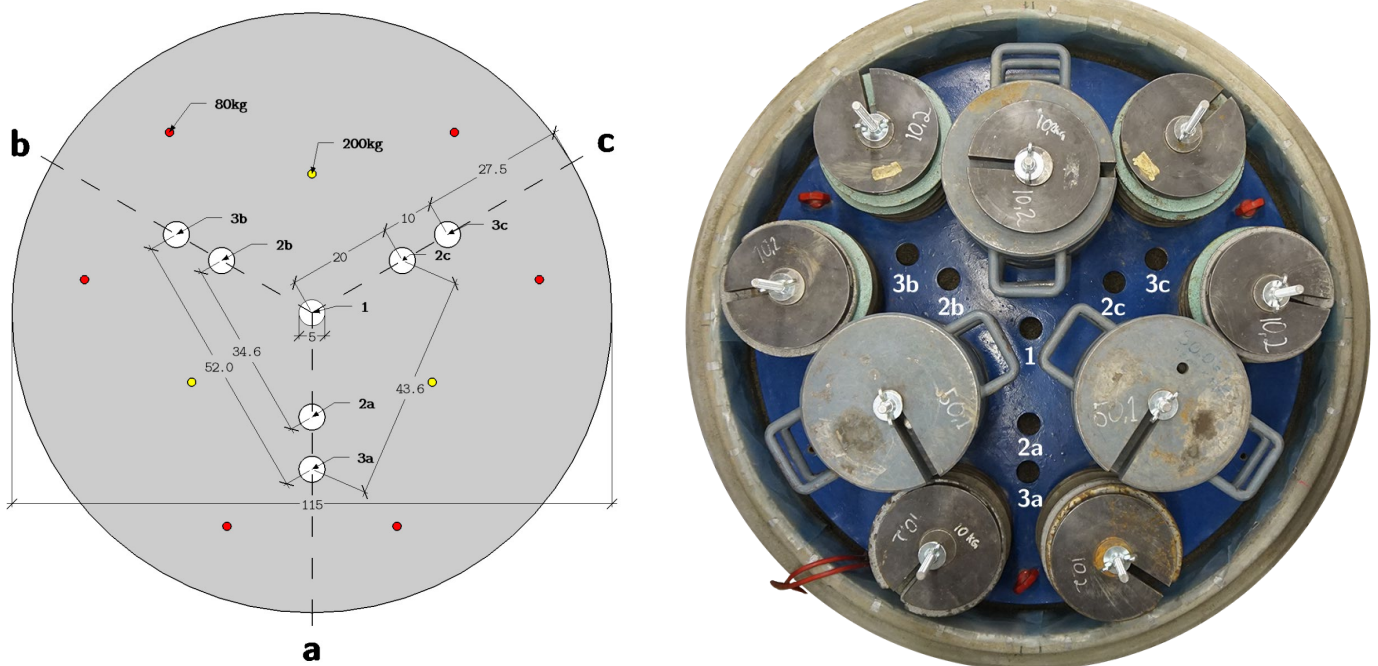
Figure 3.*3. The dead weight plate. Left: Dimensions (in centimeter) and hole names. Right: Image of the plate on top of sample.*

As presented in subsection **3.1.1**, boundary effects may be significant at low stresses when the ratio between the chamber diameter to the cone diameter is not sufficient. That ratio applies for tests performed in the center of the chamber, i.e. only if hole 1 is used. Results will be influenced by previous test when multiple tests are performed in the same sample. The influence on the measurements are then a combination of the distance to the chamber wall and distance to other test positions. The closest distance between holes of different directions, excluding hole 1, are $34.6cm$ or about ten cone diameters. Influence of nearby tests are inevitable; however, measurements affected by this were still used for interpretation. These effects are mentioned together with the results.

Earth pressure sensors were used to record the vertical total stress in the sample. The pressure cell was placed so that the stress was measured in the center. The pore pressure was logged at the bottom of the chamber.

3.2.4 Sample preparation

The procedure used to create samples of sand was developed with considerations to the literature presented in subchapter **3.1.3**. Creation of large sand samples favors automated mechanical procedures of sand for efficiency, for instance by a traveling pluviator. Samples are typically made by dry sand with the aim of a high density. However, the sand samples in this study were aimed to be of low density and sand was stored moist, with a water content of about 6%. A manual, yet repeatable procedure to create loose, uniform sand samples were developed. The sample was created in increments, called *sand layers*, though each sand layer was made the same way, i.e. no layering effects during CPTU testing was intended in the sand. The process of each sand layer consisted of three stages:

1) Slightly moist sand was rained into the chamber through a mesh,
2) The moist sand was slowly saturated from underneath, causing settlements,
3) The sand layer was compacted through vibration.

These stages for sand layer i are illustrated in **Figure 3**.**4**. Each sand layer starts after the completion of the previous sand layer, i.e. stage 3 for sand layer $i-1$ is the same as stage 0 for sand layer i. The mesh, or rainer plate, that was used had a diameter of $115cm$ and holes of about $1.5cm$ by $1.5cm$ (see **Figure A**.**27**). It was attached by chains to the top of the chamber at a selected height. This height was equal to the height of the previous sand layer, h_0, plus the filling height, Δh_f, as shown in the figure below.
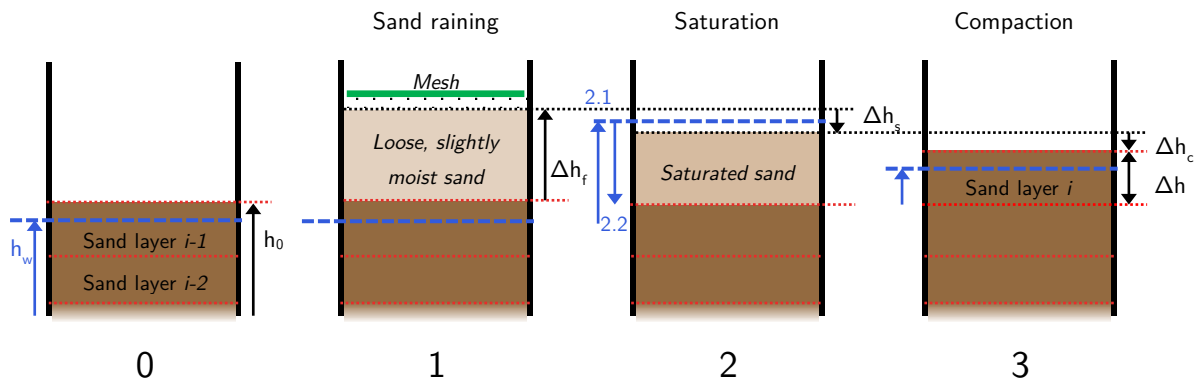
Figure 3.*4. Illustration of the stages in the preparation of each sand layer in the chamber*

As the sand was moist it could be spread over the mesh without falling through. The raining stage was done in cycles. Each cycle consisted of filling a certain amount of sand, evenly distributed over the mesh. Then, the mesh was vibrated manually until all the sand had fell through the openings. This was done until the desired filling height was reached. The moist, rained sand was very loose, with dry density of about $1.25g/cm^3$, or $e \approx 1.2$.

Stage two consisted of slowly increasing the water level until it reached the top of the sand layer (*2.1* in the figure). Settlements due to wetting (Δh_s) was found to be about 15% of the filling height. Then, the water level was lowered to the top of the previous sand layer (*2.2*).

Finally, the sand layer was compacted by a vibro plate with frequency $50Hz$. Undercompaction was considered by vibrating each layer slightly more than the previous. Settlements from the compaction (Δh_c) was approximately 10% of the fill height minus Δh_s.

Clay layers were not made to cover the entire area of the chamber. Firstly, this was not done since it would create an impermeable barrier. Secondly, the flow mechanism in clay layers has a small radius and it was therefore deemed unnecessary in order to measure the appropriate tip resistance in the clay layers. Thirdly, by creating "local" clay layers for each test position it was possible to create different layering structure for each test position. A clay layer was therefore created in direction a, b or c independently.

The clay blocks were cut with a wire saw to length $30cm$ and sides of $10cm$ in order to create flat perpendicular surfaces. Cut clay blocks were carefully placed on top of a flat, compacted sand surface according to one of the two layer types presented in **Figure 3**.**5**. The direction these layers are placed in the figure is an example. The smallest distance to the edge of a clay layer from the center of the CPTU position was made to be at least four times the cone diameter. Note that in the test case where clay layer in *1 direction* was used, no test was performed in the position 20cm from center, i.e. the "2x" hole is not used (2a for the example in the figure).
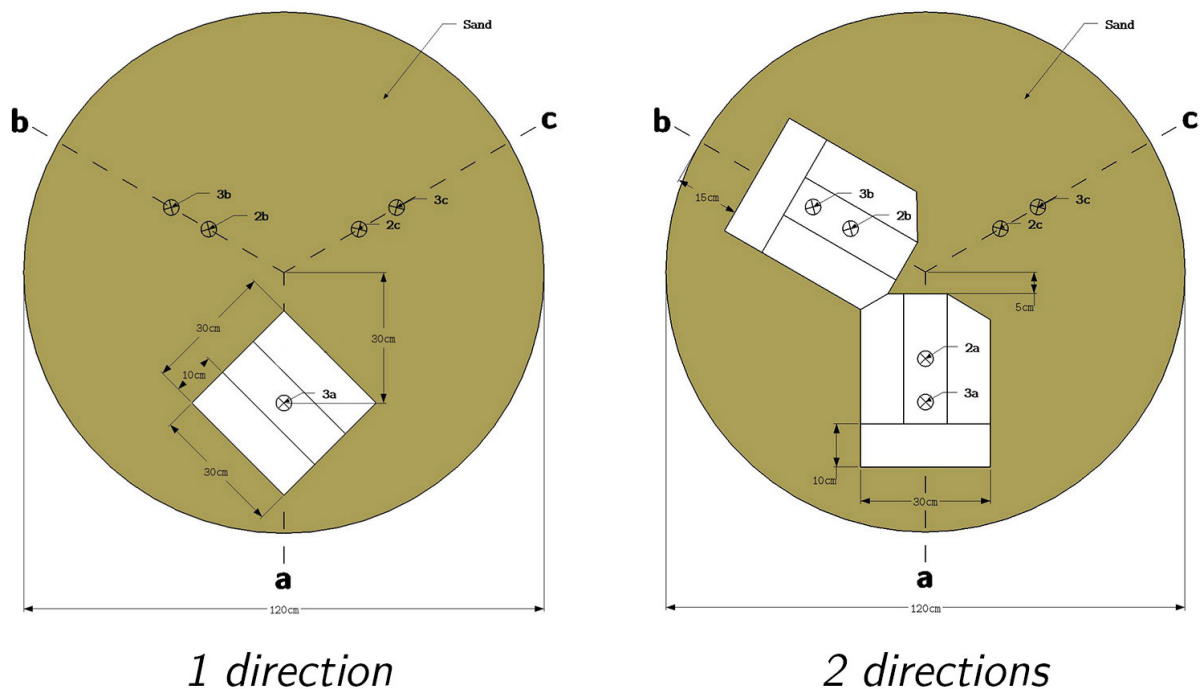
Figure 3.**5**. *Illustration of the two clay layer setups used in the experiments.*

The area around the clay layers were filled with sand according to the previously presented procedure. However, the fill height of sand layers at the same height as clay layers were increased. In addition, less sand was rained over the clay as the clay would not settle during saturation nor compaction.

Finally, as the sample was built to the desired height with a flat top surface, the dead weight plate was carefully placed in the center of the sample. In order to avoid local stress concentration at the edges of the plate, the sand along the wall had a slight inclination to about $6cm$ from the wall.

3.2.5 CPTU equipment

A recently calibrated, standard cone penetrometer of the type *CPT GEOTECH NOVA* was used. Specification of the equipment were according to the European Standard (ISO 22476-1:2012), including a cross-sectional area of $10cm^2$ and the recommended pore pressure filter placement behind the cone (u_2). A bore rig produced by *Borro* was used as thrust machine. As the chamber height was more than two meters and advantage of this machine was continuous penetration without the need of stopping for added push rods. Penetration speed was $1.5cm/s$, which is $0.5cm/s$ slower than the standard. This was done for a slightly increase in the data resolution as measurements were recorded with $1Hz$ frequency.

The accuracy of depth measurements is expected to be within $0.5cm$. The reference depth of the penetration is the depth of the cone tip. However, in order to present measurements in a more suitable manner, the measured values may also be presented against the average depth of the measurement location. These adjustments in depth were $1.6cm$ for q_t, $3.8cm$ for u_2 and $11.0cm$ for f_s. For clarification, measurements plotted against these depths are referred to as *depth adjusted to measurement location* on the depth axis of plots.

3.2.6 Dismantlement

After the tests are complete, density samples are taken continuously with depth. A cylinder with diameter of $7.2cm$ and $5cm$ was carefully pressed into the sand. The sand surrounding the cylinder was dug out in order avoid disturbance of samples. Density samples were taken at positions in the middle between directions a, b and c, called ab, bc and ca. The horizontal distance from the density sample positions to the test positions were $20-30cm$.

3.2.7 Test cases

Two test cases were made with a rough description of properties as presented in the table below. Layer profiles were defined for each direction according to **Figure 3**.**6**.

***Table 3**.**6**. Rough description of the test cases*

Test name	*Sample height* *(h)*	*Sand properties*	*Clay layers*
Case A	~$200cm$	Very loose sand $(D_r \approx 10\%)$	One *1 direction* clay layer $31.5cm$ thick
Case B	~$230cm$	Loose sand $(D_r \approx 30\%)$	Three *2 directions* clay layers 4, 8 and $12cm$ thick
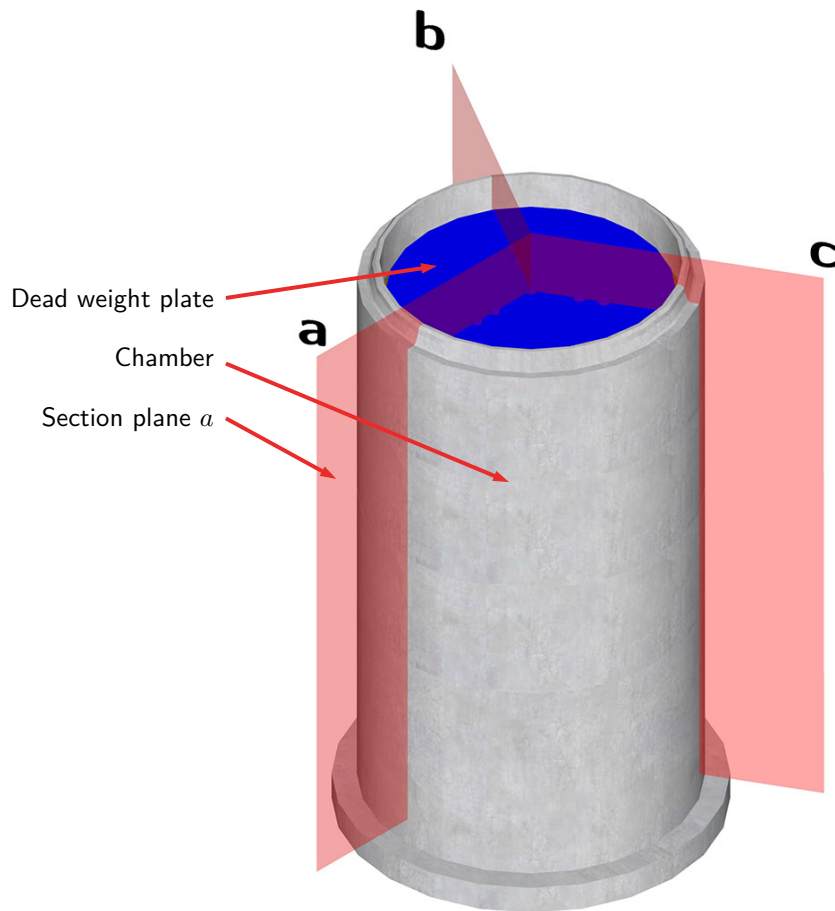
***Figure 3**.**6**. Sections planes are formed along the three directions, a, b and c. Layering profiles are defined for each of these section planes.*

Case A was primarily intended as a calibration of equipment and procedures. Preparation of sand sample was done without compaction, i.e. only stages 1 and 2 were carried out for each sand layer. The resulting sand density was very low, with relative density of $0-10\%$. A thick clay layer was made to measure the characteristic cone resistance in the clay. The clay layer was made according to *1 direction* (**Figure 3.5**) and was placed in direction a. Three levels of clay blocks were placed, the first two with height of $10cm$ and the last of $11.5cm$. The resulting clay layer at position a had a height of $31.5cm$. **Figure 3.7** presents the two different layering profiles according to the sections presented in **Figure 3.6**. The dimensions in this figure represent the positions of the completed sample. The wall of the chamber elements is illustrated in the figure. During construction, heights were recorded as *local depth* (z_L) measured from the top of a chamber element, as shown in the figure.
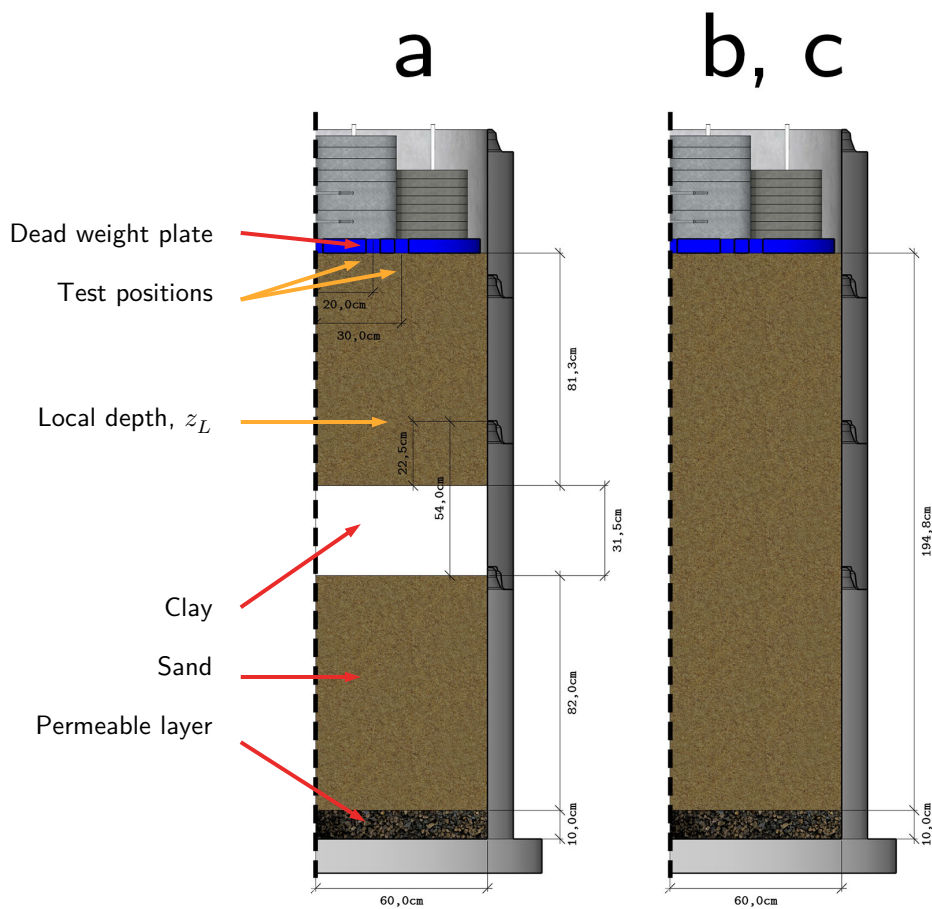
Figure 3.7. *Illustration of the Case A layering along the three sections.*

While the sand was prepared in a very loose state, two occurrences caused local densification of sand. The first was under the clay layer in direction a. Settlements of $1cm$ occurred directly under the clay layer due to the placement of the clay. The second was during the placement of the dead weight plate after the sample was built to the final height. The resulting settlement under the plate was $5.5cm$. Three test positions were used in the sample, one in each of the three directions. These were 3a, 2b and 3c.

The second sample, Case B, was made according to the aim of creating thin clay layers within a rather loose sand deposit. Sand layers were made including vibro compaction, which gave an increased density of the sand. Three clay layers were made with thicknesses of 4, 8 and $12cm$. The distance between each layer was about $50cm$ to ensure that layering effects were only influenced by one layer at a time. Clay layers were made in *2 directions* (**Figure 3**.**5**) at the time. The positions were selected so that each of the three directions had two layers of clay, as presented in **Figure 3**.**8**. This allowed for measurements in pure sand in at one direction at each height.
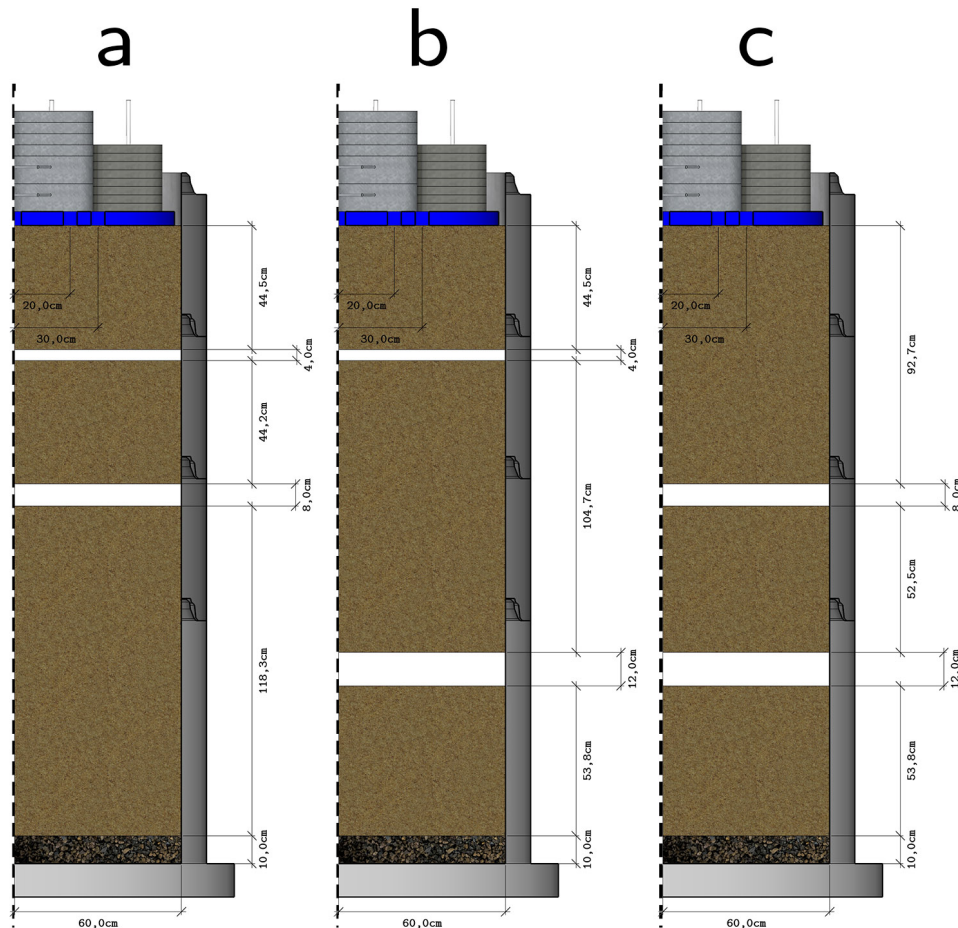
Figure 3.***8****. Illustration of the Case B layering along the three sections.*

The preparation of the sand layers was done without local settlements as experienced in the previous sample. This was partly due to a denser sand sample. However, other factors are believed to cause local variances in density, for instance the density after vibro compaction. These effects are mentioned in the analysis of results.

All test positions were used except for position 1, i.e. the center. That is, both positions in each direction were used. Since the distance between position 2x and 3x is only $10cm$, the second test was expected to be significantly affected by the neighboring test. Tests were therefore performed in two rounds, where one position in each direction was tested in each round.

4   ANALYSIS OF LAYERING EFFECTS

The primary goal in evaluation of CPTUs in thin layers is to determine the characteristic cone resistance in order to achieve better interpretations. This is usually done through correction factors of the peak measurement in the thin layer, as previously described in subsection **2.3.2**. Section **2.3** presented literature with some methods of correction for thin strong layers, while limited methods are given for thin weak layers and no general correction methods for thin clay layers in sand. A numerical procedure was developed in this study with the aim to reflect the behavior of cone resistance in layered sands and clays. The method uses advanced averaging through a spatial filter on the characteristic profile to predict a measured profile. This process resembles how the penetrating cone weights cone resistance of weak materials greater than strong materials.

The numerical method is based on the *inverse filtering procedure* presented by Boulanger & DeJong (2018), which was briefly described in subsection **2.3.3**. However, significant changes are made to the procedure. Appendix **B** presents all the details on the analysis method of this study. First, a brief description of the inverse filtering procedure by Boulanger & DeJong (2018) is given in section **B.1**. Section **B.2** first presents a detailed presentation of the spatial filter of Boulanger & DeJong followed by an in depth description of the procedure developed in this study. A parameter study is given in section **B.3** while the method is applied to some of the previous physical experiments previously presented in section **B.4**.

Important differences between the procedure of Boulanger & DeJong and that of this study includes firstly the differentiation of the dependence on soil ahead of and behind the cone depending on the soil material. Secondly, the procedure of this study aims to better reflect the continuous shape of cone resistance measurements in a layered profile. **Figure 4.1** illustrates filtered profiles from the procedure of this study (in blue) and of the original procedure by Boulanger & DeJong (2018) (in purple). The results are based on the characteristic profile in black, which consists of weak over strong soil and the opposite. The strong material has a characteristic value ten times that of the weak layer. Note that the cone resistance is not presented with units since neither of the procedures depend on it. That is, the filtered profile is determined in a relative manner rather than from the absolute values of the characteristic profile. However, a parameter which relates to the soil material is included in the developed procedure of this study while the original procedure has no such input. Only the procedure developed in this study is considered in this chapter.

The first section illustrates the spatial filter, called *the cone penetration weighting filter*, which is based on the characteristic profile and is specific for each depth. These cone penetration weighting filters results in predicted measured profiles, or *filtered profiles*.
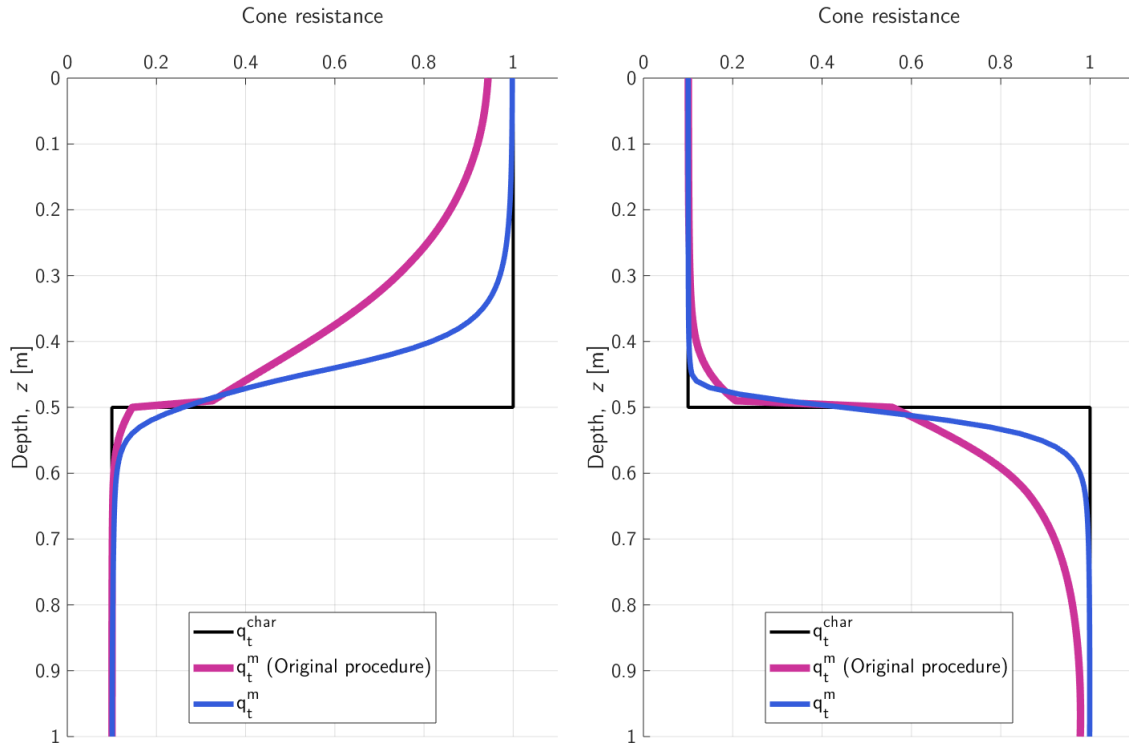
Figure 4.1. Illustration of transition from strong to weak (left) and weak to strong (right) with results of the procedure of this study in blue and of the original procedure from the article of Boulanger & DeJong (2018) in purple. These profiles are determined from the characteristic profile in black.

4.1 The cone penetration weighting filter

Filtered profiles, named q_t^m in **Figure 4.1**, are determined from convolution of a spatial filter and a characteristic cone resistance profile. The spatial filters are called cone penetration weighting filters with symbol w_f, and are defined for each depth. The characteristic cone resistance profile and some control parameters are used to determine the size and shape of the weighting filters. No normalization is done for the characteristic cone resistance regarding stress state prior to the analysis.

A parameter which control the sensing length was included, called ξ. Values of ξ are determined for each layer and is regarded as a parameter than may reflects the material behavior. Materials which is more dependent on the soil ahead of the cone than behind the cone has values of 1, while material with greater dependence on the soil behind the cone has smaller values. Lower values of ξ also give smaller weighting windows.

Weighting filters of six different depths are presented in **Figure 4.2**. This is the same as the left profile in **Figure 4.1**. Each weighting filter is valid at the evaluated depth, indicated by the circular marker, and the area under the curve is equal to one. Each value in the filtered profile is calculated as the integral of the weighting filter multiplied with the characteristic cone resistance.

The examples presented in **Figure 4.1** and **Figure 4.2** represents sand and clay as the strong and weak material, respectively. The sand is here given properties of a larger dependence on the values ahead of the cone compared to behind the cone. The larger parts of the filters in the strong layer, above depth $0.5m$ in **Figure 4.2** are in front of the cone (below). On the other hand, the clay is selected to be more dependent on the soil behind the cone which is shown by the small window ahead of the evaluated depth. While this procedure oversimplifies the cone penetration process, it is attempted to reflect these behaviors of measured profiles.
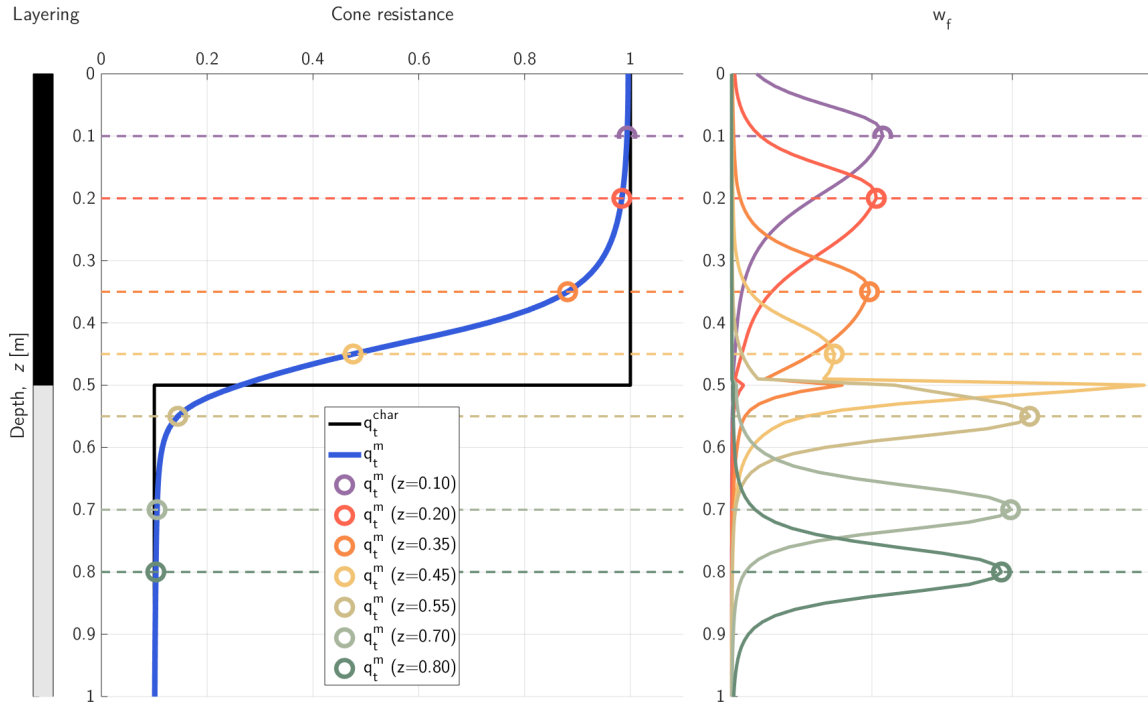
Figure 4.2. Illustration of the characteristic profile (q_t^{char}) and the filtered profile (q_t^m) of a two-layered system. Filtered measurements at seven depths are presented with their corresponding weighting filter (w_f). Circular markers represent the evaluated depth. Note the large difference in weighting of the weak and strong layers by the interface at depth $0.5m$.

4.2   Estimation of correction factors

Correction factors can be determined from measurements or they can be approximated from the filtered profiles from the procedure described above. The correction factor for thin layer effects was presented in subsection **2.3.2**, and repeated below including the definition with the cone resistance ratio:

$$K_H = \frac{q_{t,thin}^{char}}{q_{t,thin,peak}} = \frac{\eta_{min}}{\eta_{peak}} \tag{4.1}$$

Where η_{peak} is the peak cone resistance ratio in the thin layer. An example of filtered cone resistance ratio profiles of the same value of η_{min} and different layer thicknesses are presented in **Figure 4.3**.

Recall that the cone resistance ratio, η is 1 in the strong soil and η_{min} in the weak soil, as presented in subsection **2.3.4**. The depth is given in terms of cone diameters from the top layer interface. The layer interfaces are shown with vertical dotted lines. These examples are intended to represent thin clay layers of various thickness in sand. Values of η_{peak} are illustrated with the horizontal red dashed lines.
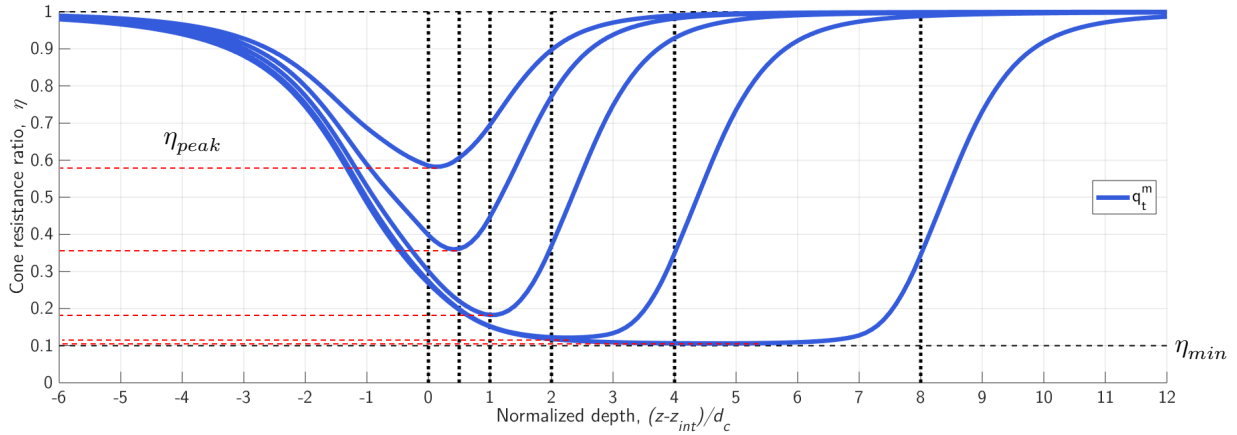
Figure 4.3. *Examples of a cone resistance ratio profiles in weak thin layers between stronger materials for varying layer thickness. The horizontal axis presents the normalized depth from the top layer interface. The minimum cone resistance ratio is given by η_{min}. Vertical dotted lines represent layer interfaces for one of the measurement profiles. η_{peak} values show the minimum measured values.*

The values of η_{peak} from **Figure 4**.3 yields correction factors K_H from equation (4.1) where η_{min} is equal to 0.1 for these examples. The resulting thin layer correction factors, K_H, are presented in **Figure 4**.4. The correction factors were selected for total cone resistance (q_t) rather than the net cone resistance (q_{net}) in this study.
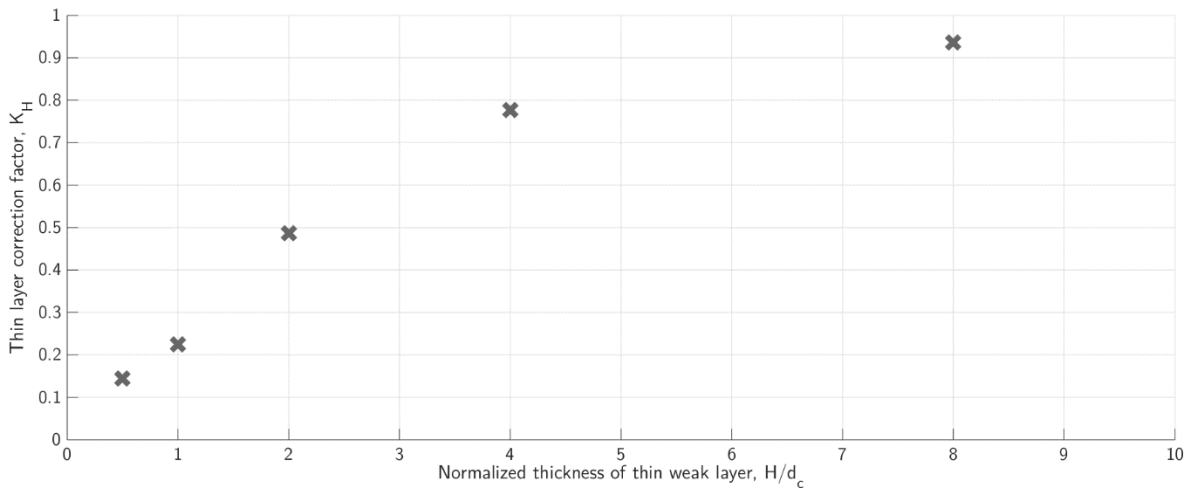
Figure 4.4. *Correction factors from the example above. The example had a minimum cone resistance ratio of η_{min} of 0.1.*

5   RESULTS AND ANALYSIS

Measurements of the experiments are presented and analyzed in this chapter. First, the CPTU measurements of the test cases are presented. The measurements are evaluated and interpreted with relative density measurements and stress state. Characteristic cone resistance profiles are determined from Case B. Following is an analysis of the results which include determination of layering effects, such as sensing distance and developing distance of the results. The filtering method presented in chapter **4** is used in the analysis. Correction factors derived from the measurements are presented in the last section.

5.1   CPTU measurements

Results of the two cases are presented in the following subsections. Measurements of the different layering profiles within the same sample (i.e. the different directions) are presented separately in order to better describe contents of the test. Most emphasis is put on Case B since Case A primarily considered as a calibration of the chamber model and procedures. Separate presentations of CPTU results for sand and clay are also given.

5.1.1   Case A – very loose sand

Three CPTU positions were used for Case A. These were tested in the order: 3c, 2b, 3a. The CPTUs are named by the test case, then position, i.e. the first test was named A3c.

The first $40cm$ of penetration for test A3c was disregarded due an issue experienced with the bore rig which caused a lack of continuous penetration. Test A3c was run again in the same hole in order to improve the execution of the tests. This test is included in the results and called A3c2. Results the tests in pure sand, A3c, A2b and A3c2 are presented in **Figure 5**.**1**. Test A3a was tested in the $31.5cm$ clay layer, the measurements of this test are presented in **Figure 5**.**2**. Layering is presented to the left of each measurement profile where gray represents sand and white represent clay. The permeable gravel layer in the bottom of the chamber is marked by solid black. The depths of the three levels of clay blocks are included in the figure of A3a.

A very low cone resistance of about $0.2MPa$ was measured in the sand below about $80cm$. The top part of the sample had values between 0.2 and $0.35MPa$ due to the compaction from the applied dead weight. The minimum cone resistance in the clay is approximately $0.25MPa$, i.e. it was larger than the cone resistance of the surrounding sand. The cone resistance increases almost symmetrically at each interface between sand and clay. The behavior is evaluated in subsection **5.2.6**. The sleeve friction measurements were $1 - 2kPa$ in sand and appear to be $6 - 8kPa$ in clay. Excess pore pressure of about $40kPa$ is measured in the clay. The increase in excess pore pressure occurs some distance into the clay. Note that these measurements are adjusted for the measurement location, i.e. the pore pressure measurement is shown at the depth of the filter.
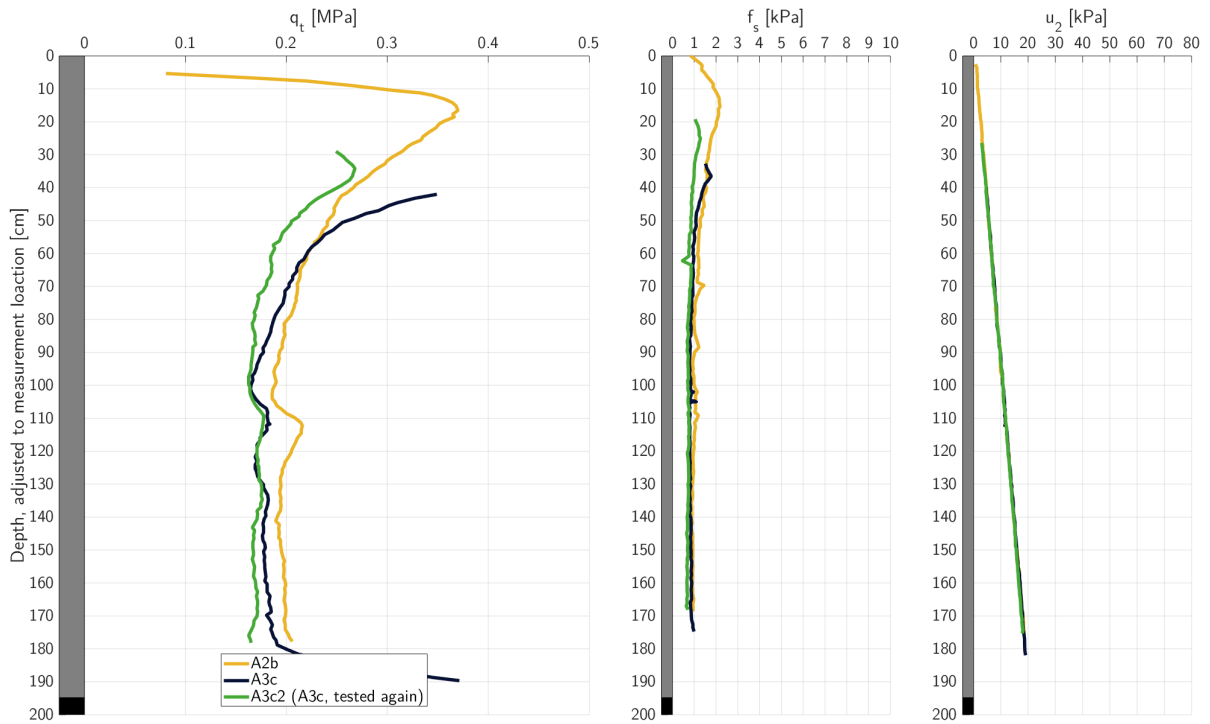
Figure 5.1. CPTU A2b, A3c and A3c2. Tests in pure, loose sand of case A.
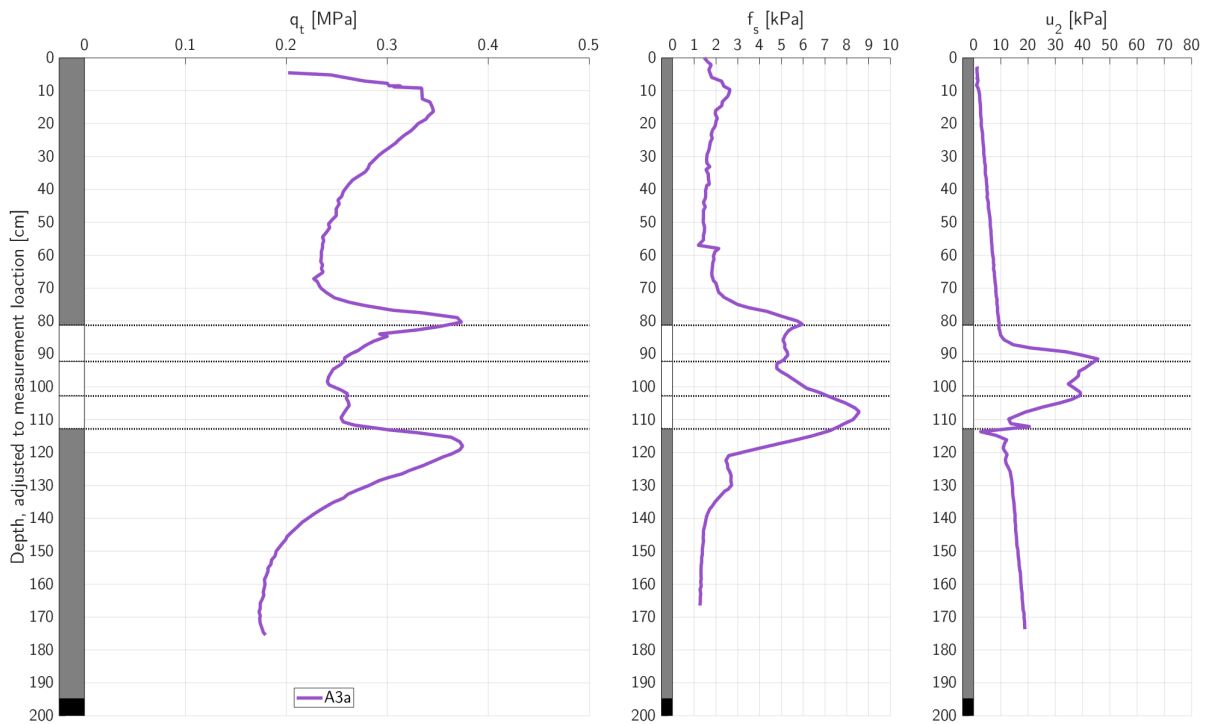
Figure 5.2. CPTU A3a. Test in the loose sand of case A with a $31.5cm$ thick clay layer.

5.1.2   Case B – loose to medium dense sand with thin clay layers

Case B consisted of three different layering profiles and CPTUs were performed in all test positions except hole 1 (center). The order of these test was 3c, 2b, 2a, 3a, 2c, 3b. Results of direction a is presented in **Figure 5**.**3**, direction b in **Figure 5**.**4** and direction c in **Figure 5**.**5**. As previously stated, two tests were performed in each section where the second of these is greatly influenced by the first test. The legend denotes which the first and second test.

These results show that the cone resistance in pure sand was mainly between 1.5 and $2.0 MPa$ for the first set of tests. Distinct changes in cone resistance occurred in all clay layers, and the minimum measured q_t increases for thinner layers, as expected. The minimum value in the $12cm$ layers was $0.33 MPa$ while it was $0.82 MPa$ in the $4cm$ layer. The influence of layer thickness on the measured pore pressure is another interesting result.

Slight issues with the bore rig was experienced during the first test, CPTU B3c, between depths 30 and 50cm, these measurements were therefore disregarded.
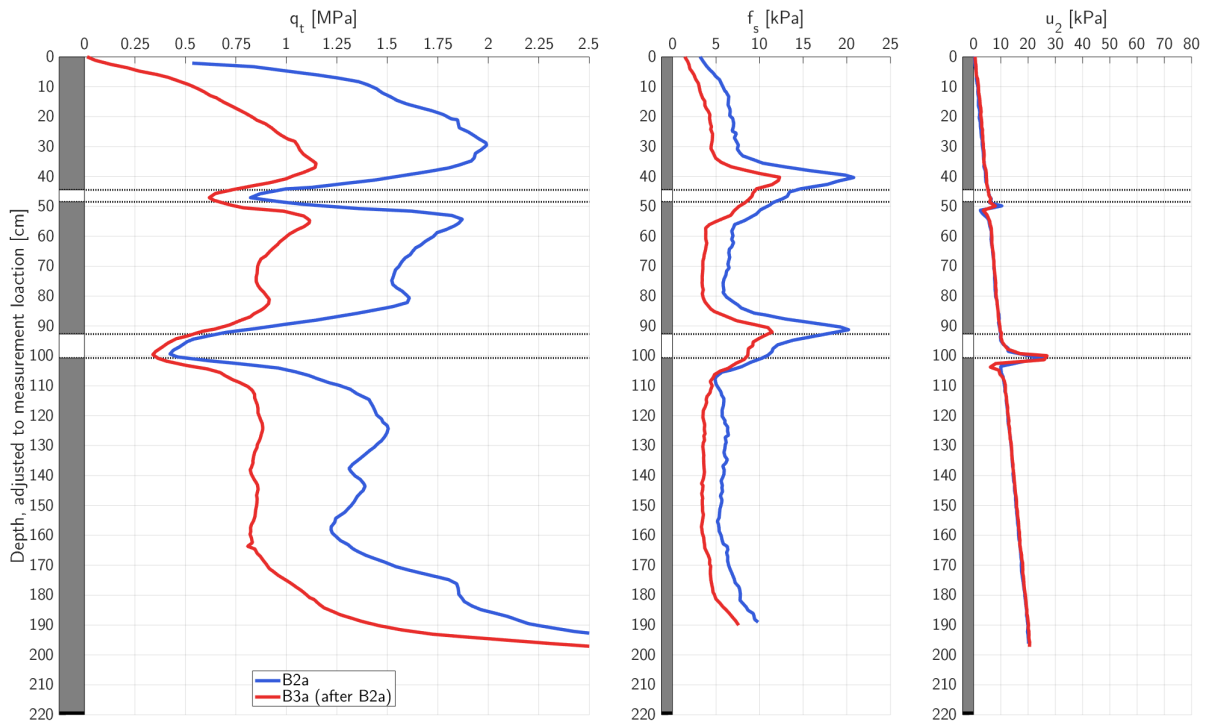
Figure 5.**3**. *CPTU B2a and B3a. Tests in loose to medium dense sand with thin clay layers.*
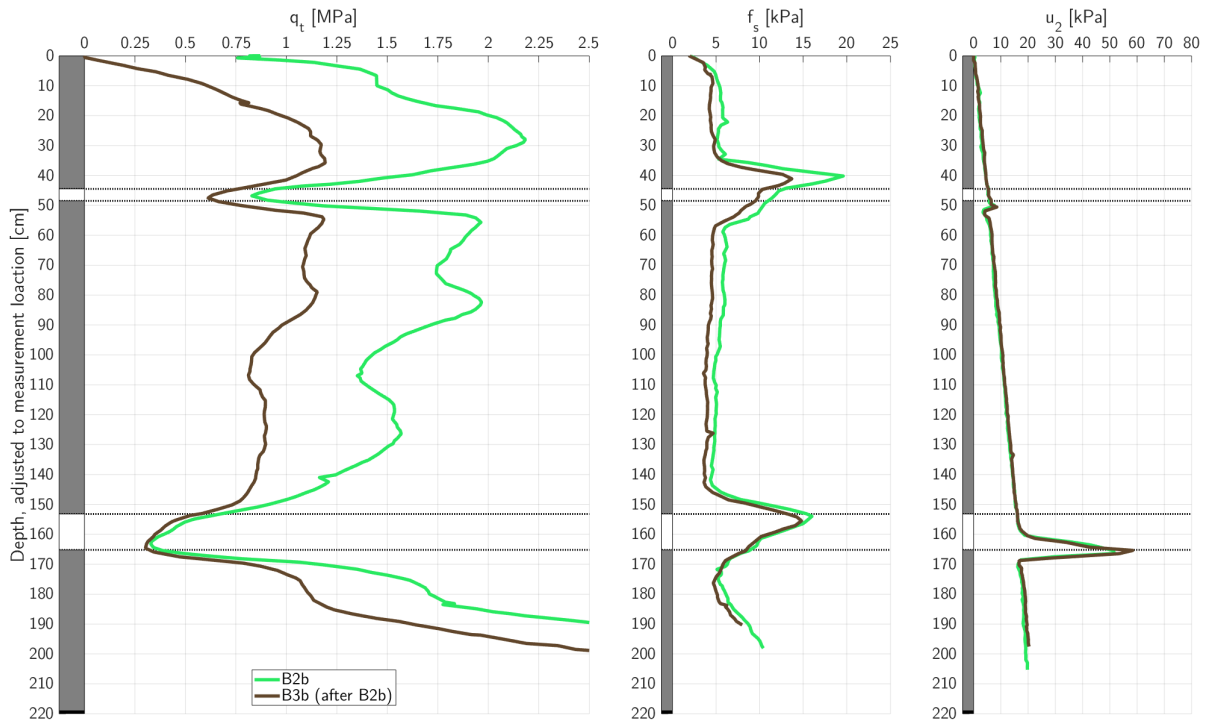
Figure 5.4. CPTU B2b and B3b. Tests in loose to medium dense sand with thin clay layers.
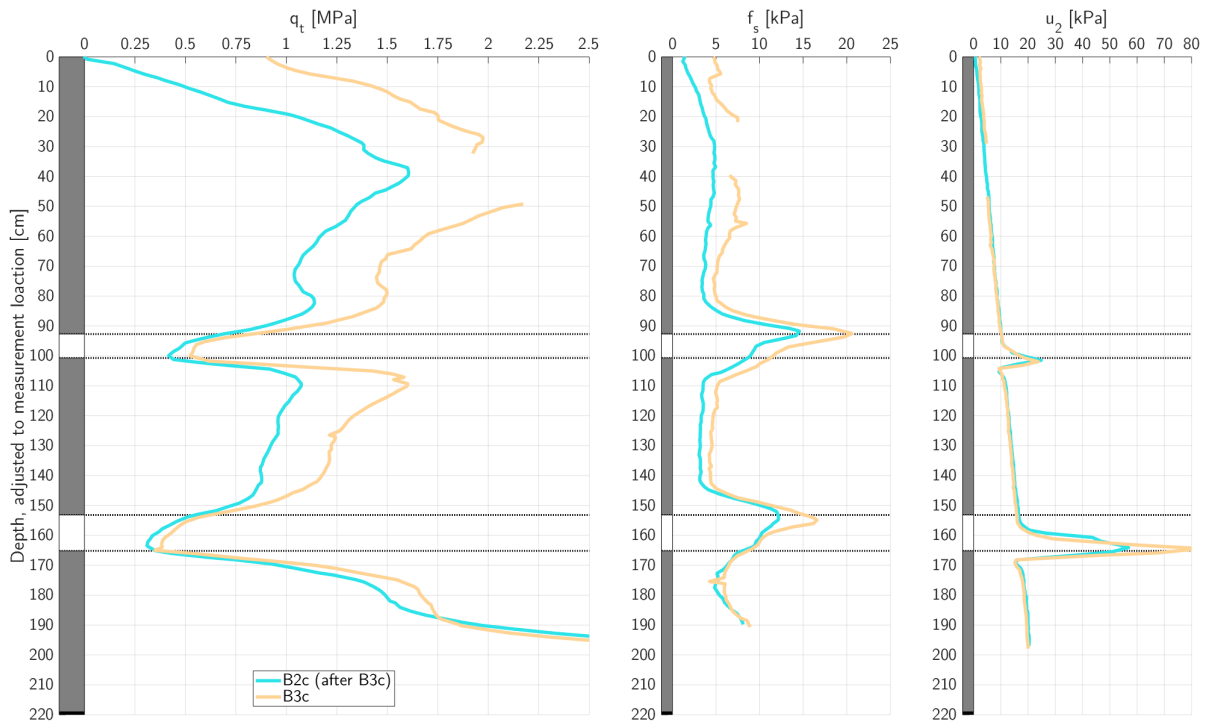
Figure 5.5. CPTU B2c and B3c. Tests in loose to medium dense sand with thin clay layers.

5.1.3 Measurements in pure sand

While **Figure 5**.1 shows the measurements of sand for Case A, a separate figure is presented for the all the measurements in sand of Case B in **Figure 5**.6. Here, measurements within three cone diameters of a clay layer are hidden. Values of q_t for the first set reaches a maximum value of about $2.2MPa$ between depths 30 to $50cm$. The cone resistance profiles are evaluated together with the relative density measurements in the next section. The sleeve friction measurements were constant at $5 - 6kPa$ while the pore pressure measurements shows a hydrostatic increase with no excess pore pressure, as expected in the sand.
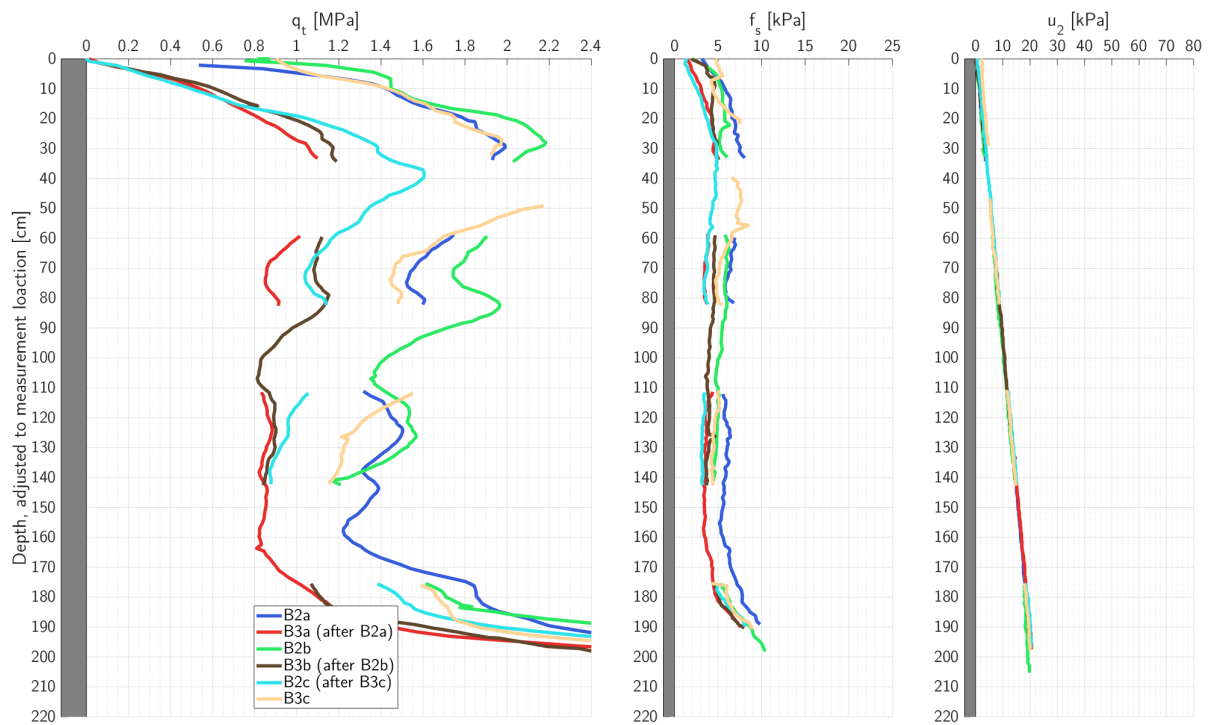
Figure 5.6. *CPTU results of case B in sand*

5.1.4 Measurements in thin clay layers

Figure 5.7 presents the sample during excavation. The test positions are clearly visible, with the positions closest to the center being hole *2x* and the outer holes being *3x*.

Measurements from the first set of tests in the clay layers are presented together for comparison. The cone resistance is presented in **Figure 5**.8, the sleeve friction in **Figure 5**.9 and the excess pore pressure in **Figure 5**.10. These figures present the depth horizontally, given as depth (z) relative to the top of the evaluated clay layer (z_{int}). For instance, for the $4cm$ clay layer in B2a, this depth becomes z minus $44.5cm$ (the depth of the top interface). Depths are given for the measurement location. Vertical dotted lines represent the different layer interfaces. The initial layer interfaces are plotted, however, as seen in **Figure 5**.7 these interfaces are significantly deformed. This contributes to delayed response, such as seen in the excess pore pressure measurement.
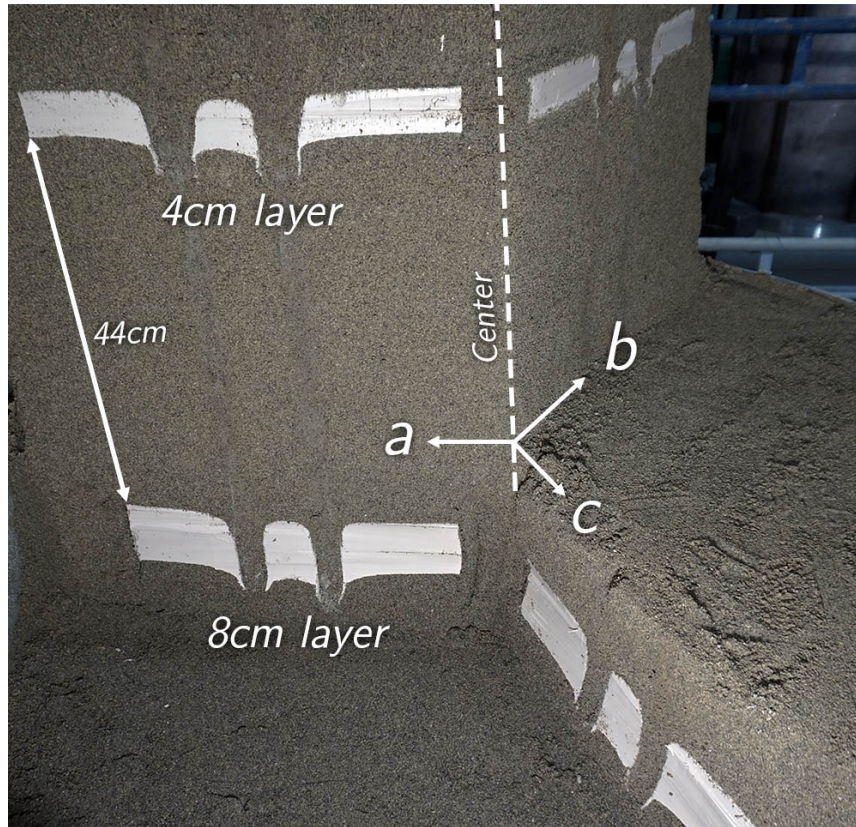
Figure 5.7. *Image of the sample from case B during excavation. The sample is cut along the three section planes, a, b and c. Clay layers of thickness 4 and $8cm$ can be seen with the position of the six tests.*

The measurements of q_t in all clay layers are presented together in **Figure 5**.8. Only the first set of tests are included for a clearer picture of the results. Here the variation in the minimum measured cone resistance depending on layer thickness is highlighted. The test in a thick clay layer, A3a, can be considered as a reference.

Values of f_s in the clay layers are presented in **Figure 5**.9. Note that the depth of these measurements is the mean depth of the measurement, which is $11cm$ for the sleeve friction measurement. This explains the increase in front of the clay layer. The difference due to layer thickness are small, while the results show higher peaks in the thin layers. A3a reflects a small increase in sleeve friction in the thick clay layer. The sleeve friction is larger in clay than in sand while it typically is the opposite. This was likely related to the overconsolidation of clay.

Excess pore pressure measurements are presented in the same way in **Figure 5**.10, where depths are given to the center of the pore pressure filter. The increase in excess pore pressure appears to start about $5cm$ below the initial depth of the clay layer. A maximum value of about $35kPa$ is reached for tests A3a and B2b, while B3c reaches almost $70kPa$.
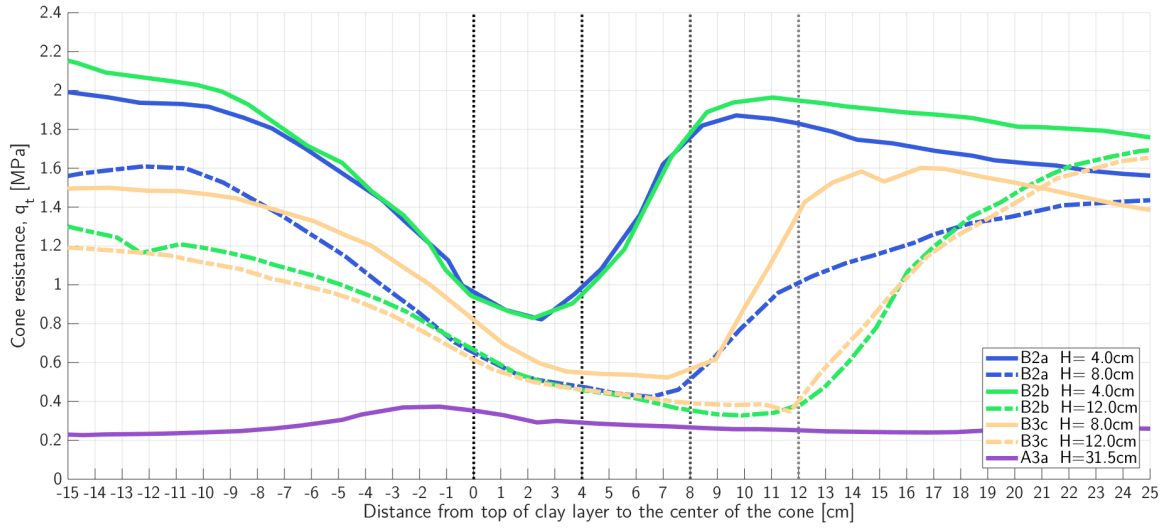
Figure 5.*8. Cone resistance in all clay layers for the first set of tests of Case B.*
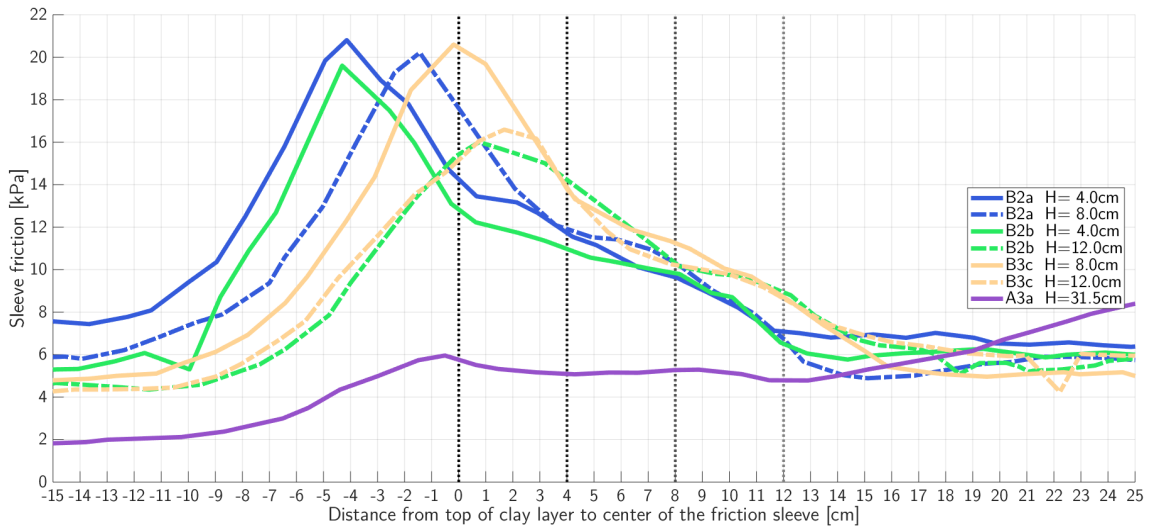
Figure 5.*9. Sleeve friction in all clay layers for the first set of tests of Case B.*
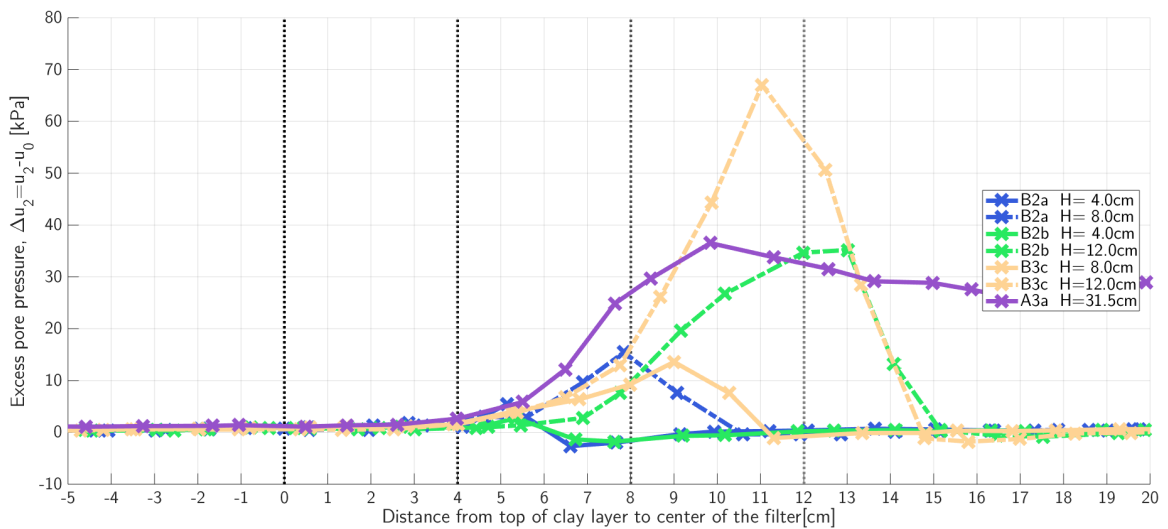
Figure 5.*10. Excess pore pressure in all clay layers for the first set of tests of Case B.*

5.2 Characteristics of the samples

The stress profile of the sample and the selected characteristic cone resistance profiles of the different sections of the layered sample in Case B are presented.

5.2.1 Stress profile

The two earth pressure sensors recorded the increase in vertical total stress during the construction of Case B. Based on the measured data, a good measure of the silo effects presented in **3.1.2** could be determined. Full details on the determination of the stress profile is given in Appendix subsection **A.9.3**. The initial stress profiles before tests were performed in the sample are presented in **Figure 5**.**11**. For comparison, the vertical effective and total stresses if silo effects are neglected are also included.

While the profiles are determined based on measurements in the center of the chamber, the stress profiles are assumed to be equal for all the test positions. The stress profile is further assumed to be valid for Case A as well.
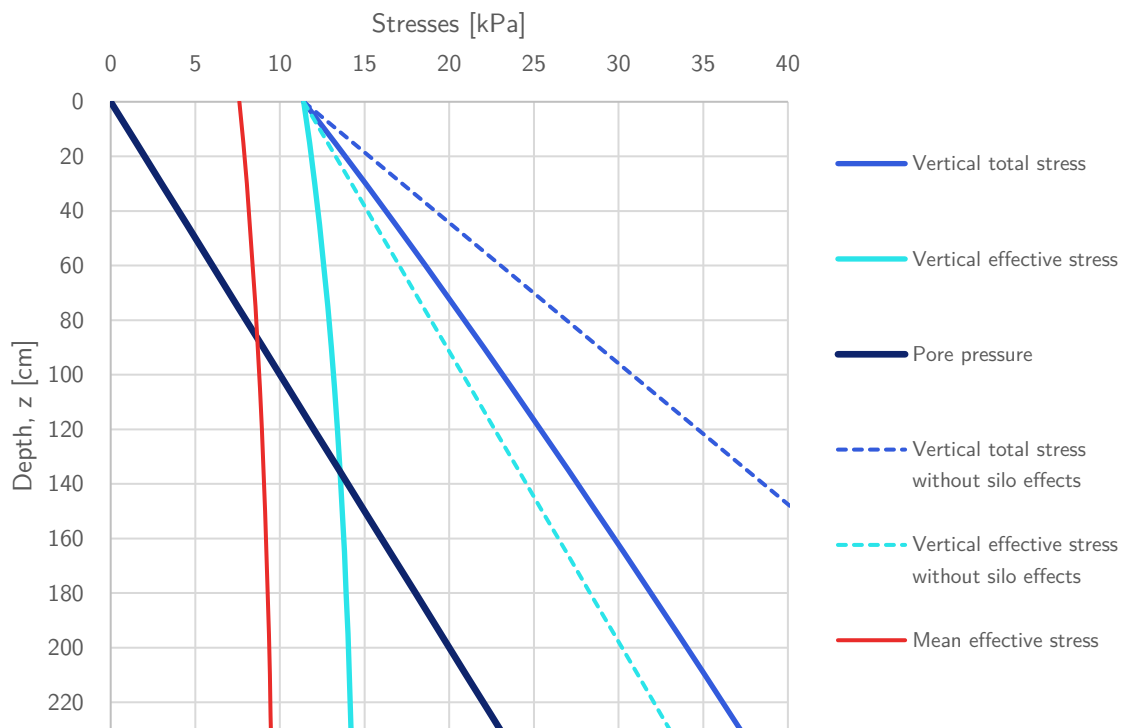
Figure 5.*11. Determined stress levels of the sample*

The result of silo effect both for the weight of the soil and from the dead weight plate causes an almost constant vertical effective stress between 12 and $14 kPa$. The lateral earth pressure coefficient, K_0, was assumed as 0.5 for the calculated mean effective stress, σ'_{m0}.

5.2.2 Relative density and characteristic cone resistance profiles in sand

Measurements of relative density of the two samples are presented in **Figure 5**.**12** and **Figure 5**.**13** together with the cone resistance measurements. The names of the positions of the density samples ab, bc and ca are given according to **Figure A**.**41**.

Simplified, representative q_t profiles were determined based on the cone resistances in sand, these are included in the figures as well. A single characteristic profile is selected for all three directions of the first round of tests in Case B. There are however certainly some differences in cone resistance at some depths. An interesting example is between depths 110 and $130cm$ where values of B3c changes in the opposite direction as B2a and B2b. These differences are believed to be due to slight variations during compaction of the sand. As shown in **Figure 5**.**8**, the peak cone resistance in the clay layer above the sand of depth $110cm$ is different for B2a and B3c. The peak value in the $8cm$ clay layer for B3c is higher than for B2a, possibly caused by the higher characteristic cone resistance in the sand layer below the clay. The cone resistance increases significantly at the bottom. This was believed to be due to the proximity to the bottom of the chamber and a more heavily compaction of the bottom sand layers. Some comments on the preparation of sand samples are given in Appendix subsection **A.9.5**. However, as the focus in this study is on layering effects between sand and clay, the layering effects in sand is neglected in the analysis.

The cone resistance and the relative density can be related through equation (**2.7**), which is here given as a function of the cone resistance:

$$D_r = \frac{1}{C_2} \cdot \left(\ln(q_t) - \ln \left(C_0 \cdot 100kPa \cdot \left(\frac{\sigma'_{v0}}{100kPa} \right)^{C_1} \right) \right) \tag{5.1}$$

The three coefficients were based on those proposed and presented in subsection **2.2.1** and altered to best fit the values of D_r with depth. The stress exponent C_1 was set to 0.7 while the C_2 was set to 2.5, similar to those of Lunne & Christoffersen (1983). C_0 was set to different values for the two cases due to the large difference in compressibility. For Case A it was selected as 7, while it was set to 30 for Case B. The dashed lines presented with the D_r values are the result of equation (**5.1**) used on the characteristic profiles in sand.
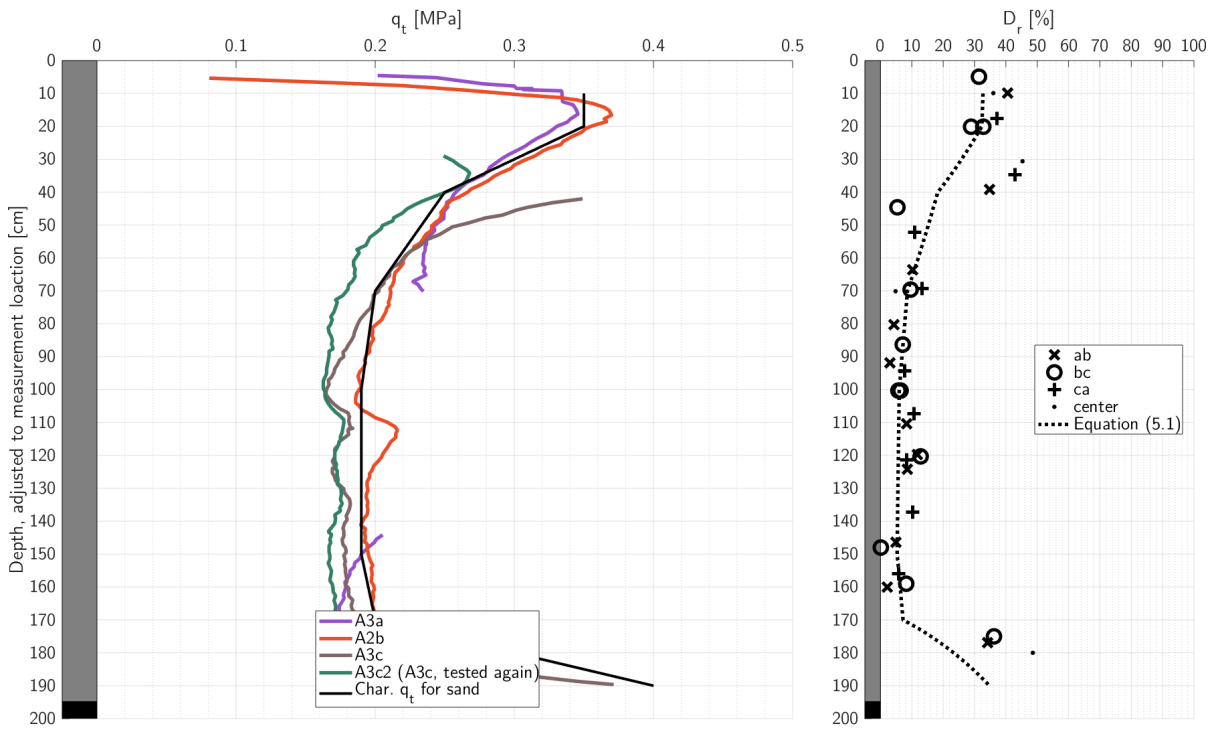
Figure 5.12. *Case A cone resistance in sand and relative density measurements.*
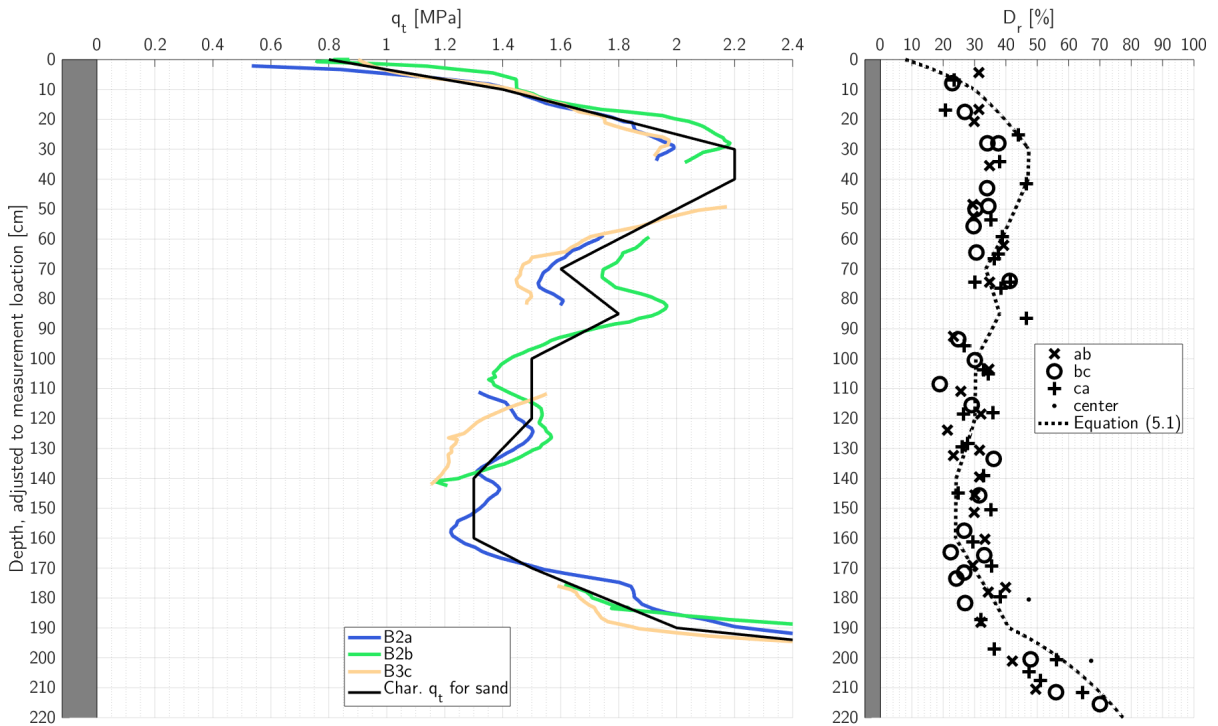
Figure 5.13. *Case B cone resistance in sand and relative density measurements.*

5.2.3 Characteristic cone resistance in clay

The characteristic cone resistance in clay was determined from test A3a. This test gave a minimum measurement of q_t of $0.245MPa$ at a depth where the total stress was $23kPa$. The characteristic net cone resistance is then $222kPa$.

$$q_{t,clay}^{char} = 0.22MPa + \sigma_{v0} \tag{5.2}$$

The compressional undrained shear strength was determined to be $27.5kPa$, yielding the following cone factor, N_{kt}:

$$N_{kt} = \frac{q_{net}}{s_u} = \frac{222kPa}{27.5kPa} = 8.1 \tag{5.3}$$

As presented in subsection **2.2.2**, there are multiple recommended formulas to determine N_{kt} and a value of 8.1 is within the typical range. The clay had a preconsolidation stress of $100kPa$, and with a vertical effective stress in the sample around $13kPa$, the overconsolidation ratio is 7.7.

5.2.4 Characteristic cone resistance profiles of Case B

The resulting characteristic cone resistance profiles are determined from the combination of the characteristic profiles of sand and clay with sharp interfaces. **Figure 5**.**14** presents the characteristic cone resistance profiles of the three directions and the measured values.
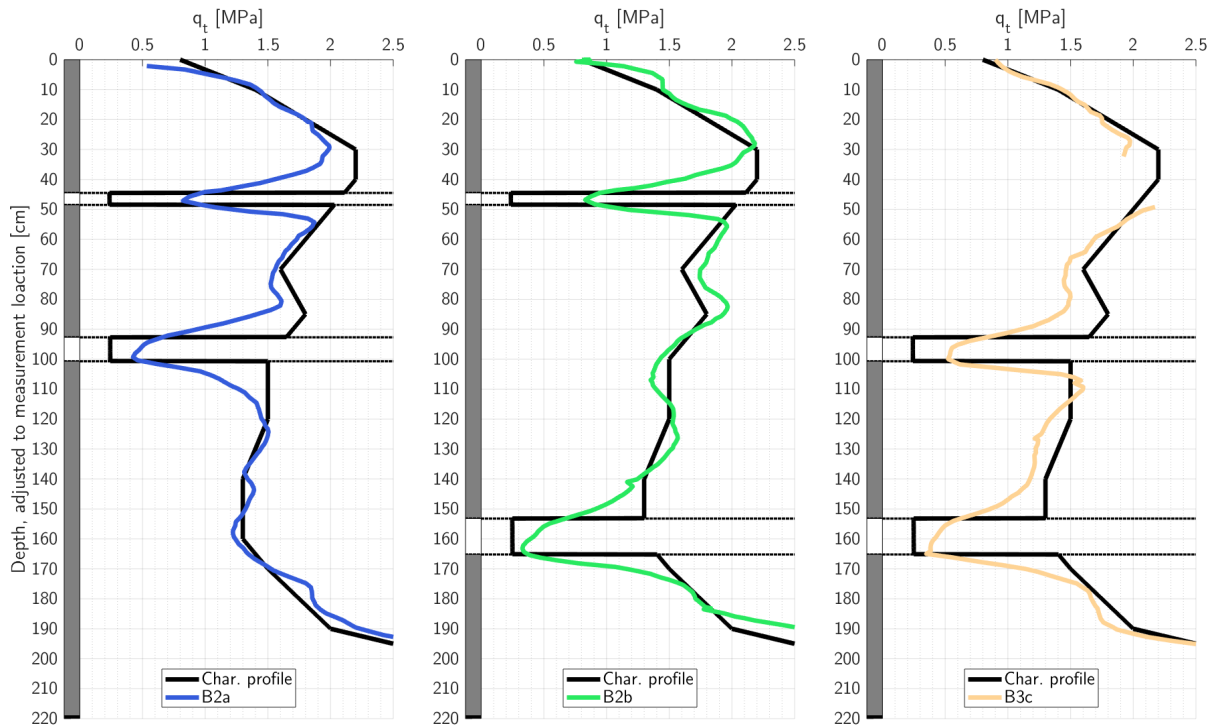
Figure 5.*14. Characteristic and measured cone resistance profiles of the three layer profiles.*

5.2.5 CPTU repeatability

The second round of tests performed in Case B per direction showed a significantly lower cone resistance than the first test. CPTUs performed in direction a and b were first tested in the position $20cm$ from center (B2a, B2b) and then $30cm$ from center (B3a, B3b), while it was done in the opposite order for direction c, (B3c, then B2c). The repeatability of the tests is evaluated in a simplified way based on the relative cone resistance values of the second test to the first test, presented in **Figure 5**.**15**. The relative profiles presented here is given as the profile of B3a divided by B2a, B3b by B2b and B2c by B3c. A relative value of 1 means the exact same measurement was measured in the first and second round of tests.

For the two direction of a and b, the relative value in sand is equal to 0.6 below a depth of about $40cm$. Direction c, however, has a higher relative value of about $0.7 - 0.8$. It is reasonable to believe that this difference is the result of the order in which the tests were conducted, as stated above. I.e., tests conducted closer to the walls first, $30cm$ from center, yield lower values for the first test compared to those first tested $20cm$ from the center. Furthermore, the relative values of direction a and b were the same even though direction b was tested before direction a. It can be assumed that tests B3a and B3b were almost solely influenced by B2a and B2b respectively. The reduction in cone resistance from tests in first to the second round is believed to be due to stress release due to compaction of nearby sand. For the clay, the flow mechanism in clay is smaller and a $10cm$ distance between tests may cause little influence on the second test. With the reduced cone resistance in the sand for the second round of tests, the ratio between the resistance in sand and clay decreases. The peak values in clay decreases which conforms to the expectation that lower ratios yield lower peak values. About 75% of the cone resistance of the first test is reached in the $4cm$ clay layer, $80 - 85\%$ in the $8cm$ clay layer and 90% in the $12cm$ clay layer.

An explanation of the lower cone resistance measurements closer to the walls can also be understood as lower vertical effective stresses due to the silo effects.

Characteristic profiles for the second round of tests was determined as 60% of the characteristic cone resistance in sand, while the values in clay were equal to the first tests. The characteristic profiles for both the first and second round of tests is presented in **Figure 5**.**16**. Except for the values at depths less than $40cm$, these profiles appear to fit well with the measurements.

Figure 5.**15**. *The ratio between the two cone resistance measurements in each direction of Case B.*

Figure 5.**16**. *Characteristic profile, measurements in sand scaled down by a factor 0.6 for the second set of tests.*

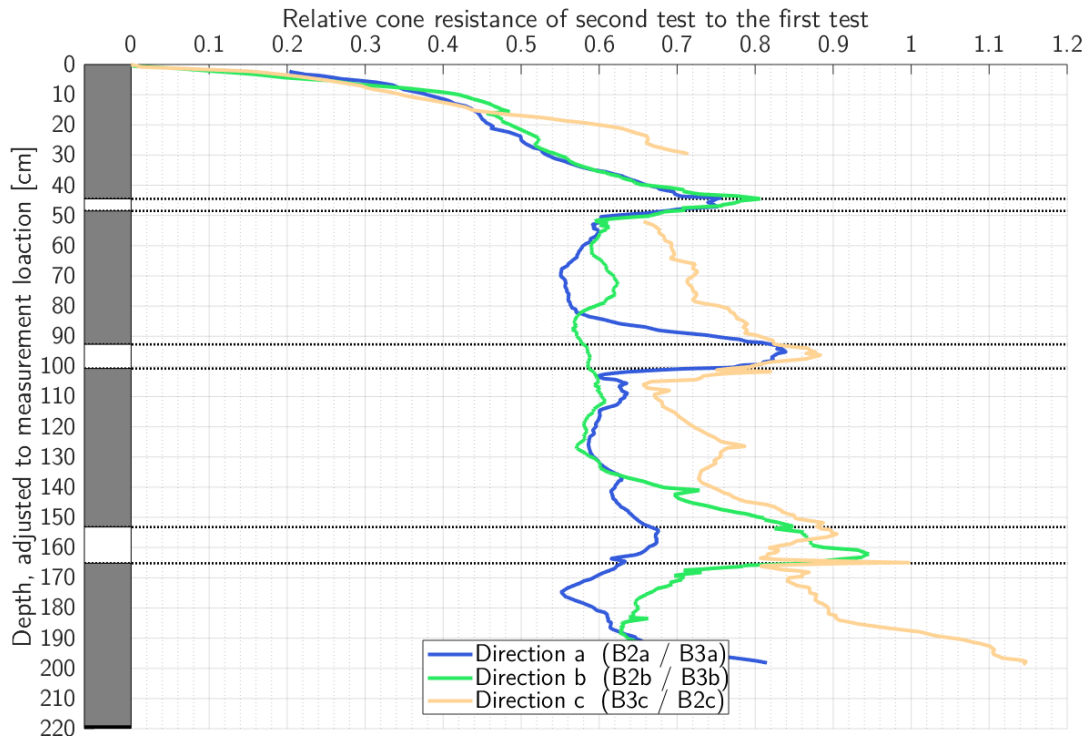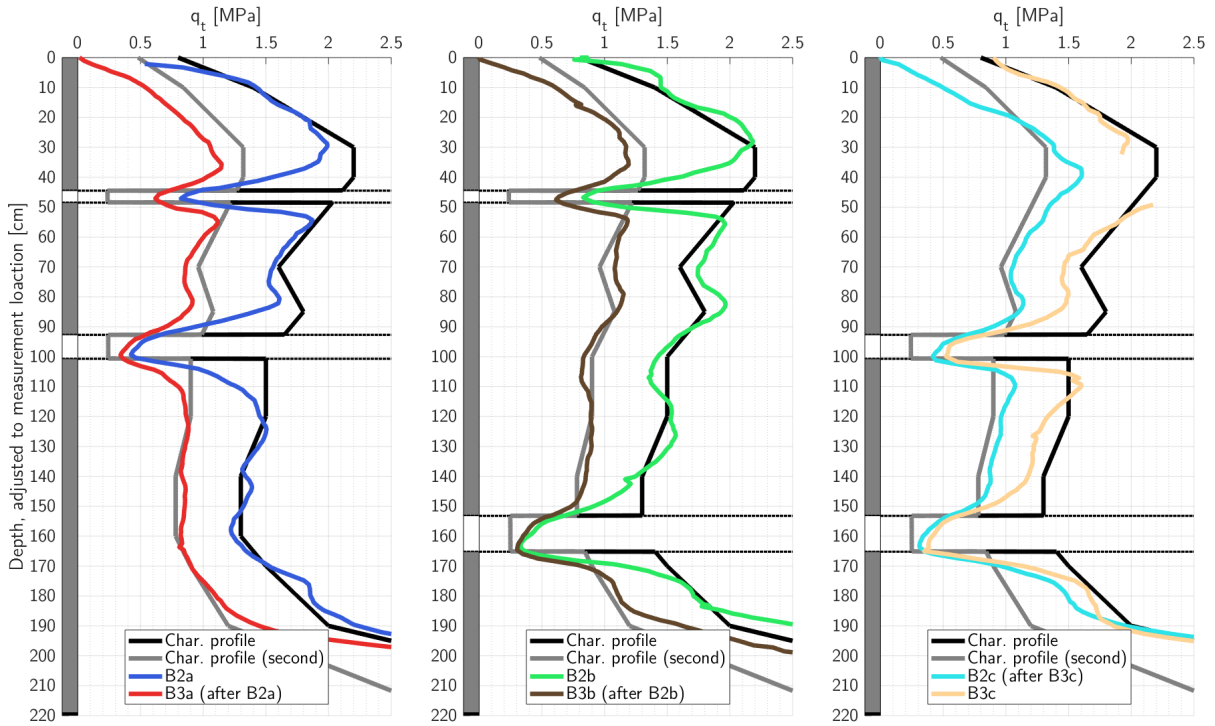### 5.2.6 Cone resistance in overconsolidated clay in very loose sand

The behavior of the cone resistance in test A3a is briefly assessed. **Figure 5**.**2** shows how the cone resistance in sand is lower than in clay, and that it increases prior to the layer interface. Furthermore, upon reaching the bottom interface the cone resistance increases again. While both situations of increased resistance is a result of sand compaction, the reasons are different at the top and bottom boundary. The compaction at the top boundary is believed to be due to the relative stiffness of clay compared to the very loose sand of Case A, which resulted in compaction of sand during penetration. As previously mentioned, the sand at the bottom boundary had settled $1cm$ from before to after the clay was placed. Furthermore, between the clay layer was placed to after it was excavated, it had settled an additional $3cm$. The settlements could be a result of either settlements during filling on top of the clay layer, the addition of dead weight plate or the penetration. The sand below the clay layer was therefore compacted and it is believed that this gave higher characteristic cone resistance at this specific depth. However, the combination somewhat stiff clay in a very loose sand is very unlikely or impossible to discover in a natural deposit. Thus, the layering effects in this sample is not further evaluated.

Little to no settlements occurred of the thin clay layers in Case B. Images and further comments are given in appendix subsection **A.8.4** and **A.9.5** for case A and B respectively.

5.3 Analysis of the cone resistance measurements

The measurements are analyzed and compared to the determined characteristic profiles. It is desired to determine the sensing and developing distances in the thick sand deposits and in the thin clay layers. Recall the definition of sensing distance as the largest distance in front of a layer where the cone resistance is influenced by the upcoming layer. Developing distance is similarly the distance until the characteristic value is reached. In thin layers the maximum developing distance is not reached. After these distances are assessed, the analysis method presented in chapter **4** is applied on the characteristic profile.

5.3.1 Sensing and developing distances in sand and clay

The sensing and developing distances are determined for the first set of tests in the layered soil in Case B. The cone resistance ratio η is used for comparison between the measurements in thin layers. Recall the definition of η as the measured cone resistance divided by the characteristic cone resistance in the strong layer. The lower boundary was then defined by η_{min}. The characteristic cone resistance in sand (strong) and clay (weak) are presented in **Table 5**.**1**. The values are determined from the characteristic profiles, though the characteristic cone resistance in sand are adjusted slightly.

Distances of sensing and development are normally given in terms of cone diameters, which is also done here. The normalized depth in the thin layers is called Z_H and defined as:

$$Z_H = \frac{z - z_{int}}{d_c} \tag{5.4}$$

where z_{int} is the depth to the top of the evaluated clay layer and z is the depth of the middle of the cone. Z_H then describes the distance in terms of cone diameters from the top layer interface.

Table 5.1. Characteristic cone resistance in the three layers of the first set of tests.

Layer thickness H	Norm. thickness H/d_c	Strong $q_{t,sand}^{char}$	Weak $q_{t,clay}^{char}$	Lower boundary $\eta_{min} = q_{t,clay}^{char}/q_{t,sand}^{char}$
$4cm$	1.1	$2\ MPa$	$0.24\ MPa$	0.12
$8cm$	2.2	$1.6\ MPa$	$0.24\ MPa$	0.15
$12cm$	3.3	$1.2\ MPa$	$0.25\ MPa$	0.21

Results of the first set of tests are presented with the cone resistance ratio against the normalized depth in **Figure 5.17**. Vertical lines represent the layer interfaces and values of η_{min} are included for each layer according to the values in the legend and the table above.
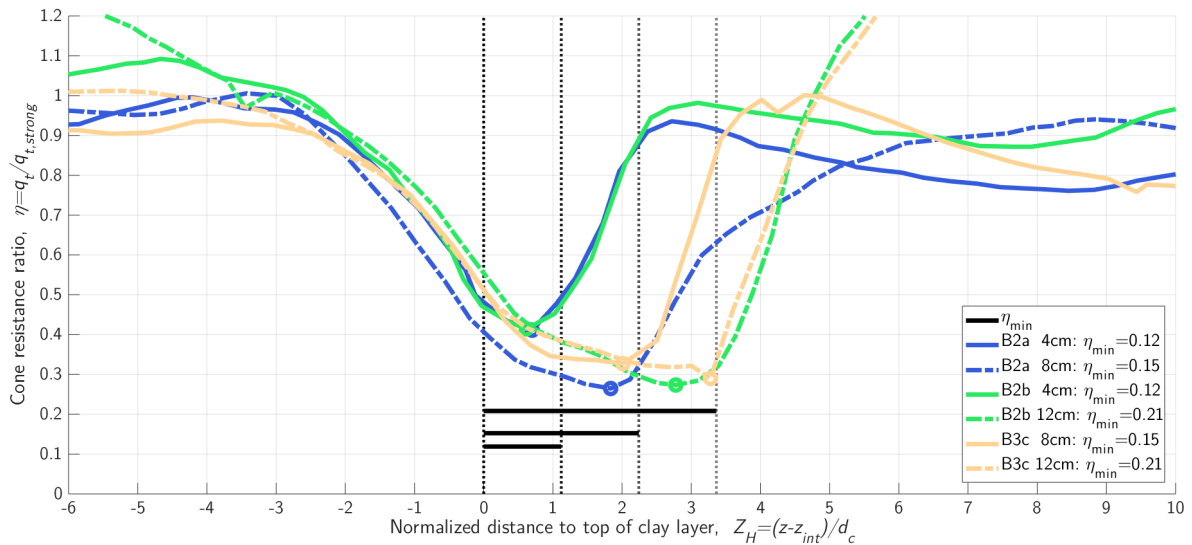
Figure 5.17. Normalized tip resistance vs. normalized depth from clay layer. First set of tests.

While **Figure 5.17** in essence presents the same information as **Figure 5.8**, the trends are better visualized through the cone resistance ratios. The similarities of the transition between the cone resistance of sand to that of clay appear to be the same for all measurements, independent of the clay layer thickness. The sensing distance is about 3 cone diameters in sand prior to all clay layers. When the first interface is passed, the cone resistance continues to decrease until a $0.5d_c$ distance to the bottom interface. Since the depth is adjusted to the center of the cone, this means that the minimum cone resistance is measured almost exactly as the cone tip reaches depth of the initial bottom layer interface. The minimum cone resistance in the clay layer is marked with a circular marker.

This means that the developing distance in the clay layers are larger than the clay layer thickness, while the sensing distance is almost zero. The developing distance in sand after the second interface is passed appear to be about $2d_c$ for all tests except for B2a in the $8cm$ layer. This is believed to be due to a locally lower characteristic cone resistance under this clay layer, which makes determining the developing distance difficult.

The derivative of the cone resistance ratio with respect to the normalized depth, $d\eta/dZ_H$ and presented in **Figure 5**.**18**. This plot gives the same information as the derivative dq_t/dz would give. The intention with this figure is to substantiate the evaluated sensing distance of about $3d_c$ in sand and to assess the developing distance in the clay layer. The decrease in η at $3d_c$ distance to the top of the clay layer is apparent and the change in derivative from zero to negative supports the determined sensing distance. This figure also shows how the derivative is the lowest when the middle of the cone is at the clay layer interface. I.e. the cone resistance profile has an inflection point at the this depth.

Another use of **Figure 5**.**18** is to estimate the layer thickness needed for the characteristic cone resistance to be correctly measured and for the full developing distance in clay to be reached. The derivative of $d\eta/dZ_H$ gradually increases towards zero for greater layer thicknesses. That is, the derivative appears to approach zero asymptoticly. The needed developing distance can be estimated to be $4 - 5d_c$ visually. A rough estimation of the steep increase of $d\eta/dZ_H$ after the bottom clay layer interface is passed is included in the figure. The large difference in the absolute value of the derivative upon entering and exiting the clay layer reflects that the sensing distance is greater than the developing distance in sand. The approximate inclination upon exiting the clay layer is $d\eta/dZ_H = 0.5$.
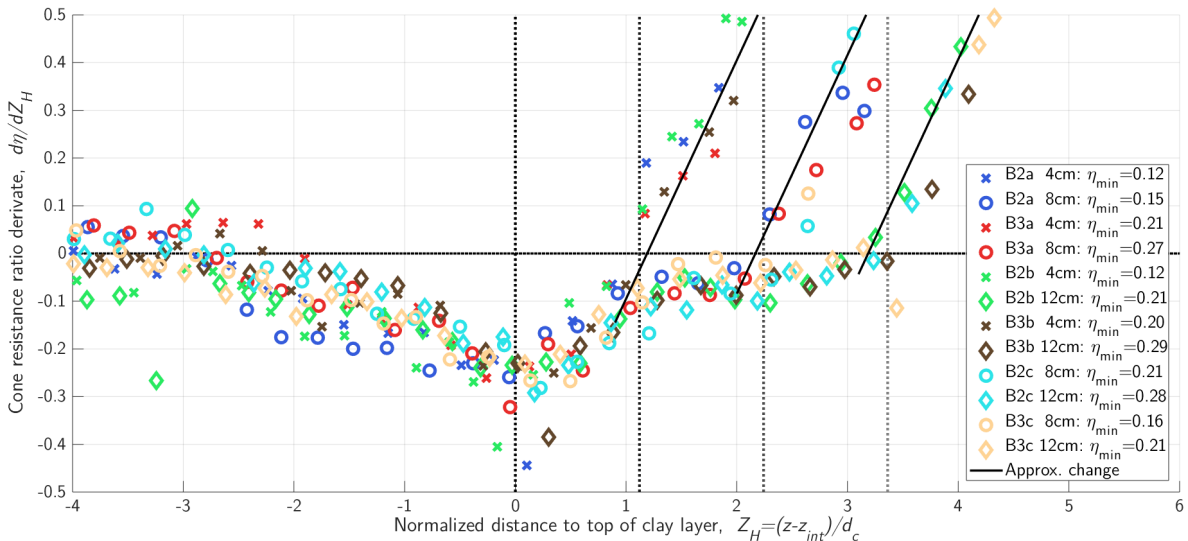
Figure 5.**18**. *Derivative of the cone resistance ratio with respect to normalized depth. Equal markers represent the same layer thickness. Vertical lines represent the respective layer interfaces, according to* **Table 5**.**1**. *Diagonal dashed lines are rough approximations to the trends found for each layer of the increase in cone resistance due to an approaching sand layer.*

5.3.2   Comparison between the filtered profile and the measurements

The procedure presented in chapter **4** was used on the determined characteristic profile. Parameters were calibrated based on measurements of previously performed physical experiments, as presented in appendix section **B.4**. The resulting filtered profiles are presented in **Figure 5**.**19**. The filtered profiles match the measured profiles well around the clay layers, which are the areas of interest. The cone resistance ratio profiles of the first round of tests are presented together with the filtered profiles in **Figure 5**.**20** for values of η_{min} of 0.1 and 0.2 in the thin layers and equal to $\eta = 1$ around it.
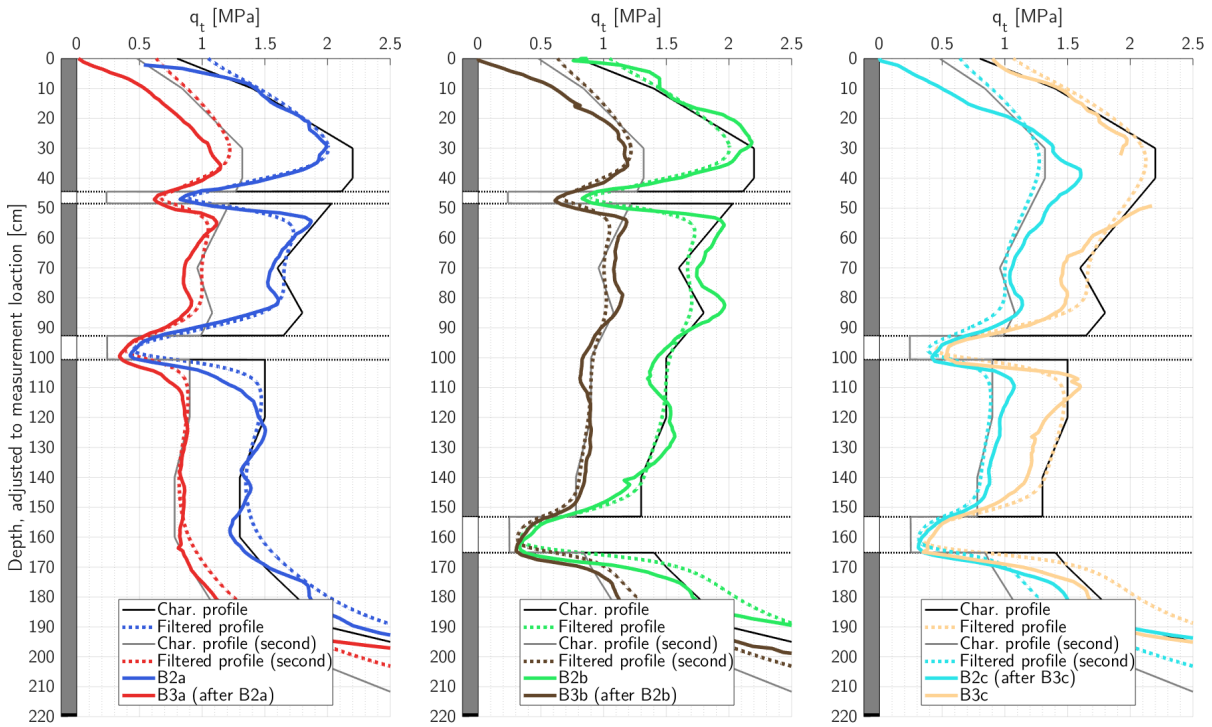
Figure 5.*19. Characteristic, filtered and measured profile of the first test in each direction of Case B.*
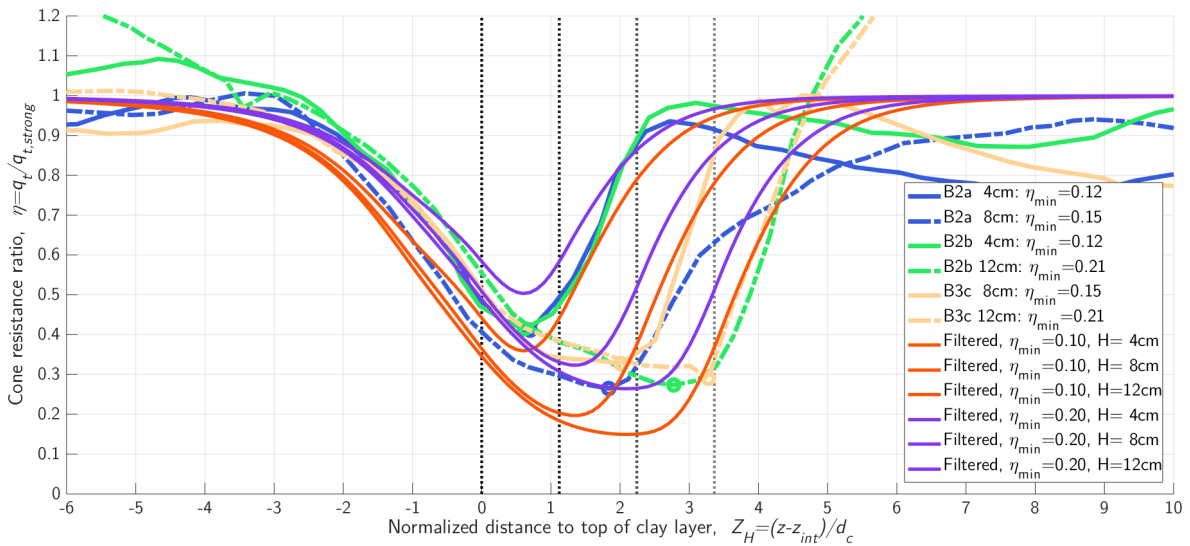
Figure 5.*20. Cone resistance ratio of the measurements with the filtered values.*

5.4 Correction of the cone resistance due to layer thickness

Correction of the cone resistance in clay of the physical experiments can be determined from comparison between the measurements and the characteristic profile. Correction factors K_H are determined according to section **4.2**, which were given as:

$$K_H = \frac{q_{t,thin}^{char}}{q_{t,thin,peak}} = \frac{q_{t,clay}^{char}}{q_{t,clay,peak}} = \frac{\eta_{min}}{\eta_{peak}} \qquad (5.5)$$

where $q_{t,clay,peak}$ is the peak (minimum) measured cone resistance in the clay layer and $q_{t,clay}^{char}$ is defined in equation (**5.2**). η_{peak}, the peak cone resistance ratio measurement, of the thin layers from the experiment are presented with circular markers in **Figure 5**.**17**.

Correction factors K_H are first presented directly from the result of the physical experiments. The method of analysis proved to fit well with the measurements in the previous section. The procedure is used to present possible correction factors for other layer thicknesses.

5.4.1 From the physical experiments

The peak measurements ($q_{t,peak}$) in each thin layer of clay is presented in **Table 5**.**2** together with the correction factors determined according to equation (**5.5**).

Table 5.*2. Correction factors K_H determined from each measurement in the thin layers.*

Test		$H = 4cm, \frac{H}{d_c} = 1.1$			$H = 8cm, \frac{H}{d_c} = 2.2$			$H = 12cm, \frac{H}{d_c} = 3.3$		
Name	Order	$q_{t,peak}$	η_{min}	K_H	$q_{t,peak}$	η_{min}	K_H	$q_{t,peak}$	η_{min}	K_H
B2a	1st	0.822	0.12	0.29	0.424	0.15	0.58			
B3a	2nd	0.612	0.20	0.39	0.339	0.22	0.72			
B2b	1st	0.829	0.12	0.29				0.328	0.21	0.76
B3b	2nd	0.618	0.20	0.39				0.302	0.28	0.83
B2c	2nd				0.417	0.22	0.59	0.309	0.28	0.81
B3c	1st				0.523	0.15	0.47	0.348	0.21	0.72

The values of **Table 5**.**2** are presented in **Figure 5**.**21** in a diagram of correction factor K_H as a function of the thin layer thickness H together with the η_{min} value.
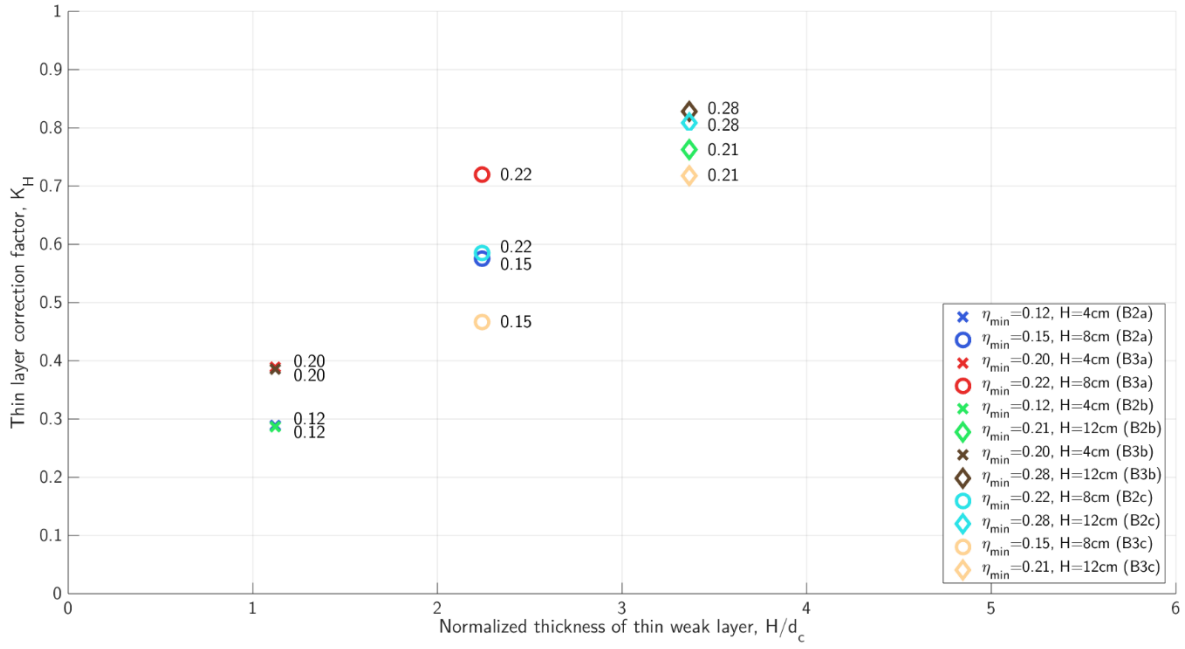
Figure 5.21. *Diagram of thin layer correction factor K_H needed from the measurements in this study. The values next to the markers are η_{min}.*

The same correction factors were determined for B2a and B2b as well as for B3a and B3b in the $4cm$ layer. This reflect how these measurements gave almost the same values in this clay layer as well as in the surrounding sand. Larger variations are seen for the $8cm$ layer. As previously stated, this is likely due to the difference in sand densities under the $8cm$ clay layer where and the characteristic cone for B3c and B2c were likely higher at this depth. The cone resistance of B3c increases rapidly at depth $105cm$ while for B2a the measurement is slowly increasing (see for instance **Figure 5**.19). Correction factors of the $12cm$ clay layer show better compliance.

5.4.2   Possible correction factors for thin weak layers from analysis

The cone penetration weighting filter proved to correspond well to the measurements in the thin layers. Possible correction factors were determined as presented in section **4.2**. Parameters used in the procedure are the same as those used in **Figure 5**.19 and **Figure 5**.20.

Figure 5.22 presents values of K_H as a function of the layer thickness H as well as η_{min}. The correction factors of the physical experiments are presented in **Figure 5**.21 are also included. The results show good compliance considering the explanation of the scatter for the $8cm$ layer from experiments.
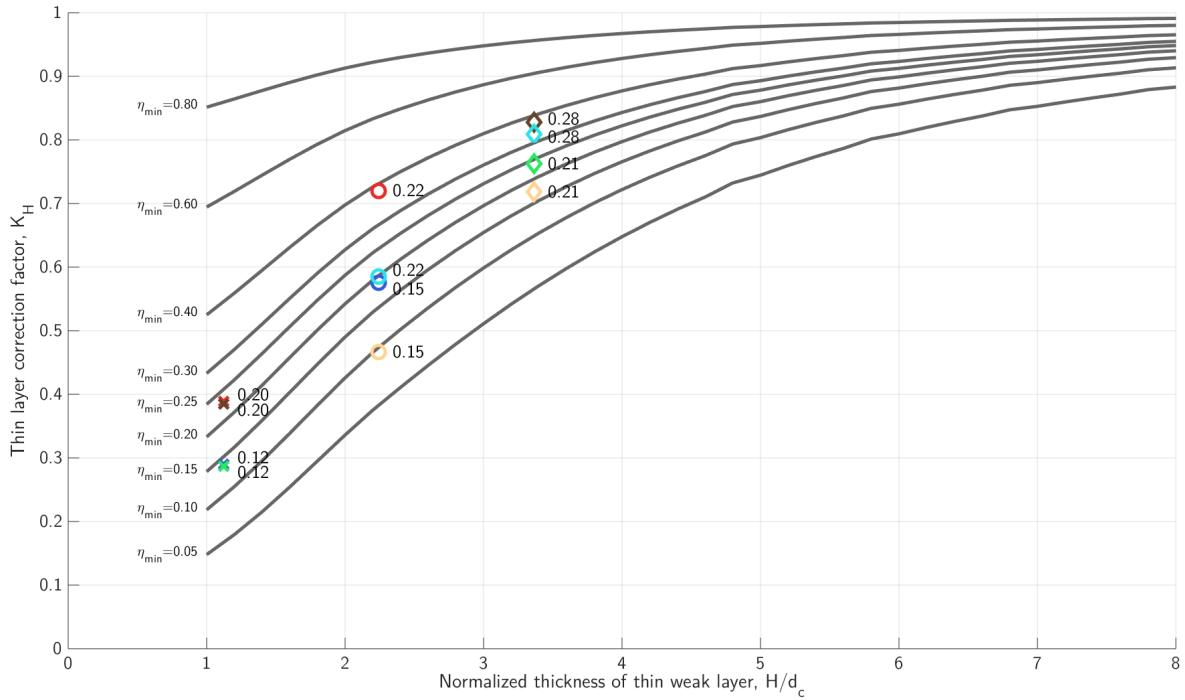
Figure 5.*22. Thin layer correction factor K_H related to thin layer thickness H and the relative cone resistance in the clay layer to the sand layer, η_{min} from estimates of the cone penetration weighting filter.*

Manual correction of peak cone resistance may be done iteratively using by assuming a layer thickness and a minimum cone resistance ration, η_{min}. However, a more convenient method is presented here where the value of η_{peak} is used instead.

$$\eta_{peak} = \frac{\eta_{min}}{K_H} = \frac{q_{t,thin,peak}}{q_{t,strong}^{char}} \tag{5.6}$$

Where $q_{t,strong}^{char}$ is the cone resistance of the strong deposit surrounding the thin layer. The values of η_{peak} as a function of H and η_{min} are presented in **Figure 5**.**23**.

The reason that this is more convenient is that η_{peak} can be determined directly from the measurement. For instance the values of η_{peak} presented in the circular marker in **Figure 5**.**20**. A value of $q_{t,strong}^{char}$ must be assumed together with a layer thickness. An example using the results of **Figure 5**.**23** is presented in section **6.4**.

Values of η_{peak} are not presented for layer thicknesses H/d_c less than one. This is due to no tests performed of layers thinner than one cone diameter. For layer thicknesses very close to zero, the values of η_{peak} should of course be expected to be equal to one.

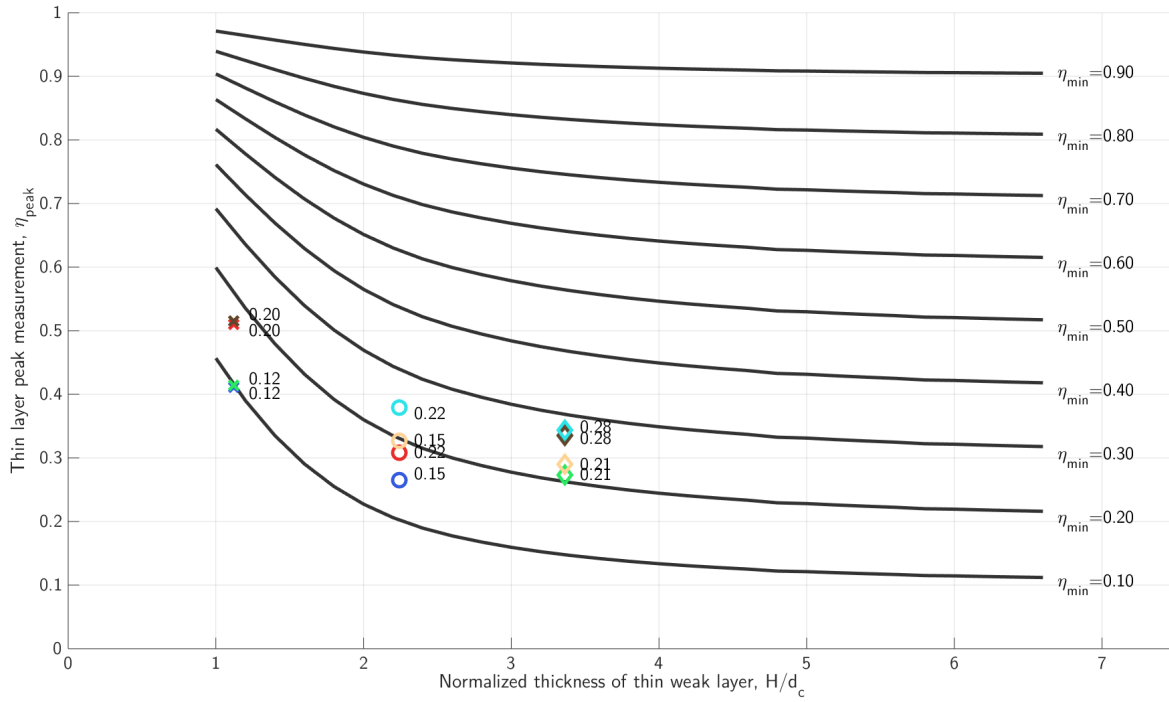**Figure 5**.**23**. *Thin layer peak cone resistance ratio, η_{peak} related to thin layer thickness H and the relative cone resistance in the clay layer to the sand layer, η_{min} from estimates of the cone penetration weighting filter.*

6 DISCUSSION

The measurement presented in the previous chapter showed how the cone resistance clearly reacts to thin clay layers in sand, though the measurements were much greater than the correct value. Through the analysis the cone resistance measurements could be corrected for the thin layer effects. CPTU measurements from field testing are normally not supported by detailed knowledge of the layering such as in this study. Instead, the measurements are used to determine the layering. The effect of layering on interpretation in practice and methods to determine and correct it are discussed in this chapter.

Properties of thin layer effects are first described through terms of sensing and developing distance in sand and clay. The thin layer correction of cone resistance from the analysis of the previous chapter and the analysis method are discussed. Following is a presentation of consequences of thin layer effects on interpretation charts and parameter interpretation and an example of correction.

6.1 Sensing/developing dominance for sand and clay

Sensing and developing distances of the results were described in subsection **5.3.1**. Sand layers were found to have large sensing distance and a smaller developing distance. The cone resistance in the thin clay layers did not reach the characteristic value, i.e. the layers were thinner than the full developing distance. Sensing distance in clay layers were almost zero.

A large sensing distance indicates a deep failure mechanism from the penetrating cone since soil at a large distance from the cone influences the resistance. The developing distance, on the other hand, reflects the influence of the soil behind the cone tip. Large developing distances can then be understood to relate to flow mechanisms dependent on soil at a large distance behind the cone.

While sensing and developing distances is only approximated and depend on the interpretation, such as those presented in the analysis in the previous chapter, it is believed that the scale of the values reflects the behavior of the soil. The behavior is here characterized by whether the sensing or developing distance is the largest. If the sensing distance is larger than the developing distance it is here given the name *sensing dominated*, while if the opposite is the case it is *developing dominated*. Sensing and developing distances that are approximately the same are labeled *symmetric*.

If the peak measurement, i.e. the minimum measurement for a weak thin layer or the maximum measurement for a strong thin layer, is closest to the upper boundary it is sensing dominated. Correspondingly, if the peak measurement is closer to the bottom boundary it is developing dominated. Illustrations of combinations of sensing and developing dominated strong and weak materials is presented in **Figure 6**.**1**, where a $6d_c$ thick layer is considered. The strong cone resistance is set to 1, while the weak cone resistance is 0.1 (the unit is not of importance). The curves are results of the filtering technique of this study. The figure shows how the cone resistance

in the thin layer is skewed to the top interface for sensing dominated materials, while it is skewed to the bottom boundary for developing dominated materials.

From the results of this study it has been showed how the sand was sensing dominated while clay was developing dominated. At the layer interface the cone resistance is closest to that of the characteristic cone resistance in the clay layer. When the interface is passed, the change in the cone resistance becomes gradually less. A consequence of this can be that the measured cone resistance in a thin clay layer can be interpreted to have stabilized at the characteristic value, while it in fact slowly converges towards the characteristic resistance.
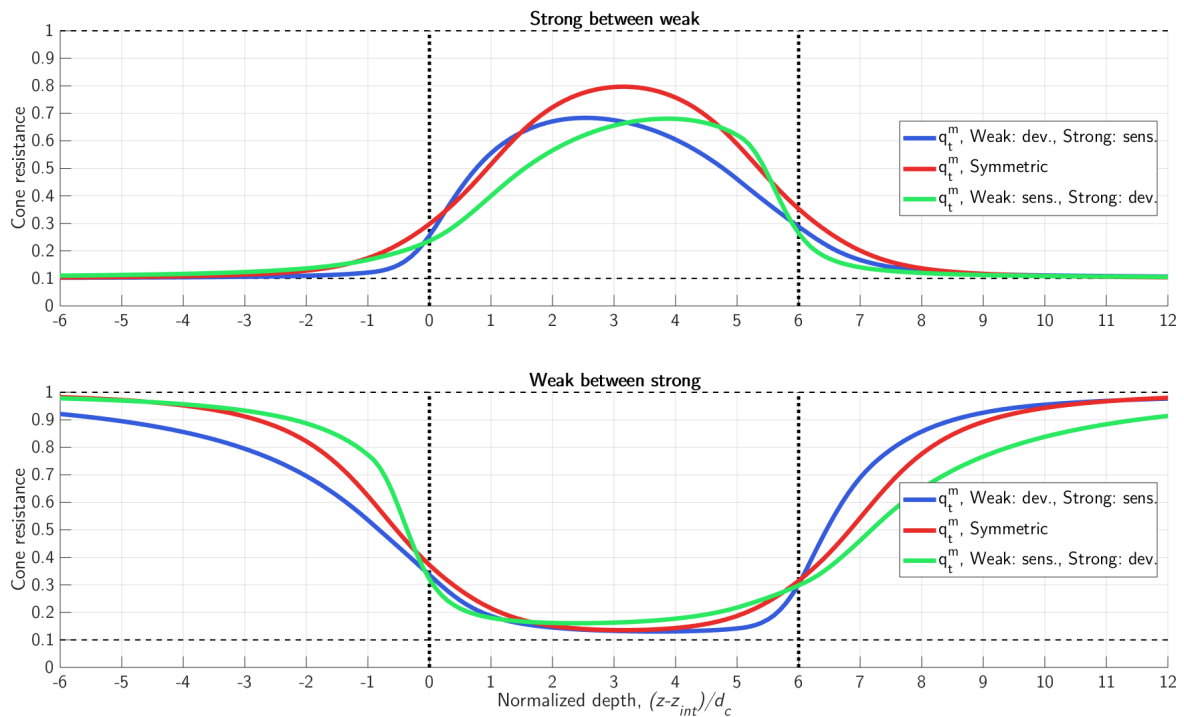

Figure 6.1. *Illustration of cone resistance profiles in thin layer depending on whether the sensing or developing distance dominates in the thin layer. Blue shows sensing as dominant for the strong material and developing for the weak material. Green shows the opposite. Red is equally dominated by sensing and developing.*

The results of this study match the blue profile in **Figure 6.1**, where the strong layers are sand and the weak layers are clay. Results of other experiments, such as those presented in subsection **2.3.5** show the same trend. These were the studies of Van der Linden (2016), de Lange et al. (2018) and Młynarek et al. (2012) presented in **Figure 2.18**, **Figure 2.19** and **Figure 2.20** respectively.

However, none of these studies recognizes the feature of developing dominance. This is not limited to strong sand and weak clays. The experiments performed in layered clay by Wang (Wang, 2019), as presented in **Figure 2.12** and **Figure 2.13**, also indicates that this is the case in layered clay. In addition to these two-layered systems of soft and stiff sand, Wang performed CPTs in three layered profiles of soft-stiff-soft and stiff-soft-stiff clays. These results also showed large developing

distance and small sensing distances. The very small sensing distance in clay can be explained by punch through at the bottom interface. **Figure 5**.**7** shows for instance the shape of the clay layers after penetration. The study of Wang commented on the punch through effect.

No study has been found that present physical experiments on thin sand layers in clay, however, results from a study on sand for instance by Joer et al. (1996) and Tehrani et al. (2017) support the sensing dominance in sand.

Correction factors are often presented for symmetric thin layers, such as presented in **Figure 2**.**14**. This assumption is not appropriate for thin clay layers in sand. The asymmetric behavior of the cone resistance is important to consider before correction of thin layer effects and determining the layer boundaries.

6.2   Correction of thin layer effects for clay layers in sand

The assumption of the thin layer correction factor, K_H, presented in **Figure 5**.**22** include equal characteristic cone resistance in the sand layers above and below the thin layer. Thicknesses of the surrounding sand layers are also assumed to be larger than the sum of sensing and developing distances (i.e. the influence length) in the sand. These conditions are normally not met when assessing an in situ CPTU measurement. The surrounding layers may have thicknesses less than the influence length and the cone resistance may be different above and below the thin layer, which will affect the correction. The results from test B2a and B3c in the $8cm$ thick clay layer gave an indication on this.

The procedure to assess layering effects with the cone penetration weighting filter gave good results when compared with the physical experiments. However, it must be emphasized that the procedure is not capable of producing unique nor perfect measurements. This was also rightfully stated in the article of the inverse filtering procedure. For instance, the measured cone resistance of A3a gave a behavior which the is impossible for the procedure to reflect. This was due to a very loose, compressible sand with even lower cone resistance than the clay layer. In situations like this the mechanism occurring the penetration process cannot be neglected such as this procedure does.

The correction factor presented uses total cone resistance (q_t) rather than the net cone resistance (q_{net}). Thin layer correction factors for layered clays proposed by Ma et al. (2015), (2017) from numerical simulations using the net cone resistance, as presented in equation (**2.21**) with symbol k. These factors were not applicable for materials other than clay. While the net cone resistance could have been used in this study it was selected not to, partly because the influence of the stress state was not studied.

While thin layers certainly were tested in the experiments of this study, very thin layers, thinner than the cone diameter was not. The experiments of this study showed how a one cone diameter thick clay layer yields a response in the sand above the clay layer which was the same as for the thicker layer. At a certain layer thickness it is expected that this is not the case, and that the layer

effect on the cone resistance can be considered as measurement noise. The smallest thickness that can be corrected for is thus not known.

The possible method of correction presented in subsection **5.4.2** is illustrated here. **Figure 6**.2 presents the cone resistance ratio from measurement B2b in the $12cm$ clay layer. While both the layer thickness and η_{min} is known in this in this case they are assumed unknown since that is the case in practice. With the determined characteristic cone resistance in the surrounding layer, the value of η_{peak} can be determined directly from the measured profile, which is 0.27 for this measurement. The layer thickness can be approximated based on the assumption that the point of inflection occurs at the top clay layer boundary, while the sudden increase in cone resistance occurs when the tip of the cone resistance is at the bottom clay layer interface. From a visual interpretation using these guidelines the clay layer is determined to be about $10cm$, slightly less than the actual thickness. However, such approximation of layer thickness should be done as a range, and the layer thickness can be for instance assumed to be $10cm \pm 2cm$, or about $3d_c \pm 0.5d_c$.

Figure 5.23 presented possible relationships of η_{min} with layer thickness. Note that these values are merely best estimates from the cone penetration weighting filter. An enlarged version is presented **Figure 6**.3. A horizontal line is drawn at the measured value of η_{peak}. Curves of different values of η_{min} crosses the line corresponding to the layer thickness yielding the given value of η_{peak}. The assumed thicknesses yield values of η_{min} between 0.13 and 0.21.

The corrected cone resistance in the thin layer is then determined by:

$$q_{t,thin} = \eta_{min} \cdot q_{t,strong}^{char} \tag{6.1}$$

While the experiments showed how measurements of sleeve friction and pore pressure are severely influenced by the layer thickness, these parameters may be used to aid the estimation of layer thickness. This is discussed in the following section.
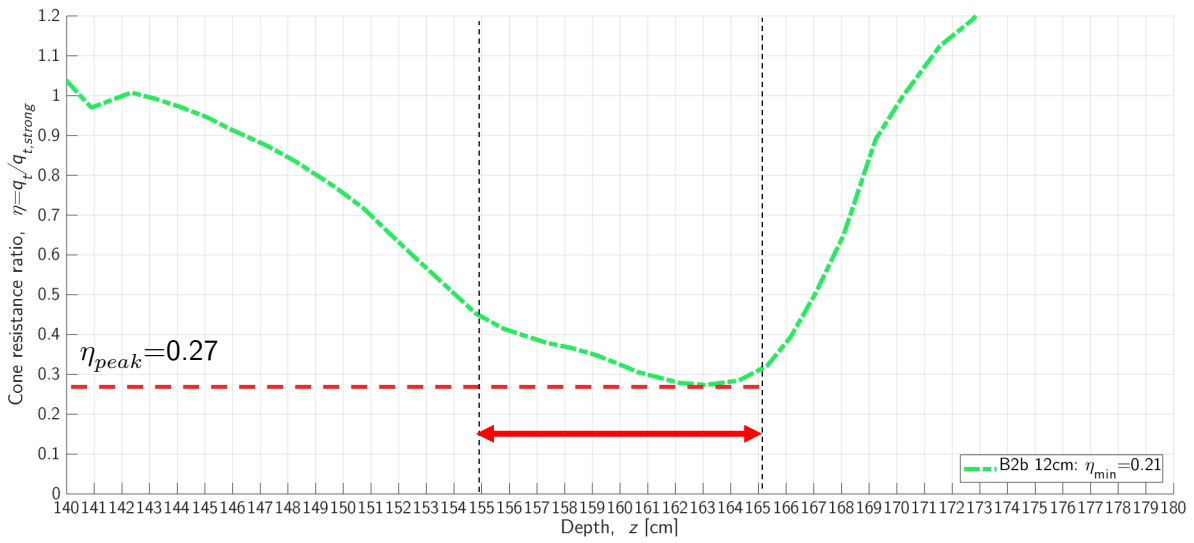
Figure 6.2. *Illustrational cone resistance ratio of a measurement. The characteristic profile, which in practice is unknown is presented as well. The thin layer has a thickness of $3d_c$ and a value of η_{min} of 0.1.*
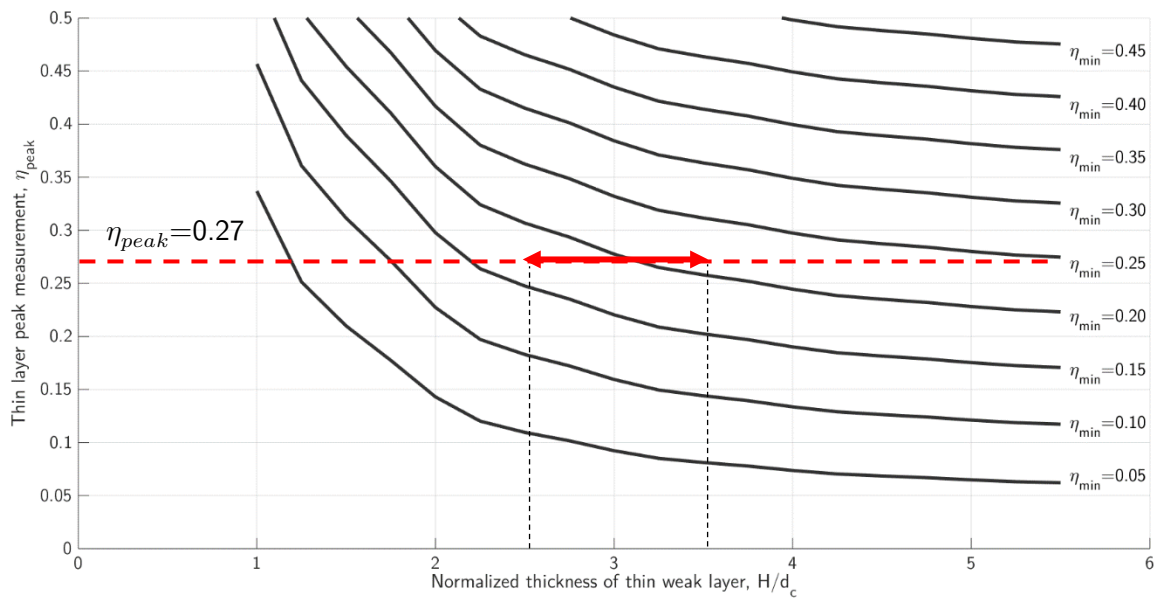

Figure 6.3. *Possible relations between η_{min} and η_{peak} and an approximated interpretation for a given value of η_{peak}.*

6.3   Effect of thin clay layer thickness on interpretation

Interpretation of CPTU measurement in practice is often done by classification of the entire measured profiles where each measured point is presented without considerations to layering effects. The consequence is highly dependent of the soil material and layer thicknesses. The effect of neglecting thin layer effects on the interpretation of clay layer in sand is discussed in this section.

A primary indicator of clay layers is the measured excess pore pressure; however, the results have shown that the measurement is greatly influenced by the layer thickness. The effect of this is first discussed. Following is an assessment of the impact of thin layer effects from the experiment of this study on classification charts. Finally the effect on parameter interpretation is discussed by assessing determined undrained shear strength values of thin clay layers.

6.3.1   Thin layer effect on excess pore pressure increase

Large deformations are caused by the penetrating cone which greatly disturbs the layer interfaces. This is likely related to the low rigidity index of the clay layer. An image of a $8cm$ clay layer after penetration of test case B of this study is presented in **Figure 6.4**. The excess pore pressure, Δu_2, of the specific test is included. This illustrates the connection between the increase in excess pore pressure and the deformation of the clay layer.
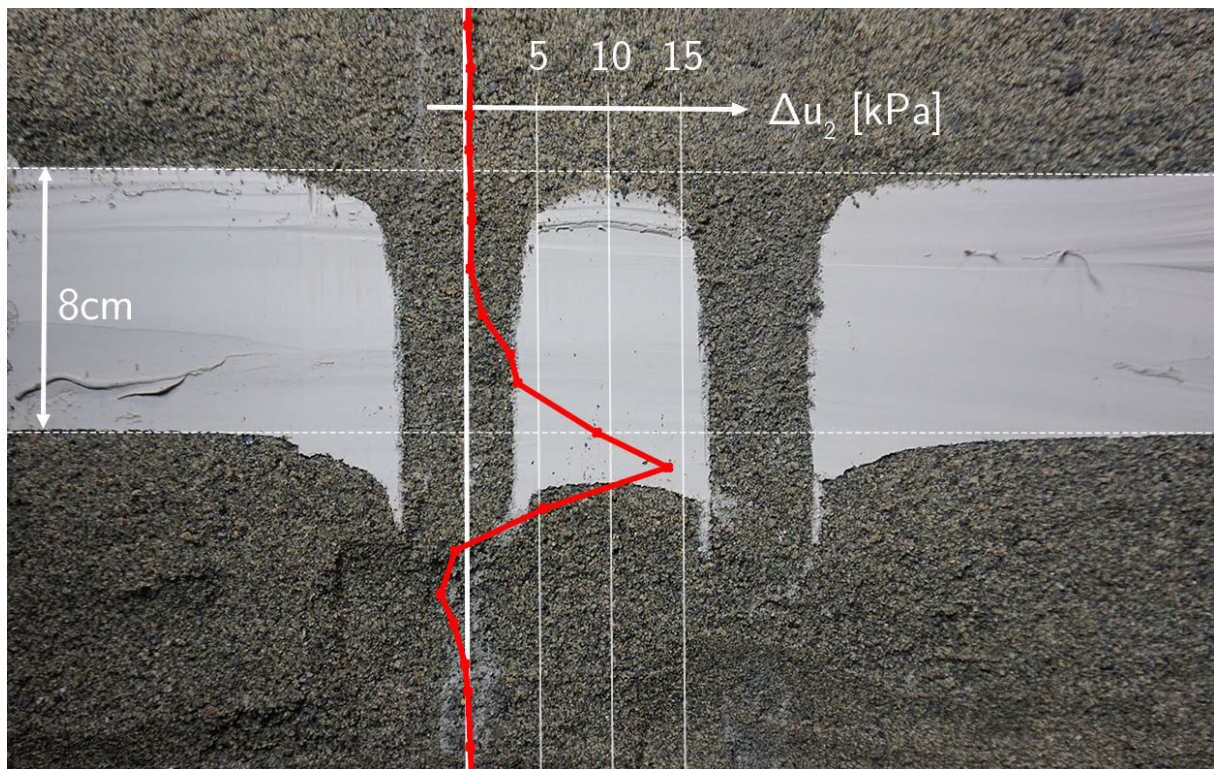

Figure 6.4. Image from the 8cm thick clay layer from case B of direction c with added excess pore pressure measurements of test B2c. The image shows how the measured excess pore pressure reaction is with depth together with the deformed clay layer. The excess pore pressure increases when the diameter of the hole in clay equals the cone diameter.

The increase in Δu_2 is only noticeable at about $3-4cm$ after the original layer interface is passed. At this depth, the diameter of the hole caused by the penetrating cone appear to be the same as the diameter of the cone. The pore pressure at the shoulder of the cone may then experience an increase in the excess pore pressure as it is surrounded by clay. Values of Δu_2 are greater than zero until a distance of about $3cm$ after the original bottom interface is passed. These measurements for other clay layers were presented in **Figure 5**.**10**.

Similar results were discovered in the study by Van der Linden (2016). If pore pressure filters at the tip or on the cone face were used, u_t and u_1 respectively, the would be expected that the excess pore pressure would increase closer to the original interface (Hird et al., 2003). The u_2 measurement should therefore not be relied on for detection of very thin clay layers.

6.3.2   Layering effect on classification charts

The measurements of cone resistance and sleeve friction for the layered profile of Case B are evaluated with the normalized parameters of Q and F_r, as presented in subsection **2.2.3**. While the characteristic cone resistance have been profile presented, the characteristic sleeve friction have not. From the measurements presented in subsection **5.1.2** the sleeve friction in sand was found to be constant and about $5kPa$ while for the clay layers the maximum measured sleeve friction was between 15 and $20kPa$. The characteristic sleeve friction profile is then determined as $5kPa$ in sand and $15kPa$ in clay. While the sleeve friction normally is higher in sand than clay, this can be related to the overconsolidation of clay compared to the sand. The soil behavior index, I_c, is also determined for the profiles, also presented in subsection **2.2.3**. Limits of I_c for classification as sand-like behavior $(1.31-2.05)$ and clay-like behavior $(2.95-3.60)$ is included in the figure.

Figure 6.**5** presents values of Q, F_r and I_c for the measurements adjusted to the measurement location, the non-adjusted depth and the characteristic values. Due to the dependence of the cone resistance the friction ratio varies for the different layers mostly due to the dependence on the cone resistance. The profiles of F_r for the adjusted and non-adjusted depths are very different. The non-adjusted profile in clay has high, narrow spikes where the cone resistance is the smallest. These peaks are wider for the adjusted measurement. Both are however much lower than the characteristic values of F_r due to the influence of the cone resistance. The measurements of F_r and I_c give indications of layering which can be used together with the correction method previously presented.

The measurements are presented in the classification chart of Robertson (2016) for Q_{tn} vs F_r and Schneider et al. (2008) for Q vs. $\Delta u_2/\sigma'_{v0}$. A characteristic value of $\Delta u_2 = 35kPa$ is assumed for the clay according to **Figure 5**.**10**. The classification charts are presented in **Figure 6**.**6** for the depth adjusted measurements. The effect of thin layers is naturally greater for the thinnest layers. Clay layers of thickness $12cm$ is detection in the chart of Schneider et al. (2008), while the thinner layers are not. Classification of Robertson (2016) is not correctly classified as clay for any of the clay layers. Though, the chart clearly show the presence of the layers through the path of the measurements.
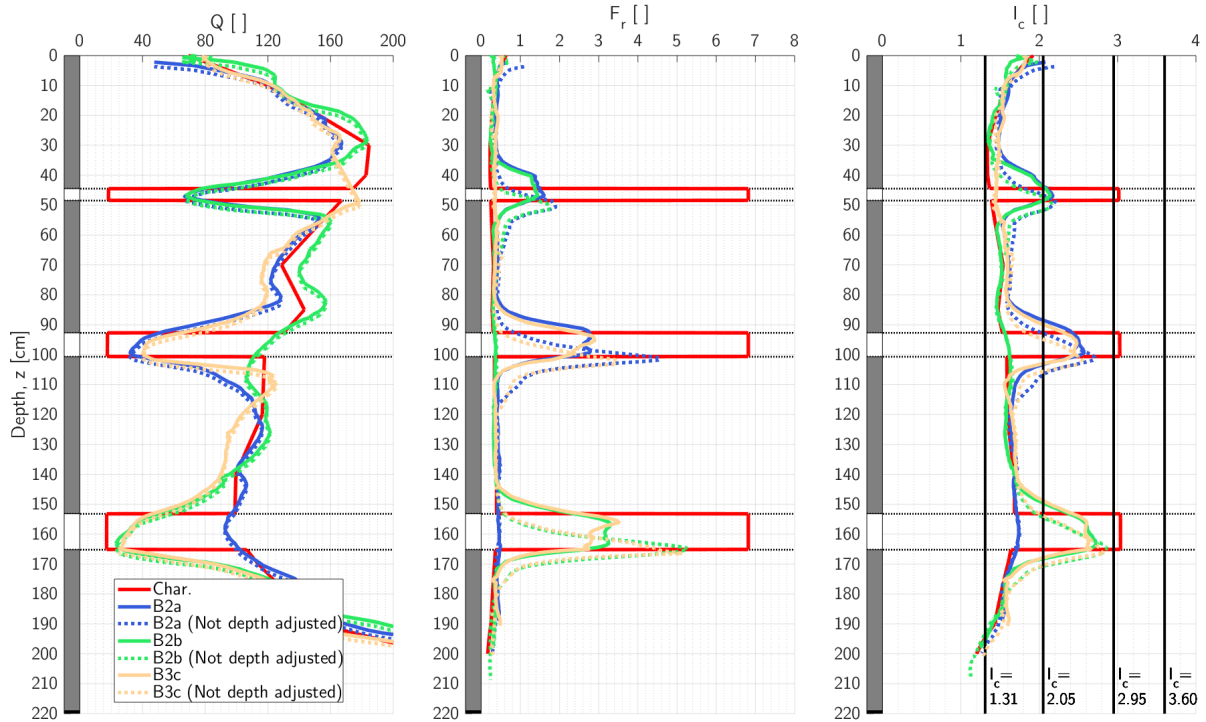
Figure 6.5. Normalized cone resistance (Q), sleeve friction ratio (F_r) and the SBT-index (I_c) for measurements of case B. Values with depth reference at the cone tip (not depth adjusted) and of the depth of the measurement location are presented. Characteristic profiles are included based on the characteristic measurements in sand and clay of cone resistance and sleeve friction.
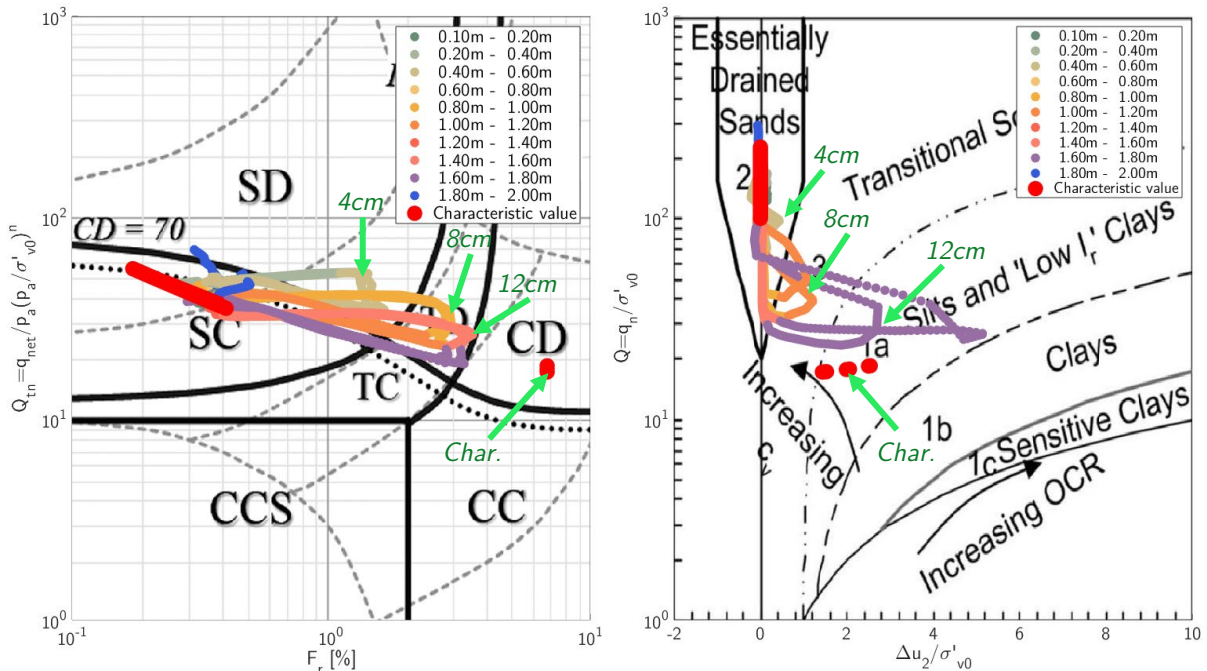

Figure 6.6. Classification charts with the measurement from the layered sample in Case B, tests B2a, B2b and B3c. Characteristic values are presented in the red dots. Left: F_r vs. Q_{tn} (Robertson, 1990). Right: $\Delta u_2/\sigma'_{v0}$ vs. Q (Schneider et al., 2008). The measurements of the different clay layers are noted with

green text and arrows. Note that the y-values are not the same for the two diagrams (see subsection
2.2.3)

6.3.3 Impact on interpretation of undrained shear strength in thin clay layers

Interpretation of undrained shear strength is typically done from the cone resistance profile using
equation (**2.10**). If thin layer effects are not corrected for before this interpretation is performed,
there resulting overprediction of the undrained shear strength can be large. The error of the cone
resistance is the relationship between the uncorrected measurement to the corrected one. The
lowest overprediction is at the peak of the thin layer. The error is here given as x and defined by
the following equation:

$$x = \frac{q_{t,thin,peak}}{q_{t,thin}^{char}} = \frac{1}{K_H} \tag{6.2}$$

The undrained shear strength determined from the uncorrected peak cone resistance in clay is here
given noted by $\tilde{s}_u$. The overpredicted undrained shear strength relative to the correct shear strength
is then given by $\tilde{s}_u/s_u$. This is then given as a function of the error, x:

$$\frac{\tilde{s}_u}{s_u} = \frac{1}{s_u} \cdot \frac{x \cdot q_t^{char} - \sigma_{v0}}{N_{kt}} = \frac{1}{s_u} \cdot \frac{x \cdot (N_{kt} \cdot s_u + \sigma_{v0}) - \sigma_{v0}}{N_{kt}} = x + (x-1) \cdot \frac{\sigma_{v0}}{N_{kt} \cdot s_u} \tag{6.3}$$

The overprediction of the undrained shear strength is quantified with an example of thin clay layers
in sand where the error, x, is defined from the correction factors in **Figure 5**.**22**. The examples is
given for the conditions of experiment Case B at $100cm$ depth. Here, the vertical effective stress
was about $13kPa$ and the vertical total stress was about $23kPa$. The cone factor N_{kt} was 8.1 in
clay and the characteristic cone resistance in the surrounding sand is about $1.5MPa$. Overprediction
of undrained shear strength is then presented for varying values of s_u and thin layer thicknesses,
H. The undrained shear strength of the clay is determined from equation (**2.9**), where α was found
to be 0.28 and m is set to one, i.e.:

$$s_u = 0.28 \cdot OCR \cdot \sigma'_{v0} \tag{6.4}$$

The following relationship of the overprediction is given when put into equation (**6.3**):

$$\frac{\tilde{s}_u}{s_u} = x + (x-1) \cdot \frac{23kPa}{8.1 \cdot 0.28 \cdot OCR \cdot 13kPa} = x + (x-1) \cdot \frac{0.78}{OCR} \tag{6.5}$$

Figure 6.**7** presents the resulting overprediction for a clay layer with varying OCR and layer
thickness in sand from the correction factors of **Figure 5**.**22** with a standard cone diameter. This
example shows the significance of the overprediction of undrained shear strength if correction is
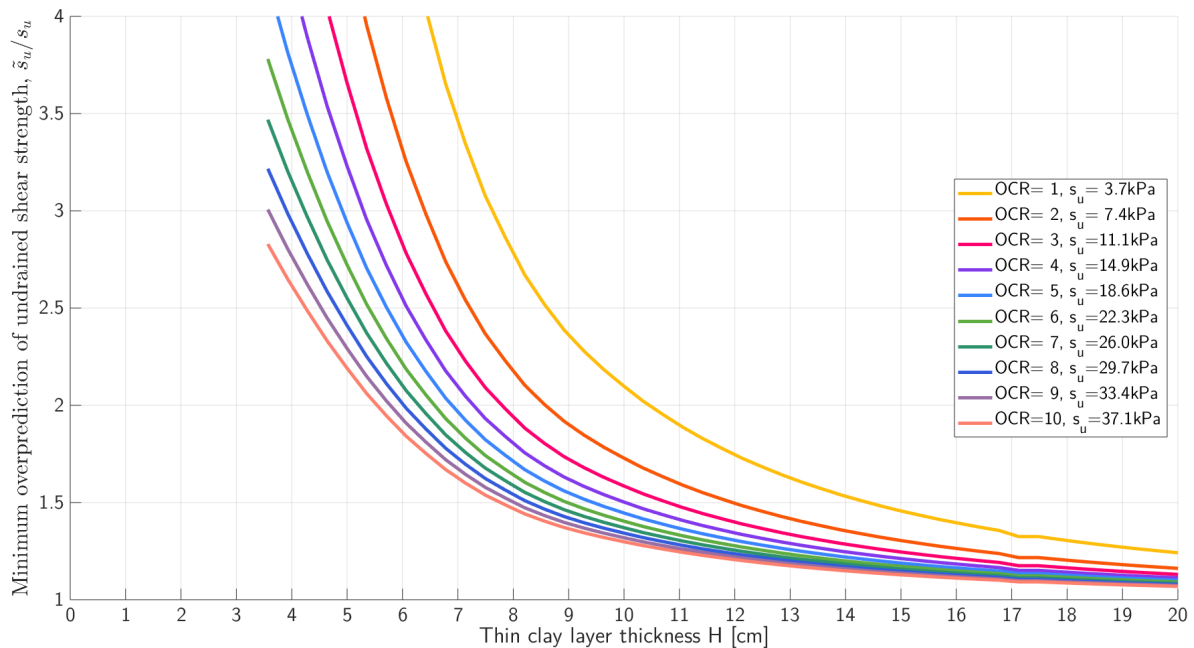not considered.

Figure 6.7. Example of overpredicted undrained shear strength due to thin layer thickness.

6.4   Example of thin layer correction

An example of thin layer correction is presented in a layered profile. The measurements from the deltaic sediments of Øysand are considered, which were presented in section **2.1**. Extensive sampling and characterization of the soil has been done at the site. **Figure 6.8** presents a sample from a bore hole close to multiple CPTUs. Here, a thin layer of what is assumed to be a clay or silty clay is marked in a circle. There is a distinct interface between this layer and overlaying silty sand, as the figure shows. Some gravel can be seen directly below the clay layer, though this is not reflected in the CPTU measurements. The correct thickness of the clay layer may not be reflected in the image.
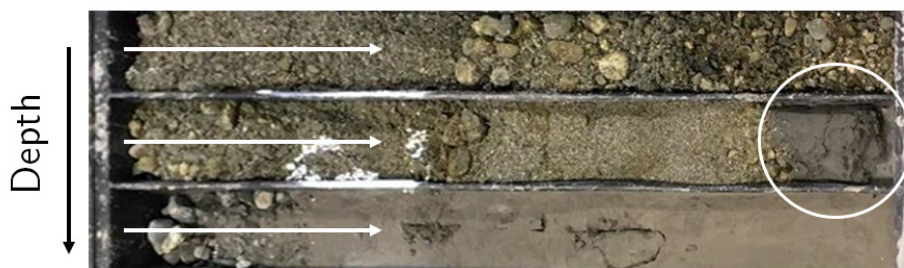

Figure 6.8. Stratigraphy of the soil from a bore hole at Øysand (each cylinder has a length of 1m). Arrows show the direction of increasing depth. The circle marks the apparent clay layer

Due to steep inclination of the deltaic sediments of as much as 0.55, the depth of the layers varied between CPTU (Hammer, 2019). Five CPTUs are presented in **Figure 6.9**, which were performed half a meter in between each. These measurements are presented towards the tip of the cone.

However, the measurements are shifted vertically to match the first CPTU (O21) at depth $6.2m$. The actual depth of these five CPTUs is decreasing with about $20cm$ for each measurement. At depth $6.2m$ the pore pressure measurements of CPTUs O21, O24 and O25 show a rapid increase, which is believed to reflect the layer of clay. CPTUs O22 and O23 show less response.
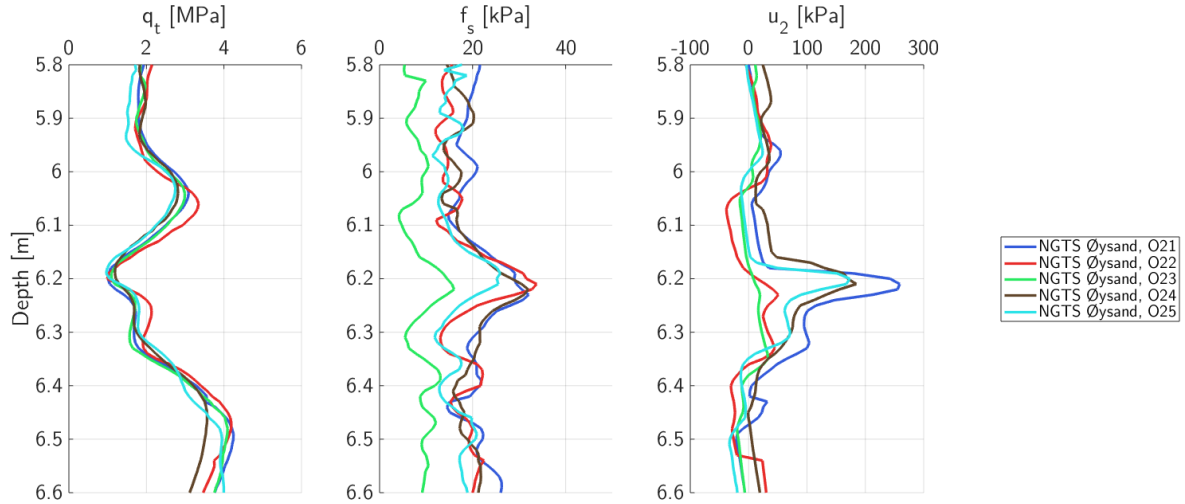

Figure 6.9. *CPTU measurements of the layered deltaic sediments at Øysand.*

Minimum values in the clay layer are about $1MPa$, while the cone resistance in the layer above, at about $6.05cm$ depth is about $3MPa$. The cone resistance ratio is determined for the profiles, and even though the layer above appear to be a thin layer, the value of $3MPa$ is used for the normalization. **Figure 6**.10 shows the cone resistance ratios. The value of η_{peak} are between 0.3 and 0.4. The thickness of the clay layer is selected from an interpreted point of inflection to the sudden increase in the measurement. A layer thickness of about $6cm$ can be approximated, or 1.7 cone diameters for a standard cone diameter.
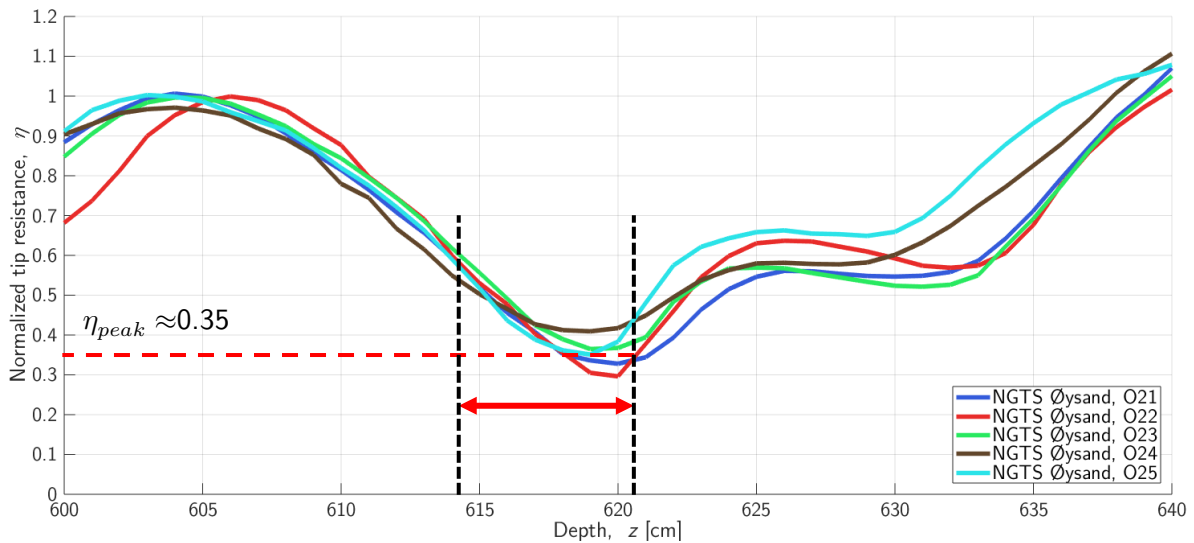

Figure 6.10. *Normalized cone resistance of depth about 6.2m at Øysand*

Using **Figure 5**.**23** to estimate η_{min} for η_{peak} of 0.35, a value of about 0.1 can be estimated, which corresponds to a cone resistance in the clay layer of:

$$q_{t,clay} \approx \eta_{min} \cdot q_{t,strong}^{char} = 0.1 \cdot 3MPa = 0.3MPa \qquad (6.6)$$

Disregarding the uncertainties of the propose correction factor, this cone resistance is likely less than the correct value due to the assumption of characteristic strength in a layer also effected by thin-layer effects. A better approximation of the characteristic cone resistance can be found from applying the filter procedure. **Figure 6**.**11** shows filtered profile from an assumed characteristic profile. The layers were selected based on the pore pressure measurement and the cone resistance measurement. At the top layer, the pore pressure is greater than zero, while for the second layer it becomes less than zero. These layers are assumed to be sand, and the behavior indicates a difference in density. The thin clay layer is assumed based on the sudden increase in pore pressure. Assuming the selected position of the clay layer is correct, the increase in pore pressure is more instantaneous than in the experiments of this study. This can be related to a greater stiffness in this thin layer. The pore pressure remains positive for some distance after the thin layer until it suddenly drops.
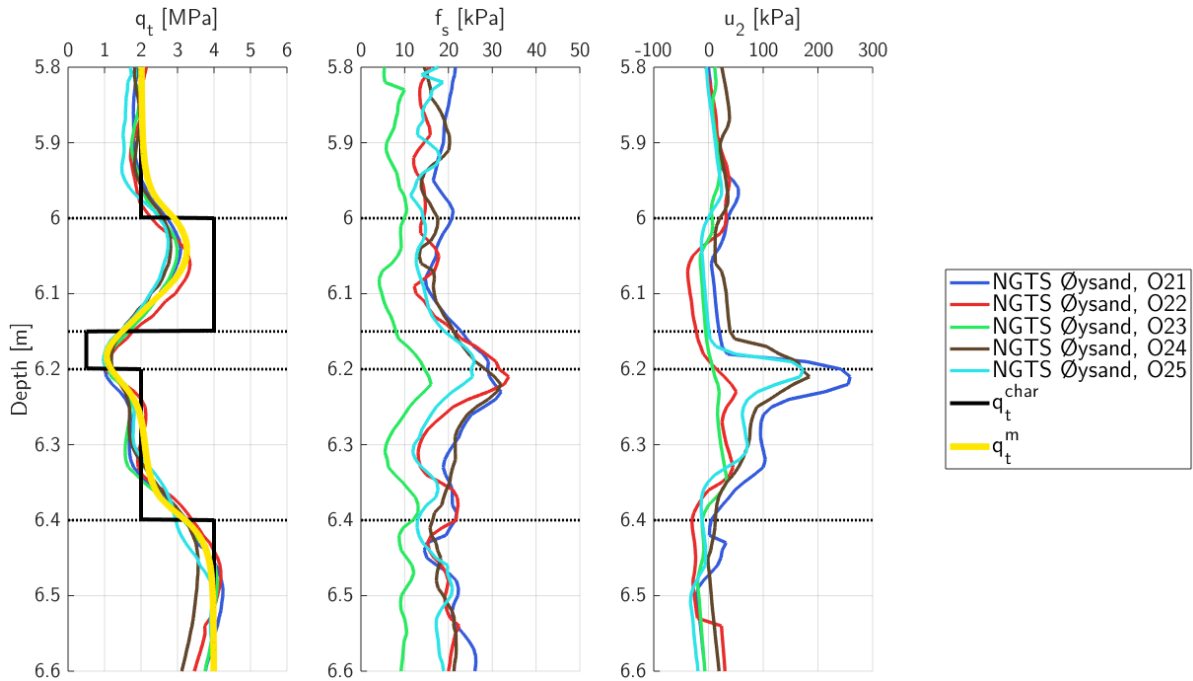

***Figure 6**.11. Normalized cone resistance from Øysand together with experiment results.*

The combination of a $5cm$ clay layer and $0.5MPa$ yields a good match. However, multiple combinations of characteristic cone resistance profiles with varying layer thickness may result in good matches. The filter procedure should not be expected to discover the exact characteristic cone resistance. Instead, the scale can be approximated. For the example presented here, only values of 0.5, 1 and $2MPa$ were assumed. In addition, the layer thicknesses were selected to the closest $5cm$. Parameters yielding the filtered profile are the same as for those presented in **Figure 5**.**19**. The layers of characteristic cone resistance of $4MPa$ are given sand-like sensing dominated sensing

parameter ($\xi = 1$) while it for clay was set to developing dominated ($\xi = 0.2$). The layers with value $2MPa$ are given equal sensing and developing dependence ($\xi = 0.5$).

At a depth of $6m$ the vertical total stress at Øysand is assumed to be $120kPa$ while the vertical effective stress is $80kPa$. Assuming a cone factor of 9, the corrected undrained shear strength may then be estimated as:

$$s_u = \frac{q_{t,corrected} - \sigma_{v0}}{N_{kt}} = \frac{500kPa - 120kPa}{9} = 42kPa \qquad (6.7)$$

The expected overconsolidation at Øysand is $OCR = 1.8$ at these depths due to the erosion of $7m$ of top soil, as presented in the extensive studies at Øysand (Quinteros et al., 2019). Using equation (**2.9**), assuming $\alpha = 0.3$ the value of s_u at $6m$ depth matches if the material factor is assumed to be $m = 1$:

$$s_u = \alpha \cdot OCR^m \cdot \sigma'_{v0} = 0.3 \cdot 1.8 \cdot 80kPa = 43kPa \qquad (6.8)$$

The interpreted s_u without this correction, from a value of $q_t = 1MPa$ is $\tilde{s}_u = 100kPa$, i.e. the expected overprediction $\left(\frac{\tilde{s}_u}{s_u}\right)$ is about 2.3.

7   CONCLUSIONS

Cone penetration is a complex process where the measurement of cone resistance depends on numerous factors. However, due to the standardized procedures of CPTUs the measurements are repeatable and reliable and good interpretations can be made in homogenous soils. Interpretation of cone resistance profiles in layered soils on the other hand requires careful considerations of layering effects in order to properly interpret the results. Previously conducted studies on layering effects on CPTUs were presented and evaluated for various soil materials. Limited literature on thin layer effects of thin clay layers in sand was available and it was concluded that more experiments were needed.

Large scale physical experiments were conducted in a chamber designed in this study. Repeatable procedures were developed to create samples of loose to medium dense sand with thin clay layers. The samples were tested with multiple CPTUs. The effect of layer thickness on the measured cone resistance in the clay layers were presented. Deviation to the characteristic cone resistance of clay increased for thinner clay layers. For a $4cm$ thick clay layer the minimum measured cone resistance was about 3.5 times the characteristic cone resistance in clay. Similarly, this value for the $8cm$ and $12cm$ clay layers were about 2 and 1.4 times greater, respectively. The characteristic cone resistance in the clay layer compared to the surrounding sand also impacted the thin layer effects.

Pore pressure measurements at the shoulder of the cone responds poorly in thin clay layers due to large deformations of the clay layer interface. Clay layers of $4cm$ thickness showed little to no pore pressure response. Interpretation using classification charts or direct interpretation of parameters from the cone resistance, such as undrained shear strength, were very much affected by the thickness of the clay layers. The primary indication of the thinnest clay layers was the rapid change in the measured cone resistance and friction ratio. The results showed how clay layers appear to have greater dependence on the soil behind the cone than in front, while the opposite is the case for sand. From this, the clay was labeled developing dominated and sand sensing dominated. The cone resistance at the top layer boundary of a thin clay layer in sand is much more influenced by the weak clay layer below the tip than the strong sand above. Though when the cone advances through the clay layer the apparent dependence on the soil above causes the cone resistance to asymptotically approach the characteristic cone resistance of clay. This causes a significant dependence on the layer thickness.

A numerical analysis method was developed to mimic the behavior of the cone resistance in layered soils. Weighting windows dependent on control parameters and the characteristic cone resistance profile was used to estimate measured cone resistance profiles with good results. Dependence on sensing and developing distances were included in the procedure. This procedure was used to approximate the trends discovered from the physical experiments. Possible correction methods of the cone resistance profile in thin clay layers in sand was presented from this. However, corrections cannot be done uniquely and may only provide better estimates of the measurements.

8 RECOMMENDATIONS

The CPTU can provide valuable parameter interpretations due to its repeatability, though special considerations must be made when evaluating measurements of layered soils. Assessment of thin clay layers through CPTU interpretation consists of first detecting the appearance of these layers followed by potential measures to improve the measurements. Corrections could of course be done with great confidence in this study due to the exact knowledge of the layering and soil parameters. In practice, however, both the layering and soil characteristics are typically determined from the CPTU measurements.

The cone resistance showed significant influence from even very thin layers of clay of one cone diameter. This suggest that the cone resistance itself may be the best indication of the presence of thin clay layers. A bottom interface between clay and sand layers was clearly seen in a rapid increase in the cone resistance. While this behavior may not be unique for clay over sand layers, it is an indication. Measurements of sleeve friction can aid in the detection for instance through the friction ratio. Pore pressure measurements at the shoulder of a may not react properly to thin clay layers, as shown in this study. The detection should therefore preferably not rely on this measurement. Accurate detection of thin layer is best done based on multiple CPTUs even though the measurement has been proven to be reliable. Thin layers can only be discovered if CPTUs are evaluated on a proper scale where variations over distances of $10cm$ are clearly shown.

Correction for thin layer effects in thin clay layers in sand should be done prior to interpretation of for instance undrained shear strength for more accurate values. A significant influence of layer thickness was evident for layers of $12cm$ thickness. The undrained shear strength approximated from correlations of CPTU is typically presented together with a profile of the assumed undrained shear strength for normal consolidated clay. In some cases the undrained shear strength in thin clay layers may be equal to the normal consolidated clay while the value from CPTU correlations are much higher due to thin layer effects. However, this does not imply that the normal consolidated undrained shear strength should always be assumed in thin clay layers. The aim of correcting the cone resistance for thin layer effects before interpretation is to extract more probable parameters from interpretation, rather than a measure simply to be conservative.

The measurements of the physical experiments in this study resulted in correction factors for the specific layering and soil materials. These results can be used for correction of similar soil conditions. Possible correction factors were included based on the analysis method of this study. While these factors are quite uncertain, the they may be used in an approximate manner, such as in the examples presented in this study. Analysis and comparison with the cone penetration weighting filter gave promising results, and this method can be applied to approximate the characteristic profile. However, the method has limitations and should not be expected to yield perfect results. The parameters used in the method should not be determined solely on a cone resistance profile that is evaluated but rather determined from previous results in similar soils.

9 FURTHER WORK

Further experiments with testing of other thin clay layer thicknesses in sand is recommended for a better understanding of the trends presented in this study. The established chamber model with procedures to create loose to medium dense sand samples facilitates further experiments. Samples can be made in the same manner as presented in this study with differences variations in sample layering, materials or equipment. Examples of variations of interest are:

- Clay layers thinner than one cone diameter could be tested. This can answer the question on how thin a clay layer can be before the sand under it dominates the cone resistance measurement, causing little or no influence from the clay layer.
- Greater compaction of sand or lower undrained shear strength of the clay will increase the contrast between sand and clay on the cone resistance (η_{min}), which is expected to influence the needed thin layer correction.
- The distance between clay layers can be reduced. The influence length in sand of the physical experiments were less than $20cm$ for the $10cm^2$ cone. If the values of η_{min} are changed, as mentioned above, the influence length may increase.
- Non-standard CPTU equipment can be used for testing with for instance pore pressure filters at the cone face, u_1, or the cone tip, u_t. CPTUs with greater sampling frequency could be used or alternatively a slower penetration speed may be used for increased resolution of the measurements. Smaller cone diameter can be used for less influence on neighboring tests.
- Lower sample height for a reduced relationship between height and chamber diameter, i.e. h/D_c. The effective stress in the samples of this study were approximated to be almost constant due to silo effects. Taller samples are more influenced by this effect. If sample heights are smaller there is less need for equipment such as scaffolding, which can save time during laboratory work. Silo effects is reduced by less friction along the walls, which for instance can be done by painting the chamber walls.

The developed analysis method for cone resistance profile may also be studied further with for instance use on field measurements, such as presented in the example in section **6.5**. Numerical analysis on the mechanisms of cone penetration in layered profile through for instance material point method (MPM) or large deformation finite element method could be used for comparison to the results of the physical experiments. For a better understanding of the layering effects between sand and clay the flow mechanism should be studied to discover the interaction of sand and clay, either through physical or numerical (for instance MPM) assessments.

BIBLIOGRAPHY

Ahmadi, M., & Robertson, P. (2005). Thin-layer effects on the CPT qc measurement. *Canadian Geotechnical Journal, 42*(5), 1302-1317.

Ahmadi, M., & Robertson, P. (2008). A numerical study of chamber size and boundary effects on cpt tip resistance in NC sand. *Geotechnical and Geophysical Site Characterization. vols, 1*, 829-833.

Been, K., & Jefferies, M. G. (1985). A state parameter for sands. *Geotechnique, 35*(2), 99-112.

Been, K., Lingnau, B., Crooks, J., & Leach, B. (1987). Cone penetration test calibration for Erksak (Beaufort Sea) sand. *Canadian Geotechnical Journal, 24*(4), 601-610.

Boulanger, R., & DeJong, J. (2018). *Inverse filtering procedure to correct cone penetration data for thin-layer and transition effects.* Paper presented at the Cone Penetration Testing 2018: Proceedings of the 4th International Symposium on Cone Penetration Testing (CPT'18), 21-22 June, 2018, Delft, The Netherlands.

Cabal, K., & Robertson, P. (2014). *Accuracy and Repeatability of CPT Sleeve Friction Measurements.* Paper presented at the Proceedings of the 3rd International Symposium on Cone Penetration Testing (CPT'14). Las Vegas, Nevada, USA.

de Lange, D., Terwindt, J., & van der Linden, T. (2018). *CPT in thinly inter-layered soils.* Paper presented at the Cone Penetration Testing 2018: Proceedings of the 4th International Symposium on Cone Penetration Testing (CPT'18), 21-22 June, 2018, Delft, The Netherlands.

Duran, J. (2000). *Sands, powders, and grains: an introduction to the physics of granular materials*: Springer-Verlag.

Ghionna, V., & Jamiolkowski, M. (1991). *A critical appraisal of calibration chamber testing of sands.* Paper presented at the Proc. of 1st Int. Conf. on Calibration Chamber Testing, Clarkson.

Hammer, H. B. (2019). *Accuracy of CPTUs in deltaic sediments and the effect of cone penetrometer type.* (Project Thesis (TBA4510)), Norwegian University of Science and Technology (NTNU), Trondheim. Retrieved from https://www.ngi.no/download/file/15722

Hansen, L., L'Heureux, J.-S., & Longva, O. (2011). Turbiditic, clay-rich event beds in fjord-marine deposits caused by landslides in emerging clay deposits–palaeoenvironmental interpretation and role for submarine mass-wasting. *Sedimentology, 58*(4), 890-915.

Hird, C., Johnson, P., & Sills, G. (2003). Performance of miniature piezocones in thinly layered soils. *Geotechnique, 53*(10), 885-900.

Houlsby, G., & Hitchman, R. (1988). Calibration chamber tests of a cone penetrometer in sand. *Geotechnique, 38*(1), 39-44.

Hryciw, R., Jung, Y., Susila, E., & Ibrahim, A. (2009). *Thin soil layer detection by VisCPT and FEM simulations.* Paper presented at the Proc., 17th Int. Conf. on Soil Mechanics and Geotechnical Engineering (ICSMGE).

Jamiolkowski, M., Lo Presti, D., & Manassero, M. (2003). Evaluation of relative density and shear strength of sands from CPT and DMT. In *Soil behavior and soft ground construction* (pp. 201-238).

Janbu, N. (1963). *Soil compressibility as determined by odometer and triaxial tests.* Paper presented at the Proc. Europ. Conf. SMFE.

Janbu, N., & Senneset, K. (1974). *Effective stress interpretation of in situ static penetration tests.* Paper presented at the Proceedings of the 1st European symposium on penetration testing.

Janssen, H. (1895). Versuche uber getreidedruck in silozellen. *Z. Ver. Dtsch. Ing., 39*(35), 1045-1049.

Joer, H., Randolph, M., & Liew, Y. (1996). *Interpretation of cone resistance in layered soils.* Paper presented at the 7th Australia New Zealand Conference on Geomechanics: Geomechanics in a Changing World: Conference Proceedings.

Karlsrud, K., Lunne, T., Kort, D., & Strandvik, S. (2005). *CPTU correlations for clays.* Paper presented at the Proceedings of the international conference on soil mechanics and geotechnical engineering.

L'Heureux, J.-S., Carroll, R., Lacasse, S., Lunne, T., Strandvik, S. O., Degago, S., . . . Sinitsyn, A. (2017). New Research Benchmark Test Sites in Norway. In *Geotechnical Frontiers 2017* (pp. 631-640).

L'Heureux, J.-S., Longva, O., Steiner, A., Hansen, L., Vardy, M. E., Vanneste, M., . . . Forsberg, C. F. (2012). Identification of weak layers and their role for the stability of slopes at

Finneidfjord, northern Norway. In *Submarine mass movements and their consequences* (pp. 321-330): Springer.

Ladd, C. C., & Foott, R. (1974). New design procedure for stability of soft clays. *Journal of Geotechnical and Geoenvironmental Engineering, 100*(Proc Paper 10064).

Ladd, R. (1978). Preparing test specimens using undercompaction. *Geotechnical testing journal, 1*(1), 16-23.

Lindgard, A., Gundersen, A., Lunne, T., L'Heureux, J.-S., Kasin, K., Haugen, E., . . . Druci, E. (2018). Effect of cone type on measured CPTU results from Tiller-Flotten quick clay test site.

Locat, J., Leroueil, S., Locat, A., & Lee, H. (2014). Weak layers: their definition and classification from a geotechnical perspective. In *Submarine mass movements and their consequences* (pp. 3-12): Springer.

Lunne, T., & Christoffersen, H. P. (1983). *Interpretation of cone penetrometer data for offshore sands.* Paper presented at the Offshore Technology Conference.

Lunne, T., Powell, J. J., & Robertson, P. (1997). *Cone penetration testing in geotechnical practice*: CRC Press.

Lunne, T., Strandvik, S., Kåsin, K., L'Heureux, J.-S., Haugen, E., Uruci, E., . . . Kassner, M. (2018). Effect of cone penetrometer type on CPTU results at a soft clay test site in Norway.

Ma, H., Zhou, M., Hu, Y., & Hossain, M. S. (2017). Interpretation of layer boundaries and shear strengths for stiff-soft-stiff clays using cone penetration test: LDFE analyses. *International Journal of Geomechanics, 17*(9), 06017011.

Ma, H., Zhou, M., Hu, Y., & Shazzad Hossain, M. (2015). Interpretation of layer boundaries and shear strengths for soft-stiff-soft clays using CPT data: LDFE analyses. *Journal of Geotechnical and Geoenvironmental Engineering, 142*(1), 04015055.

Mayne, P., & Kulhawy, F. (1991). *Calibration Chamber Data Base and Boundary Effects Correction for CPT Data.* Paper presented at the Proceedings of the 1st International Symposium on Calibration Chamber Testing.

Młynarek, Z., Gogolik, S., & Półtorak, J. (2012). The effect of varied stiffness of soil layers on interpretation of CPTU penetration characteristics. *archives of civil and mechanical engineering, 12*(2), 253-264.

Mo, P.-Q., Marshall, A., & Yu, H. (2014). *Cavity expansion analysis for interpretation of CPT data in layered soils.* Paper presented at the Proceedings of the 3rd international symposium on cone penetration testing.

Mo, P.-Q., Marshall, A. M., & Yu, H.-S. (2016). Interpretation of cone penetration test data in layered soils using cavity expansion analysis. *Journal of Geotechnical and Geoenvironmental Engineering, 143*(1), 04016084.

Mo, P.-Q., Marshall, A. M., & Yu, H.-S. (2017). Layered effects on soil displacement around a penetrometer. *Soils and Foundations, 57*(4), 669-678.

Paniagua, P., D'Ignazio, M., L'Heureux, J.-S., Lunne, T., & Karlsrud, K. (2019). CPTU correlations for Norwegian clays: an update. *AIMS Geosci, 5*, 82-103.

Puech, A., & Foray, P. (2002). *Refined model for interpreting shallow penetration CPTs in sands.* Paper presented at the Offshore Technology Conference.

Quinteros, S., Gundersen, A., L'Heureux, J.-S., Carraro, A. H., & Jardine, R. (2019). Øysand research site: Geotechnical characterisation of deltaic sandy-silty soils.

Rad, N. S., & Tumay, M. T. (1987). Factors affecting sand specimen preparation by raining. *Geotechnical testing journal, 10*(1), 31-37.

Raihane, A., Bonnefoy, O., Chaix, J.-M., Gelet, J.-L., & Thomas, G. (2011). Analysis of the densification of a vibrated sand packing. *Powder technology, 208*(2), 289-295.

Robertson, P. (1990). Soil classification using the cone penetration test. *Canadian Geotechnical Journal, 27*(1), 151-158. doi:10.1139/t90-014

Robertson, P. (2009). Interpretation of cone penetration tests — a unified approach. *Canadian Geotechnical Journal, 46*(11), 1337-1355. Retrieved from https://doi.org/10.1139/T09-065. doi:10.1139/T09-065

Robertson, P. (2016). Cone penetration test (CPT)-based soil behaviour type (SBT) classification system — an update. *Canadian Geotechnical Journal, 53*(12), 1910-1927. doi:10.1139/cgj-2016-0044

Robertson, P., & Fear, C. (1995). *Liquefaction of sands and its evaluation.* Paper presented at the Proc. of 1st Int. Conf. on Earthquake Geotech. Engrg.

Robertson, P., & Wride, C. (1998). Evaluating cyclic liquefaction potential using the cone penetration test. *Canadian Geotechnical Journal, 35*(3), 442-459.

Salgado, R., Mitchell, J., & Jamiolkowski, M. (1998). Calibration chamber size effects on penetration resistance in sand. *Journal of Geotechnical and Geoenvironmental Engineering, 124*(9), 878-888.

Sandven, R. (2010). *Influence of test equipment and procedures on obtained accuracy in CPTU.* Paper presented at the Proceedings of the 2nd International Symposium on Cone Penetration Testing (CPT'10), Huntington Beach, Calif. Edited by Mitchell et al.

Schmertmann, J. (1976). An updated correlation between relative density DR and Fugro-Type electric cone bearing, qc. *Contract Report DACW*, 39-76.

Schneider, J. A., Hotstream, J., Mayne, P., & Randolph, M. (2012). Comparing CPTU Q–F and Q–Δ u 2/σv0' soil classification charts. *Géotechnique Letters, 2*(4), 209-215.

Schneider, J. A., Randolph, M. F., Mayne, P. W., & Ramsey, N. R. (2008). Analysis of Factors Influencing Soil Classification Using Normalized Piezocone Tip Resistance and Pore Pressure Parameters. *Journal of Geotechnical and Geoenvironmental Engineering, 134*(11), 1569-1586. doi:doi:10.1061/(ASCE)1090-0241(2008)134:11(1569)

Senders, M. (2010). *Cone resistance profiles for laboratory tests in sand.* Paper presented at the Proceedings of the 2nd International Symposium on Cone Penetration Testing (CPT'10), Huntington Beach, Calif. Edited by Mitchell et al.

Silva, M., & Bolton, M. (2004). *Centrifuge penetration tests in saturated layered sands.* Paper presented at the Proceedings of 2nd International Conference on Site Characterization, vols.

Standard Norge. (2012). Geotechnical investigation and testing Field testing. In *Part 1: Electrical cone and piezocone penetration test (ISO 22476-1:2012)*.

Sweeney, B. P., & Clough, G. W. (1990). Design of a large calibration chamber. *Geotechnical testing journal, 13*(1), 36-44.

Teh, C., & Houlsby, G. (1991). An analytical study of the cone penetration test in clay. *Geotechnique, 41*(1), 17-34.

Tehrani, F. S., Arshad, M. I., Prezzi, M., & Salgado, R. (2017). Physical modeling of cone penetration in layered sand. *Journal of Geotechnical and Geoenvironmental Engineering, 144*(1), 04017101.

Treadwell, D. D. (1977). The influence of gravity prestress, compresibility, and layering on soil resistance to static penetration.

Van den Berg, P., de Borst, R., & Huétink, H. (1996). An Eulerean finite element model for penetration in layered soil. *International journal for numerical and analytical methods in geomechanics, 20*(12), 865-886.

Van der Linden, T. (2016). *Influence of multiple thin soft layers on the cone resistance in intermediate soils (Master's thesis).*

Vreugdenhil, R., Davis, R., & Berrill, J. (1994). Interpretation of cone penetration results in multilayered soils. *International journal for numerical and analytical methods in geomechanics, 18*(9), 585-599.

Walker, J., & Yu, H.-S. (2010). Analysis of the cone penetration test in layered clay. *Geotechnique, 60*(12), 939-948.

Wang, Y. (2019). *Centrifuge Modelling and Numerical Analysis of Penetrometers in Uniform and Layered Clays (Doctoral dissertation.*

Xu, X., & Lehane, B. (2008). Pile and penetrometer end bearing resistance in two-layered soil profiles. *Geotechnique, 58*(3), 187-197.

Youd, T. L., & Idriss, I. M. (2001). Liquefaction resistance of soils: summary report from the 1996 NCEER and 1998 NCEER/NSF workshops on evaluation of liquefaction resistance of soils. *Journal of Geotechnical and Geoenvironmental Engineering, 127*(4), 297-313.

Yue, Z. Q., & Yin, J. H. (1999). Layered elastic model for analysis of cone penetration testing. *International journal for numerical and analytical methods in geomechanics, 23*(8), 829-843.

APPENDICES

TABLE OF CONTENTS

LIST OF FIGURES

LIST OF TABLES

A DOCUMENTATION ON THE PHYSICAL EXPERIMENTS

The methods presented in section **3.2** are explained in detail in this appendix. Results from the tests are also presented with comments.

A.1   Sand material

The sand used in the experiment originates from the local gravel pit of *Stokke Grustak* in Kvål, near Trondheim. It was extracted and delivered by the company *Ramlo Sandtak AS* and the sand type is labeled *0/2 sand* which indicates a maximum expected grain size of $2mm$. The sand was slightly moist, with water content about 6% and stored in bags containing approximately 500kg each. These sandbags were stored under roof from it was received until it was used in the sample, as shown in **Figure A**.**1**. Little prior characterization of this specific sand was available. Multiple tests were conducted to determine properties of grain size, density and strength parameters.

*Figure **A**.**1**. Stored sandbags.*

A.1.1   Grain size distribution and minerals

Sand from multiple bags were tested. Each bag contained homogenous sand with the same grain size distribution, which is presented in **Figure A**.2.
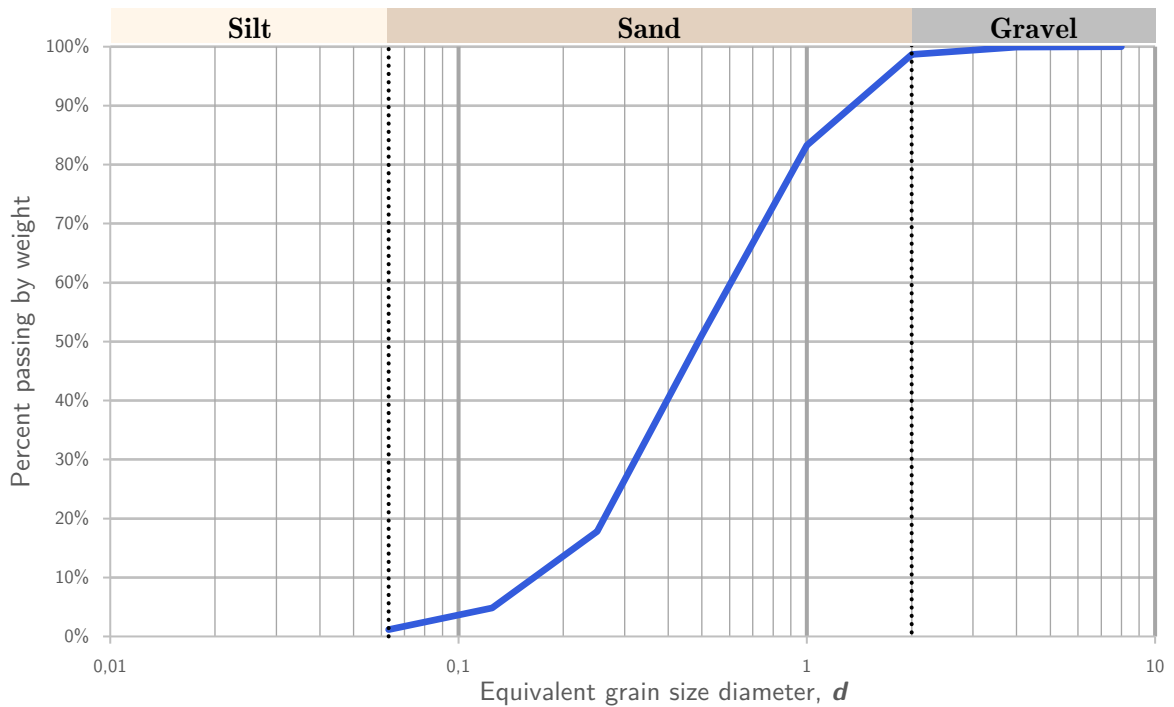
Figure A.2. *Grain size distribution of the sand.*

Characteristics from the grain size distribution are presented in **Table A**.1. A small fraction of about 1.2% of the weight has grain size less than $63\mu m$. Grains larger than $2mm$ make up less than 0.2% of the sands weight. The coefficient of uniformity is less than 5 which gives a classification as uniformly graded sand.

Table A.1. *Grain size characteristics of the sand.*

d_{10} [mm]	d_{50} [mm]	d_{60} [mm]	$C_u = \dfrac{d_{60}}{d_{10}}$
0.175	0.492	0.742	4.24

The sand was studied in a microscope to assess the grain shapes. Shapes of the grains sorted by size is presented in **Figure A**.3, these indicate that the grains appear either semi-rounded or angular. A previously conducted mineral analysis of aggregates originating from the same gravel pit has indicated a composition of approximately 34% quartz, 21% plagioclase, 15% mica, 14% alkali feldspar and 10% chlorite, 5% amphibole and 1% smectite.
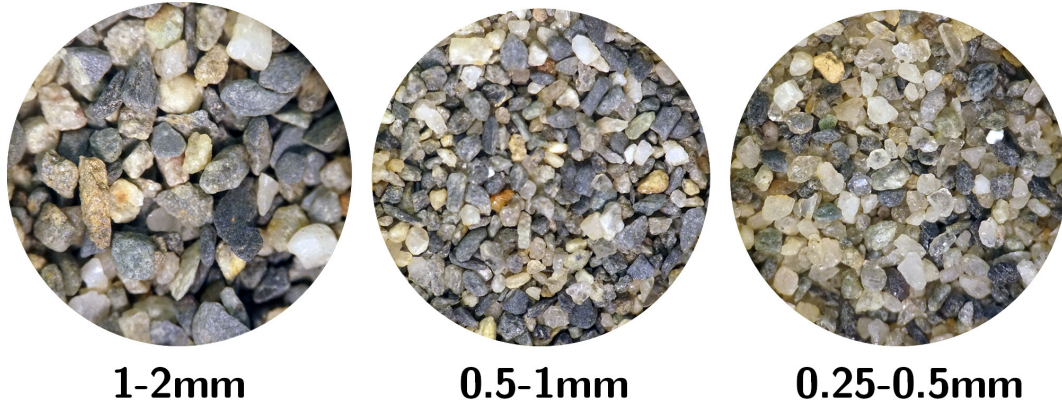
***Figure A*.3**. *Pictures of sorted sand fractions through a microscope. Note that the 0.25-0.5mm image has twice the zoom scale.*

A.1.2 Density properties

The density of the sand is an important measure of its strength and stiffness. For a given composition of soil grains, the porosity of the sand, n, given by equation (**A.1**).

$$n = 1 - \frac{\rho_d}{\rho_s} \tag{A.1}$$

where ρ_d is the dry density and ρ_s is the grain density. The void ratio is another way to express the ratio between solid material and the pores, gives by equation (**A.2**)

$$e = \frac{\rho_s}{\rho_d} - 1 = \frac{n}{1-n} \tag{A.2}$$

The grain density of the sand used in this experiment was found through the pycnometer method, according to ISO/TS 17892-3:2004. A grain density of $\rho_s = 2{,}73 g/cm^3$ was found. To indicate the density of a given state of sand grains, the relative density is used. It requires an estimation of the loosest and the densest state the sand can be reconstituted in the laboratory.

$$D_r = \frac{e_{max} - e}{e_{max} - e_{min}} \tag{A.3}$$

The estimation of the limits, e_{min} and e_{max} were done through the principles developed by the Deutsche Gesellschaft fur Bodenmechanik, DEGEBO. The loosest state of the sand (n_{max} and e_{max}) was found through pouring dry sand through a funnel into a cylinder with known volume. The funnel was moved upwards at a constant pace in order to have a neglectable drop height between the end of the funnel and the sand filled into the cylinder. Enough sand was contained in the funnel to fill the cylinder. The equipment used are shown in **Figure A**.4. Through multiple tests the highest porosity was repeatably found to be around $n = 46\%$, with the highest being $n_{max} = 46.6\%$. The latter is determined as the maximum porosity, with a maximum void ratio of $e_{max} = 0{,}873$.
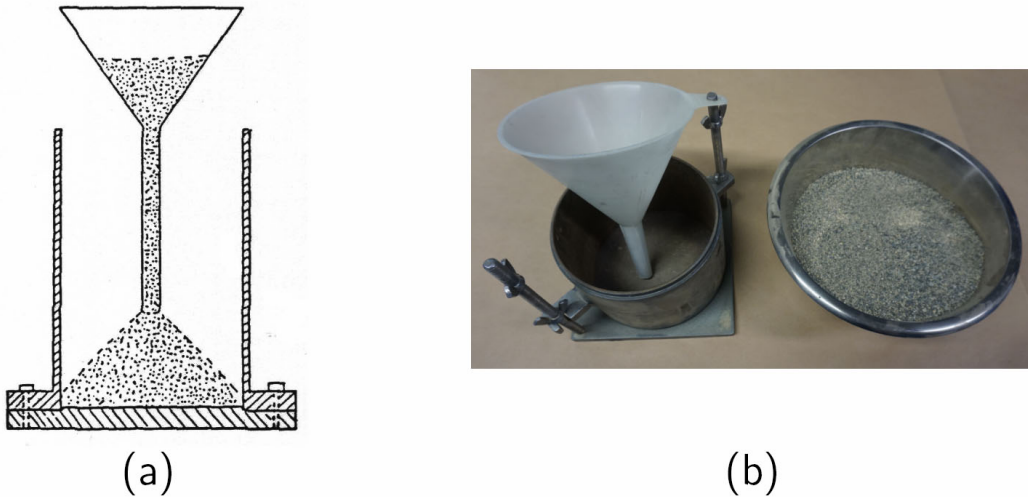
Figure A.4. Equipment used to determine the minimum density.

The procedure used to determine the densest state required a machine with two rods alternatingly hitting the container. Sand was filled in 5 layers in near fully saturated conditions. Each layer is vibrated by the two eccentric rods for 30 seconds. After the last layer was vibrated the sand was dried and weighed. This method gave a minimum porosity of $n_{min} = 33.4\%$, and minimum void ratio of $e_{min} = 0,502$.
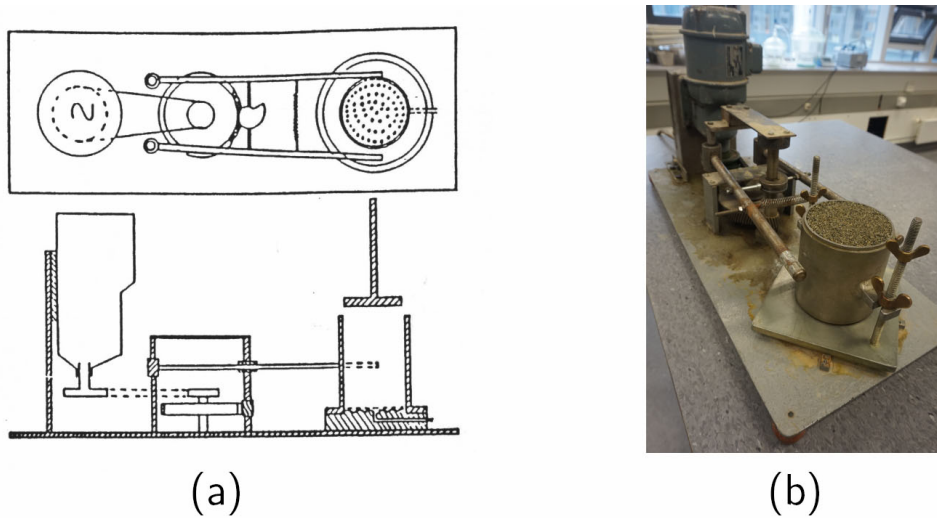
Figure A.5. Equipment used to determine the maximum density.

Figure A.6 presents the relative density as a function of the dry density using the determined e_{max} and e_{min} as well as the resulting density of fully saturated sand, as given in equation (**A.4**).

$$\rho = \rho_d + n \cdot \rho_w \tag{A.4}$$
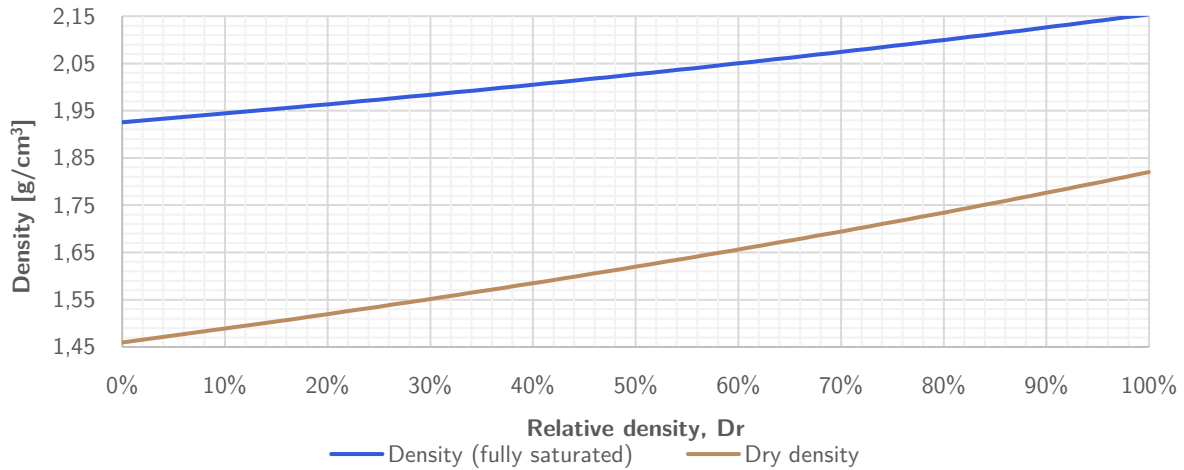
***Figure A*.*6**. *Dry density and density for a fully saturated sand, given the relative density.*

A.1.3 Strength and stiffness parameters

Characteristic strength and stiffness properties of the sand was investigated through triaxial anisotropic compression tests. Two tests were performed, one loose and one medium dense to dense. The triaxial test samples were made by tampering of layers of sand. The sand used had a water content of 6%, and triaxial samples of height 10cm and diameter of 5.4cm were created in five layers. Under tampering, as described in subchapter **3.1.2** was accounted for. Further details on the procedure is left out as the tests were done according to standard procedure and due to limited focus on the triaxial test results.

The loose sand triaxial sample had an initial void ratio of $e = 0.86$, while the medium dense sample had an initial void ration of 0.65. The tests were run in low stress level, $\sigma'_{m0} = p' = 35kPa$. The consolidation was performed with K_0 somewhat arbitrarily set to 0.67.

The effective stress paths are presented in **Figure A**.**7**. Interpreted parameters are added to the figures. While the loose test was saturated, the dense test was not. Furthermore, both tests were run with closed valves, i.e. the tests were not drained. The fully saturated loose sample was undrained, and this with constant volume, while suction occurred in the dense sample. The negative pore pressure developed noticeably as strain of about 4% was reached. An interpretation of a friction angle was done at this strain level. An attraction of about $1kPa$ was assumed, giving friction angles as presented in **Table A**.**2**. **Figure A**.**8** presents the vertical strain versus deviatoric stress, with the interpreted E_{50} stiffness.

***Table A*.*2**. *Interpreted properties of the sand*

e [ ]	ϕ [°]	E_{50} [MPa]
0.86	24	4
0.65	43	18
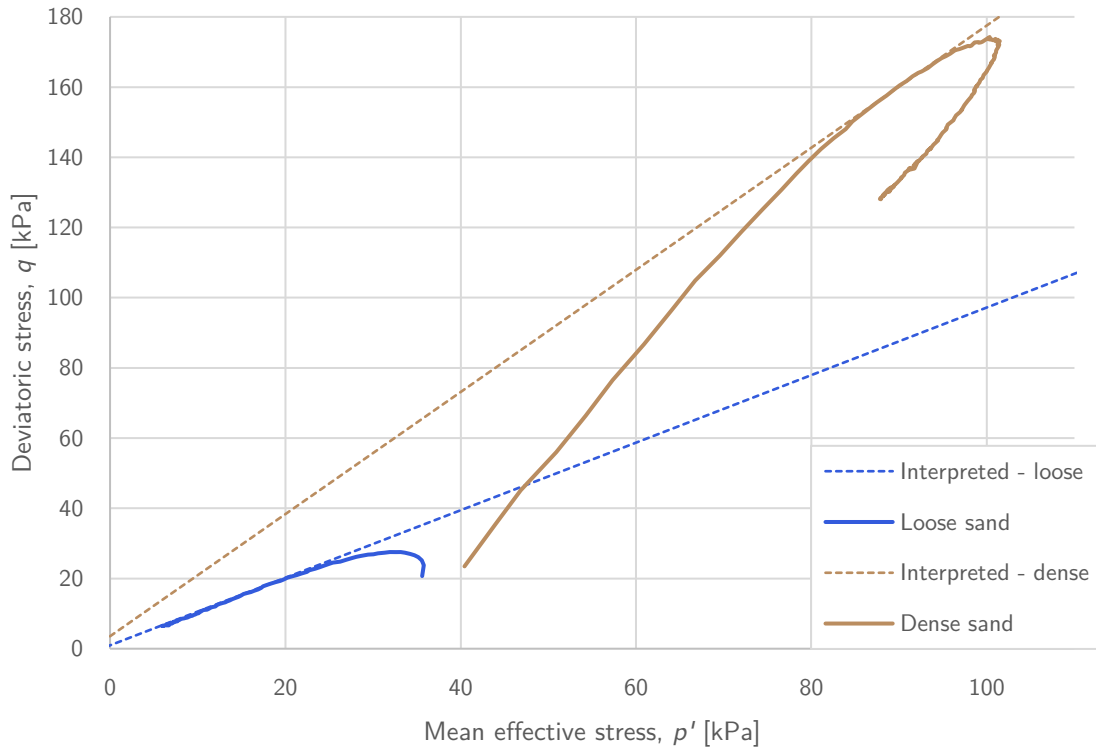
Figure A.7*. Mean effective stress vs. deviatoric stress of the triaxial tests of sand.*
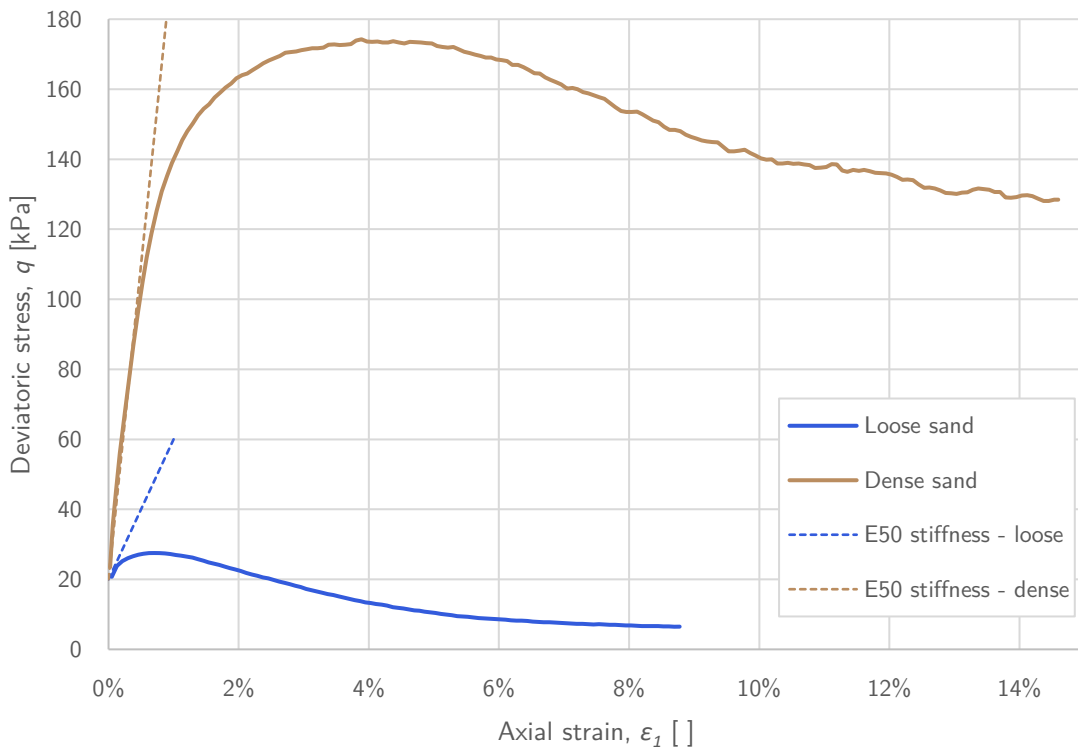
Figure A.8*. Axial strain vs. deviatoric stress of the triaxial tests of sand.*

A.2   Clay material

Multiple different alternatives of clay material and methods of creating clay layers was considered early in the project. The ideal clay material should preferably have an undrained shear strength less than about $40kPa$. It should furthermore be possible to create horizontal layers of equal thickness in a somewhat quick and simple way. Methods of creating normal consolidated clay in the chamber was considered but ruled out due to an expected complicated and time consuming procedure. In the end a practical solution was opted for and pottery clay was used. The clay is produced by *Sibelco* and has the identification of *K148*, normally used for pottery and ceramics. Units of clay, referred to as *clay blocks*, was shipped in a protected packaging (**Figure A**.**9**). Each clay block had width and height between 12 and $13cm$, and length between 30 and $32cm$. The clay has a unit density of $\rho = 2g/cm^3$ and each clay block has a mass of 10kg. The clay blocks were stored in a cold environment in the protected packaging until used.

Figure A.*9. Left: A single packaged clay block. Right: the sealed packaging of a shipment of clay blocks.*

While the details on the composition and method of production of the K148 clay is not known, it is homogenous without any impurities. It is indicated that it consists of kaolin clay. The properties of geotechnical interest were determined through tests to determine Atterberg limits, as well as triaxial and oedometer test.

A.2.1   Water content and Atterberg limits

All the clay material that was used in the model was tested for water content. As later described, the clay blocks were cut into smaller blocks with a selected size to form flat surfaces. Parts of the cut clay material of each block was dried to find the water content. These measurements would indicate whether the outer parts of the clay blocks had started to dry out. However, that was not the case, as all tests gave the approximately the same water content. The average water content was 23.8% with a standard deviation of 0.55%.

The Atterberg limits of the clay was determined through the procedures described in the European Standard ISO 17892-12:2018. The Casagrande method was used to determine the liquid limit. Results of these tests are presented in **Table A**.**3**.

Table *A*.3. *Liquid and plastic limits of the clay.*

w_L	w_P	I_P
30.5%	18.5%	12%

The clay has a liquid index, I_L, of about 44% according to the formula:

$$I_L = \frac{w - w_P}{I_P} \tag{A.5}$$

A.2.2 Triaxial test

The most important property to determine of the clay was the undrained compression shear strength, $s_{u,c}$. This was interpreted from undrained triaxial compression tests. Falling cone tests or handheld vane tests could also have been used to assess the same property, though such tests relies on calibrated factors to interpreted s_u that may not be suitable for this specific clay. Falling cone tests was however only used to compare the undisturbed and remolded clay properties, which indicated that clay had the same strength remolded, i.e. no sensitivity.

Two triaxial tests were performed, using different clay blocks. While both tests were run as undrained compression tests, one test was consolidated isotropic (CIUc) while the other was consolidated with K_0 of 0.33 (CAUc). The tests were performed with low cell pressures, like the sand triaxial tests. The resulting vertical strain against deviatoric stress plot is presented in **Figure A**.**11**, while the effective stress path is presented in **Figure A**.**12**.

Two different triaxial testing equipment was used, though both were of the same type (**Figure A**.**10**). The GDSLab software used to store data from the tests uses decimal notation with a selected precision rather than scientific notation. This was not considered before the CIUc test was initiated, and as a result the resolution of the axial piston force was set to 10N. The plot of the CIUc test does therefore appear cruder than that of the CAUc test.
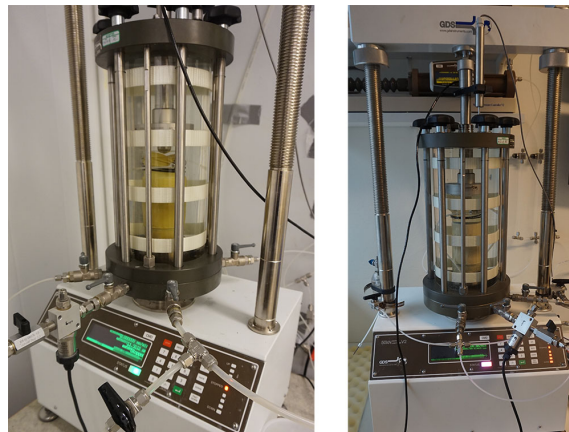
Figure A.**10**. *The two sets of GDSLab triaxial testing equipment used.*

The undrained shear strength is determined as half the maximum deviatoric stress. **Figure A**.**11** shows how the maximum deviatoric stress is approximately $55kPa$. The undrained shear strength of the clay is then assumed to be $27.5kPa$.

$$s_{u,c} = \frac{q_{max}}{2} \approx \frac{55kPa}{2} = 27.5kPa \tag{A.6}$$

Furthermore, the undrained initial stiffness of the clays is interpreted to be $E_u \approx 3MPa$. This gives an estimated initial shear stiffness, G, of $1MPa$.

$$G = \frac{E_u}{2 \cdot (1 + \nu_u)} = \frac{3MPa}{2 \cdot (1 + 0.5)} = 1MPa \tag{A.7}$$
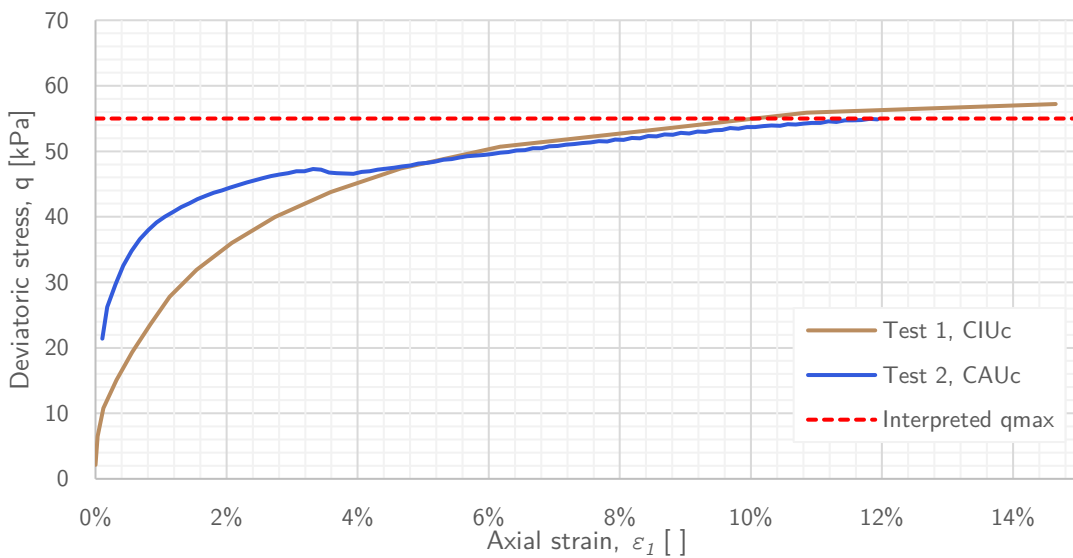
Figure A.*11*. *Triaxial tests of clay.*
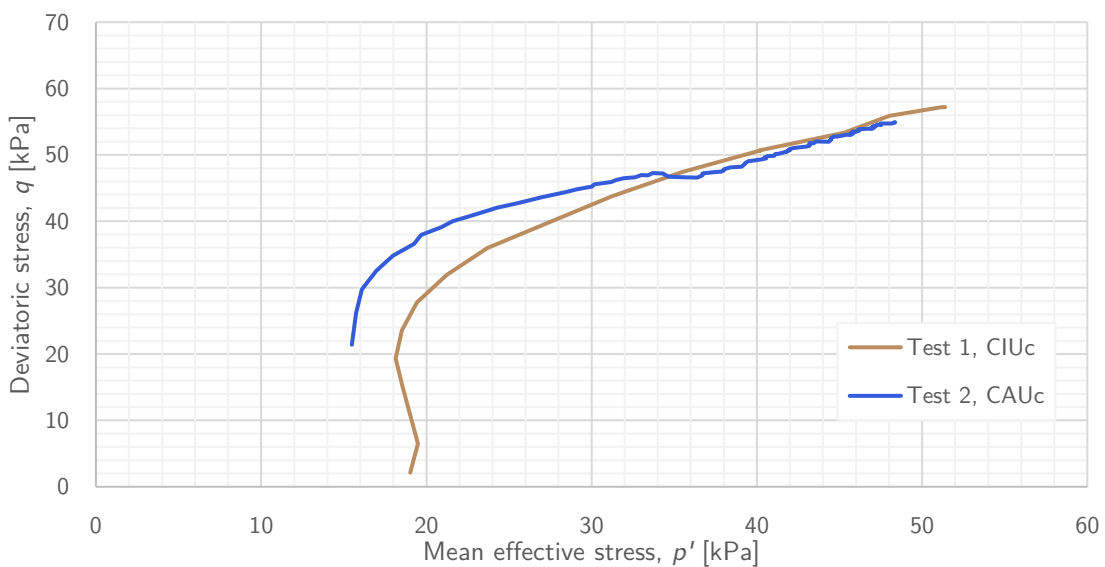
Figure A.*12*. *Effective stress path of triaxial tests.*

A.2.3 Oedometer test

An oedometer test was performed of the clay in order to assess preconsolidation stress and oedometer stiffness. Again, the procedure is left out due to the low importance of this study. The result of the test, and the derivative of the vertical stress with respect to the strain is presented in **Figure A**.13.
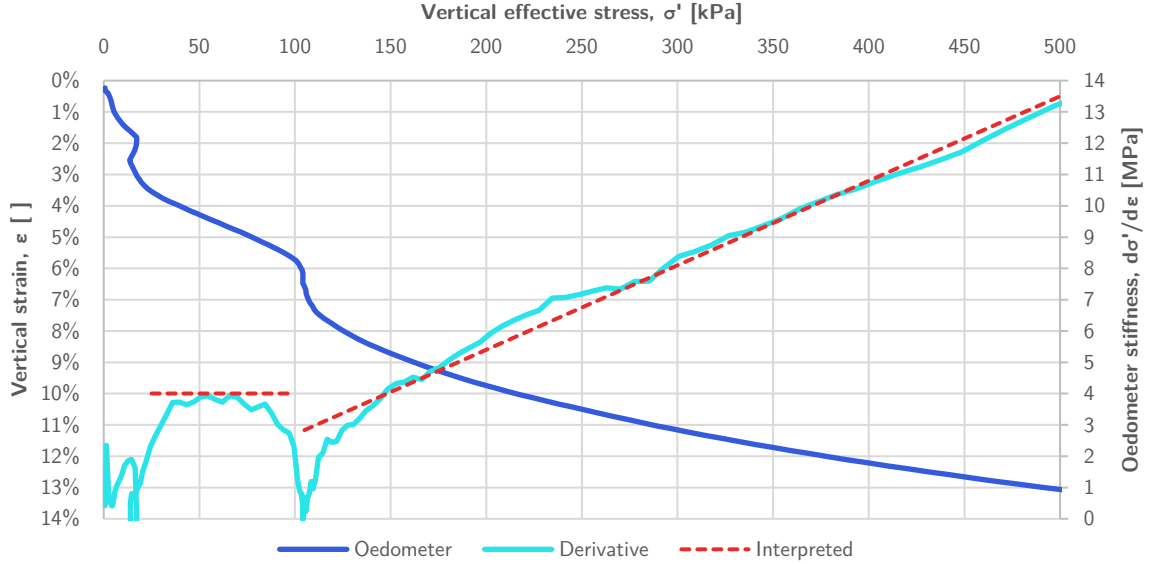
***Figure A**.13. Result of oedometer test of clay*

The behavior of the clay from σ'_v lower than 30kPa is believed to be due to the preparation of the oedometer. Ignoring these values, the oedometer response of the artificial clay is as expected of a clay. That is, a constant oedometer stiffness, E_{oed}, of 4MPa is found for vertical stress below about 100kPa, i.e. the clay has a preconsolidation stress of 100kPa. The normally consolidated region is interpreted to have a linearly increasing stiffness, as expected (Janbu, 1963). The increase is determined to be:

$$\frac{d\sigma'}{d\varepsilon} = 27 \cdot \sigma' \qquad (A.8)$$

Though the method used to create the Sibelco K147 clay is not known by the author, it is believed that vacuum-consolidation is used due to the over consolidation of approximately 1atm. The relationship between the preconsolidation stress and the undrained compression shear strength is given in equation (**2.9**), where α is equal to $s_{u,c}/\sigma'_{v0}$ for OCR of 1, or $s_{u,c}/\sigma'_c$ where σ'_c is the over consolidation stress. Values of α are normally close to 0.3. For the clay used in this study the relationship is given in equation (**A.9**).

$$\alpha = \frac{s_{u,c}}{\sigma'_c} = \frac{27.5kPa}{100kPa} = 0.275 \qquad (A.9)$$

The rigidity index of the clay can be estimated using a shear stiffness of $1MPa$, which gives:

$$I_r = \frac{G}{s_u} \approx 37 \tag{A.10}$$

A.3   Chamber model

A new chamber model was established for this experiment. The term *chamber model* refers to the components surrounding the soil in the experiment, mainly the cylinder walls. In addition, a plate with added dead weight was used to achieve a higher stress state. A large size of the chamber was desired, which also yielded the need for a large laboratory space to construct the sample and perform the tests.

A.3.1   Laboratory area

The experiment was executed in one of the laboratory areas of the Department of Civil and Environmental Engineering at NTNU in Trondheim. With a height of more than $6m$, sufficient space was available to construct large samples. Samples were manually constructed using the procedure described in section **A.4**. In order to safely execute the work needed, a scaffold structure was constructed around the chamber, as illustrated in **Figure A**.**14**. The scaffold had two important functions, the first being the working area while making the sample which is presented in the figure with 1.3m elevation above the laboratory floor. This level could be adjusted as needed with 0.5m height increments. The second function was the top of the scaffold, with an elevation of approximately 3.3m, used as a platform for the drilling rig when CPTUs were performed. Another important feature of the laboratory was an overhead crane for lifting operations, as shown in **Figure A**.**15**.
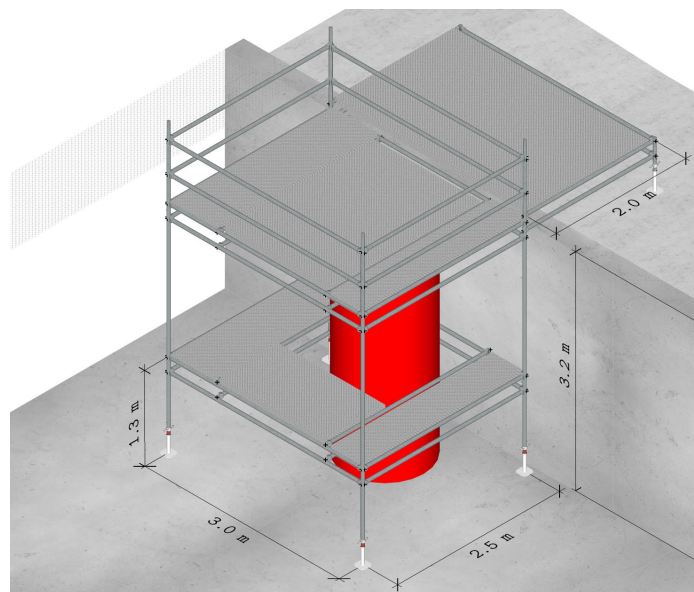
Figure A.*14. Model of the laboratory area with dimensions. The red cylinder represents a chamber of diameter 120cm.*

Figure A.*15. Lab area with scaffolding around chamber.*

A.3.2 Chamber elements

The chamber was desired to have a diameter of 1.2m and a total height of 2.5m. Steel cylinders are typically used for calibration chambers, especially for chamber boundary conditions BC1 or BC4 (see subchapter 3.1.1) where horizontal stress is applied. However, the selected properties for the chamber of this study was rigid walls without applied horizontal stress. Cylinders of concrete, a product which normally is intended to be used as drainage pipes, was acquired as it was a practical solution that met these requirements. These cylinders are sufficiently rigid, watertight and simple to handle. The drainage pipes were produced in Trondheim by the company *Loe Rør*. The cylinder elements are hereafter called chamber elements. The bottom chamber element is presented in **Figure A**.**16**.

Figure A.*16. The bottom chamber element.*

The bottom cylinder has a height of 95cm and a diameter of 120cm. Together with three additional extension chamber elements, each of height 51cm height, the total chamber height was 248cm.
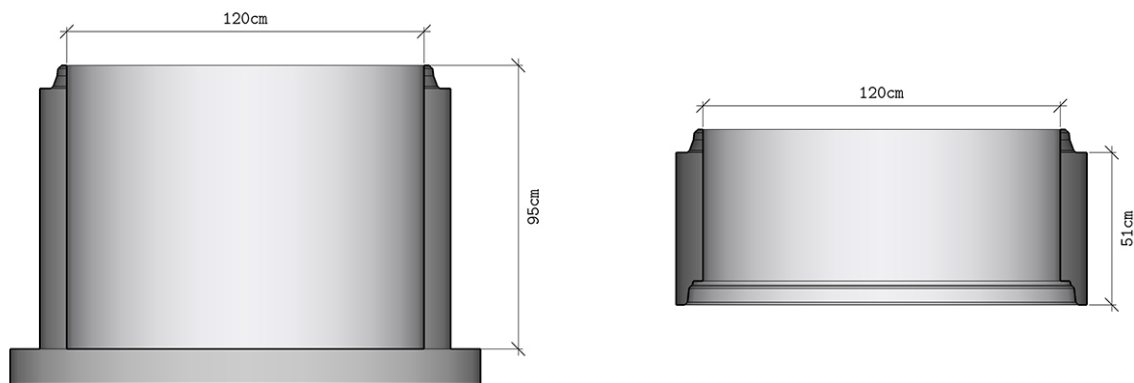
Figure A.*17. Chamber element dimensions.*

In order to keep track of depth measurements in an organized fashion, different depth references were used depending on situation. These are presented in **Figure A**.**18**. The absolute position was given as height above the floor of the bottom chamber element, h. Measurements were taken during construction as local depth, z_L, which was the distance below the top of the upper chamber element. Measurements of CPTUs were performed with depth z, given as the depth below the final sample build height.
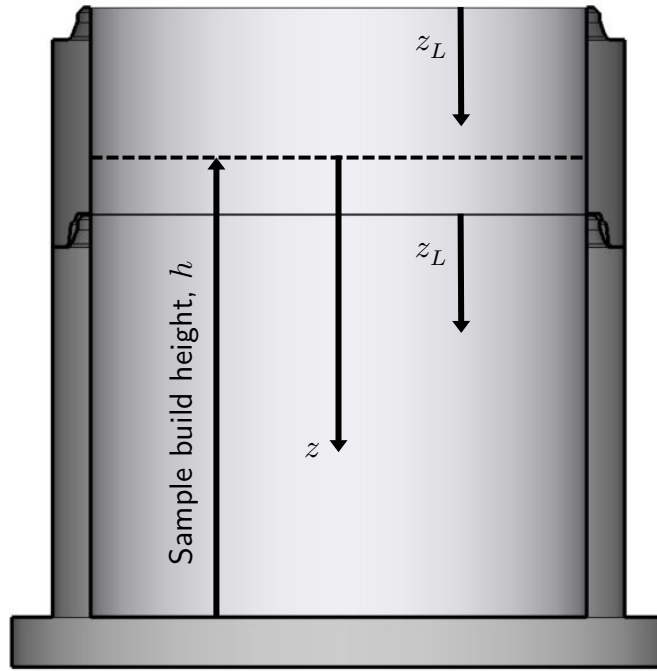
Figure A.*18. Depth references of the chamber.*

Horizontal positions in the sample were given as distance from the center and a direction. Three primary directions were used in the sample, these were called *a*, *b* and *c*, with $120°$ angles in between (see **Figure A**.**19**). As later described, CPTU tests were performed along these three lines of the sample.
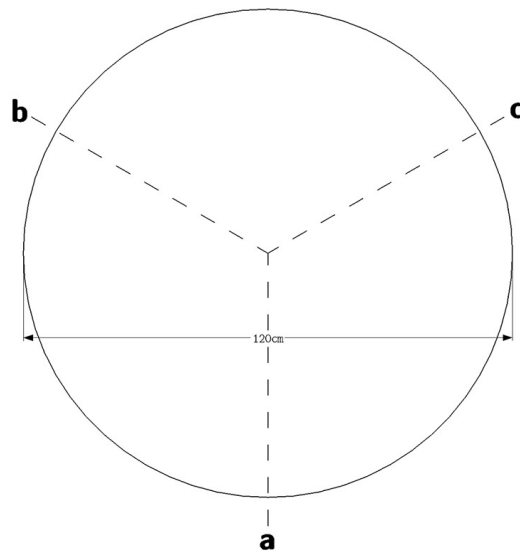
Figure A.*19. Section lines of the chamber, as seen from above.*

Much considerations were put into management of the water level. An illustration of the components is presented in **Figure A**.**20**. Firstly, water was filled in from the bottom as it normally is for sand samples since saturation from underneath results in a more uniform density of sand.

Water pipes entered the chamber through a hole with 5cm diameter, 3cm above the floor of the bottom chamber. To ensure a uniform vertical flow of water through the sand, a 10cm thick very permeable layer of gravel was formed. The gravel consisted of grain sizes between 8 and 16mm (**Figure A**.**21**). A permeable filter was then placed between the gravel and sand to prevent washing of the sand. A container of water at a selected height was used for a constant potential of water flowing into the sample, see **Figure A**.**20**. Water tightness between the joints was ensured with rubber gaskets.
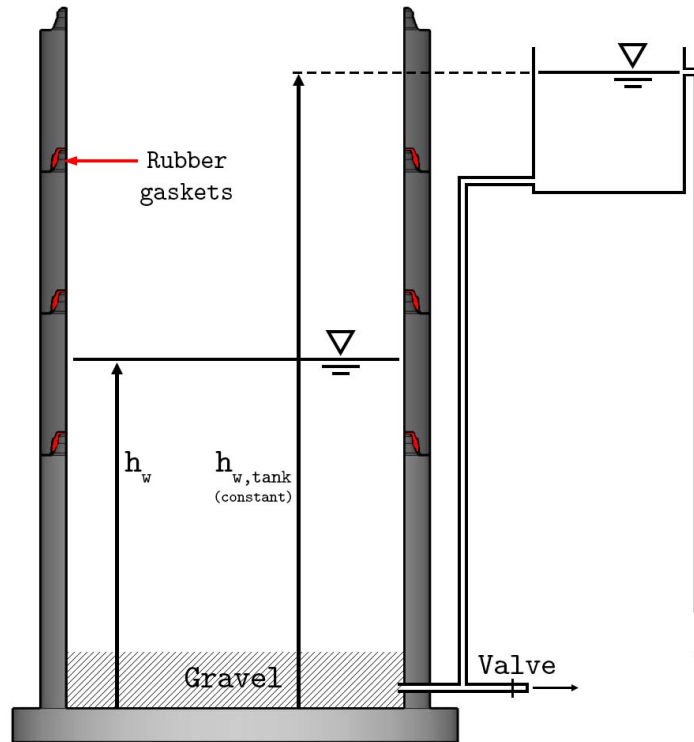
Figure A.**20**. *Illustration of the water management.*

Figure A.**21**. *Left: Gravel layer and filter, Right: Sand above the filter.*

The roughness of the chamber wall influences the vertical stress due to the silo effect, as presented in subchapter **3.1.2**. A larger friction coefficient between the soil and chamber walls cause larger shear stress along the walls and a lower vertical stress level. A measure to reduce the friction, and to allow for relative movement between soil and walls was through using plastic sheets along the walls. These sheets were placed along the wall of all chamber elements.

***Figure A**.22. Concrete wall roughness. Left: With plastic sheets, Right: Without.*

A.3.3   Test positions and added dead weight

Dead weight was added to the sample in order to achieve a higher stress state. Dead weights were attached to a circular steel plate of diameter 115cm and 2.5cm thickness. Holes were cut out of the plate where the CPTUs were to be performed, thus ensuring that the positions were correct. The design of the plate is shown in **Figure A**.**23**. As previously mentioned, the CPTUs were performed along the three primary directions *a*, *b* and *c*, which have a 120 degree angle between each. Seven holes were cut out of the plate, including one in the center of the plate, named hole **1**. Two holes were placed in each of the three primary directions, one 20cm from center and one 30cm from center. These holes were named **2x** and **3x**, respectively, where *x* is the name of the direction. The distance between the holes are presented in the figure below.

Dead weights were placed symmetrically over the plate, i.e. the center of gravity was exactly in the middle of the plate. Three stacks of dead weights were placed between the three primary directions. Of these, one stack had a total mass of 200kg while the other two had a mass of 80kg each. The position of these stacks is illustrated in the figure below, where yellow represents the 200kg stacks

and red the 80kg stacks. Together with the mass of the plate of 230kg the entire plate with dead weights (referred to as the dead weight plate) has a mass of 1310kg. This results in a pressure of $12.4kPa$ directly under the plate of diameter $115cm$. TJe distributed weight over the entire chamber diameter of 120cm is assumed to be $11.4kPa$.
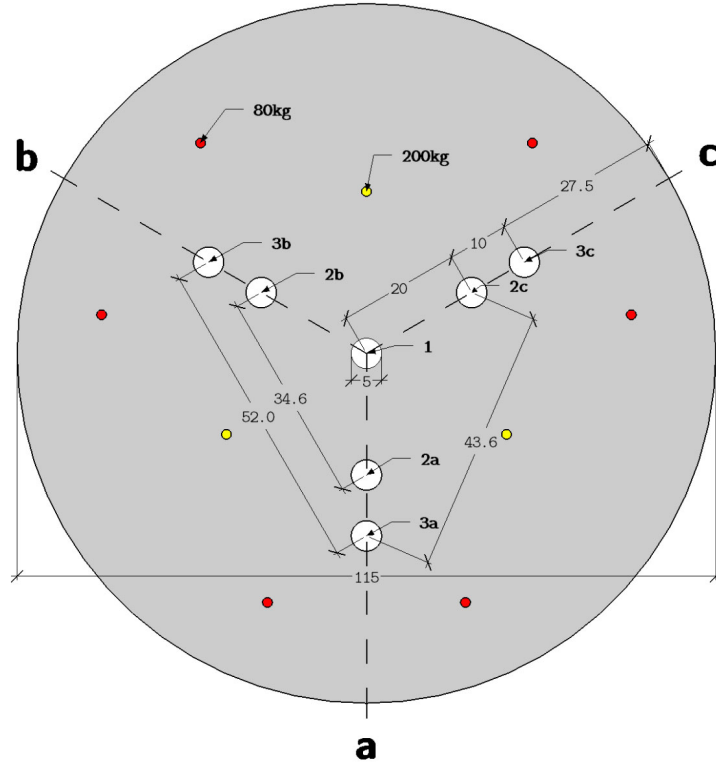
Figure A.23. Plate with test positions and length in centimeter.

In order to safely perform lifting operations with the dead weight plate, all dead weights were firmly locked using rods and wingnuts, as shown in **Figure A.24**. Padeyes were attached 5cm from the edge along the three primary directions.

Figure A.24. Plate with deadweights.

A.3.4 Sensors

Geokon Model 3500 earth pressure sensors were used to measure the vertical stress of the sample. The pressure is measured in disk cell with diameter 23cm and a thickness of 0.6cm connected to a transducer that sends analogue signals that were digitized and recorded continuously. To properly measure the vertical stresses of the soil, the sensors must be placed horizontally with full contact between the soil on top of and underneath the disk cell. Also, the stiffness of nearby soil may influence the measured stress, and ideally the cell should be equally stiff as the soil. If the cell is stiffer than nearby soil an increased measurement is recorded, and vice versa. Calibration of the equipment, using dead weights, was therefore done of the sensors when it was placed in the chamber. Another calibration was performed during dismantling. The placement of a sensor in the chamber is shown in **Figure A**.**25**, the center of the pressure cells was in the center of the chamber. The sensors were placed at a height (h) of less than 60cm to minimize potential influence on CPTU results. A known amount of soil was added in increments during sample construction. By comparing the pressure recorded in the earth pressure cell with a the known amount of soil on top allowed for an estimation of the silo effects.

Additionally, a pressure sensor was used to record the pore pressure at the bottom of the chamber.
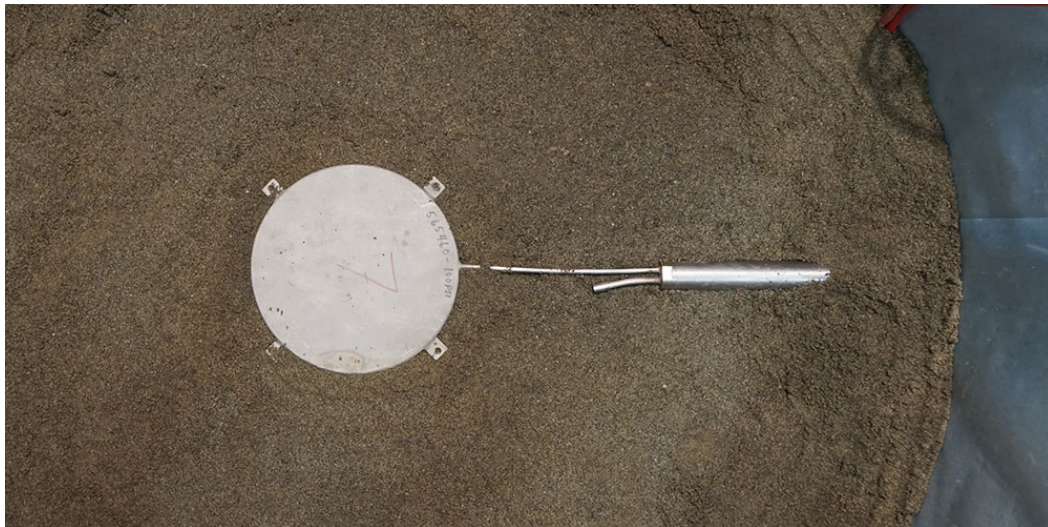
Figure A.***25***. *A partly buried Geokon 3500 earth pressure cell.*

A.4 Sample preparation

Each experiment is referred to as a *test case*, while the *sample* is the soil material in each test case. The samples primary consisted of sand, with some clay layers. A procedure was developed to allow for a repeatable preparation of uniform sand samples. The creation of the samples was done in height increments, referred to as sand layers. However, note that each sand layer in the sample is made the same way and the entire sand sample is therefore expected to be uniform. A sample of sand is made through a certain number of layers in order to form the total desired sample height. The preparation of each sand layer consists of three main stages. These are:

1) Slightly moist sand is rained into the chamber through a mesh,
2) The moist sand is slowly saturated from underneath, causing settlements,
3) The sand layer is compacted through vibration.

Each of these stages are presented in the following two subsections. A general overview of these stages is given here, described through **Figure A**.**26**. This figure presents the preparation of sand layer i through the stages as a function of the two height measurements, h and h_w. These are the sample build height, and the water level, respectively, after **Figure A**.**18**. **Figure A**.**26** presents stage 0 of a sand layer (i) as the completion of stage 3 of previous sand layer ($i-1$). At this point, the sample height is $h = h_0$ with the water level at height $h_w = h_{w,0}$. As described in the next subchapter, stage 1 was done through raining of slightly moist sand through a mesh in order to reconstitute a loose state. After the completion of stage 1 the height of the sample has increased with a certain filling height called Δh_f. The height of the sample is then given as $h = h_1 = h_0 + \Delta h_f$. Stage 2 consisted of slowly increasing the water level, h_w, until $h_w \approx h_1$ (2.1 in the figure). The saturation causes a settlement in the sand of Δh_s. After the water level is above the top of the sample, it is slowly decreased to about the height of the previous sand layer, i.e. $h_w \approx h_0$ (2.2 in the figure). Lastly, the sand is compacted using a vibroplate in stage 3, causing an additional settlement, Δh_c. The compaction of sand and consequent decrease in porosity causes the water level to rise.
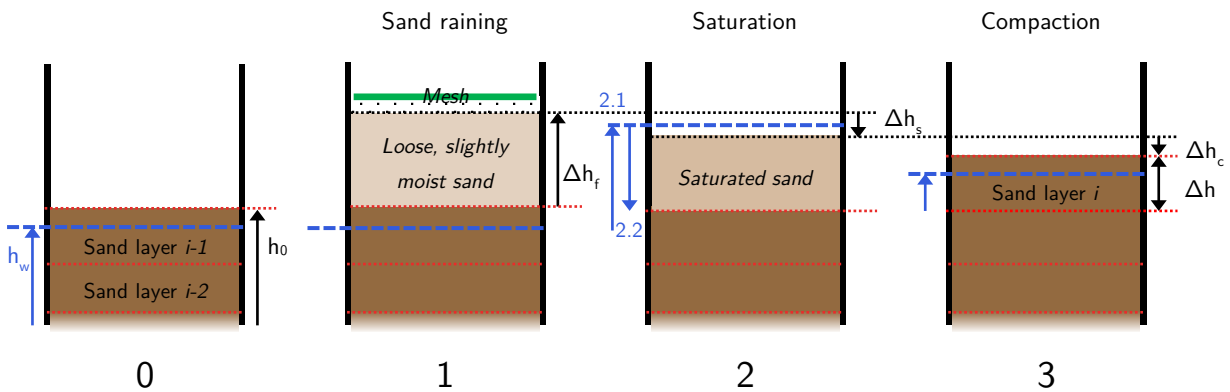
Figure A.*26*. *Illustration of the stages in the preparation of each sand layer.*

The achieved height increase of sand, Δh, after the three stages of a sand layer is given as the fill height minus the settlements due to saturation and compaction (**A.11**).

$$\Delta h = \Delta h_f - \Delta h_s - \Delta h_c \qquad (A.11)$$

A.4.1 Sand raining

The sand was filled into the chamber through raining. A typical raining procedure is described in section 3.1.2, where sand falls a certain height on to a diffuser and is then rained on to the sample. However, such a procedure requires dry sand while the sand used in this experiment had a water content of about 6% giving the sand cohesive properties. Rather than falling onto a diffuser, sand was poured on to a mesh and manually vibrated for grains to rain into the sample.

The equipment used to rain the sand was a circular mesh with diameter 115cm. This gives a space of 2.5cm between the mesh and chamber wall which allows for movement through vibration of the mesh. Chains attached the mesh to fixed positions on the chamber, as shown in **Figure A**.**27**. The vertical position of the mesh was determined by the number of chain elements between the mesh and four fixed positions (only three fixed positions are used in **Figure A**.**27**).

The mesh is made of two expanded metal sheets aligned perpendicular to each other. The openings in each expanded metal is diamond shaped with width 15mm and height 40mm. The who sheets then gives varied opening sizes the largest being less than 15mm by 15mm.

Figure A.*27*. *Mesh as used in chamber, seen from above. Chains are attached to the mesh and held at a fixed height from the top of the chamber elements. Three such fixed positions are shown in this illustration image.*

Figure A.**31** shows steps in the process of raining sand to form a sand layer of a certain filling height, Δh_f. The mesh is positioned at the desired filling height, Δh_f, above the previous sand layer. Image (a) shows how the mesh is filled with a certain amount of sand, evenly spread out. The mesh was then manually vibrated horizontally which caused small clusters of sand grains to rain through. This was done until no sand remained on the mesh (b). This process was repeated until the height of the sample equals that of the mesh (c).
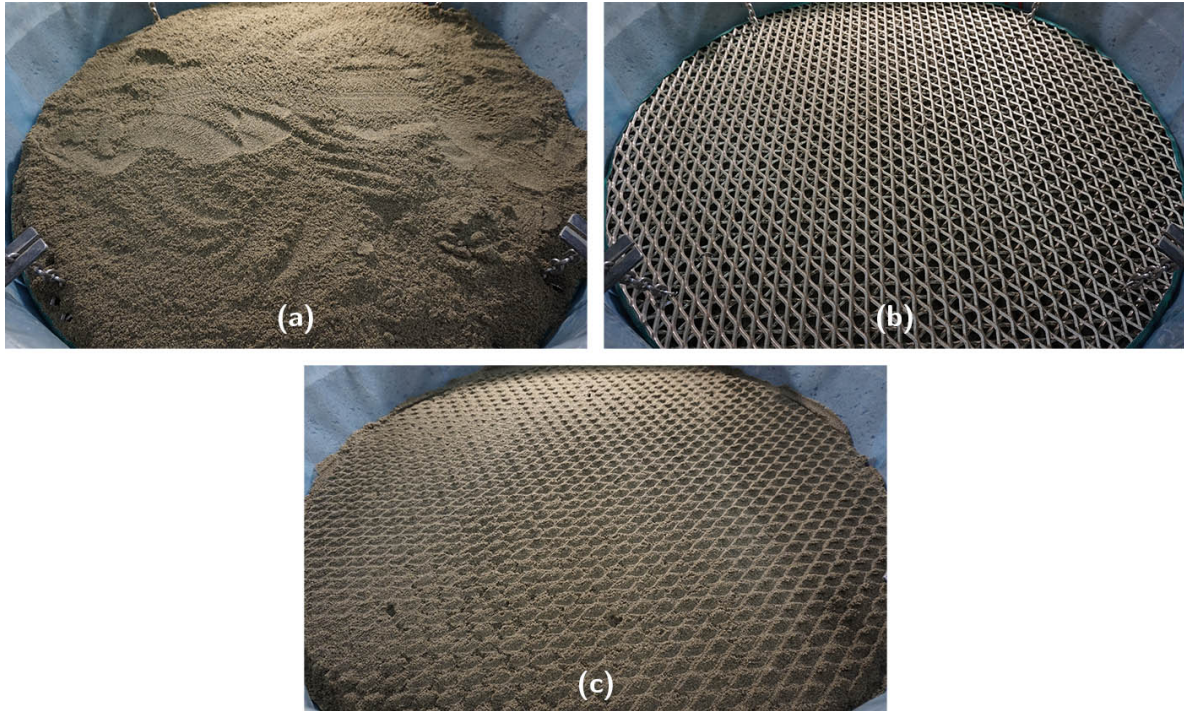
Figure A.*28*. *Raining of sand through mesh.*

This raining procedure was tested before the samples in the test cases were made. **Figure A**.**29** shows a container of volume 1L placed in the sample and filled up through raining. The estimated dry density of the sand in the container was $1.2g/cm^3$, the typical dry density of the filled sand was between 1.2 and $1.25g/cm^3$. Sand located around the container shows how loosely the rained sand was packed. Multiple of such density measurements were taken, all indicating a very loose state and a uniform porosity ($e \approx 1.2$). Comparing this to the loosest state of sand created through the procedure presented in **A.1.2**, where e_{max} was found to be 0.873, it is evident that the raining of slightly moist sand creates a very loose compaction of sand. It is important to note that the determined e_{max} is merely an estimation of a loose state which may naturally occur. However, it is not the loosest state possible of the sand, and the raining of moist sand results in a more porous packing due to the sands slightly cohesive properties.

***Figure A**.29. Density sample and the porous sand surrounding it after raining.*

A.4.2 Saturation

The very loose, slightly moist sand was then carefully saturated. Water was filled in from the bottom (as shown in **Figure A**.20) and the layer of gravel ensured that water flowed vertically upwards. The water tank has a constant height while the water level in the sample, h_w, increases with the sand layers. The difference in the hydraulic head of the water in the sample and the water flowing in is therefore small. To further ensure a cautious saturation with minimal transportation of fines, the valve feeding water into the sample was adjusted so that the increase of water level was approximately 3-4 minutes per centimeter increase.

Figure A.30 shows how the three steps of saturation. Image (a) is the situation right after raining. The local depth (z_L) is in this situation approximately 45.5, as the image shows. Following the saturation, water has reached the top of the sand, resulting in a settlement of about 1.4cm (b). Finally, the water level is lowered (c), as presented in **Figure A**.26.

The settlements caused by saturation were found to be approximately 15% of the fill height, Δh_f, i.e.

$$\frac{\Delta h_s}{\Delta h_f} \approx 0.15 \tag{A.12}$$

The relationship between the saturation settlement and the fill height is the approximated settlement strain. This was also the case for the sand layer of **Figure A**.30, where the fill height was 9.3cm and the settlement due to saturation was 1.4cm.

(a)   (b)   (c)
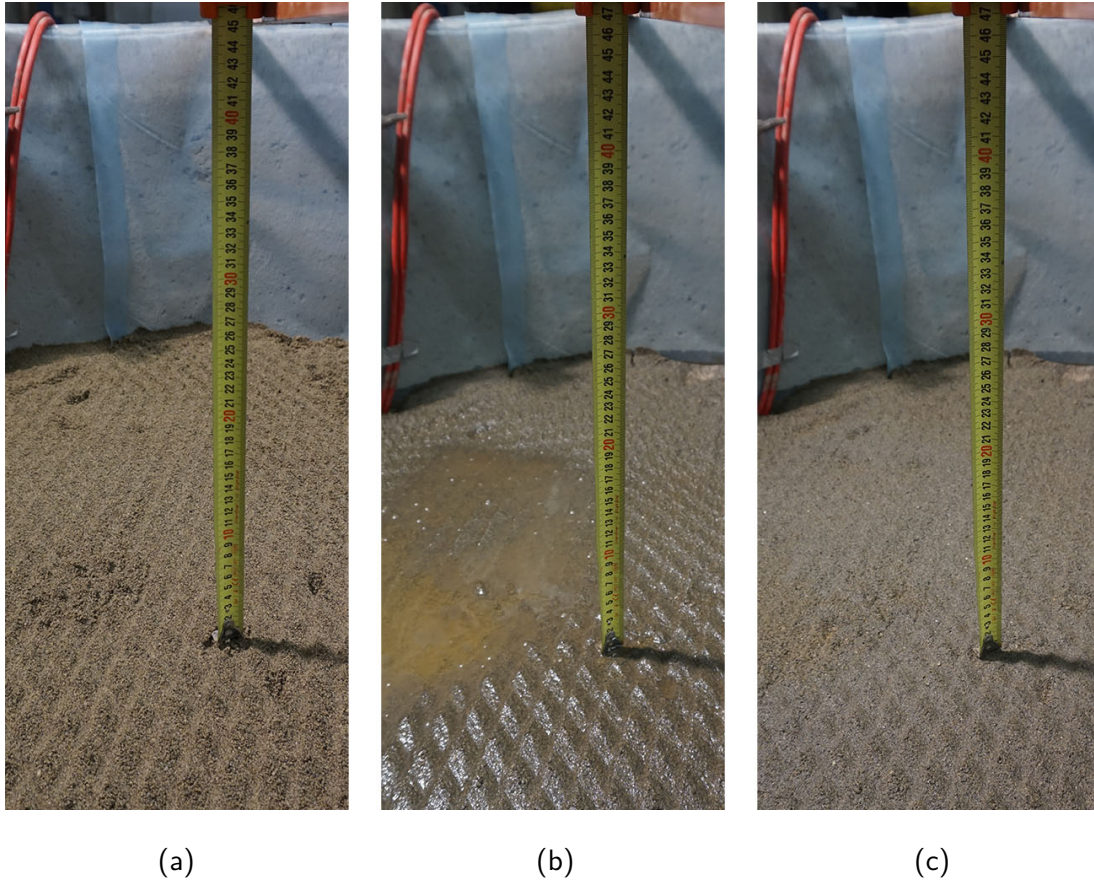
***Figure A**.30. The steps in the saturation.*

Samples taken after the saturation of a sand layer proved that the procedure of moist raining of sand and consequently saturation is a repeatable process to create very loose and uniform sand samples. The dry density of the saturated sand was measured to be between 1.46 and $1.48 g/cm^3$

A.4.3 Compaction of sand

The uniform, loose sand, was then densified with a vibro plate. Starting with a flat, leveled surface, a circular plate with diameter 115cm was placed on top with a vibro plate in the center (**Figure A**.**31**). The vibro plate vibrates on a 50Hz frequence, and tests were done to measure the effect of the densification as a function of time induced to vibration. Effects similar to that of under tampering was considered, i.e. the lower sand layers were vibrated for a shorter time than the upper. In a 2m tall sample, the lower layers were vibrated for 30 seconds while the upper were vibrated for about 60 seconds. The resulting dry density was estimated to be between 1.53 and $1.6 g/cm^3$, depending on the layer thickness.

Settlements due to vibro compaction was experienced to be approximately 10% of the fill height minus the saturation settlements. This is the approximated settlement strain due to compaction.

$$\frac{\Delta h_c}{\Delta h_f - \Delta h_s} \approx 0.10 \tag{A.13}$$

Figure A.31. Equipment used for compaction of sand.

The vibration of sand caused some transport fines from the upper part of the sand layer the top, shown in **Figure A.32**. As the image shows, this resulted in either some concentrations of fines, or as seen in the bottom of the image, some porous structures were made. However, the extent of the transportation of fines was assumed have a neglectable effect.

Figure A.32. Example of result of vibro compaction.

A.4.4 Clay layers

Clay blocks were carefully cut with a wire saw to form smaller blocks with completely flat sides. All clay blocks were cut to a length of 30cm and width 10cm while the height depended on the clay layer. **Figure A**.**33** shows a clay block cut to 30cm length, 10cm width and 12cm height. After the block was cut in the correct size it was put on a plastic tray and moved to the sample. The handling of clay blocks was a delicate procedure, lifting was done through using two plastic plates on each side of the clay block to add an equal pressure. A clay layer was formed of multiple such clay blocks, and it was important that neighboring clay blocks had full contact along the entire boundary. With two clay blocks with flat sides, this was done through adding a bit of water in between and then to slide the second block along the surface of the first. Then, a clamp could be used to gently force the blocks together.

Figure A.*33. Prepared clay block.*

Clay layers were not made to cover the entire area of the chamber. Firstly, this was not done since it would create an impermeable barrier. Secondly, the flow mechanism in clay layers has a small radius and it was therefore deemed unnecessary in order to measure the appropriate tip resistance in the clay layers. Thirdly, by creating "local" clay layers for each test position it was possible to create different layering structure for each test position. A clay layer was therefore created in direction a, b or c independently.

The shortest distance to end of clay layer from the center of a CPTU test was decided to be $15cm$. Thus, the ratio between this distance and the diameter of the cone was 4.2. The orientation of the clay blocks was selected so that test positions did not coincide with the boundary between two clay blocks.

Two types of clay layers were made in the test cases in this study, these are illustrated in **Figure A**.**34**. This illustrates the sample composition at a given height. These are illustrated with clay layers in direction a, and a + b, respectively as an example, while the remaining parts of the sample consists of sand. Note that in the test case where 1 direction was used, no test was performed in the position 20cm from center, i.e. the "2x" hole.

1 direction *2 directions*
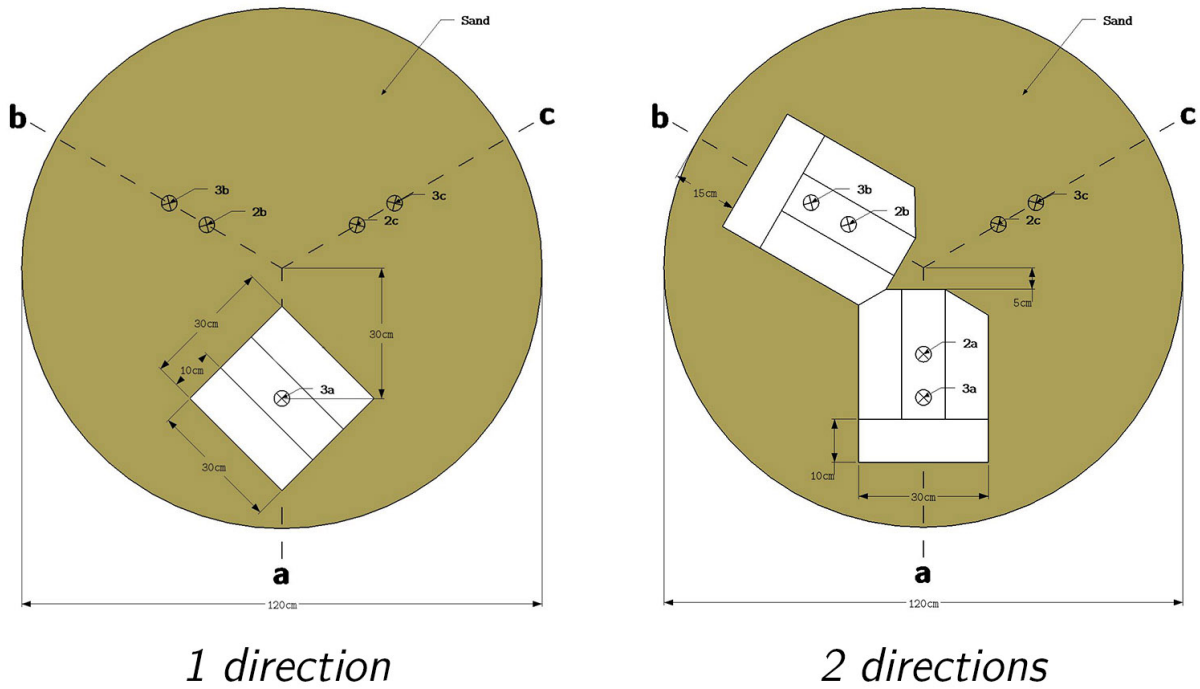
*Figure **A**.34. The two different clay layer setups used in this experiment.*

The 2 directions setup illustrates how, at a given height, tests in two of the directions are done in clay, while tests in the remaining direction is done in sand. Though it is expected that the size of the clay layer is expected to be sufficient to achieve the correct tip resistance, the influence of the distance from a test in sand to a nearby clay layer largely depends on the density of the sand. The shortest distance from a test in sand to nearby clay layer, which for the case in **Figure A**.34 would be the distance from 2c, is 20cm.

An example of a clay layer, of one of the directions of the Type 2 setup is presented in **Figure A**.35. Though small shadows are visible between the clay blocks this is primarily due to height differences of the clay blocks of about 0.1cm.

*Figure **A**.35. A 4cm thick Type 2 clay layer.*

The clay layer was placed on a flat surface after the three stages of sand layer preparation presented above. The water level was decreased for minimal compaction under the clay layers. A following sand layer over clay layers had to have a fill height of at least the height of the clay layer. Furthermore, due to the large settlement caused by saturation and compaction, the fill height of sand layers around a clay layer was about one and a half times the clay layer height while less sand was filled directly above the clay layers. That was done due to neglectable settlements of clay layers.

A.4.5 Applying dead weight

After the completion of the sample, the dead weight plate was placed on top. As a measure to avoid a large local shear stress around the edge of the plate, a slight slope of was made in the sand around the walls. The top of the sample was flat with a radius of approximately 54cm, while the outer 6cm had an inclination of about 1:2 (**Figure A**.36). As the dead weight plate was placed, settlement occurred without the edges cutting though the soil.

Figure A.36. *Illustration of shape of the top part of sample.*

The water level was kept at the same height as top of sample, i.e. at the level directly below the dead weight plate.

A.5 Bore rig and CPTU equipment

CPTUs were desired to be performed in a manner that resembled a typical in situ test. This primarily meant that a standard cone penetrometer should be used, with CPTU performed according to the standard.

A.5.1 Bore rig

The requirements of the pushing mechanism used was capability of continuous pushing to approximately $2.5m$ length with a selected speed, and to have sufficient pushing capacity. Two options were available, these were a bore rig and a screw driven cylinder. The former was selected early in the process. Though the typical modern bore rig in Norway *Geotech GEORIG 697* was available, it would not be suitable due to both size and weight limitations. Instead, a *Borro* bore rig made in 1977 was used. Though the rig had been unused for many years the bore rig worked well after some adjustments. An advantage with the Borro rig was a continuous pressing mechanism with two arms that alternating grips and presses the rods, thus the CPTU did not have to pause in order to additional rods.

Figure A.37. The Borro bore rig on top of the scaffolding platform.

A.5.2 CPTU equipment

A CPTU probe of the type *CPT GEOTECH NOVA* was used in this experiment, a probe that is very commonly used in Norway. It has a standard cone area of $10cm^2$, i.e. the diameter is $3.6cm$, and with a $60°$ apex. The area factor of the specific piezocone was $a = 0.864$. The pore pressure filter of brass was used with the located behind the cone, i.e. the u_2 pore pressure is measured. The filter was saturated in de-aired glycerine. The sleeve had a standard area of $150cm^3$ and length of $13.4cm$. An image of the specific cone penetrometer used in shown in **Figure A.38**.

Figure A.38. Image of the Geotech NOVA CPTU probe used in this experiment.

The CPTU probe was calibrated by *Geotech AB* in Gothenburg in September 2019. With the exception of a single test conducted in the winter of 2020 with the Borro rig, the probe was not

used until the experiments in this study were conducted. Measurements were transferred through microphone and also stored in the memory as illustrated in the schematic in **Figure A**.**39**.
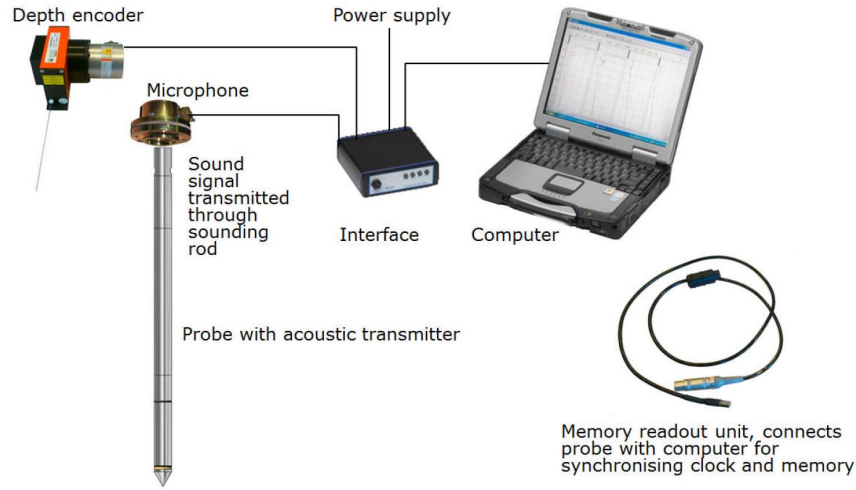
***Figure A**.39. Schematic of CPTU data equipment*
(http://www.geotech.eu/images/manual/NOVA_manual.pdf).

A.5.3   CPTU data processing

The CPT GEOTECH NOVA records measurements of q_c, f_s and u_2 alternating every 0.8s and 1.2s, i.e. the average sampling frequency is $1Hz$. The penetration speed was set to $1.5cm/s$ rather than the standard of $2cm/s$ for slightly better resolution.

While a commercial software normally is used to extract the measurements at a desired interval that is not used here. Instead the raw data from the CPTU is presented as it is, i.e. only actual measurements are presented.

During testing, the depth reference was selected as the tip of the cone. Presentations of the results are done either with depth as the tip of the cone, noted *depth*, or adjusted to the depth of each measurement separately. If the latter is done, the results were presented as *depth adjusted to measurement location*.

A.6   Dismantlement

After the all CPTUs were performed for the test case the sample was carefully dismantled and the density of the sand was assessed through density measurements. These density measurements were done using a sampler cylinder with 7.2cm diameter and 5cm height, the sand within the sampler is referred to as a density sample. The edge of the sampler was sharpened, as presented in **Figure A**.**40**. The image also shows an extension used to press the sampler into the sand.

Figure A.40. Density sampler ring, 7.2cm diameter and 5cm height, with an extension to the right.

The CPTUs disturb the sand at some distance, and measurements of density was taken in the least disturbed areas. These positions are presented in **Figure A.41** with cyan, and illustrate how density samples were taken in the middle of the primary directions a, b and c, called ab, bc and ca respectively. The density samples were mostly taken between 30 and 40 centimeters from the center along these lines.
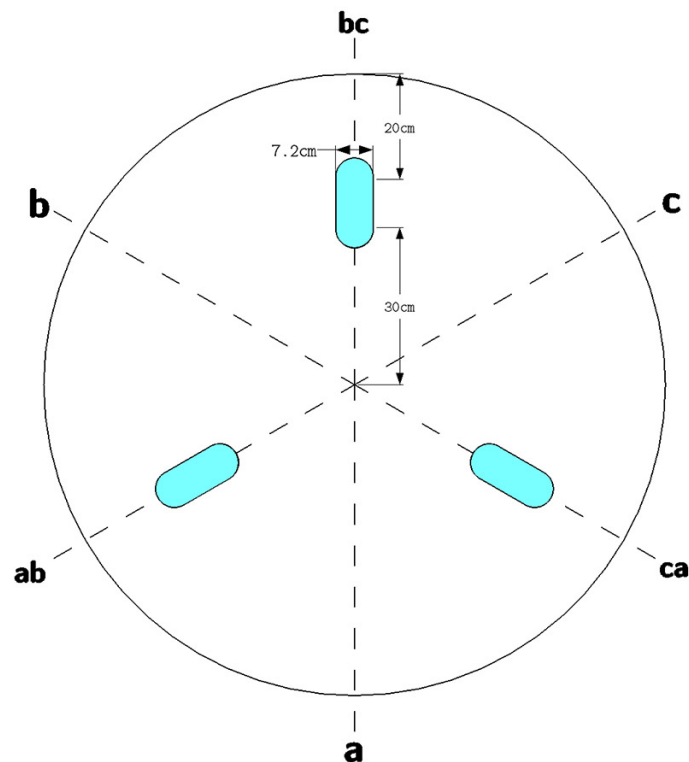
Figure A.41. Positions of density measurements in the chamber, as seen from above.

Figure A.42 illustrates the procedure of extracting density samples. Image (a) shows the sampler and the extension cylinder on top of the sampler ring. The extension was then aligned with the sampler and a square metal plate with sides 30cm was placed on top. By pressing the sampler

down using the plate, the verticality of the sampler was ensured. The sampler was pressed down until a depth showed in image (b), approximately $0.1 - 0.5cm$ below the top surface and the depth was recorded. The small amount of sand above the samples was removed to achieve a horizontal top. Finally, the sand around the sampler was removed and a masonry trowel was used to carefully cut out the bottom of the sampler horizontally. The sampler with the density sample was then lifted out (c). The surface on the top and bottom of each density sample was controlled to ensure that it properly filled the sampler.
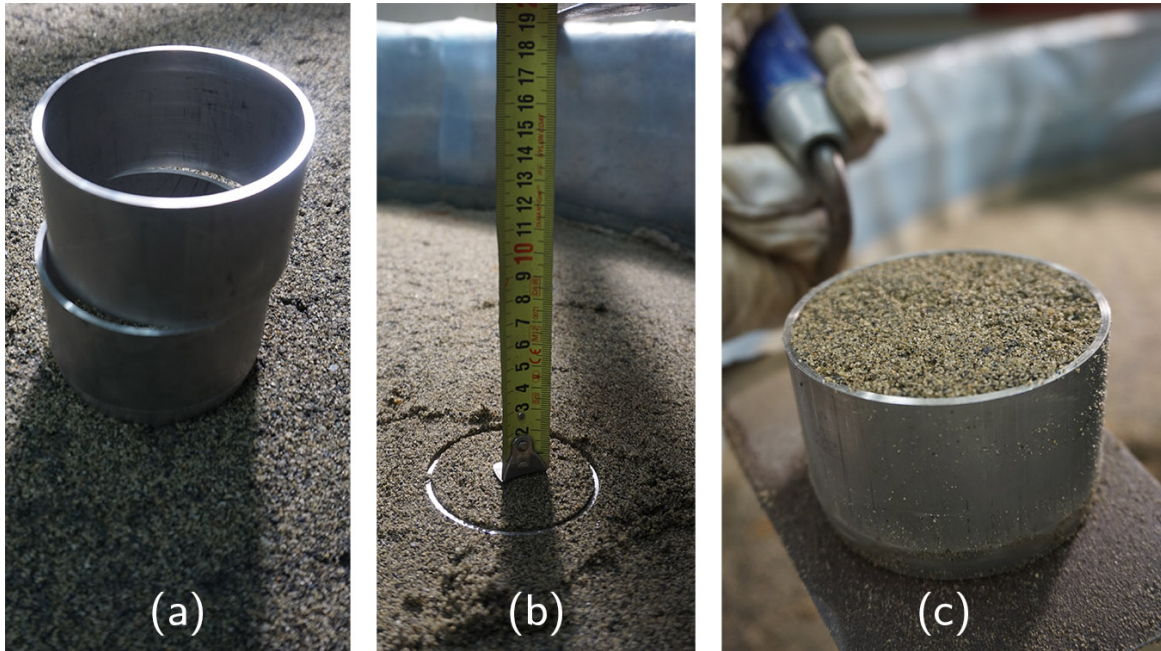
***Figure A**.42. Procedure for a density measurement.*

The sand in the sampler was then dried at 105° until the dry mass (m_s) was constant. The dry density of the sand was given as:

$$\rho_d = \frac{m_s}{V} \tag{A.14}$$

where V is the volume of the sampler. The complete volume of the was $203.6 cm^3$, however, this may be regarded as an upper limit of the volume. As stated, the excess sand on the top and bottom of the sampler was removed, thus the true volume of the sampled sand is very close to, but not larger than the complete volume. It was believed to be more representative to assume a slightly lower volume. This was done by assuming a that the true volume of the sampler was the sampler's diameter and height minus d_{50}. The sand had a d_{50} of approximately $0.5mm$, giving an assumed diameter of $7.15cm$ and height of $4.95cm$ and a volume of $198.8 cm^3$.

The sand was dug out of the chamber and into sandbags. Sand was not reused in this experiment due to the large amount of sand available.

A.7   Test cases

The procedures above was used to create samples of desired properties and layering. Test cases were selected with the intention of testing the properties of CPTUs in thin clay layers in thick sand deposits. It was desired to also create a sample without layering as well in order to gain experience on sample creation and the execution of CPTU in the designed chamber model. This sample is referred to as the calibration sample.

Preparations and acquisition of material and equipment took place in the winter of 2020. Unfortunately, the period planned for work in the laboratory coincided with the events of early spring 2020 and the work was postponed for seven weeks. That is, the preparation of the calibration sample had just started before laboratory areas were closed. When work in laboratory commenced a few changes to the plan of the calibration sample was done in order to get more results from the tests. It was also questionable whether the author could invest the time needed to create another sample. The preparation, testing and dismantling of a sample required about three weeks of work. However, due to the great desire to execute the initially planned test in thin clay layers two tests were made.

These two tests were named Case A and Case B, the former being the calibration sample. A rough description is presented in **Table A**.4, full details on the setup on each of these tests are given in the next two sections.

Table A.4. *Tests performed.*

Sample name	*Sample height (h)*	*Sand properties*	*Clay layers*
Case A	$\approx 200cm$	Very loose sand $(D_r \approx 10\%)$	One *Type 1* clay layer 30cm thick
Case B	$\approx 230cm$	Loose sand $(D_r \approx 30\%)$	Three *Type 2* clay layers 4, 8 and 12cm thick (~50cm between each layer)

A.8   Case A

This test case was initially planned as a calibration sample of pure, very loose sand without any clay layers. At the time when the work was interrupted, the sample was built to a height of $90cm$. Earth pressure sensors were not included in this experiment as the equipment was not ready for use at the time. Plastic sheets were also not used in this experiment. However, when work commenced seven weeks after the first $90cm$ were made, it was decided that a clay layer should be included. A $30cm$ clay thick layer was introduced in order to have an estimation of the tip resistance in a sufficiently thick clay layer.

A.8.1   Model setup

The Case A sand sample consisted of sand sample up to height $205cm$. The clay layer was of *Type 1* (**Figure A**.**34**, a single 30x30cm area of clay) was placed at direction a, at height h from $92cm$ to $123.5cm$. Thus, the layering profile of direction a was different than that of direction b and c. To clarify the different layering profiles of the directions section profiles are illustrated according to **Figure A**.**43**.
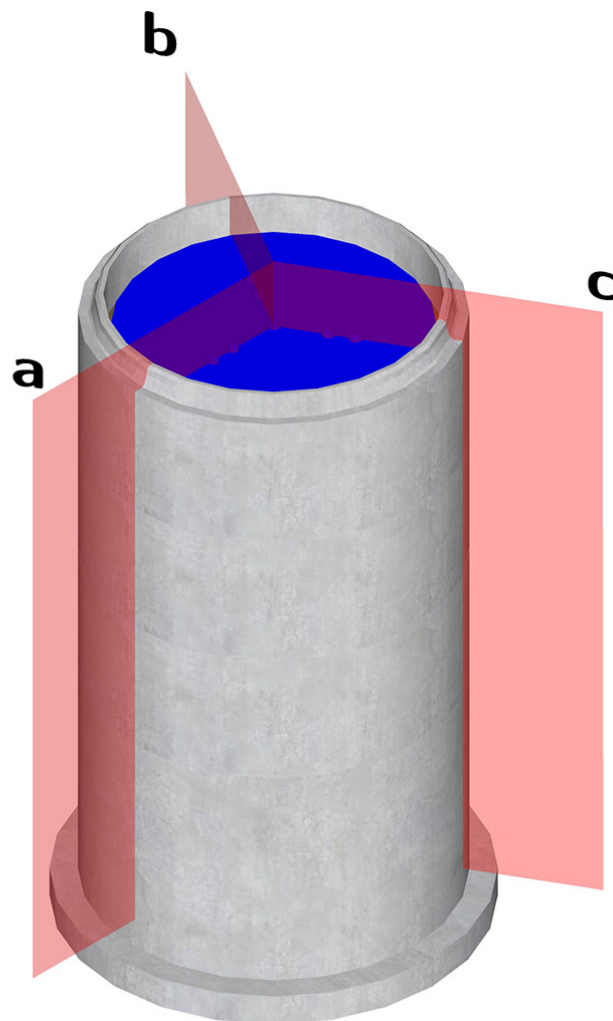
***Figure A**.43. Sections along the three directions.*

The layer profiles of the sections are presented in **Figure A**.**44**. Heights represents the final position of layering rather than the planned heights. The bottom of the dead weight plate was placed at height $h = 204.8cm$.
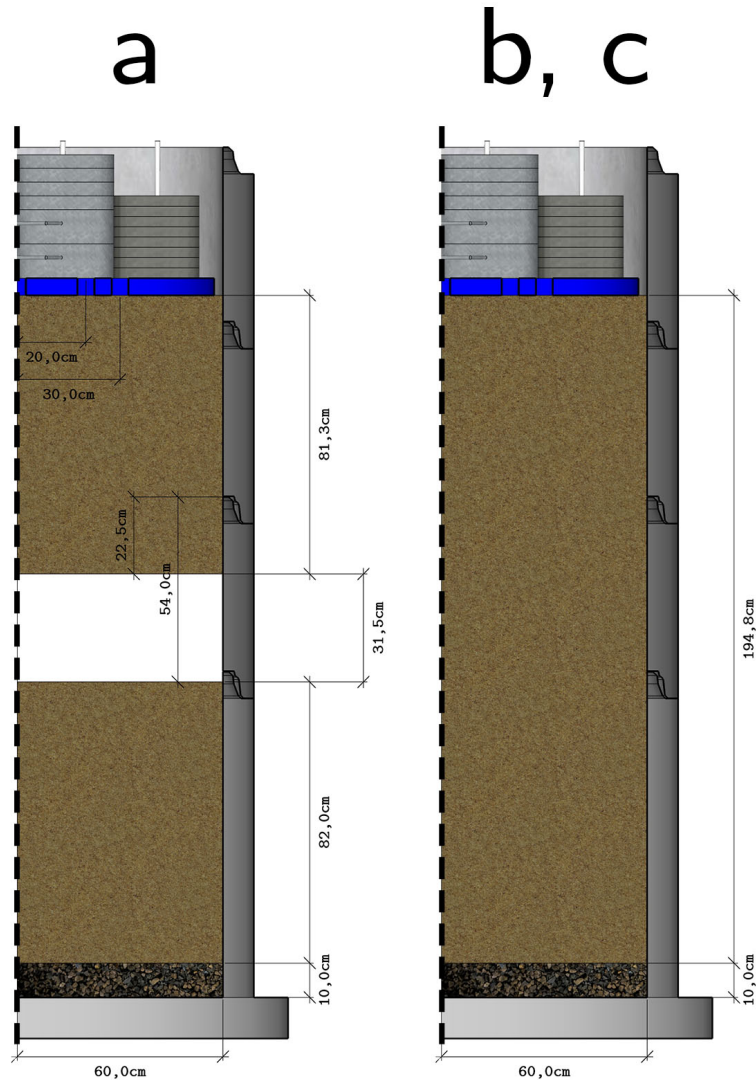
Figure A.*44*. *Section profiles of Case A.*

A.8.2 Sample preparation

In order to make a very loose sand sample it was decided not to compact the sand layers with the vibro plate. Only the first two stages of the previously presented sand layer preparation procedure were done, which were raining of moist sand and saturation. Sand was rained in with fill height of about $20cm$ increments, though the fill height is of little importance when no compaction was performed.

Clay blocks were cut to make layers of square shape with sides of $30cm$, as previously shown in **Figure A**.**34**. Three levels of these clay blocks were added on top of each other. The first two of

these had a height of $10cm$ with the third of height $11.5cm$, thus making the clay layer $31.5cm$ thick.

Before placing the clay layer, the water level was at 2-5cm below the top of the sand sample. The water management was at this time not complete, as it was presented in **Figure A**.**20**, as the system for letting water out was not made. Thus, the water level had to stay at this level. It was evident that this caused issues with compaction of sand directly under the clay. After the first level of clay blocks was placed there was an evident increase in water level, as shown in **Figure A**.**45**. The left image shows a green square cardboard of sides 30cm while the image to the right shows the three clay blocks. The shadow between the top left block and the next is due to the difference in settlement, of about $0.5cm$, as the top left block was the first to be laid down. 10cm of clay equals an added pressure of $2kPa$, and the loose sand promptly compacted after the blocks were placed.

Figure A.*45. Left: before clay layer is placed, with cardboard placeholder, Right: After the first three clay blocks were placed.*

In the end, settlements directly under the $31.5cm$ clay thick layer amounted to approximately $1cm$. Clay layers should preferably be made in a short amount of time until it is surrounded in water to avoid drying of the clay blocks. For this layer, there was a night in between level one and two were made. I order to minimize the drying, water was added to all air-exposed sides.

With the clay layer complete, the procedure of creating sand layers were repeated until the desired sample height was reached. The top of the sand was then shaped with a slope along the walls as explained in subsection **A.4.5**. A this point the water system was complete, which allowed for expulsion of water. The water level was lowered to about 10cm below the top of the sample before the dead weight plate was added. As expected, upon the addition of the dead weight plate large compaction of the top of the sample occurred. The dead weight place was carefully placed on top of the sample, the settlement caused by the added stress was $5.5cm$, as shown through the local

depth measurements in **Figure A**.46. The image to the left shows that before the dead weight plate was placed the top of the sample had a local depth of $z_L = 37cm$, while the it was $z_L = 42.5cm$ after (the measured value of $z_L = 40cm$ was the depth to the plate, which has thickness of $2.5cm$). The resulting height of the sample was then the height of the chambers used, which was $248cm$, minus the local depth at the top of $42.5cm$, which gives $h = 205cm$.

Figure A.46. *Compaction of top of sample due to the dead weight plate. Left: Before. Right: After.*

A.8.3 CPTU results

Three different positions were used to perform CPTUs in case A. Two of these were the outermost holes (3x) and one was the middle hole (2x). The order of the CPTUs were: 3c, 2b, 3a. Position 3a was the only test in a clay layer.

Some issues were experienced with the bore rig, causing sudden halts in penetration. In the following presentation of the CPTU results a line has been drawn excluding these stationary points, though all the measured points are presented.

The first test position, 3c, was tested twice in order to make some adjustments to the bore rig. The results of test A3a is presented in **Figure A**.47 while tests A3c, A3c2 and A2b are presented in **Figure A**.48.
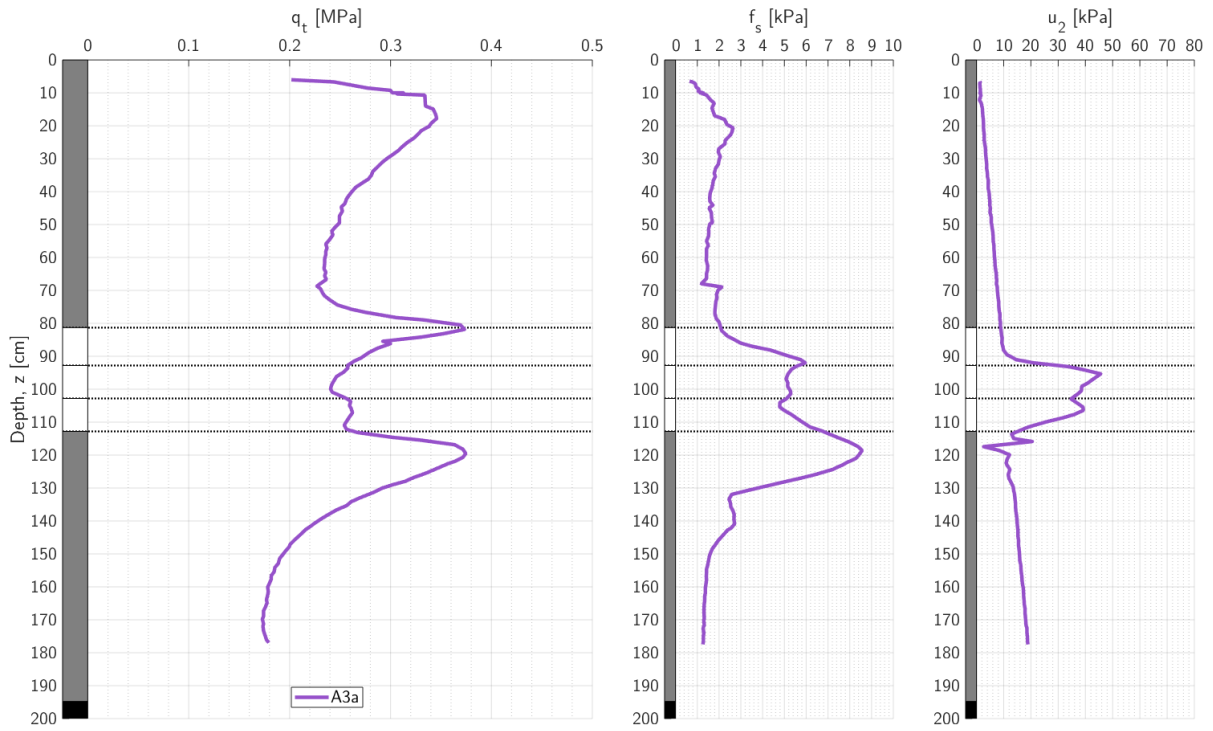
Figure A.47. CPTU A3a.
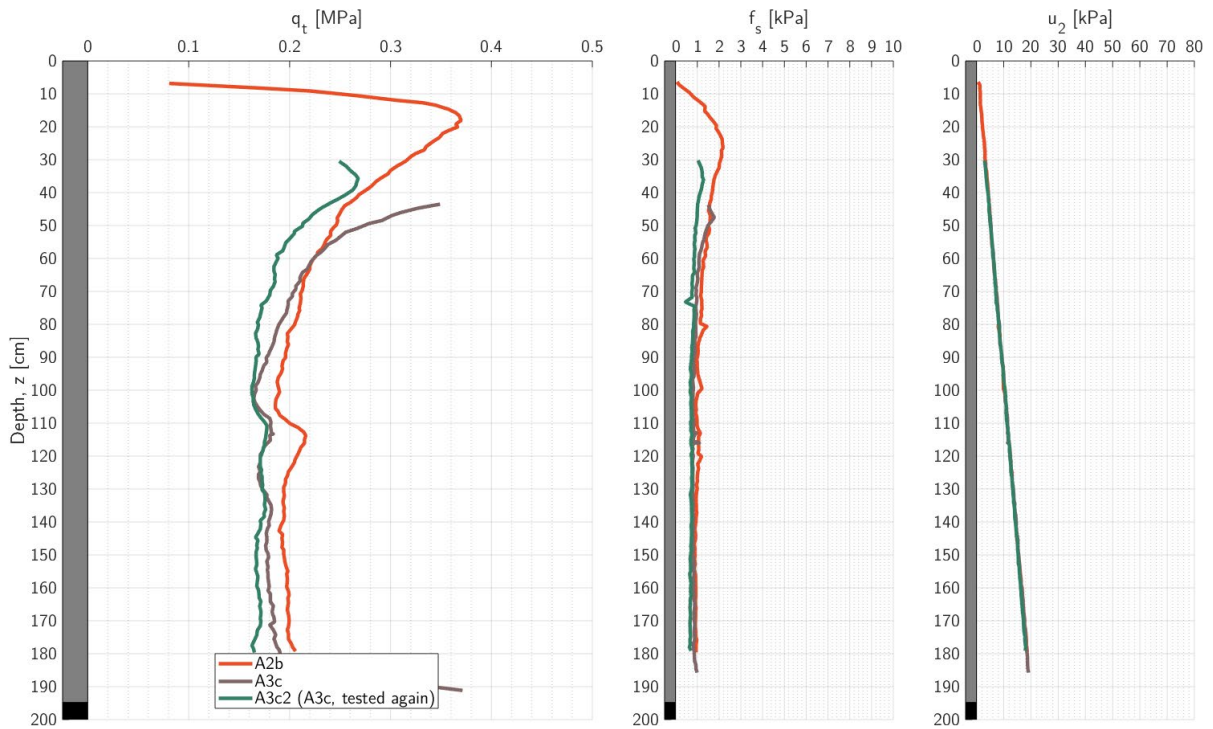
Figure A.48. CPTU A2b, A3c and A3c2.

Density measurements were taken continuously with depth. The measured values are presented in **Figure A**.**49** with its position. A few density samples were taken in center as well as along the three density sample positions presented in **Figure A**.**41**. Furthermore, at some positions, such as at depth $20cm$ and $100cm$, two measurements were taken in the same direction. These measurements were taken with at least 10cm distance and it was done to control the reliability of the density measurements.
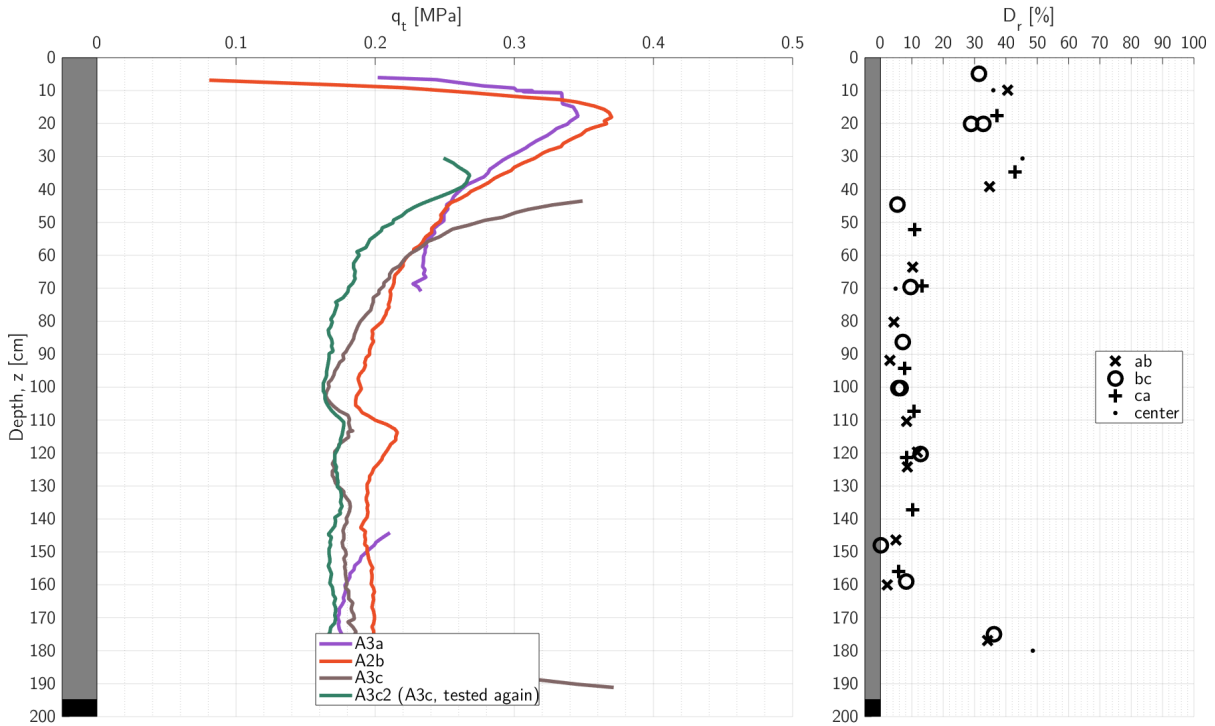
Figure A.*49*. *All Case A measurements in sand with relative density measurements.*

A.8.4 Images and comments

As previously mentioned, the sand directly under the clay layer settled by $1cm$ when it was placed. The clay layer further settled after this and until the sample was dismantled. **Figure A**.**50** presents images of the local depth at the top of the clay layer after it was placed and when it was excavated. A settlement of $3cm$ was measured. This could be due to the filling of sand over the clay layer, from the addition of the dead weight plate and from the penetration of the clay layer.

Settlements on top of the sample due to the addition of the dead weight plate was $5.5cm$, as noted above. The result of the compaction of sand on the top of the sample, as well as under the clay layer caused local increase in cone resistance during testing.

The minimum cone resistance measured in clay was about $0.24MPa$. Slight variations of cone resistance occurred in the three levels of clay layers. When the clay layer was studied during excavation, no sign of inhomogeneities or lack of contact between clay blocks were found (**Figure A**.**51**).

Figure A.50. Local depth of the top of clay layer. Left: When constructed. Right: When excavated.

1cm of clay removed

30.5cm

Figure A.51. Section cut of the 31.5cm clay layer of Case A. 1cm of clay was removed on the top of the sample.

A.9 Case B

The goal of the setup of the second sample was to discover the effects of layer thickness on the measurements. Layers of clay with different thicknesses were created within a sand sample that was created in a constant manner to achieve uniform properties.

A.9.1 Model setup

The three clay layers of thickness 4, 8 and $12cm$ were placed depending on the direction. The three levels of clay layers had a vertical distance of approximately $50cm$. This is about 14 cone diameters, which is assumed to be more than enough to avoid influence on the tip resistance of multiple clay layers at any depth. In order to determine a characteristic tip resistance profile in sand, only two of the three primary directions had clay layers at the same depth. The clay layers were made according to *2 directions* (**Figure A**.**34**). Layering profiles of the three sections are shown in **Figure A**.**52**.
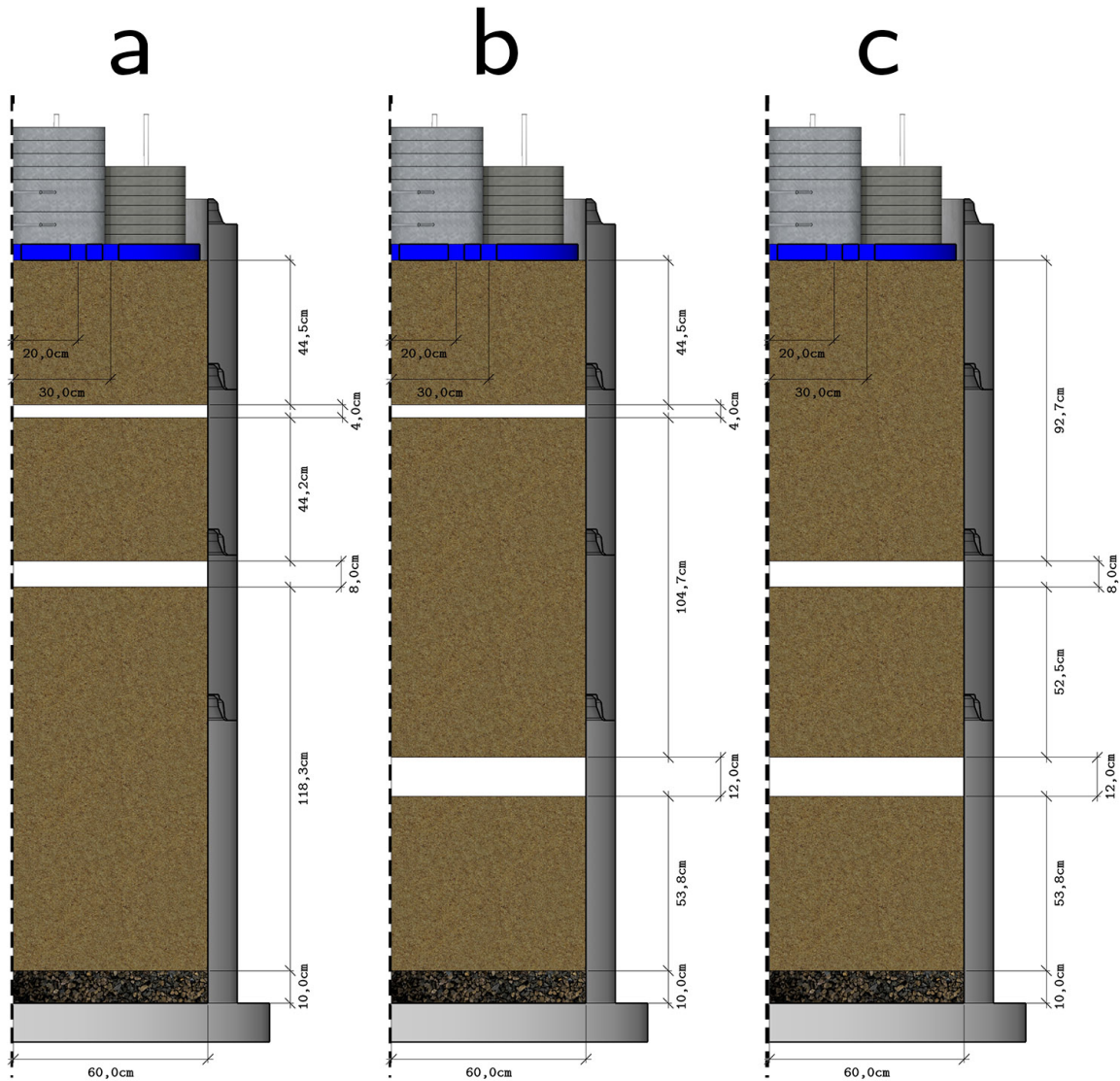
Figure A.*52*. Section profiles of Case B

A.9.2 Sample preparation

The sample was prepared through about 20 sand layers which were made through the three stages of raining, saturation and compaction. Each layer had a fill height between 10 and 20cm.

Heights of the sample was measured during the three stages of preparation of almost every layer. From this, the fill height (Δh_f), "saturation strain" $\left(\frac{\Delta h_s}{\Delta h_f}\right)$ and "compaction strain" $\left(\frac{\Delta h_c}{\Delta h_f - \Delta h_s}\right)$ was estimated. The values are presented in the two graphs in **Figure A.53**. The heights of the clay layers are included in the graph of the fill height as it for example explains that a fill height of 21cm was added at height $h = 64cm$ due to the 12cm thick clay layer at the same height.

The measurements of the approximated strain are merely an indication of the effects of the saturation and vibro compaction. Low settlements occurred for two of the layers close to the top (height 190 and 197cm). An explanation of this was that the sand filled in at these sand layers were fairly dry, thus causing a denser state when rained.
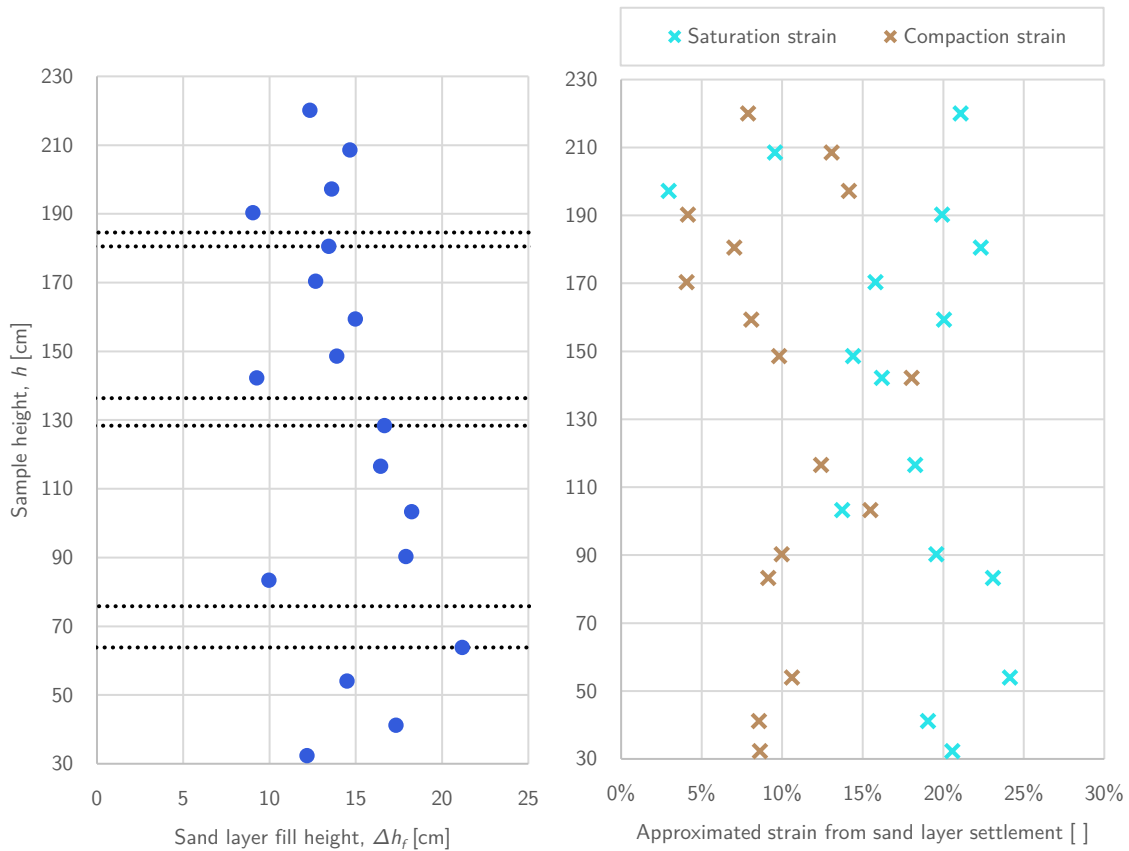
Figure A.53. Graphs on the preparation of sand layers in Case B

The three clay layers were prepared as previously described. Each clay layer had a shape as shown in **Figure A.54**. Marginal settlements were caused by the addition of the dead weight plate (**Figure A.55**). An image of the full setup during testing of the sample case is presented in **Figure A.56**.
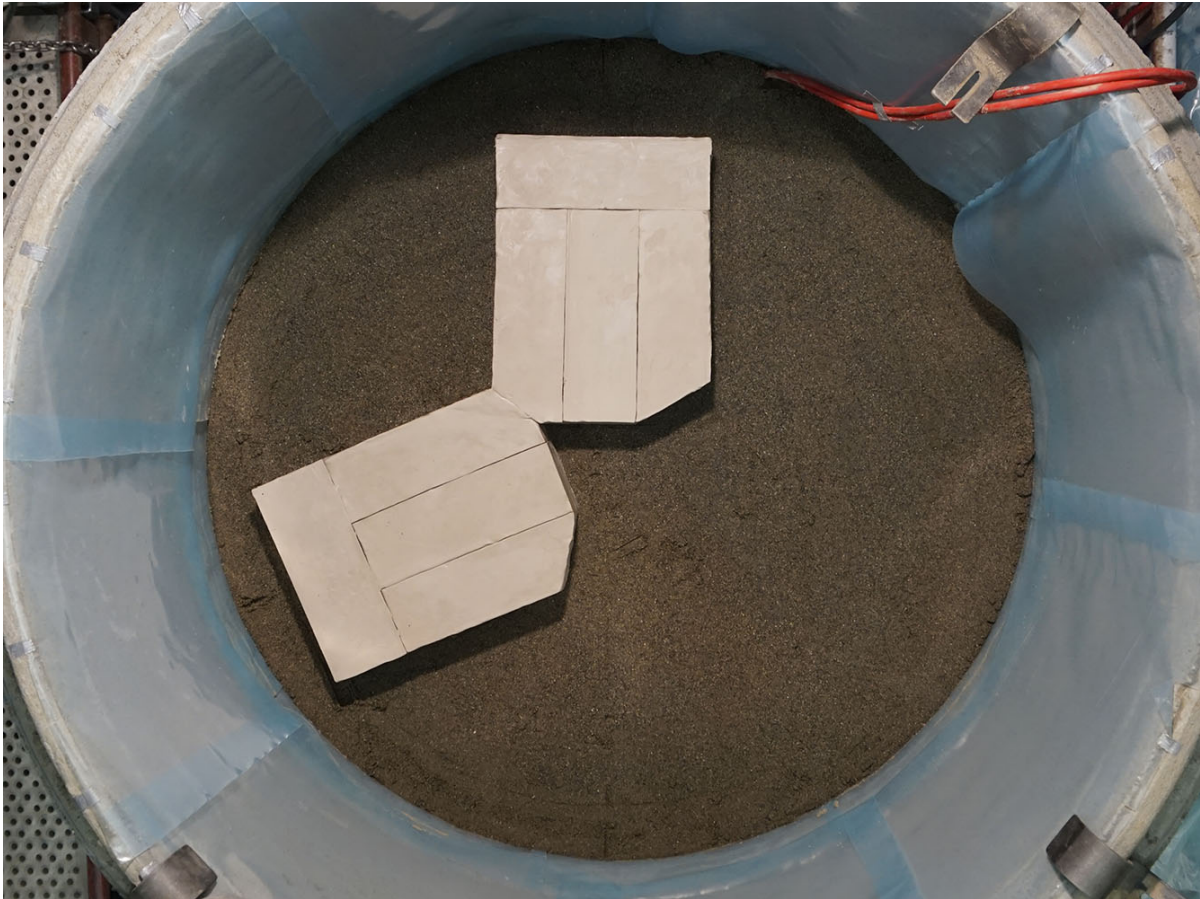
Figure A.**54**. *Image of the 8cm thick clay layer at direction a and c*
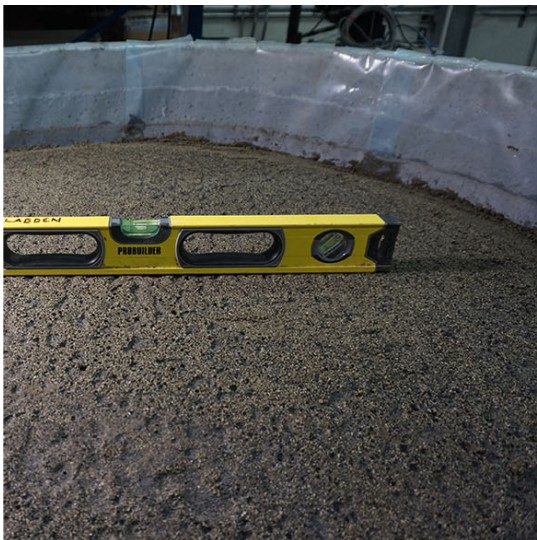
Figure A.**55**. *Left: Levelled surface on top of sample. Right: Added dead weight plate*

Figure A.56. Image of the chamber, platform and bore rig

A.9.3   Stress state

Two earth pressure sensors were installed, one at height $h = 34cm$, called sensor 1, and a second at height $h = 54cm$, sensor 2 (**Figure A**.**57**)

Figure A.57. The local depths of the two earth pressure sensors in the sample

The earth pressure sensors were carefully placed, ensuring proper contact between sand underneath and on top of the pressure cell. Furthermore, the sensors were calibrated by adding dead weights that properly covered the pressure cell. This was done both before and after they were placed in the sample. It is therefore expected that the measurements are correct.

The recorded stresses from the two earth pressure sensors as well as the recorded water pressure (u_0) at depth $h = 0$ is presented in **Figure A**.**58**. Vertical dashed lines are placed at the time after the compaction of a layer was finished. The height of the finished sand layer is presented next to the vertical line. The measured stress at this point, of a completed layer is presented with a circular marker. A vertical red dashed line marks the time when the dead weight plate was added.

From these measurements, the stress state at the center of the sample was interpreted. The representative stresses could then be compared to the stresses that would occur if no silo effects were present, as presented in subsection **3.1.2**.

$$\sigma_v = \gamma' \cdot (h - h_{sensor}) + \gamma_w \cdot (h_w - h_{sensor}) + \Delta\sigma'_v \qquad \text{(A.15)}$$

The effective unit weight, $\gamma' = \gamma - \gamma_w$, is equal to $(\rho - \rho_w) \cdot g$ (where g is $9.82 m/s^2$) and ρ depends on the relative density, as presented in **Figure A**.**6**. Assuming a relative density of 30%, the unit weight of fully saturated soil is expected to be $19.4 kN/m^3$. The effective unit weight is $9.6 kN/m^2$ as the unit weight of water is $\gamma_w = 9.8 kN/m^3$.
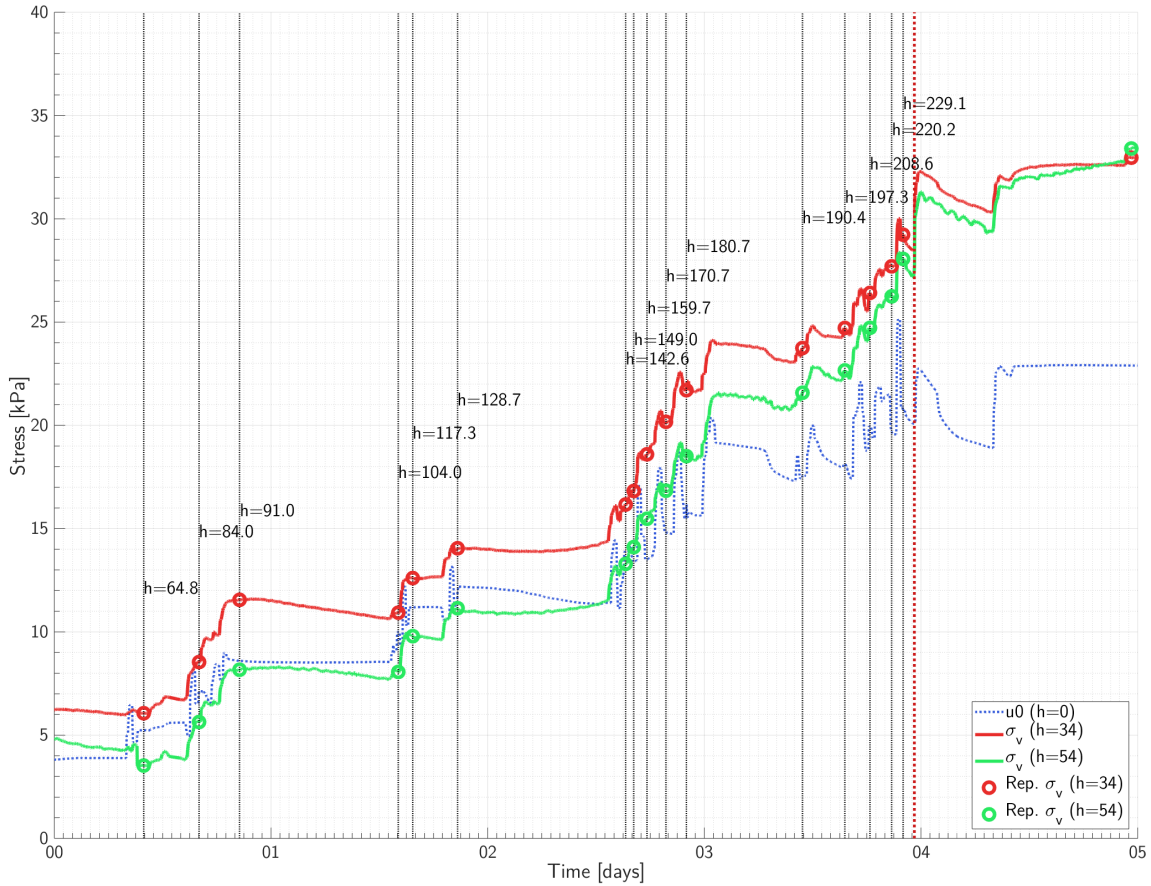
Figure A.*58. Log of stresses from the sensors recorded while constructing the sample*

Figure A.**59** presents the measured vertical total stresses from the two sensors against the values without silo effects (from equation (**A.15**)). The measurements after the dead weight plate was placed on top of the sample also included. These values have estimated vertical stresses without silo effects of the weight of the soil plus the distributed weight of the he dead weight plate, which is $11.4 kPa$. Note that there are two measurements from each of the sensors after the dead weight plate was added, and the explanation is found in **Figure A**.**58**. After the dead weight plate was added, which is presented with the vertical dashed line, there is an instant increase of stress in each of the sensors. Then there is an apparent decrease, however, that is due to the decrease in pore pressure. After the water level is raised and stabilized at $u_0 = 23 kPa$ ($h_w = 230 cm$) the stresses in both sensors increases, though sensor 2 increases more than sensor 1. The two measurements the stresses immediately after the load was applied and after 24 hours, as presented in the figure.
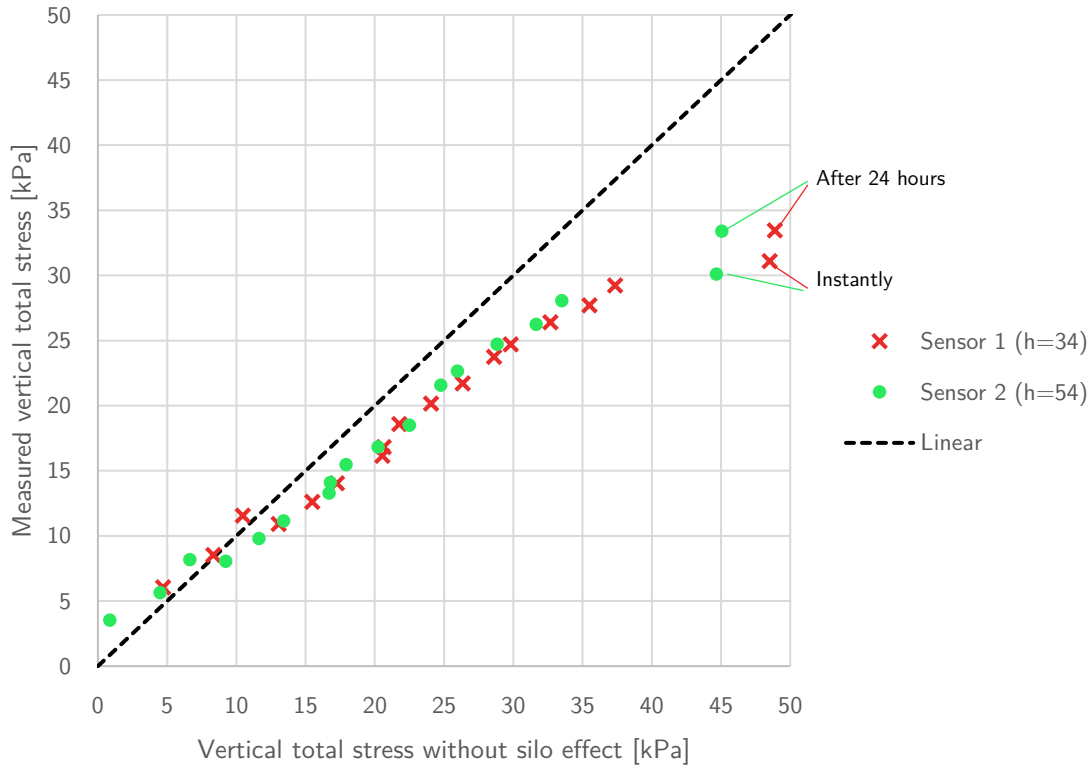
Figure A.*59. Measured stresses vs. expected stresses without silo effect*

The estimation of vertical stress was done according to the silo effects, as presented in subchapter **3.1.2**. The vertical total stress is the sum of the effective stress and pore pressure. The vertical effective stress has a limited maximum value which was defined as the decay length, l, multiplied by the effective unit weight, γ'.

$$\sigma_v = \gamma' \cdot l \cdot \left(1 - \exp\left(-\frac{z}{l}\right)\right) + \gamma_w \cdot z \tag{A.16}$$

The decay length depends on the chamber diameter, D_c, the earth pressure coefficient, K, and the soil-wall friction coefficient $\tan(\delta)$. Assuming a relationship of $K \cdot \tan(\delta)$ of 0.18, which for instance is the case for values of $K = 0.5$ and $\tan(\delta) = 0.36$ the decay length, l, becomes:

$$l = \frac{D_c}{4 \cdot K \cdot \tan(\delta)} = \frac{1.2m}{4 \cdot 0.18} = 1.67m \tag{A.17}$$

Using the decay length of $1.67m$, equation (A.16) is presented together with the measurements in **Figure A**.**60**. This relationship seems to fit the measured data well. Note that this stress state is estimated purely due to self-weight of soil and without the dead weight plate, therefore the measurements marked in the circle should not be expected to fit the estimated stress.
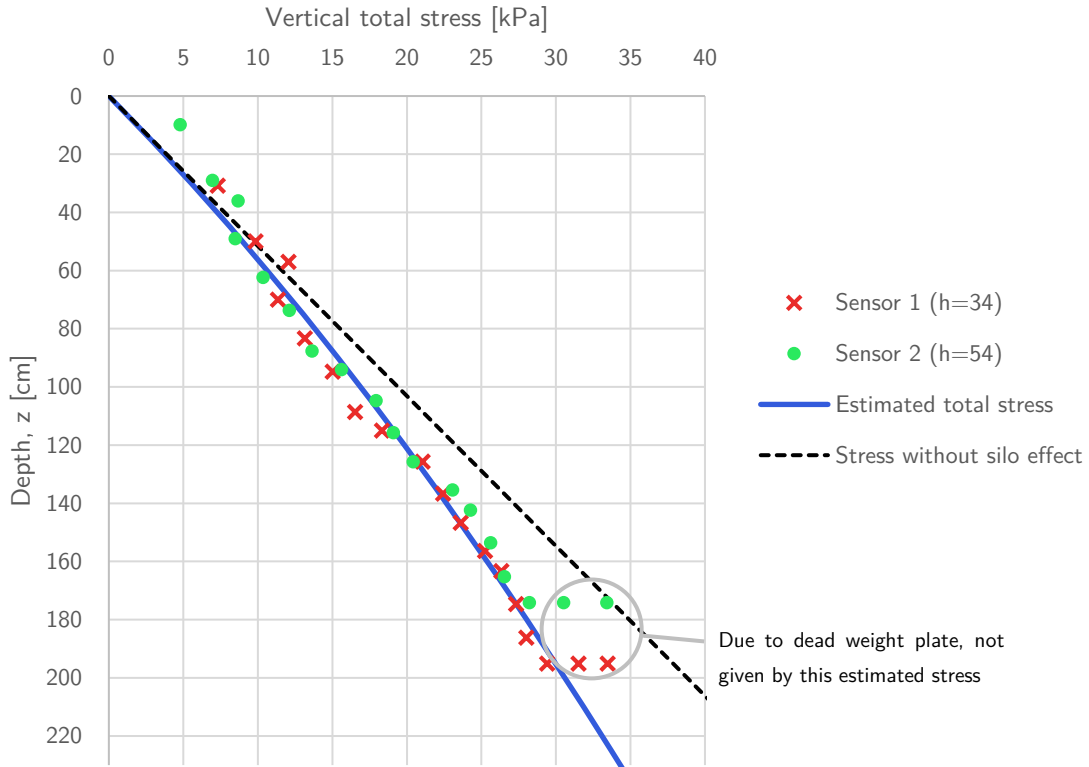
Figure A.**60**. *Estimated vertical stress due to silo effects with the measured stresses*

The vertical stress including the dead weight plate was then estimated, where the increase at the top of the sample was given by $\Delta\sigma'_{v1} = 11.4 kPa$. The vertical effective stress increase with depth due to the added stress at $z = 0$ was given by:

$$\Delta\sigma'_v = \Delta\sigma'_{v1} \cdot \exp\left(-\frac{z}{l}\right) \tag{A.18}$$

This is effectivity the same pretending that an additional amount of sand, with and height of Δz, was added on top of the sample which then gives and increased effective stress at $z = 0$:

$$\sigma'_v(z=0) = \gamma' \cdot l \cdot \left(1 - \exp\left(-\frac{\Delta z}{l}\right)\right) = 11.4 kPa \tag{A.19}$$

where Δz would be defined by;

$$\Delta z = -l \cdot \ln\left(1 - \frac{\Delta\sigma'}{\gamma' \cdot l}\right) = -1.5m \cdot \ln\left(1 - \frac{11.4 kPa}{14.1 kPa}\right) = 2.48m \tag{A.20}$$

Adding the dead weight plate, which results in a $11.4 kPa$ effective stress increase on top of the sample is in other words estimated to be equal to two and a half meters of fully saturated sand in this chamber. However, the calculated stress using this method gives the same as using equation

(A.18). Furthermore, the method presented in equation (A.20) is limited to stress increases lower than the effective unit weight times the decay length, i.e. $\Delta\sigma'_v \leq \gamma' \cdot l$.

The following formula was then used to describe the vertical total stress after the dead weight plate was added:

$$\sigma_v = \gamma' \cdot l \cdot \left(1 - \exp\left(-\frac{z}{l}\right)\right) + \Delta\sigma'_{v1} \cdot \exp\left(-\frac{z}{l}\right) + \gamma_w \cdot z \tag{A.21}$$

The estimated vertical total stress after the dead weight plate was added is included in **Figure A**.**61**. Comparing the resulting total stress with the actual measurements indicates a good fit, as the estimated stress is between that of the immediate and longtime stress level at both depths.
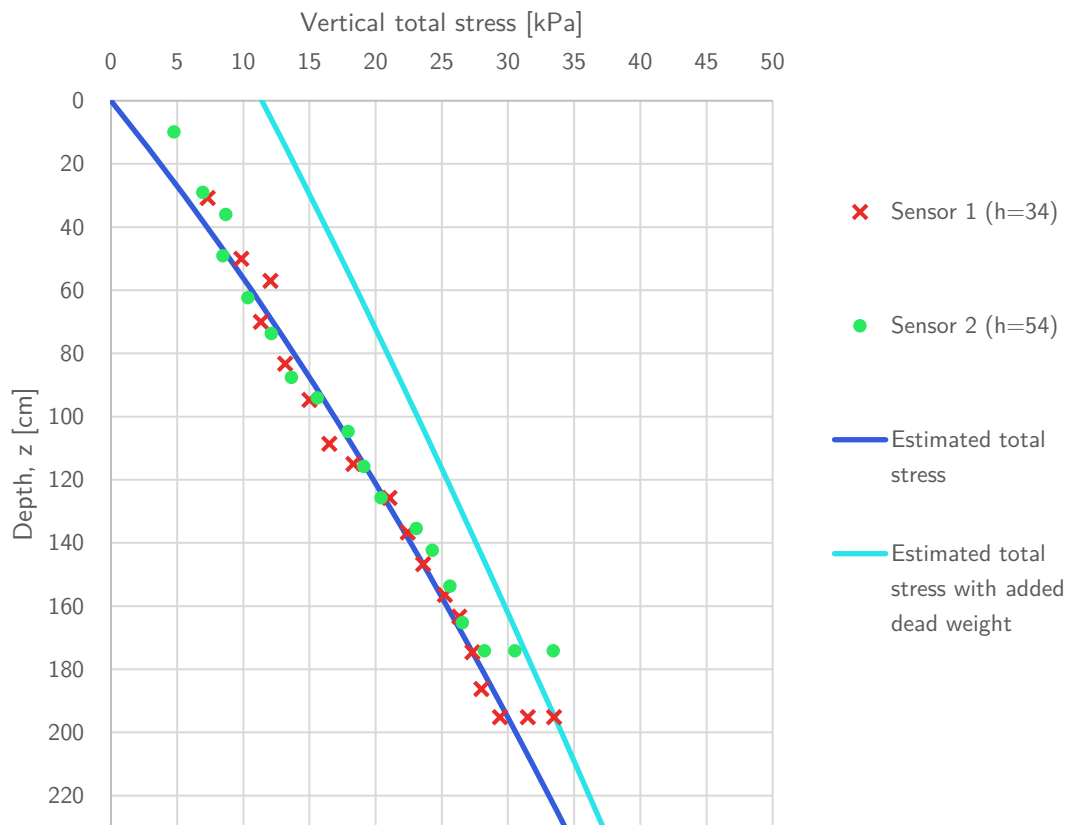
Figure A.**61**. *The total stress with and without the dead weight plate, together with measurements.*

Using this as the estimated vertical total stress level in the sample, the vertical and horizontal effective stresses were calculated. The values of σ_{v0}, σ'_{v0}, u_0 and the mean effective stress, p', are presented in **Figure A**.**62**. An earth pressure coefficient of 0.5 is still assumed. To emphasize the importance of taking silo effect into account, the stresses without silo effects (w/o SE) are included.
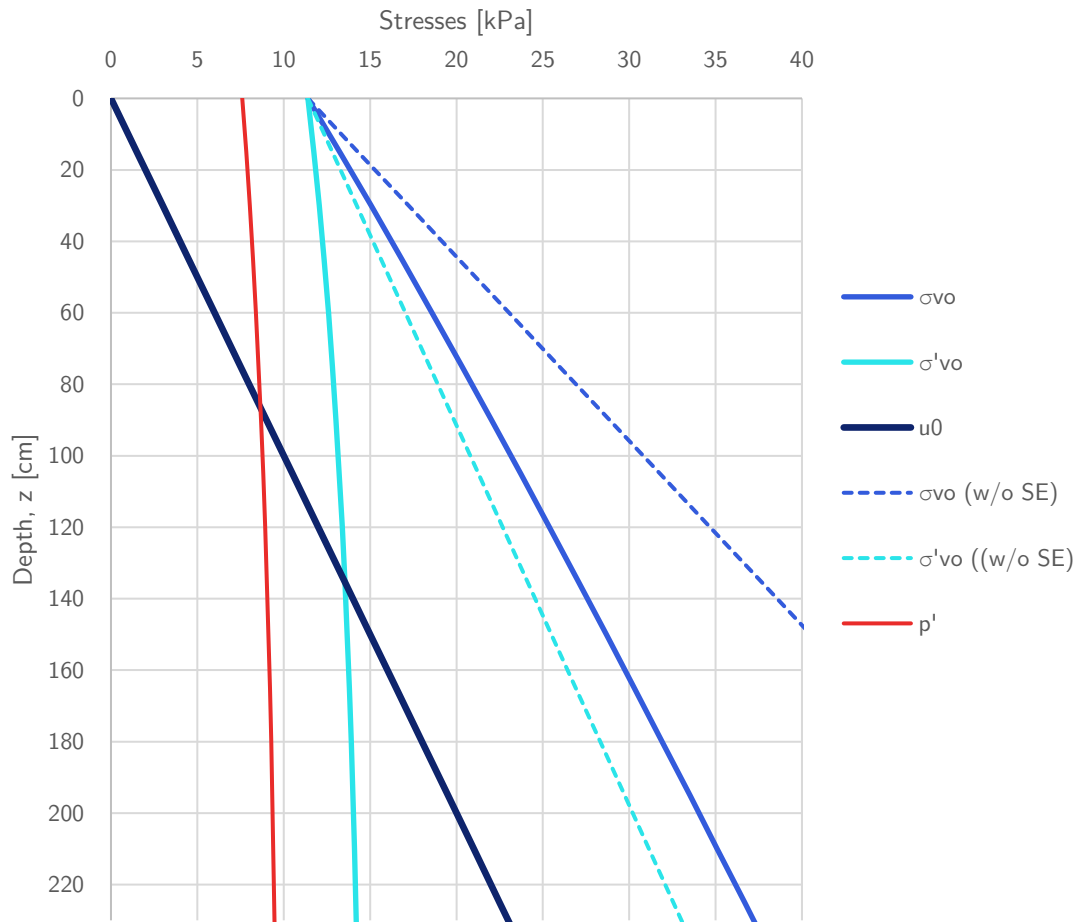
Figure A.*62. Estimated stress state of the sample of Case B*

A.9.4 CPTU results

Six CPTUs were performed in the sample of Case B. These were, in the order of execution 3c, 2b, 2a, 3a, 2c, 3b. The measurements of direction a is presented in **Figure A**.**63**, direction b in **Figure A**.**64** and direction c in **Figure A**.**65**. Similarly as for the results of Case A presented above, all measured points are presented in the figures. All measurements are presented together in **Figure A**.**66**.

The results of cone resistance for the two tests in the same direction gave the same variations in sand, however, the maximum values were much lower for the second test in each direction. The first tests, i.e B3c, B2b and B2a, are therefore considered to be the representative tests, while the second round (B3a, B2c and B3b) are considered only as controls of variations.
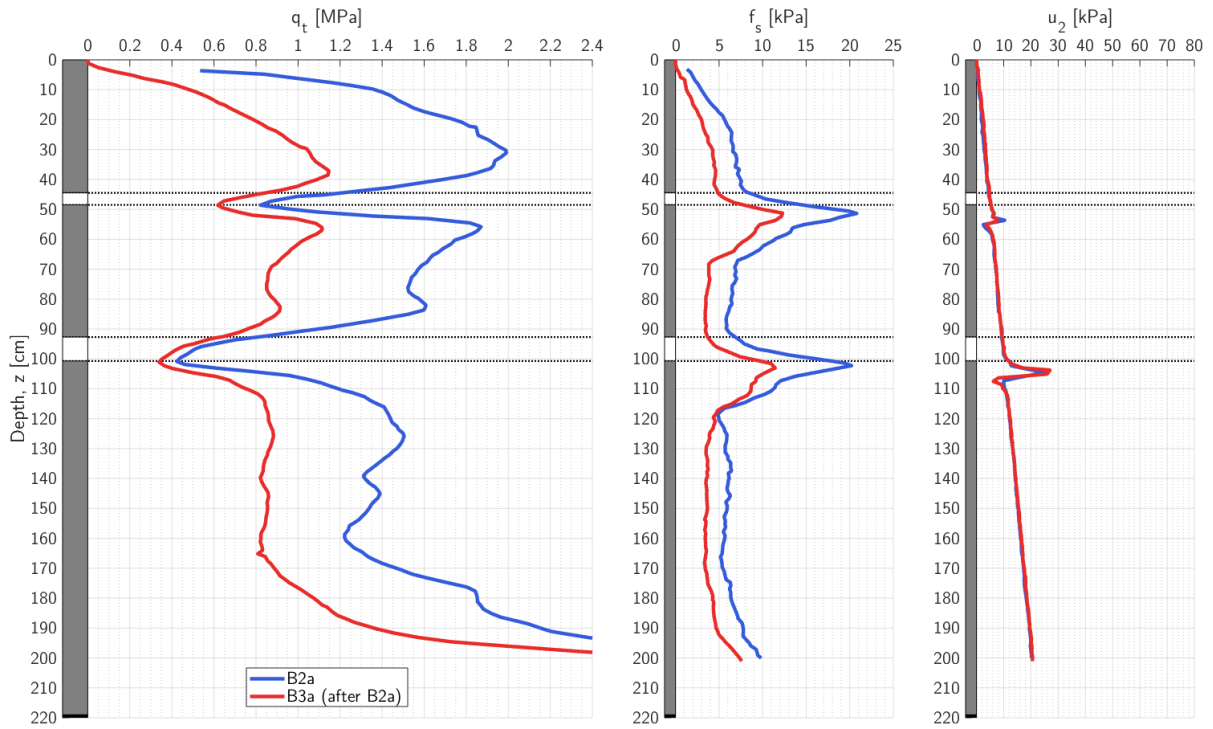
Figure A.63. Case B CPTUs of direction a.
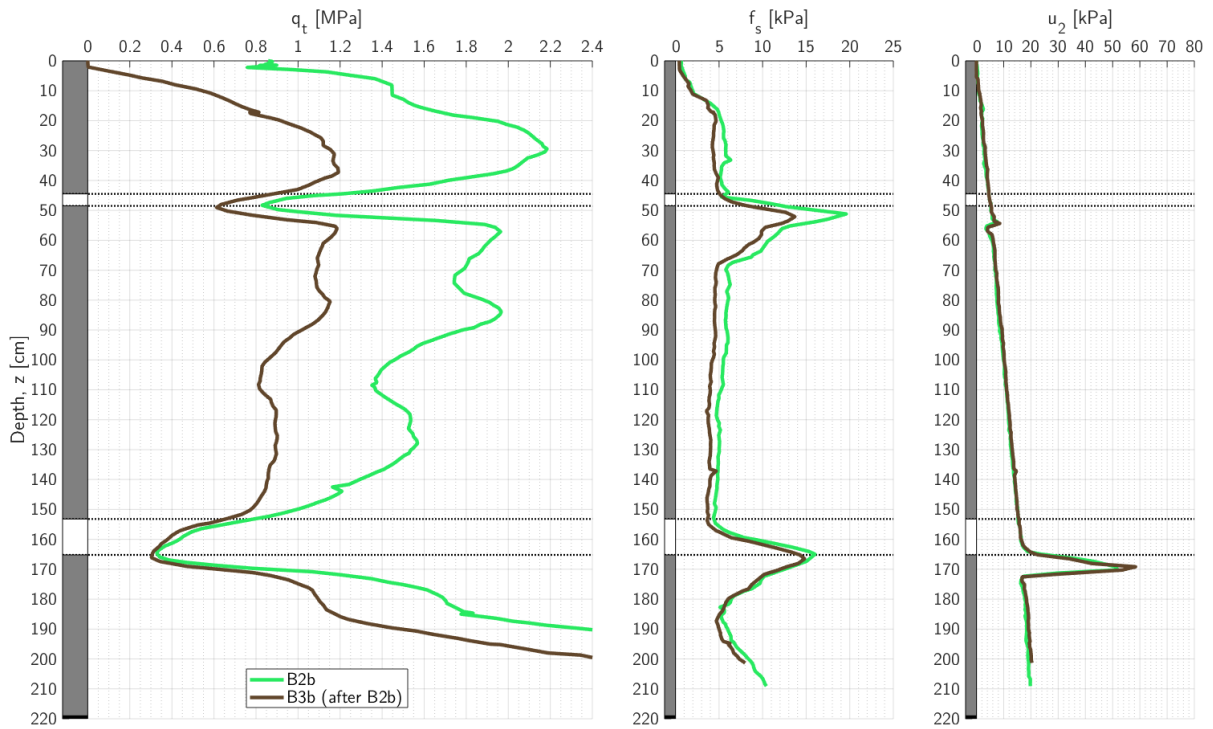
Figure A.64. Case B CPTUs of direction b.
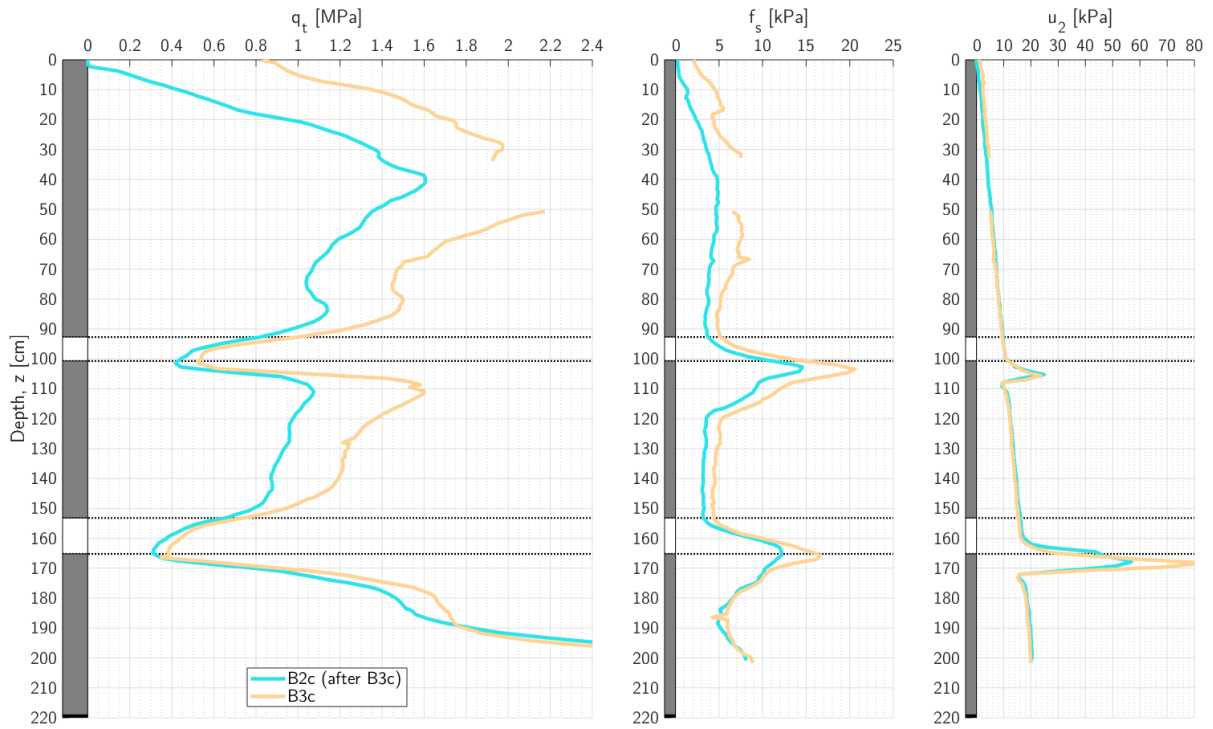
Figure A.65. *Case B CPTUs of direction c.*
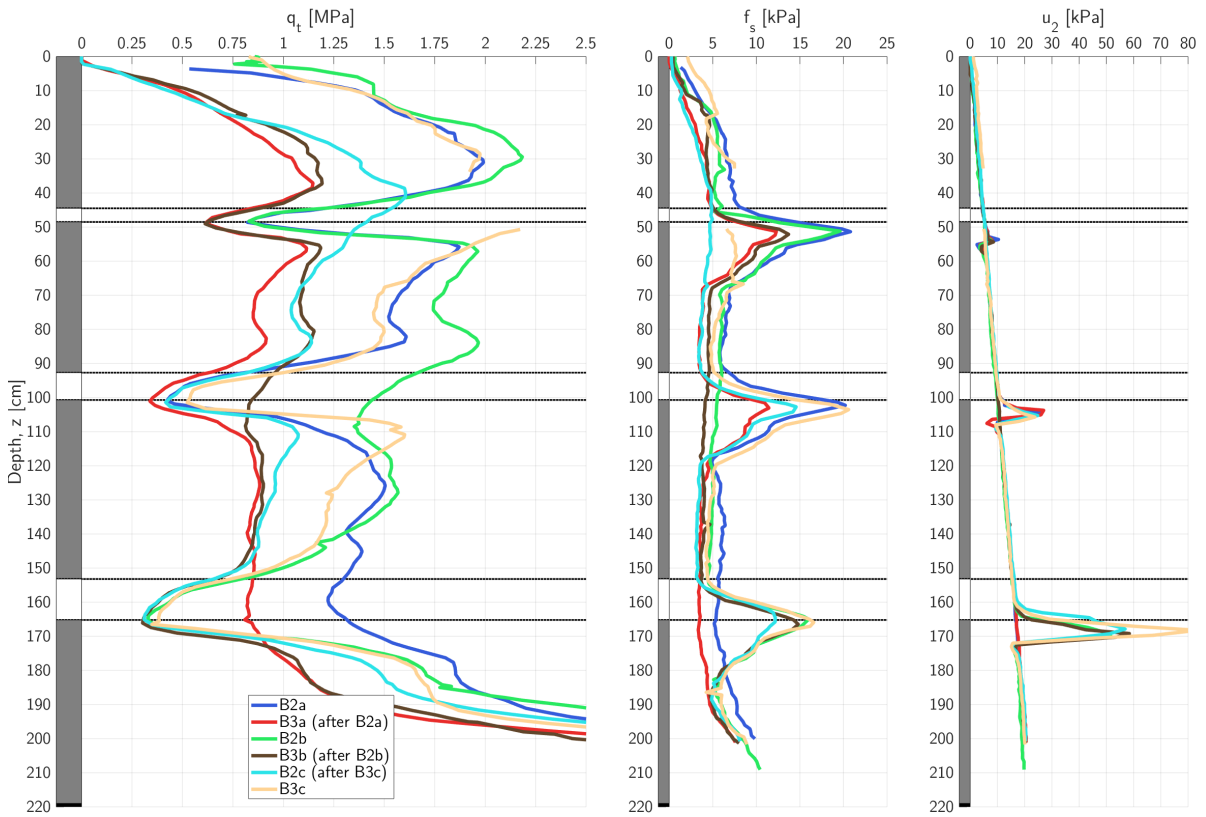
Figure A.66. *All case B CPTUs combined.*

Figure A.**67** presents the cone resistance of all the tests where the measurements in clay layers are removed. Density measurements were taken continuously with depth during dismantling and the measured relative density from the excavation is also included. The positions of the relative density measurements are given according to **Figure A**.**41**. Horizontal lines in **Figure A**.**67** represents the heights of the completed sand layers. Some variations in cone resistance in sand can be attributed to different density of the different sand layers.
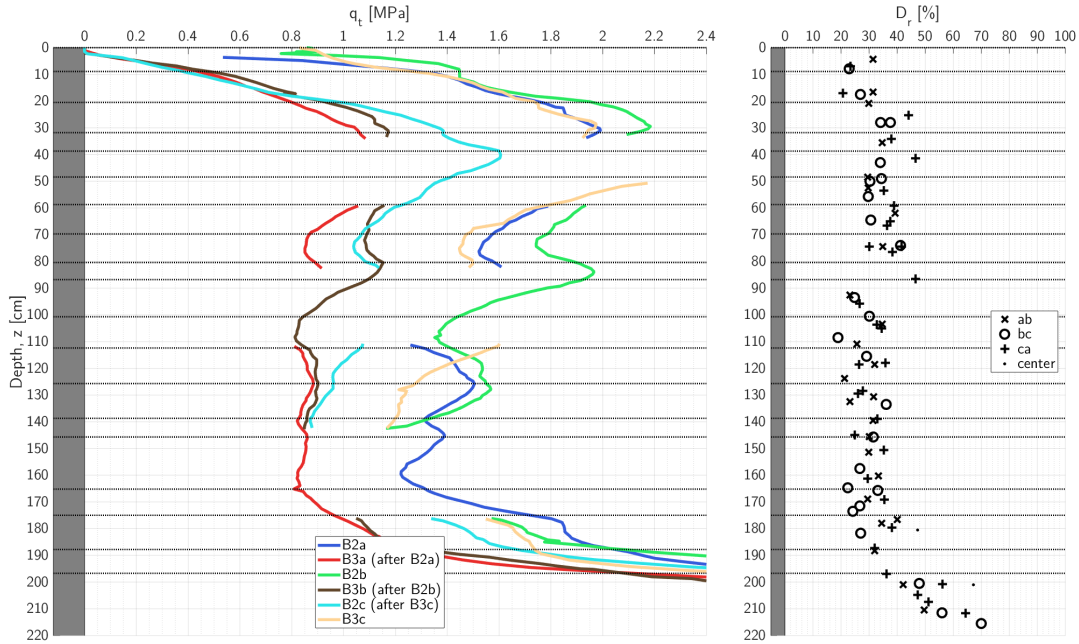

Figure A.*67*. *All Case B measurements in sand with relative density measurements*

A.9.5 Images and comments

Figure A.**68** presents an image from when the sand was excavated, and spherical voids were seen in the sand. This was likely the result of the vibro compaction of sand where some transportation of fines occurred. The water level, h_w, during compaction is believed to influence this.

Figure A.*68*. *Local spherical voids in the sand.*

An image of the 4 and $8cm$ clay layers are shown in **Figure A**.**69**. The large deformation in the clay layers are shown here. The size of the clay layers of 30 by $40cm$ appear to be enough to avoid rotation of the sides of the clay layers. **Figure A**.**70** show an image of the sand directly under a clay layer with lines representing the deformed shape visually. The clay layers were deformed only to about $10cm$ from the CPTU positions.
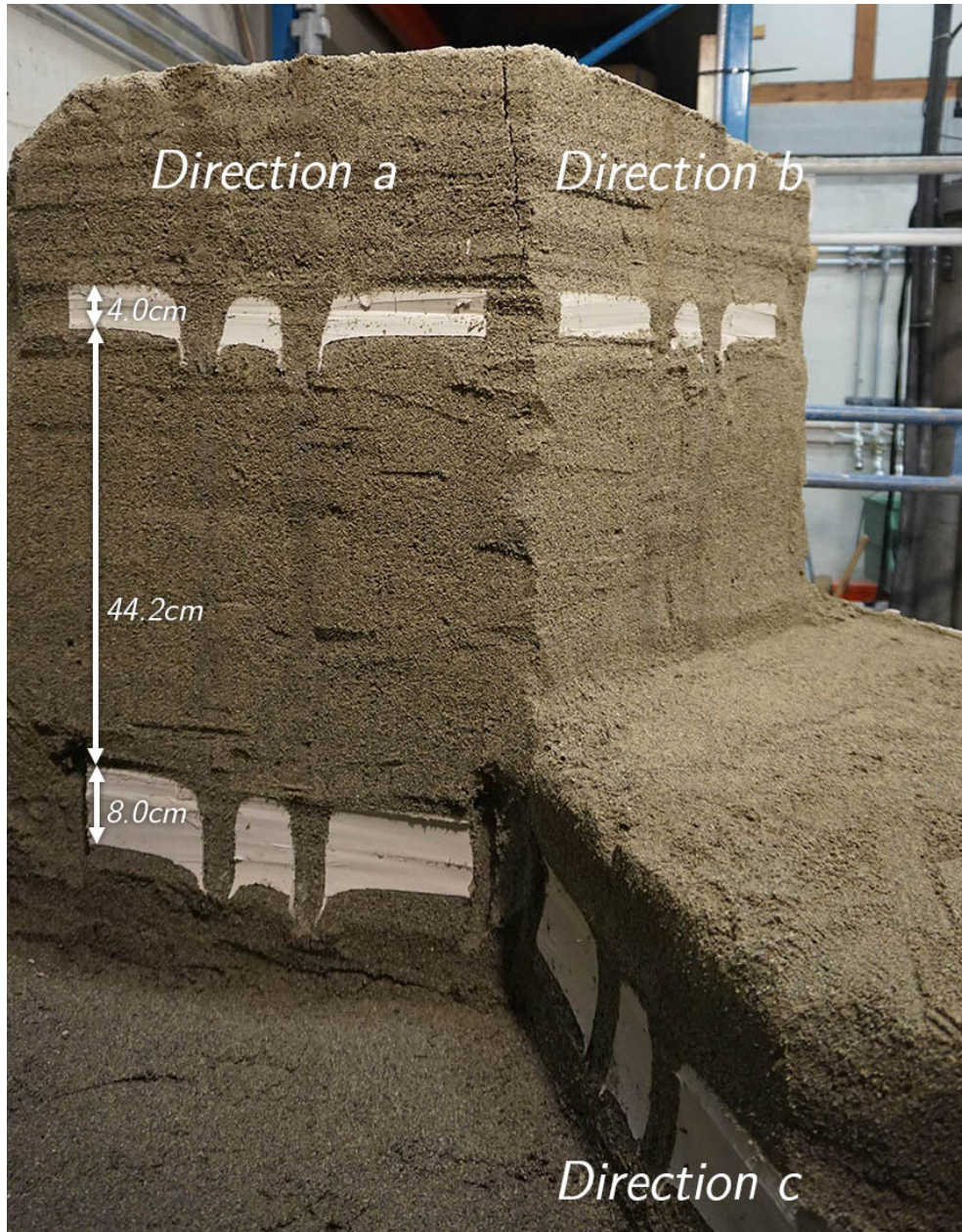
Figure A.*69*. *Image of the 4 and 8cm thick clay layers. Directions are presented in the picture.*
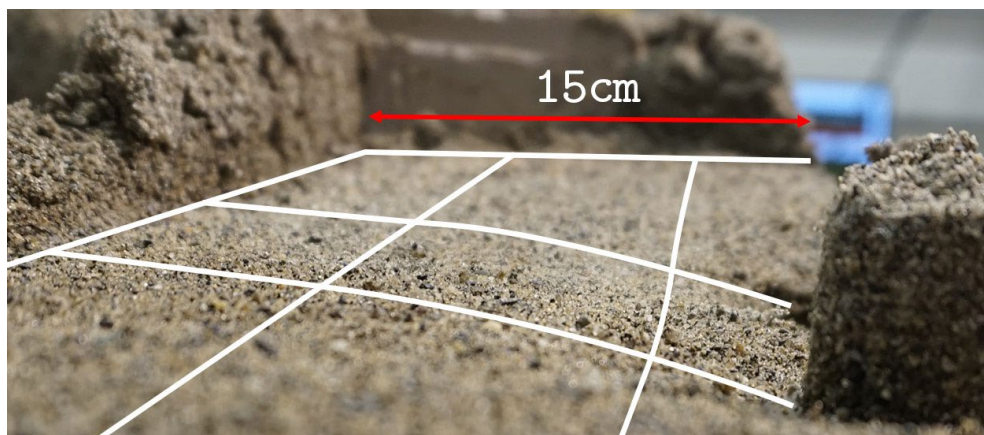
Figure A.*70*. *Image with illustration of the deformation under a clay layer*

B PROCEDURE FOR LAYERING EFFECTS ANALYSIS

This appendix contains the description of a method of cone resistance analysis in layered profiles. The method intends to determine a "measured" cone resistance profile through advanced averaging, or weighting, of values in a characteristic cone resistance profile. It is based on the inverse filtering procedure developed by Boulanger and DeJong and presented at the CPT'18 conference (2018). The article is hereafter referred to simply as *the original article*, while the procedure presented in the article is referred to as the *original procedure*.

Figure B.**1** presents an illustration of a characteristic cone resistance profile, q_t^{char}, with two predicted measured cone resistance profiles, q_t^m. One of these is from the original procedure using the baseline control parameters. The other is from the procedure developed in this study. The terms and symbols from this study is used rather than from the original article.
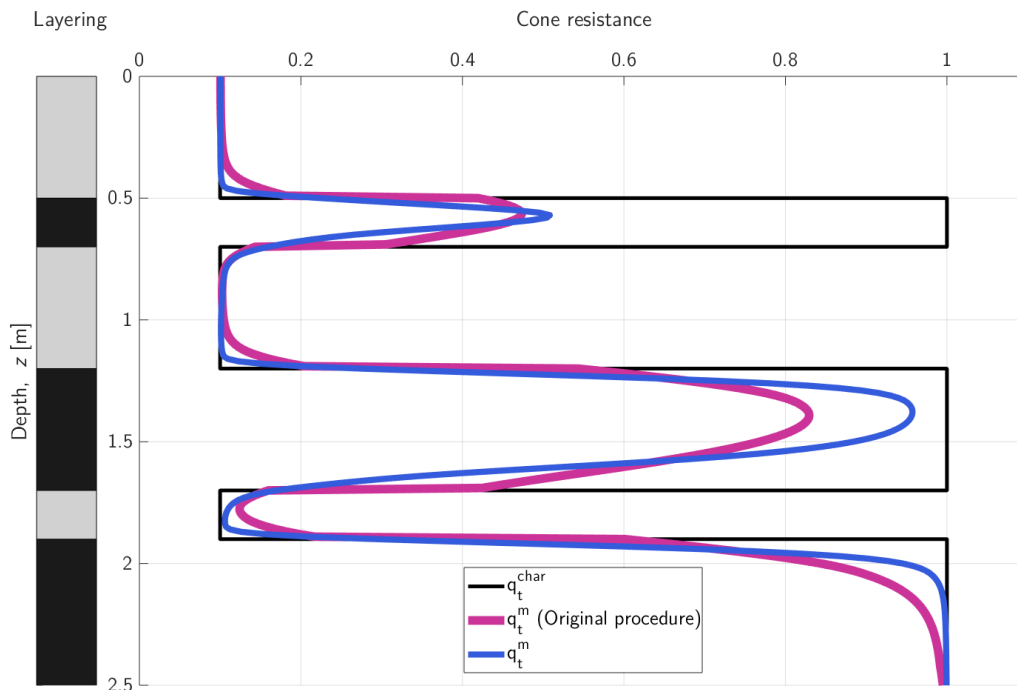

Figure B.***1***. *Illustrational characteristic profile, q_t^{char}, with two different measured profiles, q_t^m, from the original procedure and the procedure of this study.*

This layered profile is assumed to consist of clay with cone resistance of 0.1 and sand with cone resistance 1. The unit is not included since none of the procedures depend on it. However, a unit of MPa can be used for these values to correspond to likely characteristic cone resistance in clay and sand. While the original procedure does not have any parameters that may differentiate between different soils, the developed procedure includes input values that allow for differentiation of the behavior of clay and sand. This will be described in subsection **B.2.2**.

The maximum values of the profiles in **Figure B**.**1** are not of essence – it depends on the parameters selected. However, there are important features that favors the procedure presented of this study.

These are firstly the lack of distinct jumps in the profile. The original procedure contains dependencies of relative values of cone resistance which causes sudden jumps in the profile at interfaces. Secondly, while the original procedure considers all soils to be equally dependent of the soil ahead of the cone compared to that of behind the cone, the developed procedure allows to differentiate between these dependencies. I.e., some soils can for instance be more dependent on the soil behind the cone than in front of the cone. This is labeled *sensing* or *development distance dominated* in the discussion of the current study. Notice how the profile from this study (blue) has long sensing distance in sand and short sensing distance in clay. The original profile, on the other hand, is sensing dominated in both types of materials.

The inverse filtering procedure from the original article is briefly presented in the first section, however, the original article should be read for full detail on the procedures. Next is a presentation of the method in determining the weighting filter where the original procedure is presented first followed by the procedure developed in this study. Note that the explanation of the procedure is done in an efficient rather than intuitive way. The procedure is visualized through the parameter study and application in the following sections. Section three describes methods to visualize layering effects. The last section is a parameter study of the parameters in the developed procedure. Parameters are then selected based on three cases of physical experiments of thin clay layers in sand.

B.1 Inverse filtering procedure

The predicted measured profile presented in **Figure B**.**1** is only a component of the inverse filtering procedure. The goal of the inverse filtering procedure is to determine the characteristic cone resistance profile from a measured profile. Simplified, the procedure intends to discover the cone resistance profile of a cone penetrometer with a diameter approaching zero, if effects of cone diameter to grain size is ignored. An example of an inverted profile is presented in **Figure B**.**2**. The measured profile is one of the CPTU presented in **Figure 2**.**3**, from a layered deltaic deposit. The article summarized the procedure in three primary components:

> *(1) a model for how the cone penetrometer acts as a low-pass spatial filter in sampling the true distribution of soil resistance versus depth,*
>
> *(2) a solution procedure for iteratively determining an estimate of the true cone penetration resistance profile from the measured profile given the cone penetration filter model, and*
>
> *(3) a procedure for identifying sharp transition interfaces and correcting the data at those interfaces.*

The inverse filtered profile in **Figure B**.**2** was the result of these three components. Component (1) presents the spatial filter which is used to determine the predicted measured profiles of **Figure B**.**1**, which transforms a characteristic profile to a predicted measured profile. Only this component is considered in this study, though a very brief summary of component (2) is presented below. The

inverse filtering procedure only depends on the measured cone resistance profile with depth and the given control parameters.
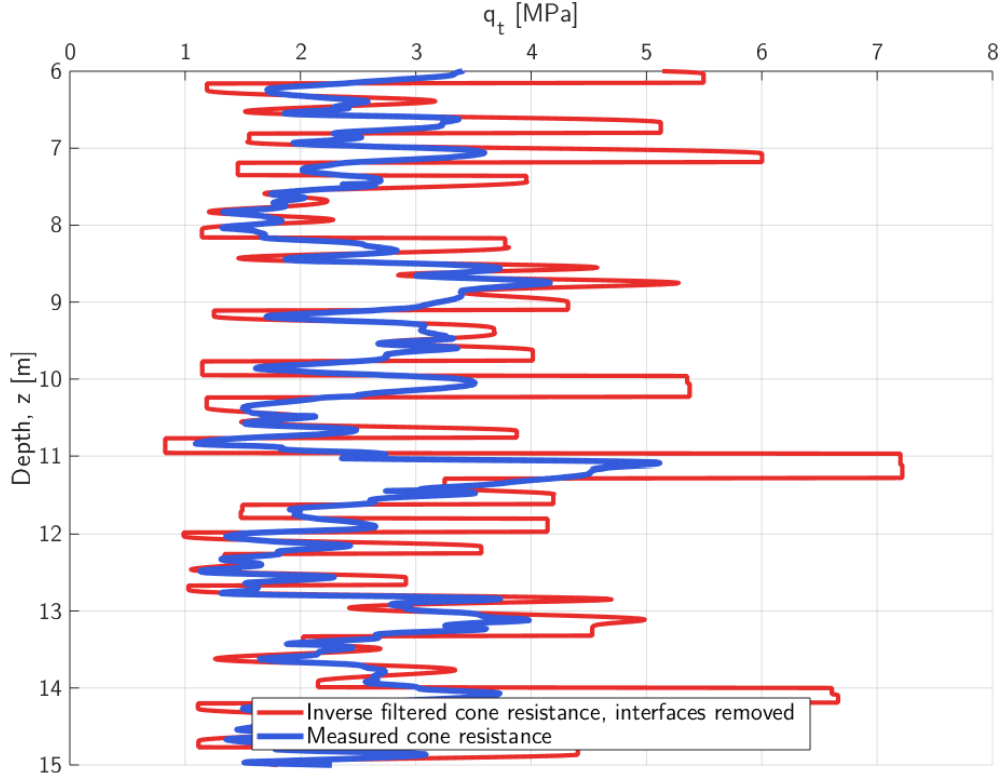
***Figure B**.2. Illustration of an inverse filtered cone resistance profile*

Component (1) consists of converting a true profile to a measured profile through a spatial filter. This is done through convolution of the characteristic profile with the cone penetration filter, w_c, as presented in equation (**B.1**):

$$q_t^m(z) = q_t^{char}(z) * w_c(z) = \int_{-\infty}^{\infty} q_t^{char}(\tau)w_c(z-\tau)d\tau \qquad \text{(B.1)}$$

The cone penetration filter, w_c, is a dynamic weighting window of cone resistance values. This filter represents the influence of nearby characteristic values on the measured value at a given depth. The penetrating cone weights low values of cone resistance greater than higher values, i.e. it is a *low-pass spatial filter*. A complete explanation of the filter is presented in chapter **B.2**.

An estimated characteristic cone resistance profile may then be achieved by iteratively performing the following equation on an actual measured cone resistance profile:

$$q_t^{char} = q_t^m + dq_t^{char} = q_t^m + (q_t^{char} - q_t^m) = q_t^m + (q_t^{char} - q_t^{char} * w_c) \qquad \text{(B.2)}$$

where the dependency of z is hidden for clarity. At iteration number $k+1$ the estimated characteristic cone resistance is:

$$q_{t,inv,k+1}^{char} = q_t^m + (q_{t,inv,k}^{char} - q_{t,inv,k}^{char} * w_c)$$ (B.3)

The cone penetration filter w_c is strongly nonlinear. High spatial frequencies must be removed for this procedure to converge. Such measures to filter out high frequencies are presented in the article. This procedure is continued until a convergence criterion is satisfied.

B.2   Procedure in the cone penetration weighting filter

Rather than using this procedure to invert a measured profile, this study focuses solely on component (1) with the filter presented in equation (**B.1**). That is, it desired to use the equation to predict a measured cone resistance given a characteristic profile. The characteristic cone resistance profile is hereafter noted as simply q rather tham q_t^{char}, while the predicted "measurement" is noted $\tilde{q}$ rather than q_t^m. The predicted "measured" profile is referred to as the *filtered* profile.

A cone resistance profile may be treated as a continuous function of depth as done above; however, the measured cone resistance is of course a vector of a finite number of values with a resolution limited by the recording frequency of the penetrometer. In the original article the procedure of the filtering procedure is given through formulas only, while the following description of the method is given in terms of vector and matrix notation. This is done for an efficient and accurate description of the procedure and since the computation is programmed, such a notation is convenient. The procedure presented in **B.2.1** is however the exact same as that described in the original article, only presented in a different form.

The procedure starts with a vector of characteristic cone resistance values:

$$\boldsymbol{q} = \begin{bmatrix} q_1 \\ q_2 \\ \vdots \\ q_i \\ \vdots \\ q_n \end{bmatrix}$$ (B.4)

where $\boldsymbol{q}$ is the vertical vector of n elements. All cone resistance values must have a corresponding depth, that is given by the depth vector $\boldsymbol{z}$, of equal length. It is assumed that the depth vector consists of strictly increasing values with equal spacing (e.g. the standard for CPTUs of $2cm$). Vector index i can then be interpreted as directly related to the depth. Note that vectors and matrices are marked with bold.

A simple example of a characteristic cone penetration profile is used for the explanation of the procedure. The selected profile is presented in **Figure B**.**3**, showing a two layered system. The two layers have thickness of $50cm$, where the top layer has a characteristic cone resistance of 10 times that of the underlaying layer. The two filtered profiles are described in the following two subsections, first the original procedure is presented, then the one developed in this study. Filtered

profiles of these two procedures are presented in the figure. All figures in the appendix assumes a standard cone diameter of $d_c = 3.6cm$.
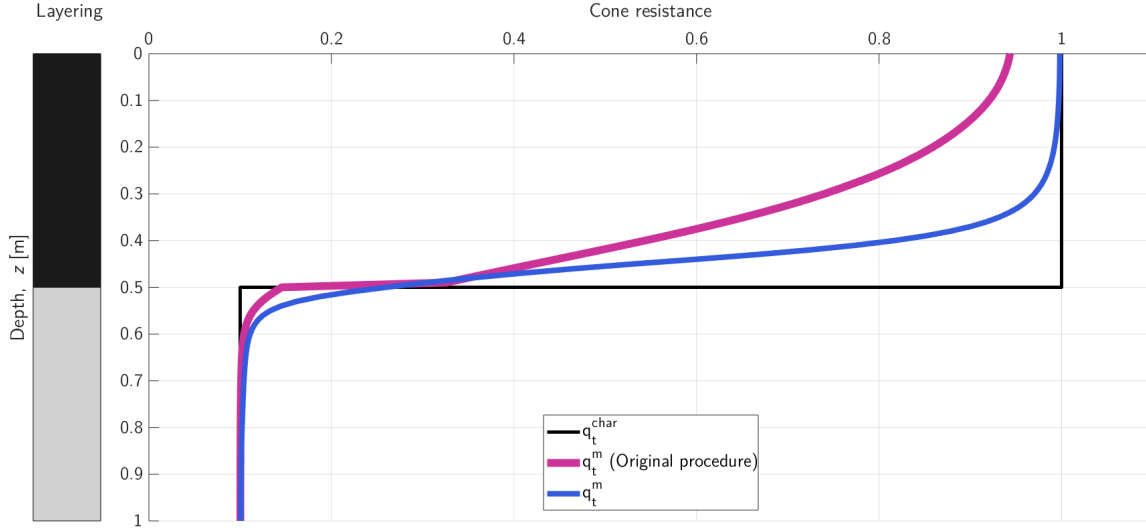
Figure B.3. *Illustrational q^t profile. This example is based on the procedure developed in this study.*

Multiple parameters control the behavior of the weighting filters, these are presented in the formulas. The evaluation of these parameters is done in the parameter study in section **B.3**. Parameters for the original procedure is selected as the baseline parameters from the original article.

B.2.1 The original procedure

In matrix multiplication, equation (**B.1**) is given as:

$$\tilde{q} = w_c q \tag{B.5}$$

where $\tilde{q}$ and q both are vertical vectors of n elements. The cone penetration filter matrix w_c has dimensions n-by-n as it consists of n horizontal vectors of length n. Each horizontal vector in a matrix is here noted with a subscript i.

$$w_c = \begin{bmatrix} w_{c,1} \\ w_{c,2} \\ \vdots \\ w_{c,i} \\ \vdots \\ w_{c,n} \end{bmatrix} \tag{B.6}$$

where the horizontal vector $w_{c,i}$ consists of n elements:

$$w_{c,i} = \begin{bmatrix} w_{c,i1} & w_{c,i2} & \dots & w_{c,ij} \dots & w_{c,in} \end{bmatrix} \tag{B.7}$$

The element $w_{c,ij}$ is the value of row i and column j in matrix $\boldsymbol{w_c}$ and is thus not marked in bold. While vector element i can be imagined representing the physical depth, vector element j represents the virtual depth. A single filtered cone resistance value is calculated by:

$$\tilde{q}_i = \boldsymbol{w_{c,i}} \boldsymbol{q} \tag{B.8}$$

Where $\tilde{q}_i$ is a single filtered value and is the i-th value of the filtered vector of $\tilde{\boldsymbol{q}}$. An example of six filtered values is presented as markers in **Figure B**.**4** for the original procedure. The figure also includes the cone penetration filters, $\boldsymbol{w_{c,i}}$, of these six points.
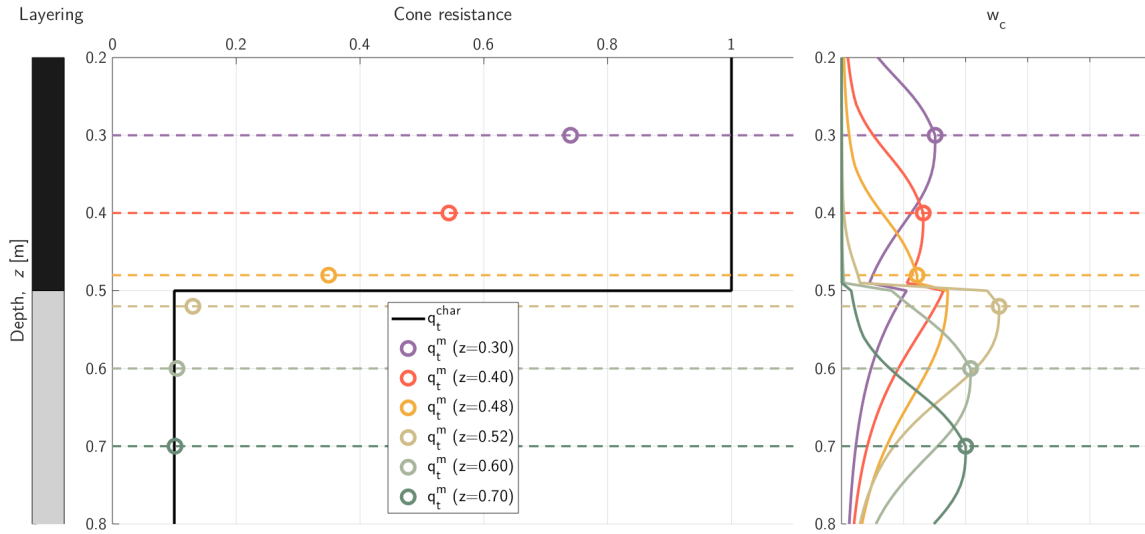
Figure B.**4**. *Six filtered values with their corresponding w_c filter for the original procedure.*

The cone penetration weighting filter consists of two weighting filter. These are weighting filters $\boldsymbol{w_{1,i}}$ and $\boldsymbol{w_{2,i}}$. Each value of ij of $\boldsymbol{w_c}$ is the product of two weight filters $w_{1,ij}$ and $w_{2,ij}$ normalized by the sum of the vectors $\boldsymbol{w_1^i}$ and $\boldsymbol{w_2^i}$:

$$w_{c,ij} = \frac{w_{1,ij} w_{2,ij}}{\boldsymbol{w_{1,i}} (\boldsymbol{w_{2,i}})^T} \tag{B.9}$$

where vector $(\boldsymbol{w_{2,i}})^T$ is the transposed vector. Thus, the sum of elements in $\boldsymbol{w_{c,i}}$ becomes 1:

$$\sum_{j=1}^{n} w_{c,ij} = 1 \tag{B.10}$$

The first weighting filter, $\boldsymbol{w_{1,i}}$, determines the size of the filter window. This window is defined as:

$$w_{1,ij} = \frac{C_{1,ij}}{1 + \left(\dfrac{|Z_{ij}|}{Z_{50,ij}}\right)^{m_z}} \tag{B.11}$$

As indicated by the subscripts, Z_{ij}, $z_{50,ij}$ and $C_{1,ij}$, are all matrices and are presented in turn. Control parameters are emphasized in red, such as m_z in the equation above. $\boldsymbol{Z_i}$ is the normalized depth vector on the cone diameter and set to zero at the evaluated depth (**B.12**). The depth of the cone at this evaluated depth is the i-th value in the depth vector $\boldsymbol{z}$, the value z_i. The depth vector $\boldsymbol{z}$ is transposed to form a horizontal vector.

$$\boldsymbol{Z_i} = \frac{\boldsymbol{z}^T - z_i}{d_c} \tag{B.12}$$

The matrix $\boldsymbol{Z}$ has therefore zeros along the diagonal, i.e., $Z_{ii} = 0$. Since $\boldsymbol{z}$ is strictly increasing the lower triangle of the matrix (values of Z_{ij} for $i > j$) is positive while the upper triangle is negative. The intention of $C_{1,ij}$ is to put larger emphasize on values ahead of the cone tip.

$$C_{1,ij} = \begin{cases} 1 & for\ Z_{ij} \geq 0 \\ 1 + \dfrac{Z_{ij}}{8} & for\ -4 \leq Z_{ij} < 0 \\ 0.5 & for\ Z_{ij} < -4 \end{cases} \tag{B.13}$$

The value of $Z_{50,ij}$ largely determine the spatial length of the filter window and can be called a decay length of the filter window. Lower values of $Z_{50,ij}$ yields smaller windows. It is defined as:

$$Z_{50,ij} = 1 + 2(C_{2,ij} \cdot Z_{50,ref} - 1)\left(1 - \frac{1}{1 + \left(\frac{q_j}{q_i}\right)^{-m_{50}}}\right) \tag{B.14}$$

where $C_{2,ij}$ is a weighting of values ahead of and behind the cone, $Z_{50,ref}$ and m_{50} are constants and q_j/q_i is the relative cone resistance. The expression is formed so that for $q_i = q_j$, the value of $Z_{50,ij}$ is equal to $Z_{50,ref}$. A larger value of $z_{50,ij}$ gives a larger filter window. The ratio of q_i/q_j is the relative characteristic value at the evaluated depth compared to another depth. If $q_j > q_i$, the value of $Z_{50,ij}$ becomes less than $Z_{50,ref}$ while if $q_j < q_i$ it becomes larger than $z_{50,ref}$. The exponent m_{50} controls the influence of the ratio.

The factor $C_{2,ij}$ is defined as:

$$C_{2,ij} = \begin{cases} 1 & for\ j \geq i \\ 0.8 & for\ j < i \end{cases} \tag{B.15}$$

The second weighting filter has the function of putting greater emphasis on weak values. This also uses the ratio of cone resistances q_j/q_i:

$$w_{2,ij} = \sqrt{\frac{2}{1 + \left(\frac{q_j}{q_i}\right)^{m_q}}} \tag{B.16}$$

The minimum and maximum values of $w_{2,ij}$ are then 0 and $\sqrt{2}$ respectively. The weight filters w_1 and w_2 are intentionally selected such that $w_{1,ii} = 1$ and $w_{2,ii} = 1$. However, since the weighting filter are normalized by the sums, as shown in equation (**B.9**), the magnitude of the value is not of importance.

A limit to the largest distance of the cone tip which can influence the tip resistance is added, called ΔZ_{max}. This distance represents the maximum zone of influence and is set to 30 cone diameters in the original article. For depth vector $\boldsymbol{Z_i}$, the filter window has an upper limit index k_1, where $Z_{ik_1} = -\Delta Z_{max}$ and lower limit index k_2 where $Z_{ik_2} = \Delta Z_{max}$ as long as $k_1 \geq 1$ and $k_2 \leq n$. Elements outside this window of $\pm \Delta Z_{max}$ are set to zero (**B.17**).

$$
\begin{aligned}
w_{1,ij} &= \begin{cases} w_{1,ij} & k_1 \leq j \leq k_2 \\ 0 & otherwise \end{cases} \\
w_{2,ij} &= \begin{cases} w_{2,ij} & k_1 \leq j \leq k_2 \\ 0 & otherwise \end{cases}
\end{aligned}
\tag{B.17}
$$

The cone penetration filter is then computed through (**B.9**) with the weighting vectors given in (**B.17**).

An example of a filtered profile is presented in **Figure B.5**, where the measurement of the study of Młynarek et al. (2012) are presented. A description of the result was presented in subsection **2.3.5**. Characteristic profiles were determined from the empirical formulas presented in subsection **2.2.1**. The filtered profiles is determined from the original procedure presented here, with the baseline control parameters of $Z_{50,ref} = 4.2$, $m_z = 3$, $m_{50} = 0.5$ and $m_q = 2$.

The reason for the sudden "jumps" in values of the original procedure presented in **Figure B.5**, as well as in **Figure B.1** and **Figure B.2**, is the dependency of q_j/q_i. This causes an inaccurate representation of the cone penetration process. Furthermore, the filtered cone resistance in the upper layer for the third test ($10cm$ clay layer) is seen to increase prior to the clay interface as a reaction of the sand layer below the clay layer. While a slightly better fit can be achieved by other parameters, this procedure is not able to properly reflect the measurements of a physical experiment as presented.
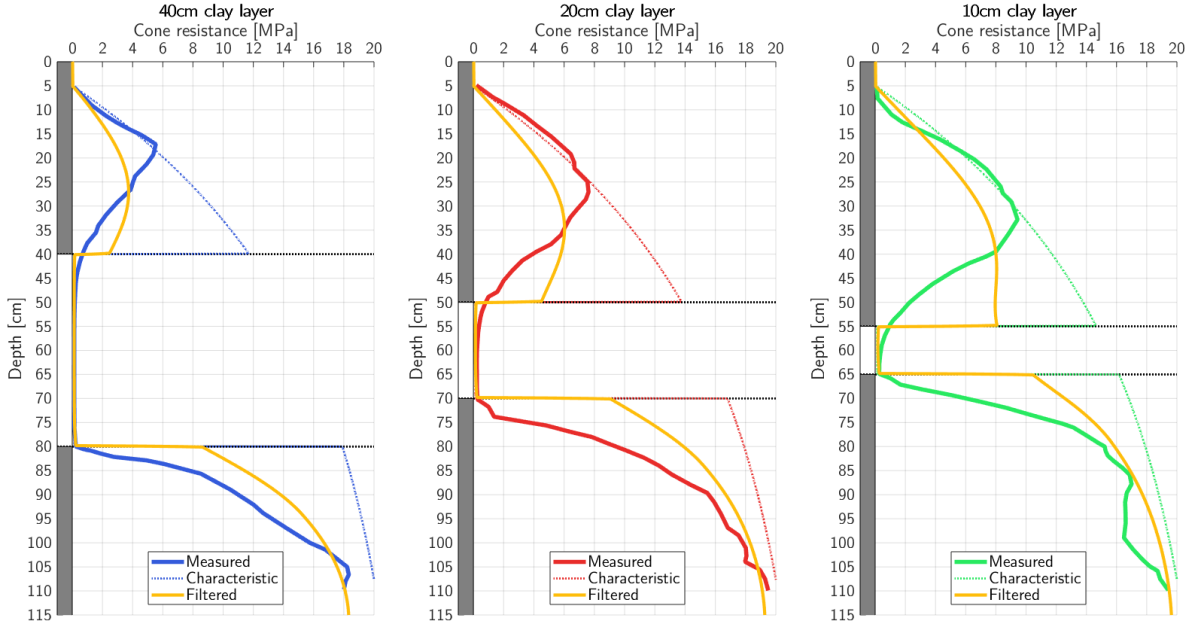
Figure B.5. *Measured profiles from the presented study of Młynarek et al. (2012). The filtered profiles in the figure were determined using the original procedure on the characteristic profiles presented. The characteristic profiles were based on a figure presented in the mentioned study.*

B.2.2   Developed procedure of this study

The framework of the developed procedure is the same as from original presented above, though significant differences are included. The cone penetration weighting filter is done as in equation (**B.9**), however the filter w_2 is not used. Instead, the new filter w_3 is used. The new cone penetration weighting filter is given symbol w_f to emphasize the difference.

$$w_{f,ij} = \frac{w_{1,ij}^{mod} w_{3,j}}{\boldsymbol{w_{1,i}^{mod}} (\boldsymbol{w_3})^T} \tag{B.18}$$

The filter w_3 is here called the *interface weighting filter* since its function is to weight the influence of measurements along interfaces where weak/low values are weighted more than strong/high values. While the weight w_2 had the same function, the weight w_3 is believed reflect the importance of the contrast in cone resistance along interfaces. Note that w_3 is not the i-th vector. Instead, w_3 is constant for every vector element i. The calculation of w_1 is also calculated in a different way and is called $\boldsymbol{w_1^{mod}}$.

Figure B.6 presents the cone penetration weighting filters, w_f, for several depths of the profile presented **Figure B**.3. This can be compared to those of **Figure B**.4 from the original procedure. Significant difference includes the large dependence on the soil ahead of the cone in sand (e.g. at depth $z = 0.3$) compared to in clay (e.g. at depth $z = 0.6$)..
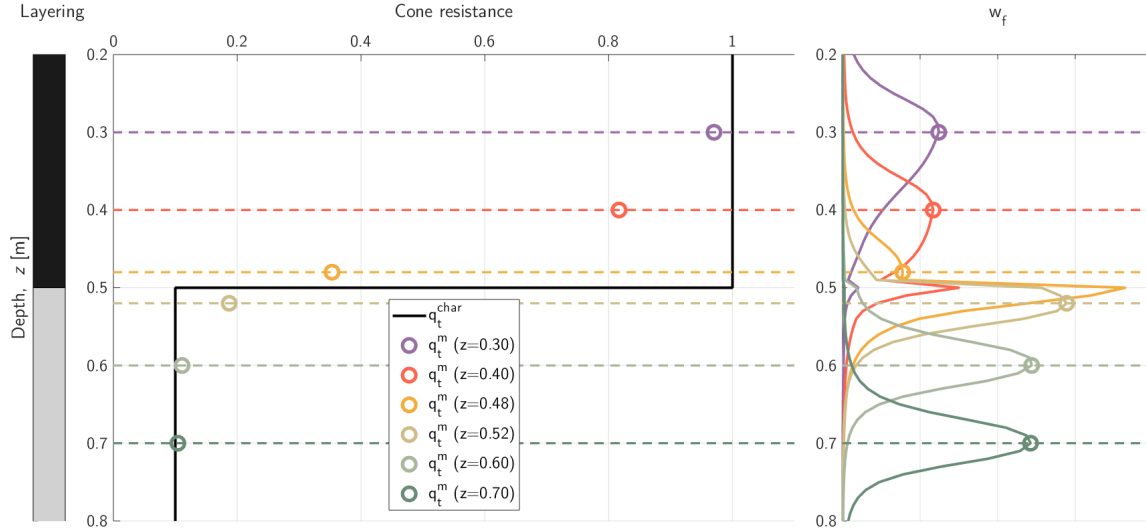
Figure B.6. *Six filtered values with their corresponding w_c filter for the procedure procedure developed in this study. Note the length of the weighting window at depth $0.3m$ in sand compared to that in clay at depth $0.7m$. In sand the length is greater ahead of the position, while in clay it is longer behind the cone.*

While values of $w_{1,ij}^{mod}$ are still determined as $w_{1,ij}$ from equation (**B.11**), however values of $Z_{50,ij}$ are determined differently:

$$Z_{50,ij} = 1 + 2\big(F_{ij} \cdot Z_{50,ref} - 1\big) \left(1 - \frac{1}{1 + (\xi_j)^{m_{50}}}\right) \tag{B.19}$$

where, F_{ij} and ξ_i are new factors. $\boldsymbol{\xi}$ is an input vector of equal length as the true cone resistance vector $\boldsymbol{q}$, i.e. of n elements. Values of ξ_i represent the influence of material ahead of the cone compared to that of behind the cone. Due to this, the $\boldsymbol{\xi}$ values are called the *sensing* parameters. Values of the sensing control parameters are input values which means that these are selected based on the assumed material. For values of ξ_i equal to one, the value of $Z_{50,ij}$ is equal to $Z_{50,ref}$. In a sand, values can be set to one, while values in clay are lower due to greater dependence on the soil behind the cone.

In order to approximate the behavior of the cone, and the lack of distinct jumps in cone resistance values, the $\boldsymbol{\xi}$ vector is smoothed with a running average. The running average is over half the length of the cone diameter in both directions. This running average on the vector $\boldsymbol{\xi}$ is performed twice for a smooth transition.

Values of the factor F_{ij} are defined as the following:

$$F_{ij} = \begin{cases} \xi_i & for\ j \geq i \\ 0.5 & for\ j < i \end{cases} \tag{B.20}$$

I.e., the weighting of values behind the cone is constant equal to 0.5 while the weighting of values ahead of the cone is given by ξ_i. Values of $\boldsymbol{\xi}$ and the resulting values of $\boldsymbol{Z_{50}}$ and $\boldsymbol{w_{1,i}}$ are presented

in **Figure B**.**7**. In this example, which is the same as presented in **Figure B**.**6**, the value of ξ_i is 1 in sand and 0.2 in clay. Values are studied in the parameter study in the next section.
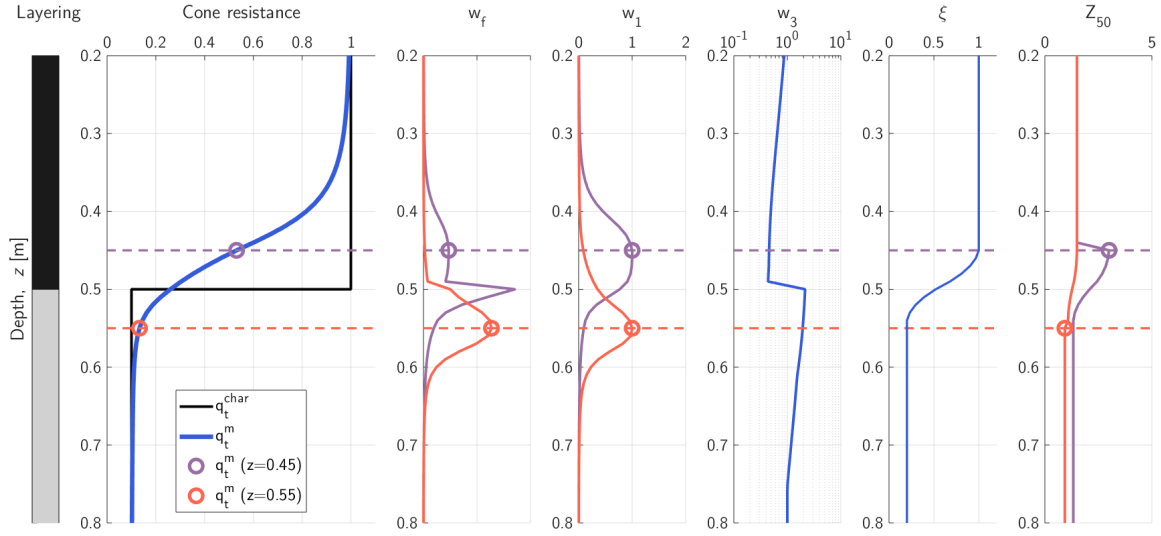

***Figure B**.7. Example of a filtered profile*

The $\boldsymbol{w_3}$ profile is also shown above. As mentioned, it reflects the larger weighting of weak values of the cone resistance. This weighting function is the same for all evaluated values. It is determined through an evaluation of the contrast in cone resistance where relative strong values yield values of $w_{3,i}$ less than one, while relative weak values are greater than one.

The elements of this weighting function are found through the following procedure. Relative strong and weak values are found by evaluating the minimum of nearby cone resistance measurements (q_j) against the evaluated cone resistance (q_i):

$$I_{weak,ij} = \min \left(\frac{q_j}{q_i}, I_{lim,weak} \right)$$

$$\text{(B.21)}$$

$$I_{strong,ij} = \min \left(\frac{q_i}{q_j}, I_{lim,strong} \right)$$

$I_{lim,weak}$ and $I_{lim,strong}$ are the upper boundary for the contrast considered. Values of $I_{lim,weak}$ and $I_{lim,strong}$ are for simplicity set to be equal for this study. Furthermore, the value of I_{lim} are set to 100, meaning that only contrasts between cone resistance causes increased weighting of the weak values relative to the strong values. The value of I_{lim} must be larger than 1. The vectors of $\boldsymbol{I_{weak,i}}$ and $\boldsymbol{I_{strong,i}}$ are then multiplied with a weighting filter like $\boldsymbol{w_{1,i}}$, which is called $\boldsymbol{w_1^{int}}$:

$$W_{weak,ij} = w_{1,ij}^{int} \cdot I_{weak,ij}$$

$$\text{(B.22)}$$

$$W_{strong,ij} = w_{1,ij}^{int} \cdot I_{strong,ij}$$

where the values of $w_{1,ij}^{int}$ are determined as the weighting filter $\boldsymbol{w_1}$, however the decay length Z_{50} is set to a constant value of Z_c.

$$w_{1,ij}^{int} = \frac{C_{1,ij}}{1 + \left(\frac{|Z_{ij}|}{Z_c}\right)^{m_z}} \tag{B.23}$$

The size of Z_c is not very significant and is set to a constant value of 5. Only the maximum values of the vectors $\boldsymbol{W_{weak,i}}$ and $\boldsymbol{W_{strong,i}}$ are of interest:

$$w_{weak,i} = \max(\boldsymbol{W_{weak,i}})$$
$$w_{strong,i} = \max(\boldsymbol{W_{strong,i}}) \tag{B.24}$$

The two vectors of $\boldsymbol{w_{weak}}$ and $\boldsymbol{w_{strong}}$ consist of values between 1 and I_{lim}. In a weak layer directly next to a strong layer interface at index i the value of $w_{weak,i}$ is greater than one while $w_{strong,i}$ is equal to one. Similarly, when index i is on the other side of the boundary in the strong layer, the value of $w_{weak,i}$ is equal to one while $w_{strong,i}$ is greater than one. Finally, the vector of the w_3 is determined as the values of $w_{weak,i}$ divided by $w_{strong,i}$:

$$w_{3,i} = \left(\frac{w_{weak,i}}{w_{strong,i}}\right)^{m_3} \tag{B.25}$$

This results in the intended result that weak layers have an increased weight while the strong layer has a decreased weight. The exponent m_3 is determined by:

$$m_3 = \frac{\ln(w_{3,max})}{\ln(I_{lim})} \tag{B.26}$$

where $w_{3,max}$ defines the maximum resulting increased weight of weak values and decreased weight of strong values. $w_{3,max}$ is the value where the cone resistance contrast is equal to I_{lim}, which was previously stated set to 100. If $w_{3,max}$ is set to 1, all values of $w_{3,i}$ will be equal to one.

An illustration of the $\boldsymbol{w_3}$ profile is presented in **Figure B**.**9**. Values of Z_c is 5 and I_{lim} is 100. In this example, the layers with cone resistance 0.2 or less are considered as clay layer with the corresponding sensing parameter. Further evaluation of the $w_{3,max}$ parameter is given in the next section.

The procedure is evaluated towards physical experiments in section **B.4** in the same manner as the original procedure was presented in **Figure B**.**5**.
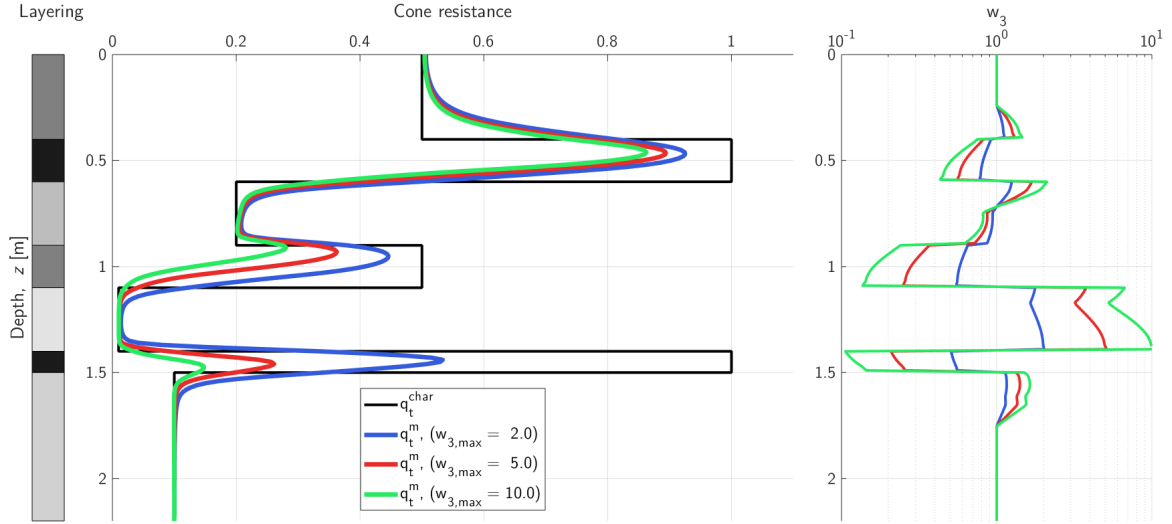
Figure B.*8. Filtered profiles of an arbitrary characteristic cone resistance profile with the corresponding values of $\mathbf{w_3}$. The contrast at depth 1.4 is equal to 100, values of $\mathbf{w_3}$ at this depth are thus equal to*

$$w_{3,max}.$$

B.3   Parameter study

The parameters of the weighting filter $\mathbf{w_f}$ are studied, which are $Z_{50,ref}$, m_z, m_{50} and $w_{3.max}$. In addition, the influence of the sensing parameter values ξ_i are studied. The examples above uses parameters of $Z_{50,ref} = 3$, $m_z = 3$, $m_{50} = 1.5$ and $w_{3.max} = 5$. While the effect of varying the parameters are very much non-linear, only one parameter is evaluated at a time while the rest are set to these values.

Comparison of filtered cone resistance measurements are presented horizontally, where the filtered cone resistances (q_t^m) are plotted against the depth. Moreover, the normalized depth is used which is given in terms of cone diameters from the to the top layer interface, written as $(z - z_{int})/d_c$. A simple example is presented in **Figure B**.**9**. Here, the top plot presents a weak layer on top of a strong layer, while the opposite is the case in the bottom plot. Since this study considers clays in sands, the weak layers are clay while the strong layers are sand. This is attempted reflected in the sensing and developing distances. For simplicity the cone resistance in sand is set to 1 while the cone resistance in clay is 0.1. **Figure B**.**10** then presents filtered profiles for thin layers of varying thickness. The vertical dashed lines each represent a layer interface. Five different layer thicknesses are presented in **Figure B**.**10**, thus six layer interfaces are plotted since the top layer interface are the same for all. Note that if the layer thickness is large enough, the transitions from strong to weak, and opposite, are equal to those presented in **Figure B**.**9**. The value of η_{min} is used to describe the ratio of the cone resistance of the strong layer the weak layer. As stated, these examples in **Figure B**.**9** and **Figure B**.**10** used a value of $\eta_{min} = 0.1$. **Figure B**.**11** presents the filtered cone resistance for different values of η_{min}. An example of a combination of varying layer thickness and η_{min} is shown in **Figure B**.**12**.
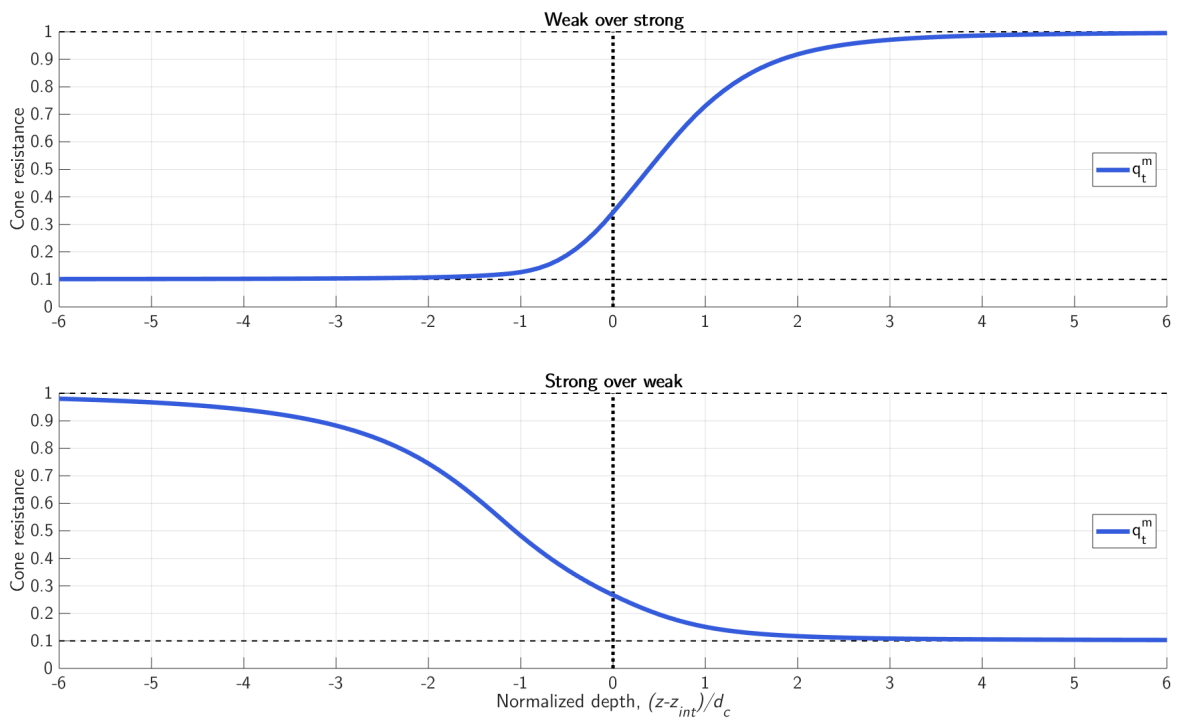
Figure B.*9. Presentation of cone resistance with normalized depth along the x-axis. The interface is presented with a vertical line. Dotted lines on top of 1 and at the bottom of 0.1 represents the strong and weak cone resistances, respectively.*
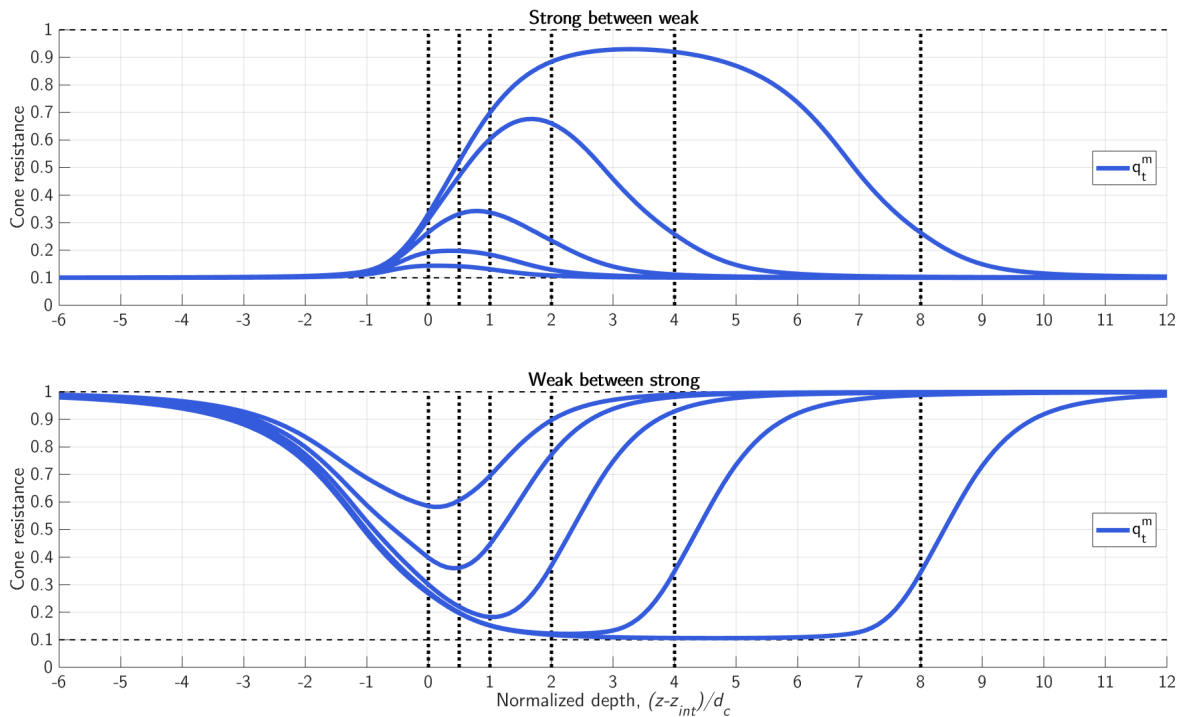

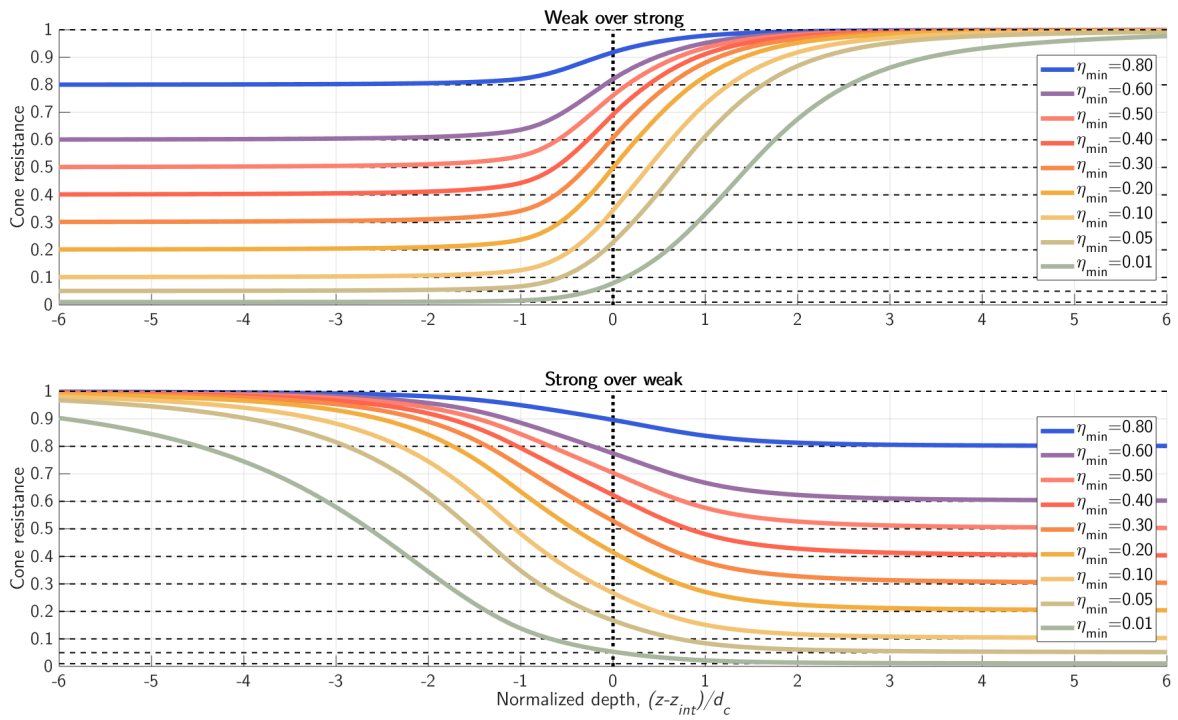**Figure B**.*10. Layering effect of thin layer layers of varying thickness.*

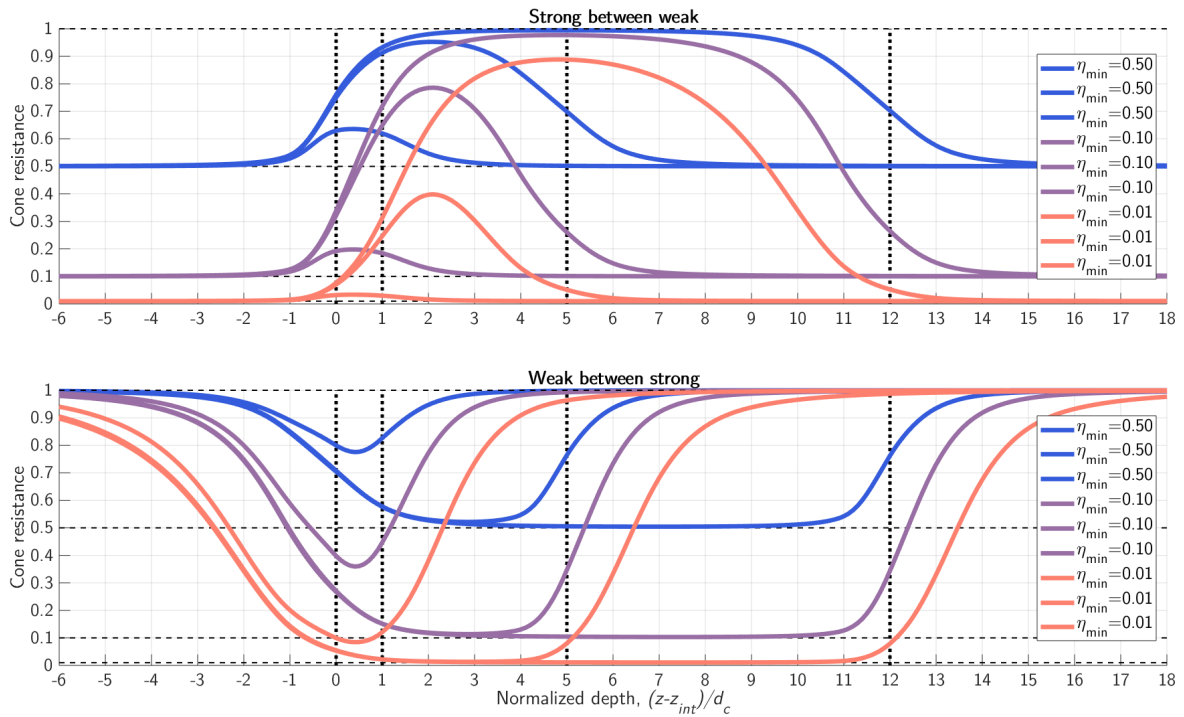**Figure B**.11. *Layering transition from strong to weak and weak to strong for varied values of η_{min}.*

Figure B.12. *Filtered values for both varying layer thickness and values of η_{min}.*

The parameters of $Z_{50,ref}$, m_z and m_{50} are evaluated using the same value of η_{min} equal 0.1, while the layer thickness is varied, while parameter $w_{3,max}$ is evaluated for varying values of η_{min}. Layer thicknesses of 1, 3 and 6 cone diameters are presented.

The two primary considerations when evaluating the shape of the filtered profiles are firstly the peak values in sand and clay. Secondly is the transition between the materials.

Figure B.**13** presents the result of different values of $Z_{50,ref}$. As mentioned in the presentation of weighting filter, this parameter can be understood as the control parameter for the zone of influence. A larger value of $Z_{50,ref}$ reflects a soil material that has a large influence length. The figure shows how larger values cause *more averaged* filtered profiles, i.e. the peaks of the thin layers are closer to the cone resistance of the surround layers.

Parameter m_z also influence the peak values and is also significant for particularly the influence lengths, as shown in **Figure B**.**14**. The original procedure used a value of 3 for m_z, which is also done her.

While parameter m_{50} also was included in the original procedure, it depends on different input the procedure of this study. m_{50} is the exponent of the sensing parameter ξ_i, which are presented later. **Figure B**.**15** shows the result of values between 0.5 and 3. The largest variations are seen upon the transition from strong to weak materials. This is due to the values of the sensing parameter changing from that of the strong layer to the weak layer. The differences elsewhere are neglectable. A value of 1.5 or height yields smooth transitions.

Parameter $w_{3,max}$ of the interface filter control the peak values in thin layers. Various values are presented for thin layers in **Figure B**.**16**. In important difference to how parameters $Z_{50,ref}$ and m_z influences the peak value is how greater values of $w_{3,max}$ yields lower peak values for both the weak and strong material, i.e. more distinct peaks in the weak material and less distinct in the strong material. **Figure B**.**17** presents the influence of $w_{3,max}$ depending on the contrast in cone resistance, η_{min}, with values of 0.5 and 0.01. The difference in transition increases significantly for larger contrasts. **Figure B**.**16** shows these differences for a value of 0.1.
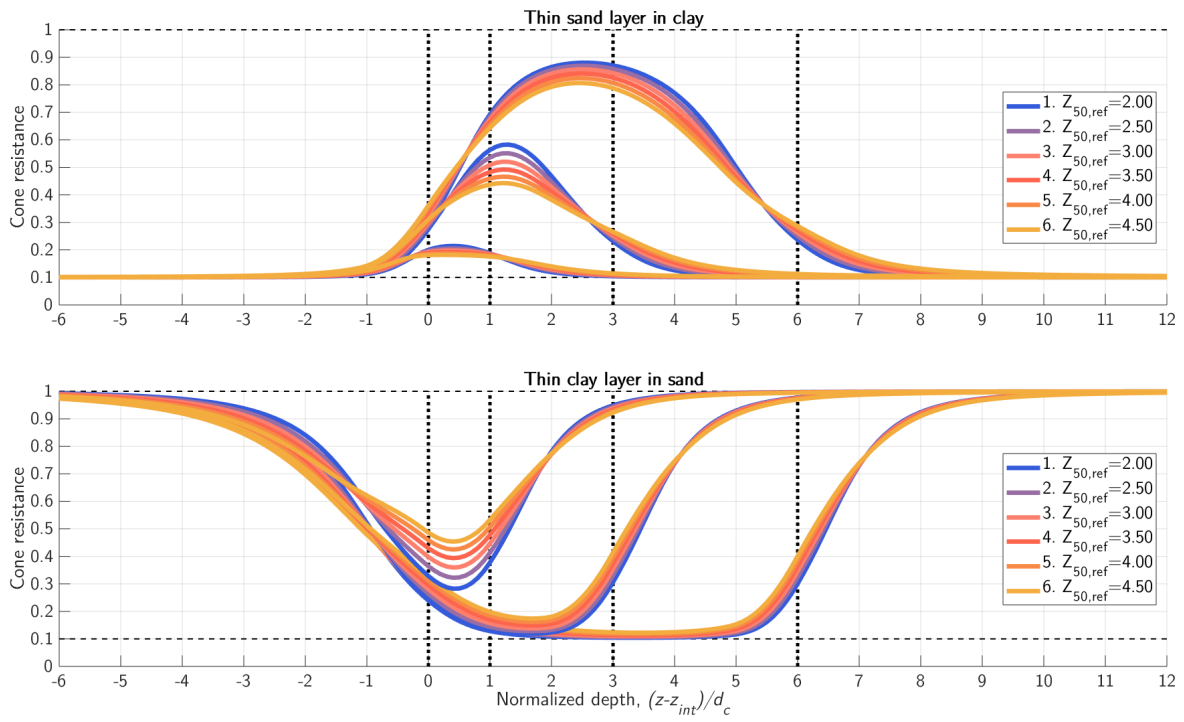
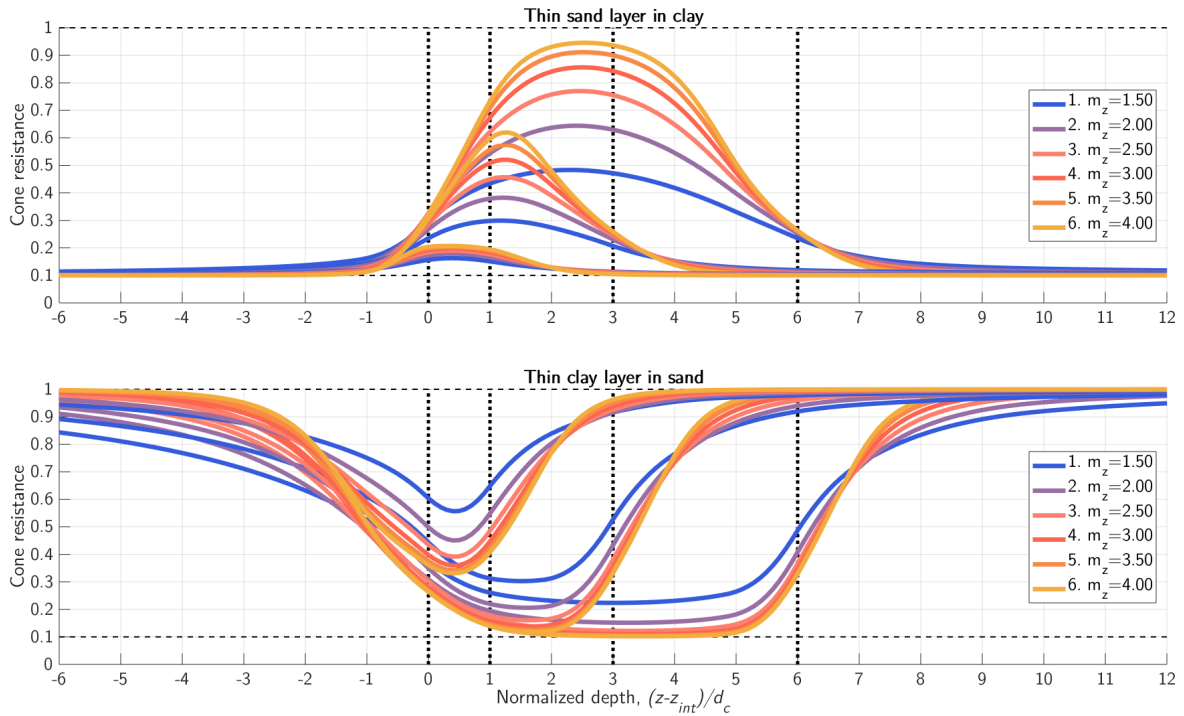**Figure B**.13. *Variation of parameter* $Z_{50,ref}$.

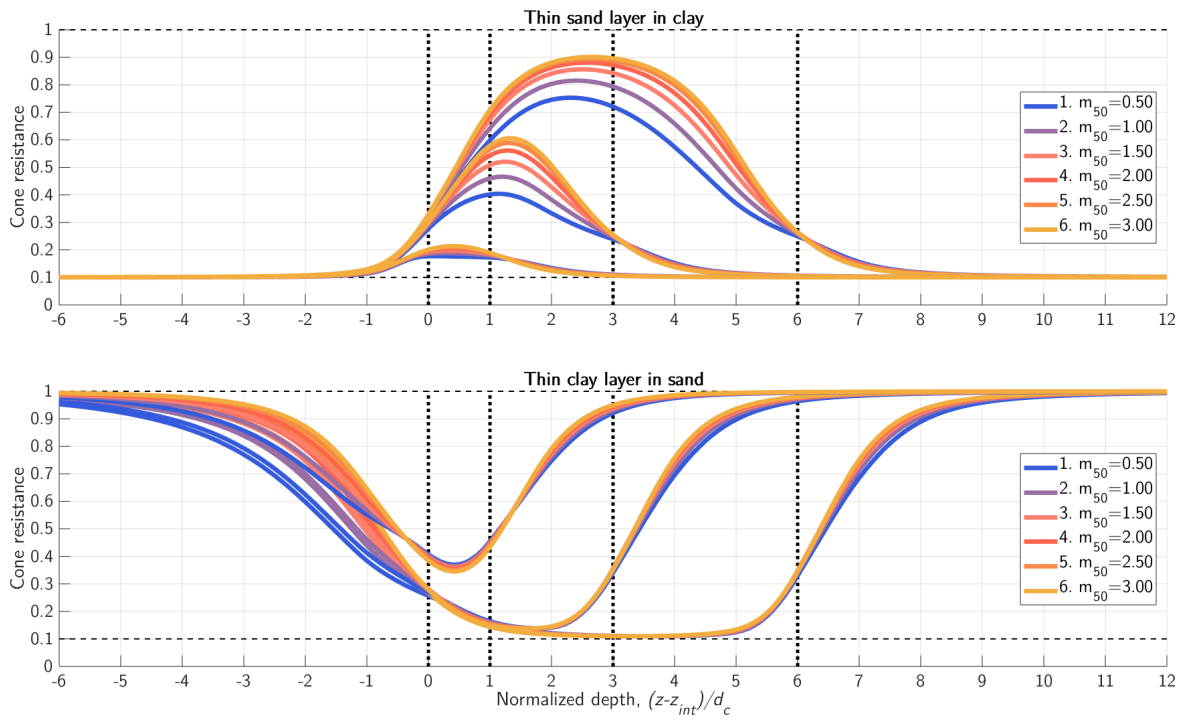**Figure B**.14. *Variation of parameter* m_z.

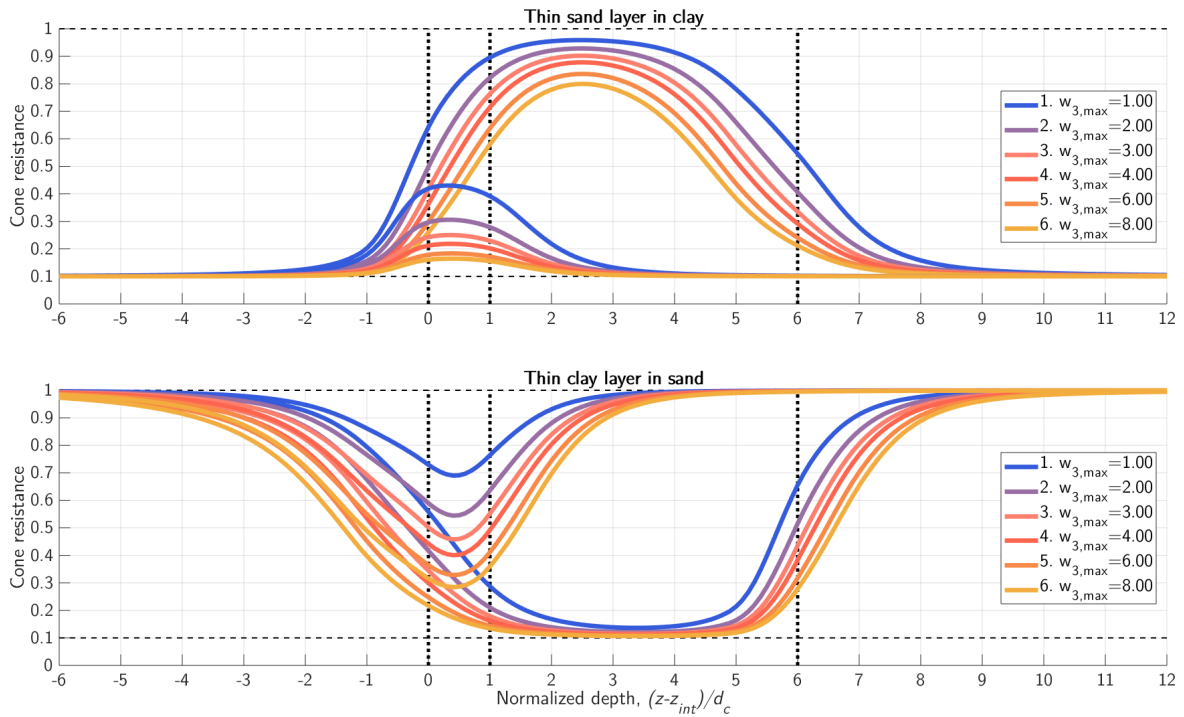**Figure B**.15. *Variation of parameter m_{50}.*

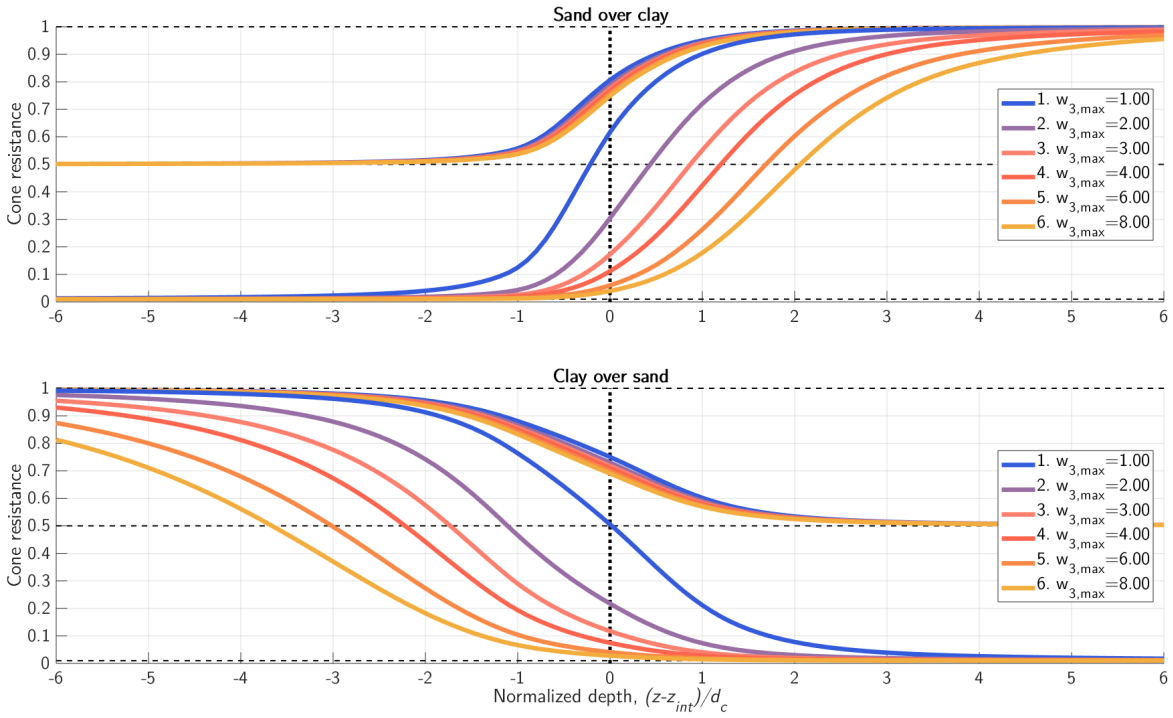**Figure B**.16. *Variation of parameter $w_{3,max}$.*

Figure B.**17**. *Influence of parameter $w_{3,max}$ on the transition between clay and sand layers for η_{min} equal to 0.01 and 0.5.*

In addition to the four control parameters presented above, the procedure requires inputs of the sensing parameter, $\boldsymbol{\xi}$. These values reflect the sensing length compared to the developing length for the evaluated soil. As presented in subsection **B.2.2**, the length of the filter window Z_{50} is dependent on the value of ξ_i, i.e. at the evaluated depth. If ξ_i is equal to 0.5 values ahead of and behind the cone is weighted equally.

The previously presented examples and parameter variations uses ξ_i equal to 1 in sand and ξ_i equal to 0.2 in clay. **Figure B**.**18** and **Figure B**.**19** show variation of these values and its effect on the filtered profile. Lower values of ξ_i influences the filter window through m_{50} and the resulting Z_{50}. The figures show how smaller values of ξ_i in sand results in greater developing dominance, i.e. the filtered cone resistance increases only at a short distance to the bottom interface. Larger values in sand results in peaks occurring closer to the top layer interface.
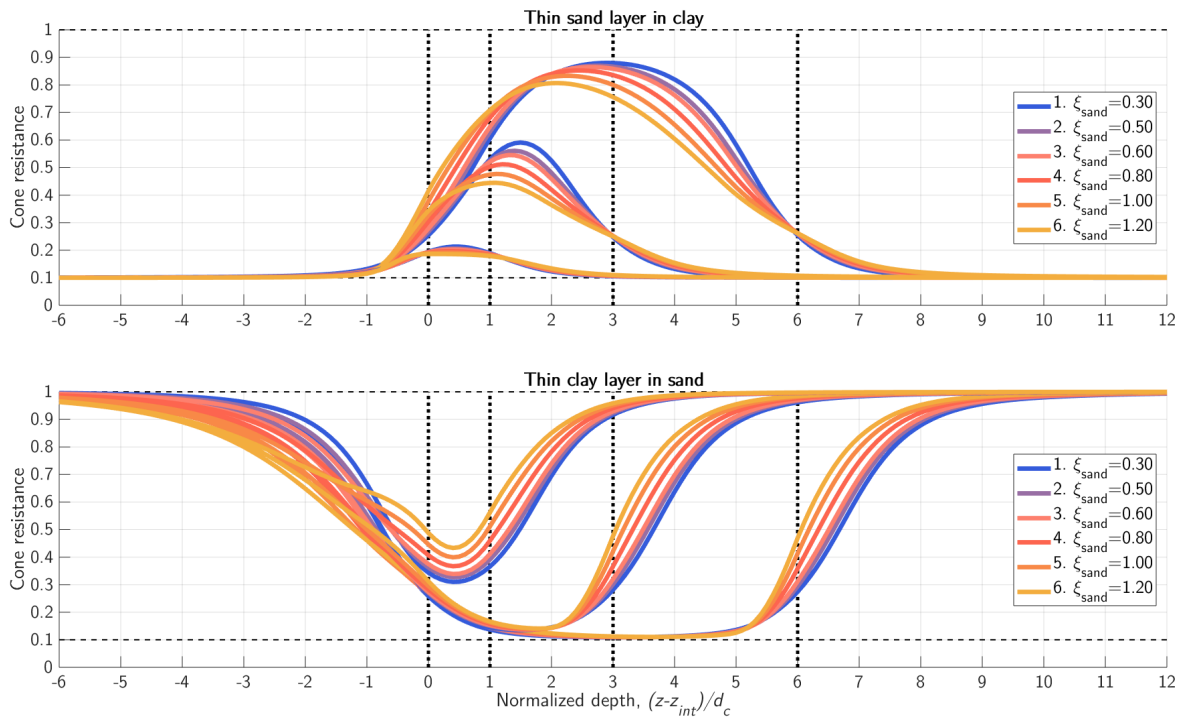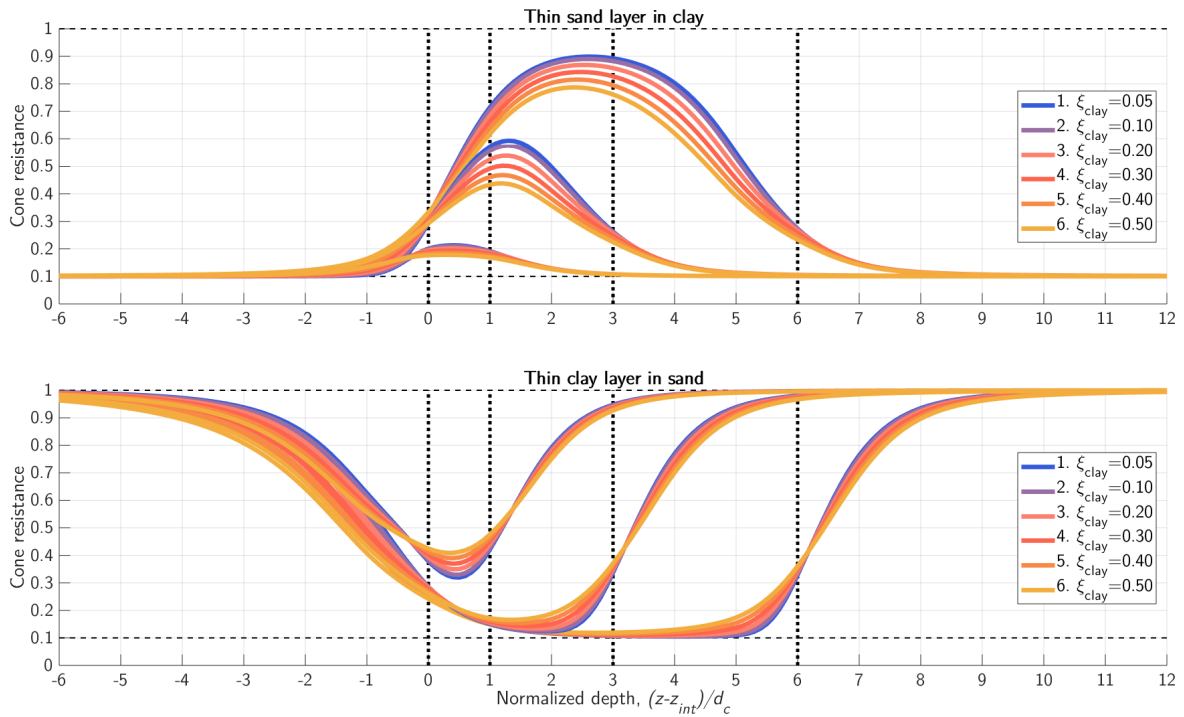
Figure B.*18. Variation of values of ξ in sand.*

Figure B.*19. Variation of values of ξ in clay.*

B.4 Filtered profiles for previously performed physical experiments

The aim of the procedure is to produce filtered profiles which resembles measurements based on assumed characteristic profiles. The procedure is by applying the filter on previously conducted physical experiments with samples of sand with clay layers. Three studies were presented in subsection **2.3.5**, these are considered here. These are the studies of Młynarek et al. (2012), Van der Linden (2016) and de Lange et al. (2018).

Characteristic profiles of the sand layers were determined from the equation presented in subsection **2.2.1** though some adjustments were made for the profiles to fit with the measurements. The equations proposed by Senders (2010) to account for free surface was used. Characteristic cone resistances in clay were determined from the undrained shear strength.

The baseline values were set to $Z_{50,ref} = 3$, $m_z = 3$, $m_{50} = 1.5$ and $w_{3.max} = 4$. Values of ξ_{clay} is set to 0.2 while ξ_{sand} is set to 1.

The study of Młynarek et al. (2012) does not explicitly mention the size of the cone diameter while it is believed to be a standard cone with diameter of $3.6cm$. The results of the applied filter are presented with the measured and the determined characteristic profiles in **Figure B**.**20**. Two additional filtered profiles are presented in addition to the baseline values from other values of $w_{3,max}$. The result compares well for the baseline in the clay layer, while the sensing distance is shorter than the measurements indicates.

Results of the procedure applied to the experiments of Van der Linden (2016) is shown in **Figure B**.**21** for the baseline values and the two other values of $w_{3,max}$. Higher values of this parameter result in lower peak values in clay, as shown, which is particularly evident in the layering with $2cm$ clay layers.

Finally, the method is applied to the measurements of de Lange et al. (2018), shown in **Figure B**.**22** with the baseline parameters.

As expected, the procedure does not perfectly match the behavior of the cone resistance measurements. However, with the exception of the tests in multiple $2cm$ thick clay layers, the behavior in clay is well represented.
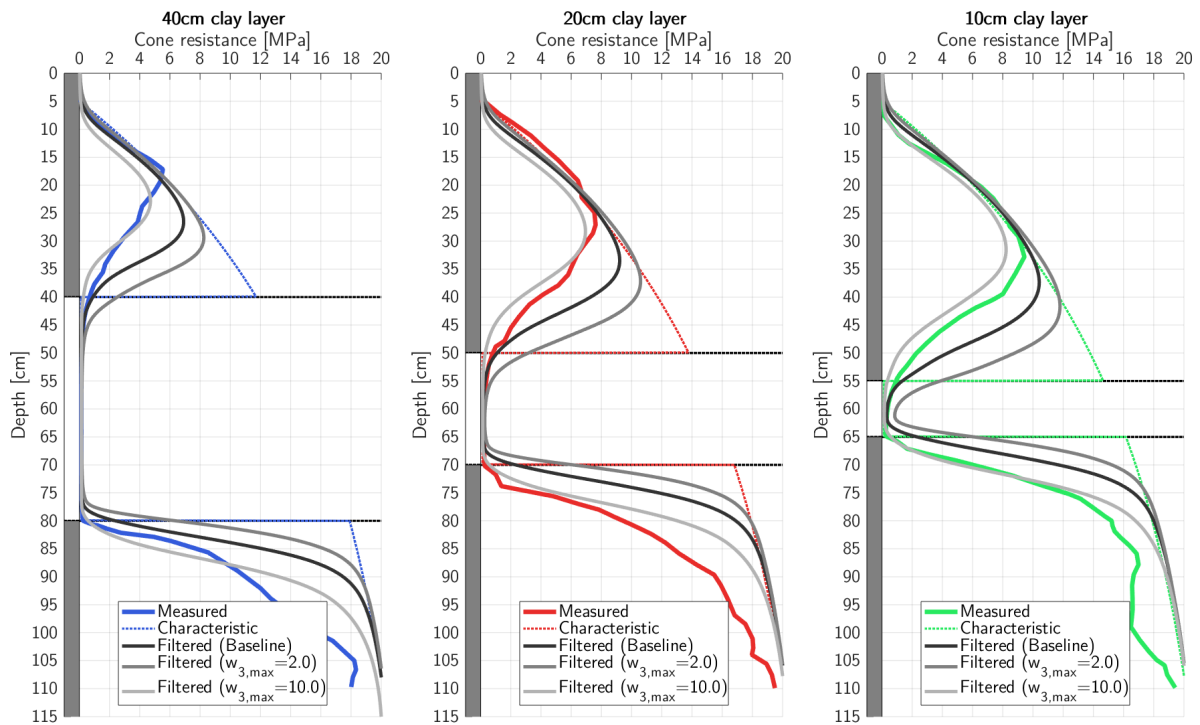
Figure B.20. *Measured profiles from the study of Młynarek et al. (2012). A characteristic profile is determined, and filtered profiles for different parameters are shown.*
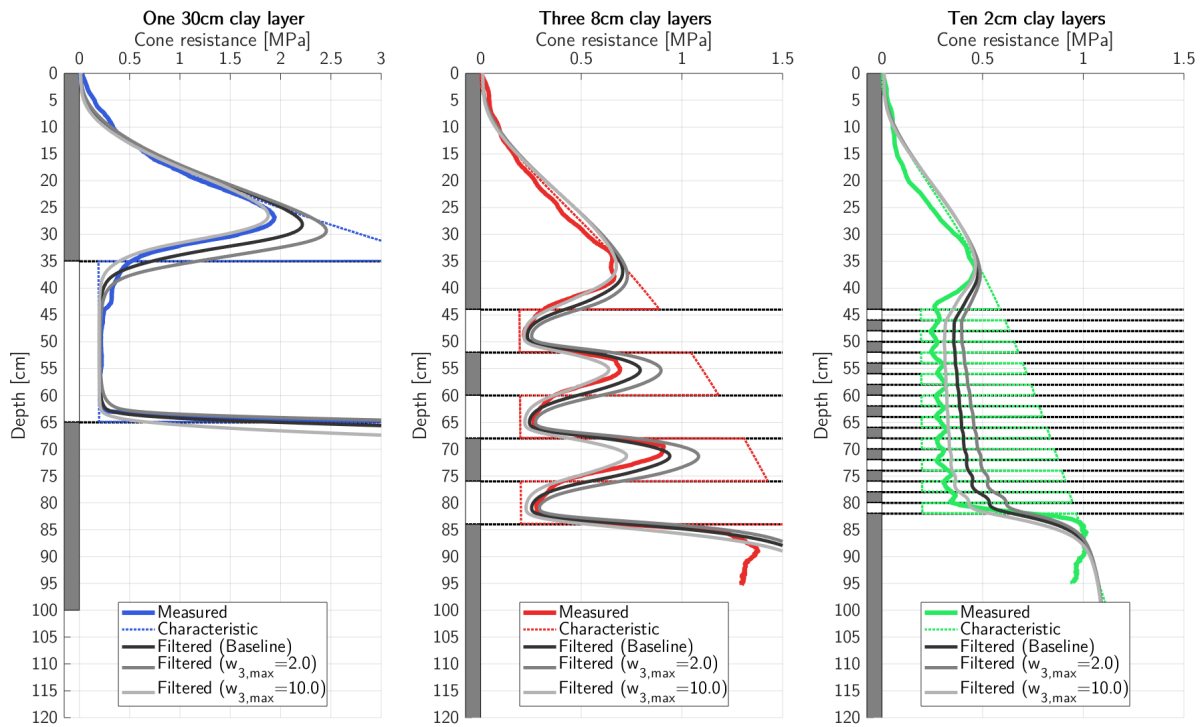

Figure B.21. *Measured profiles from the study of Van der Linden (2016). A characteristic profile is determined, and filtered profiles for different parameters are shown.*
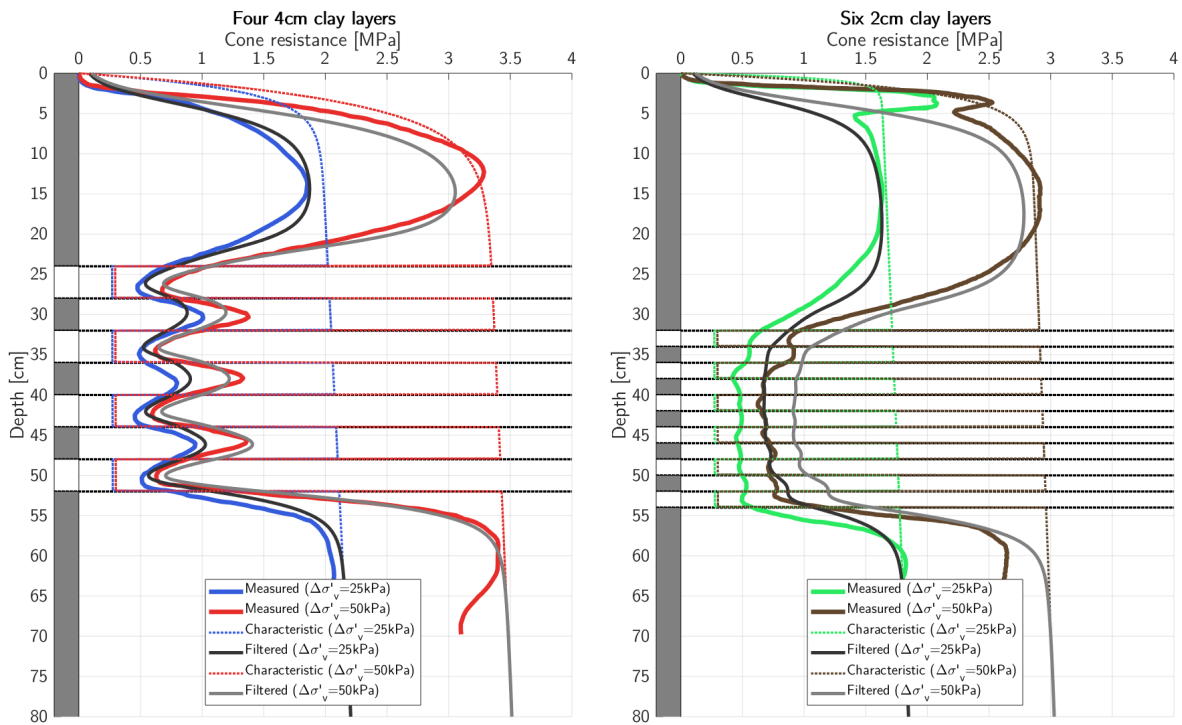
Figure B.22. *Measured profiles from the study of de Lange et al. (2018). A characteristic profile is determined, and filtered profiles are shown.*

Hallvard B. Hammer

Physical experiments on CPTU thin-layer effects of thin clay layers embedded in sand

NTNU
Norwegian University of
Science and Technology